UNIVERSITÀ DEGLI STUDI FIRENZE

DOTTORATO DI RICERCA IN SCIENZE CHIMICHE

CICLO XXIX

COORDINATORE Prof. PIERO BAGLIONI

Biodegradble Polymer/Clay nanotubes composites

Nanocompositi a base di polimeri biodegradabili e nanotubi alluminosilicatici

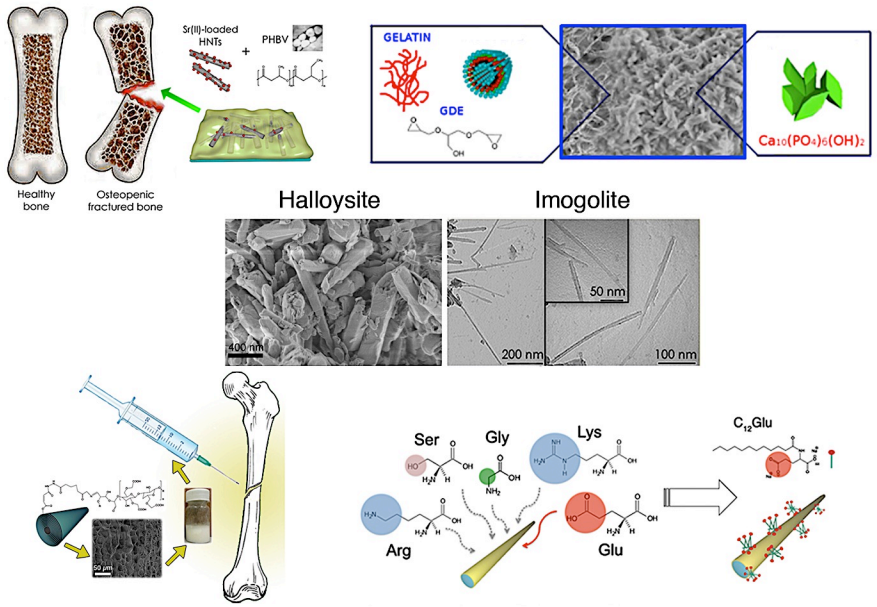

Dottorando
Dott. Stefano Del Buffa

Tutore
Prof. Massimo Bonini

UNIVERSITÀ
DEGLI STUDI
FIRENZE

DOTTORATO DI RICERCA IN SCIENZE CHIMICHE

CICLO XXIX

COORDINATORE Prof. PIERO BAGLIONI

Biodegradable Polymer/Clay Nanotubes Composites

Nanocompositi a base di polimeri biodegradabili

e nanotubi alluminosilicatici

Settore Scientifico Disciplinare CHIM/02

Dottorando
Dott. Stefano Del Buffa

Tutore
Prof. Massimo Bonini

Coordinatore
Prof. Piero Baglioni

Anni 2013/2016

Table of Contents

List of Abbreviations

(in order of appearance)

PHBV= poly(3-hydroxybutyrate-co-3-hydroxyvalerate)
SEM= scanning electron microscopy
AFM= atomic force microscopy
FT-IR= Fourier transform infrared
ICP-AES= inductively coupled plasma atomic emission spectroscopy
HNT= Halloysite nanotubes
Glu= glutamate
C_{12}Glu= lauroyl glutamate
CMC= carboxymethylcellulose
XRD= X-ray diffraction
PVA= poly(vinyl alcohol)
PHA= polyhydroxyalkanoates
APTES= (3-aminopropyl)triethoxysilane
ATRP= atom transfer radical polymerization
RAFT= reversible addition–fragmentation chain transfer
NMR= nuclear magnetic resonance
XPS= X-ray photoelectron spectroscopy
PMMA= poly(methyl methacrylate)
IMO= imogolite nanotubes
DFT= density functional theory
MTES= methyltriethoxysilane
AMTES= (aminomethyl)trimethoxysilane
MTEG= methyltriethoxygermanate
TEM= transmission electron microscopy
STM= scanning tunneling microscopy
PVC= poly(vinyl chloride)
EDX= energy dispersive X-ray analysis
DNA= deoxyribonucleic acid
UV= ultraviolet
BET= Brunauer-Emmett-Teller
BJH= Barrett-Joyner-Halenda
ATR= attenuated total reflection
HNT-Sr-PHBV= nanocomposite made of strontium-loaded Halloysite and poly(3-hydroxybutyrate-co-3-hydroxyvalerate)
TEOS= tetraethyl orthosilicate
PBS= phosphate-buffered saline
MTT= 3-(4,5-dimethylthiazol-2-yl)-2,5-diphenyltetrazolium bromide
BrdU= 5-bromo-2'-deoxyuridine
HNT-PHBV= nanocomposite made of Halloysite and poly(3-hydroxybutyrate-co-3-hydroxyvalerate)

HNT-Sr= strontium-loaded Halloysite
Rho110= rhodamine 110
CF= carboxyfluorescein
APTMS= (3-aminopropyl)triemethoxysilane
HNT-C= nanocomposite made of Halloysite and chitosan
HNT-H= nanocomposite made of Halloysite and hyaluronic acid
EDC= 1-Ethyl-3-(3-dimethylaminopropyl)carbodiimide
TGA= thermogravimetric analysis
ICDD= international center for diffraction data
DLS= dynamic light scattering
Arg= arginine
Lys= lysine
Gly= glycine
Ser= serine
PZC= point of zero charge
QCM-D= quartz crystal microbalance with dissipation monitoring
cmc= critical micelle concentration
csac= critical surface association concentration
IMO-C_{12}Glu = nanocomposite made of sodium lauroyl glutamate adsorbed onto imogolite
RHO= rhodamine B isothiocyanate
UV-Vis= ultyraviolet-visible
MA= maleic anhydride
AAD= adipic acid dihydrazide
oxCMC= partially oxidized carboxymethylcellulose
NC-MA= nanocomposite made of maleic anhydride-functionalized Halloysite nanotubes and partially oxidized carboxymethylcellulose, linked via a hydrazone bond
Gel= gelatin
GDE= glycerol diglycidyl ether
EGDE= ethylene glycol diglycidyl ether
HA= hydroxyapatite
Gel_{GDE}= gelatin hydrogel cross-linked with glycerol diglycidyl ether
Gel_{GDE}-IMO= nanocomposite hydrogel made of imogolite and gelatin cross-linked with glycerol diglycidyl ether
FE-SEM= field-emission scanning electron microscopy
SAXS= small angle X-ray scattering
Gel_{GDE}-CaP= mineralized gelatin hydrogel cross-linked with glycerol diglycidyl ether
Gel_{GDE}-IMO-CaP= mineralized nanocomposite hydrogel made of imogolite and gelatin cross-linked with glycerol diglycidyl ether
CHA= carbonated hydroxyapatite

List of Figures

List of Tables

1 Introduction

Polymeric materials are nowadays essential to several technologic applications and play a ubiquitous role in improving people's everyday life. From packaging, textiles and microelectronics to building materials, coatings, adhesives and cosmetic products, the use of polymers in different forms (*i.e.*, pods, films, fibers, foams, polymeric solutions and suspensions, solid plastics, gels, etc.) is globally widespread, with a total production exceeding 300 million metric tons worldwide[1]. Such an extensive use of polymers necessarily poses some serious environmental issues. The production of polymers and plastics, still to this day, mainly comes from petrochemical sources, raising global concerns about the depletion of fossil reserves, supply security, greenhouse gas emissions, and feedstock costs[1]. Furthermore, since at least 40% of the total production is used in short-term applications (*i.e.*, packaging), the tremendous accumulation of petrochemical plastic wastes represents another harm for the environment, with a direct impact on marine and terrestrial life[2].

To this regard, biodegradability (*i.e.*, degradation caused by enzymatic process resulting from the action of cells[3]) definitely stands out as an added value to polymeric materials, and both fundamental and applied research in the field have remarkably grown in the recent years. However, what is generally considered as a limitation to the large-scale usage of biodegradable polymers is the lack of processability, thermal stability and barrier properties, as compared with traditional plastic materials. In this respect, a promising solution may be represented by biodegradable polymer nanocomposites[4]. A nanocomposite is as a multiphase solid material where one of the phases has one, two or three dimensions of less than 100 nm, or structures having nano-scale repeat distances between the different phases that make up the material. At the nano-scale, materials display peculiar and size-dependent properties that can be attributed, for instance, to a large fraction of surface atoms, large surface energy, spatial confinement and reduced imperfections[5]. Incorporation of nano-fillers into polymer matrices can lead to enhanced mechanical, thermal, and optical properties that can be fine-tuned by varying shape, dimensions and surface chemistry of the filler. Regardless the application, the control of the spatial and orientational order (in the case of non-spherical objects) of

the nanostructures in the bulk matrix, and the transfer of this order up to the macroscale is crucial in determining the final performance of the composite[6]. The literature in the field of polymer nanocomposites is huge and covers a broad range of materials, processing methods, characterization set-ups, and applications[7–12].

Biodegradable polymers not only represent a credible solution to the issue of plastic waste accumulation, but they are also ideal candidates for the design of bio-nanocomposites, biomaterials [a] and bio-devices. Biodegradable polymers can either be produced from conversion of biological sources or from synthetic routes, since their biodegradability (in water, air or soil) is not strictly dependent on the origin of the material but rather on its composition, structure (*e.g.*, the higher the degree of crystallization, the higher the stability to water and enzymatic degradation) and on the concomitance of favorable external factors such as T, pH, presence of microorganisms and exposure to radiations[1]. Biodegradable polymers are generally biocompatible (*i.e.* able to come in contact with a biological system without producing an adverse effect) and particularly indicated for all those applications where a permanent support (*e.g.*, bone implants, vascular prosthesis) is not requested, so the biomaterial has to be safely cleared from the organism after having accomplished its mission[13]. Drug-delivery systems, scaffolds for tissue engineering, capsules and coatings used in pharmaceutical and food products, for instance, should all meet this requirement.

The design of efficacious devices for biomedical applications is a complex and multidisciplinary task. The role of chemists is central in the selection and proper modification of the constituent materials, in the formulation/realization of the product at the lab-scale and in the physico-chemical characterization during the pre-clinical stages, but a synergy between different figures (physicists, biochemists, materials scientists and doctors) is indeed essential. The best strategy is to learn from Nature[14] that is, completely understanding how natural biosystems work (at the molecular, nano-, micro- and macro-scale) and then trying to mimic them[15]. Biological systems are extremely complex and possess unique features such as self-assembly properties (*i.e.*, the structures are

[a] A biomaterial is defined by IUPAC as a material exploited in contact with living tissues, organisms, or microorganisms[3]

constructed from the bottom up), hierarchical scale-dependent structures operating in a synergistic fashion, multi-functionality, high specificity, and an intimate connection between materials and design. Therefore, depending on the medical target, several factors must be taken into account in the design of a biomaterial, such as:

- bioactivity[b];
- composition, size and surface chemistry (*i.e.*, molecular recognition), which are key features for a site-specific application;
- well-suited mechanical and interfacial properties, as well as a precise resistance to physiological media;
- responsiveness to external stimuli such as pH, T, ionic strength gradients and exposure to radiations;
- internal structure and surface texture of the right scale in order to promote, or avoid, cell adhesion, tissue integration and vascularization.

Since no single material can meet all the requirements for any particular biomedical applications, a great attention is devoted to the development of multifunctional composites. In particular, thanks to the structural and chemical versatility offered by nanomaterials, together with the possibility of tailoring the properties with *ad hoc* synthetic/formulative strategies, bionanocomposites have recently gather a lot of consideration[16].
Biological materials display a range of remarkable physico-chemical properties that have evolved for a specific application, such as defense, lightweight, adhesion, impact resistance, and so forth. As a matter of fact, to obtain such properties Nature often utilizes nanocomposites. Fox *et al.*[17] got inspired from the water-enhanced mechanical gradient character of the squid beak, for instance, to prepare a nanocomposite able to mimic the architecture and properties of the natural material. By using functionalized cellulose nanocrystals, a poly(vinyl acetate) matrix and a photo-induced cross-linking strategy, they were able to synthesize a mechanically dynamic nanocomposite, in which the degree of mechanical softening, upon exposure to water, can be controlled by altering the degree of cross-linking,

[b] Defined by IUPAC as the capability of a substance, such as a *drug* or a vaccine, to provoke a response from a living matter[3]

or the exposure time of different parts of the material. The use of nanostructured engineered biomaterials is also particularly indicated for theranostic devices, *i.e.* multifunctional nanomedical platforms for simultaneous diagnosis and therapy. For example, silica-based nanostructured materials can be easily modified, allowing for the immobilization of fluorescent dyes and paramagnetic metal complexes to be used as imaging probes. At the same time, the large surface area and pore volume of mesoporous silica ensure facile adsorption and high loading of various therapeutic materials. Moreover, the pore surface and opening of mesoporous silica nanoparticles can be functionalized with stimuli-responsive groups, inorganic nanoparticles, supramolecules, and proteins that can work as caps and gatekeepers, so that the controlled release of encapsulated drugs can be triggered in response to internal or external stimuli[18].

Another field that has been remarkably influenced by the recent progresses in the research on bionanocomposites is bone tissue engineering. Bone is an extraordinary example of naturally occurring bionanocomposites, in which the components are organized hierarchically, from the macro to the nanometer scale (see Figure 1.1). It is a complex and a highly specialized form of connective tissue that provides mechanical support and serves as a reservoir for minerals, particularly calcium and phosphate[19]. The bone matrix is composed of two major phases at the nanoscale, namely: organic (protein) and inorganic (mineral). These phases have multiple components, which consist of, in decreasing amounts, minerals, collagen, water, non-collagenous proteins, lipids, vascular elements, and cells. The bone mineral is mainly composed of hydroxyapatite and the bone protein is mainly composed of collagen. Here, collagen acts as a structural framework in which plate-like tiny hydroxyapatite crystals are embedded: the prime role of minerals is to provide toughness and rigidity to the bone, whereas collagen provides tensile strength and flexibility. The bone collagen has a typical fibrous structure, whose diameter varies from 100 to 2000 nm. Similarly, hydroxyapatite in the bone mineral is in the form of nanocrystals, with dimensions ranging from 4 to 50 nm[20]. Bone is a highly vascularized dynamic tissue, since it undergoes a constant re-modeling and chemical exchange with the rest of the body, and has a unique ability for self-repair

as a result of cellular activity and external mechanical demands [21]. Bone formation occurs biologically by intramembranous ossification (as in the case of flat bones, like skull) and endochondral ossification (as in the case of long bones and fracture healing). In the first case, there is a direct differentiation of mesenchymal progenitor cells into bone-forming osteoblasts, while in the other case the progenitor cells form an intermediate cartilaginous template that is later mineralized[22,23].

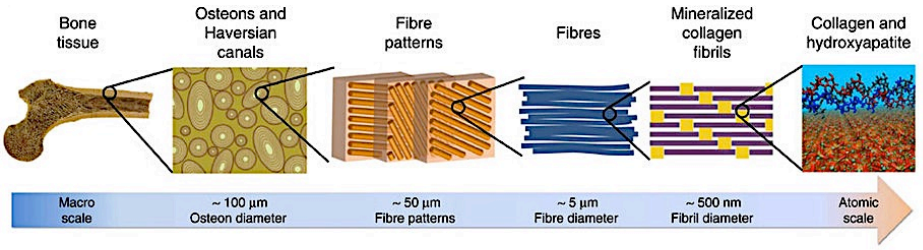

Figure 1.1 Hierarchical structure of bone (reprinted from ref.23)

The final structure is an ordered mineral–collagen composite, with several levels of hierarchy, and unique mechanical properties. However, bone defects and bone loss can originate from the imbalance between bone formation and resorption (*i.e.*, osteoporosis), congenital malformations, fractures and other injuries. The need for synthetic bone grafts and/or medical treatment depends on the complication of bone defects. In the case of severe defects and loss of volume, bone would not heal by itself and grafting/medication is required to restore natural functions. There is, therefore, a great need for engineering multi-phase materials with structure, composition and mechanical properties similar to natural bone[24], in order to reverse bone defects and/or regenerate bone tissue. Grafting is a widely applied, conventional surgical procedure for bone repairing, but it is limited to complications such as donor-site morbidity, rejection, infections and disease transmission. On the other hand, bone tissue engineering and bioinspired fabrication of bone analogues represent viable alternatives. A general goal of bioinspired bone tissue engineering is to generate bone grafts that: (i) mimic the chemical composition and nanostructure of bone, (ii) provide sufficient initial mechanical strength and stiffness to substitute for lost bone, (iii) support proliferation and differentiation of osteoblasts and the expression of bone extracellular matrix, (iiii) possess a three-

dimensional porous interconnected network with adequate mechanical strength for vascular tissue ingrowth[22]. Due to the inherent complexity of bone tissue, a perfect scaffold able to precisely mimic the hierarchical structure, morphology and functions of bone has not yet been developed. Significant advances in terms of adopted materials and processing techniques, as well as in the understanding of biochemical factors regulating the mineralization process have been done in the recent years[25,26], but still a lot of research needs to be carried out in order to ultimately bring technology into clinical application.

1.1 Aim of the thesis and outline

The research described in this thesis is aimed at the preparation and physico-chemical characterization of nanostructured polymer-based systems for biomedical application, especially in the bone medication field. The focus of this work is the use of biodegradable polymers in combination with inorganic nanostructures, namely 1D nano-clays, but rather than focusing on a specific system, different materials and processing techniques have been investigated, each of them connected to a particular physico-chemical aspect of a determined biomedical need.

In **Chapter 2**, a general description of the materials used in this work is given. In particular, greater attention will be devoted to the structural and physico-chemical properties of the adopted 1D nanoclays (halloysite and imogolite), and on their role in nanocomposites for industrial and biomedical applications. A brief overview of the biodegradable polymer matrices adopted in the work is also given in **Chapter 1**.

In the subsequent sections, four case studies on the use of nanocomposite systems in different biomedical areas will be described. In **Chapter 3**, the preparation and characterization of a bioactive hybrid film made of Sr-loaded halloysite embedded within a biopolymer matrix is reported. The adopted polymer (3-polyhydroxybutyrate-co-3-hydroxyvalerate, PHBV) is a biocompatible and biodegradable material already used in several environmental and biomedical applications, while the inorganic component is a clay nanotube with peculiar mechanical and cation-exchange properties. In particular, we chose to adsorb strontium(II) ions on the surface of the clay nanotube in order to enhance its bioactivity. In fact, strontium-based drugs have been widely prescribed over the years to treat osteoporosis, but when Sr(II) is orally administered at high doses it could increase the risk of heart attack and other side effects. Rather than through its systemic administration, it is therefore crucial to deliver strontium(II) at the treatment site, so that its bioactivity could be locally exploited, avoiding the associated collateral effects. A possible carrier for Sr(II) is thus represented by the synthetic graft matrix constituted by the clay nanotube and PHBV. The composite material has been thoroughly characterized by means of physico-chemical methods (SEM, AFM, FT-IR, ICP-AES, N_2 porosimetry, calorimetry) and the *in vitro* biocompatibility was demonstrated through cytotoxicity tests on fibroblast cells. Results

have shown that the interaction of the hybrid system with the physiological environment is mediated by the biopolymer coating, which acts as a binder, as well as a diffusional barrier to the Sr(II) release. Furthermore, the material can be applied as a filmable coating to enhance the bone regeneration capacity of synthetic bone grafts, but it can also be fabricated as a self-standing biomaterial.

Chapter 4 reports on the study of the upload/release capacity of engineered nanoclays. In a first example, halloysite nanotubes (HNT) were integrated with chitosan and hyaluronic acid to obtain hybrid nanocomposites with opposing charges, and their potential in the controlled release of drug model probes was investigated. The high surface area and the hollow nanometric sized lumen of HNT allowed for the efficient loading of rhodamine 110 and carboxyfluorescein, used as models for oppositely charged drugs. In the case of chitosan, the preparation of the nanocomposite was carried out exploiting the electrostatic interaction between the polymer and HNT in water, while with hyaluronic acid a covalent functionalization strategy was employed to couple the polymer and the clay. For the release experiments, a fixed amount of nanocomposite material loaded with the fluorescent dyes was placed in water and kept under agitation. At specific intervals of time (up to a period of 48 hours) an aliquot of the dispersion was centrifuged, and the concentration of the released probes was evaluated from the fluorescence intensity of the supernatant solution. Results showed that the polymeric coatings were successful in modulating the charge of the halloysite surface and altering the release kinetics of the probes. In particular, the model adopted to fit the release kinetics described very well the experimental data, indicating that both charge and coating composition play a key role in the desorption process from halloysite-based composites.

In a second example, the adsorption of different amino acids onto imogolite nanotubes was investigated by means of turbidimetry, ζ-potential measurements, and FT-IR spectroscopy. A high affinity of glutamic acid (Glu) for imogolite surface was observed, and this finding was exploited to prepare a composite material made of lauroyl glutamate (C_{12}Glu) adsorbed onto imogolite nanotubes. The obtained hybrid was then used in a proof of concept experiment for the upload of a model drug. The amount of uploaded drug drastically increases when C_{12}Glu is

present, highlighting the crucial role of the surfactant's alkyl chains as hydrophobic pockets. The obtained results strongly point out towards the possibility of using glutamate-based surfactants and imogolite nanotubes for the design of hybrid systems for biomedical applications, and that the approach used can be generalized towards any aluminum oxide surface. Furthermore, the interaction of glutamate with imogolite surface could be exploited for modulating the chemical affinity between polymers bearing glutamate-based functionalities and the nanotube wall, paving the way to a more extended use of imogolite in the fabrication of nanocomposites.

Chapter 5 deals with the structural and rheological characterization of an injectable composite hydrogel, made of carboxymethyl cellulose (CMC) and halloysite nanotubes (HNT), conceived for minimally invasive surgery. Chemical modification of the clay surface followed by an hydrazide-aldehyde coupling protocol with partially oxidized cellulose successfully produced a CMC-HNT hybrid, able to form a hydrogel when dispersed in water. Structural and rheological properties of the composite are driven by chemical and structural design, with nanotubular fillers playing a crucial role as rheo-modifiers. Results highlight that halloysite nanotubes are homogeneously distributed in the composite material and that the hydrogel-forming properties of CMC are retained. The introduction of HNTs in the CMC matrix, due to their chemical functionalities favoring inter-chain interactions, substantially modifies the rheological behavior of the system, making it significantly more viscous (at least twice as much) in the entire range of explored shear rates. A key aspect of the work was the careful evaluation of the material's injectability, which represents a critical factor for the use of new materials in the biomedical field. In spite of the presence of inorganic nanostructures that could in principle aggregate and obstruct the orifice, the injectability was mostly dictated by the cellulose matrix, as no major difference was observed between the composite and the reference hydrogels. This was attributed to the 1D structure of the clay nanotubes, which tend to align with the direction of the flow. Injection, *i.e.* high stress, produced a strong change in the structure of the polymer matrix at the microscale and this was reflected in the rheological properties of the material.

Chapter 6 reports on the preparation and on the mineralization properties of macroporous composite hydrogel made of chemically cross-linked

gelatin and imogolite nanotubes. Imogolite nanotubes have been synthesized and successfully integrated in a cross-linked gelatin matrix, then an extensive characterization has been conducted highlighting the role of the cross-linking agent and the inorganic filler in determining the stability in physiological conditions and the mineralization properties. The composite hydrogel was properly designed so to address multiple requisites in the bone tissue engineering field: the polymer matrix, as well as the adopted chemical cross-linking agent (glycerol diglycidyl ether), is fully biocompatible and biodegradable; the inorganic matrix has high surface area, low toxicity, a remarkable mechanical strength and stability; the composite material has a multi-scale macro-sized porosity that should favor osteoconductivity and cell permeation *in vivo*. The key finding of the work is that the presence of imogolite nanotubes in the hydrogel enhances the formation of hydroxyapatite crystals, as observed by means of thermogravimetry and XRD after simulation of a mineralization process with a standard protocol, presumably acting as crystallization seeds. Further studies need to be performed before any *in-vitro* or *in-vivo* application, but still there are strong evidences that imogolite nanotubes could represent promising scaffolds in the field of bone tissue engineering.

All the papers (published and submitted) related to the presented work, including all experimental details about the preparation and characterization of the materials described in this thesis, are finally given in the appendix. A paper pertaining to a work not related to the PhD project, but published during the same period, is also given in the appendix.

2 Materials

2.1 Polysaccharides

Polysaccharides are a class of macromolecules ubiquitous in Nature that primarily serve as energy source for many organisms and as structural building blocks for animal tissues, plant walls and bacteria membranes. Polysaccharide constituting units, *i.e.* carbohydrates, are also involved in several biochemical processes such as healing, blood clotting, molecular recognition, signal transduction and so on. Polysaccharides generally possess a strong affinity for water, since each hydroxyl group along the glycosyl units can establish intramolecular hydrogen bonding interactions with water molecules. However, solubility and rheological properties of their solutions are strongly dependent on concentration, composition, structural configuration (*i.e.*, branched *vs* linear), molecular weight, molecular weight distribution, temperature, pH, and presence of salts. Depending on the system, at sufficiently high concentration polysaccharides in water can also form gels. The state of water in such complex systems drives their physico-chemical properties, and thus their applicative potential. Polysaccharide solutions and gels are commonly used as binders, swelling agents, plasticizers, thickening agents, moisture retaining and film forming materials. Among all polysaccharides, chitosan and hyaluronic acid have been extensively studied and used to make hydrogels, nanocomposites and drug carriers[27–30], thanks to their chemical versatility, biocompatibility and biodegradability.

Hyaluronic acid is a natural polysaccharide in which the repeating unit is constituted by glucuronic acid and N-acetylglucosamine linked via alternating β-1,4 and β-1,3 glycosidic bonds. Hyaluronic acid is a natural, water-soluble polysaccharide (in its sodium salt form) omnipresent in the tissues of humans and other mammalians (*e.g.*, sinovial fluid, cartilage, skin, etc.). It is an essential component of the extra cellular matrix in which its structural and biological properties mediate cellular signaling, wound repair, morphogenesis, and tissue hydrodynamics[31]. Hyaluronic acid and its derivatives find application as dermal fillers[32], therapeutic agents[33], and as

building blocks in biomaterials for tissue engineering and regenerative medicine[34].

Chitosan is a linear polysaccharide constituted by D-glucosamine and N-acetyl-D-glucosamine linked via β-1,4 glycosidic bonds, that is obtained from deacetylation of chitin, the major constituent of the arthropods exoskeleton and the second most abundant biopolymer on earth. Due to the presence of basic amino groups in the polysaccharide backbone, chitosan is soluble in acidic solvent mixtures, *e.g.* dilute acetic acid solution (pH~5). The main parameters influencing its characteristics are molecular weight and degree of de-acetylation. Chitosan is biocompatible, biodegradable, it promotes wound-healing and has bacteriostatic effects, allowing its use in several biomedical applications in various forms, like physically and chemically cross-linked hydrogels, sponges, fibers, films and membranes[35,36]. The use of chitosan in the fabrication of nanocomposite materials for biomedical applications is extensively reported as well[37–40].

Cellulose is another important natural polysaccharide made by glucopyranose monomers linked via β-1,4 glycosidic bonds. The polymer configuration and the presence of a great number of hydroxyl groups able to form intermolecular hydrogen bonds, allows for the alignment of different polymer chains and the formation of crystalline domains (*i.e.*, micro fibrils) with high tensile strength. The same effect is at the basis of the insolubility of cellulose in water and other common polar solvents. The discovery of cellulose dates back to 19th century, and since then it has been used for the fabrication of several materials such as paper and paperboard, celluloid, textile fibers (*e.g.*, rayon), films, and so on. Recently, nanocrystalline cellulose has been also widely used as filler in nanocomposite materials to increase mechanical and thermal properties of various polymer matrices[41,42]. The hydroxyl groups of cellulose can be partially or fully reacted with several reagents, giving rise to a huge number of cellulose derivatives with different properties and applications. Carboxymethyl cellulose (CMC) is a cellulose derivative in which some of the hydroxyl groups are substituted with carboxymethyl residues *via* esterification. CMC is highly soluble in water, in which it forms a hydrogel, and it is commonly adopted as a rheological modifier or additive in several

water-based industrial formulations (*e.g.*, it is used in food industry under the E number E466). CMC and its derivatives found also wide use in biomaterials and bio-based applications[43–45] thanks to its good adhesive and film forming properties, together with biocompatibility and biodegradability. For instance, some CMC-based calcium phosphate cements already exist as marketed products (CALSTRUX®, MBCP® gel).

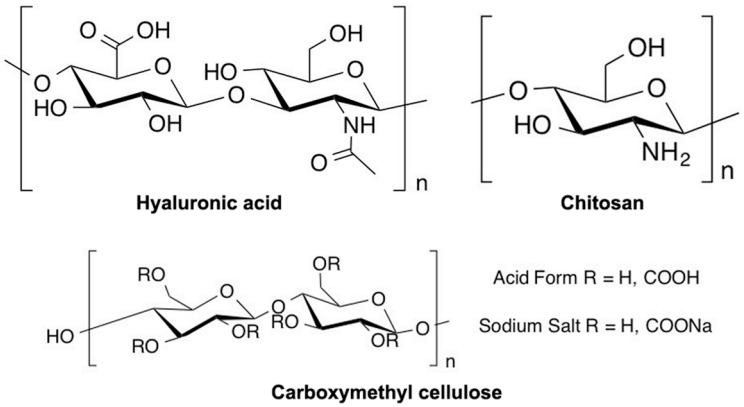

Figure 2.1 Molecular structure of polysaccharides adopted in this work: hyaluronic acid, chitosan (see **Chapter 4**) and carboxymethyl cellulose (see **Chapter 5**).

2.2 Aliphatic polyesters

Polyesters are a class of polymers containing the ester functional group in their main chain, largely employed to make fibers, textiles, and many other consumer goods, such as plastic bottles, films, liquid-crystal displays, etc. Aliphatic polyesters can be obtained from synthetic monomers of both petrochemical and natural origin, as well as from microbic fermentation of biotechnologically engineered bacteria.

Poly(vinylalcohol) (PVA) represent on of the most important and common polyester. PVA is a water-soluble synthetic polymer produced by hydrolysis of poly(vinylacetate). The degree of hydrolysis, together with molecular weight, is a critical parameter in determining the crystallinity, swelling behavior, solubility and mechanical properties of the final material. Thanks to its good processability, thermal and chemical resistance, PVA is widely used to make adhesives, coatings, water-soluble packaging and gels.

PVA is also non-toxic and biocompatible, and for these reasons it finds wide use in personal care and biomedical applications including cosmetics[46,47], drug-delivery[48], cartilage replacement[49] and many others.

Among the great variety of bio-plastics and bio-polymers available today, polyhydroxyalkanoates (PHAs) represent one of the most promising classes because of their tunable properties[50] and especially because of their 100%-natural origin. PHAs are thermoplastic polyesters completely synthesized by microorganisms, such as *Pseudomonas putida*, *Ralstonia eutropha* and *Aeromonas hydrophila*, and are biodegraded by several bacteria commonly found in soils, activated sludge and seawater[51]. Depending on the bacterial species and growth conditions, a great variety of molecular building blocks can be obtained. Thermal, chemical and physical properties are strongly affected by polymer composition and degree of crystallinity, so the choice of the appropriate PHA depends strictly on the designated use. PHA-based products are currently used as degradable shopping bags, molding containers, disposable razors, surgical pins, and as additives in food products and surfactants[1].

The biopolymer adopted in this work is poly(3-hydroxybutyrate-co-3-hydroxyvalerate) (PHBV), a copolymer of 3-hydroxybutanoic acid and 3-hydroxypentanoic acid. The physico-chemical properties of PHBV are affected by the ratio of the two monomers: in particular, a 5-20 %mol in 3-hydroxypentanoic acid content provides a useful range of properties broadly similar to those of polyethylene and polypropylene, and markedly improves the melt-processability. Several *in-vitro* and *in-vivo* studies have demonstrated that PHBV can be safely employed to make biodegradable, implantable devices for the local delivery of therapeutics and to make scaffolds for tissue engineering, since it generally does not cause any inflammatory response in the organism[52]. In the field of bone medication, for instance, PHBV finds use as the polymer matrix of hydroxyapatite-based composites[53,54]. The suitable mechanical and biological properties of the prepared scaffolds, together with the great processability and chemical versatility of the polymer, are claimed as major advantages of the use of PHBV compared to other biodegradable polymers.

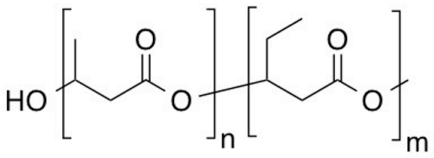

poly(3-hydroxybutyrate-*co*-3-hydroxyvalerate)
PHBV

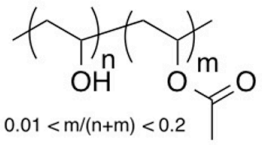

poly(vinyl alcohol)
PVA

Figure 2.2 Molecular structure of poly(3-hydroxybutyrate-co-3-hydroxyvalerate) (see **Chapter 3**) and poly(vinyl alcohol).

2.3 Gelatin

Gelatin is a biopolymer obtained by denaturation of collagen, which is the major constituent of tissues such as skin, tendons and bones. A collagen molecule is formed by right-handed triple helices with a length of about 300 nm and a pitch of 8.6 nm, formed by three left-handed helices each having a pitch of 0.9 nm and a molecular weight of approximately 100 kDa. Acid or alkaline hydrolysis of collagen leads to the breakage of bonds between the triple helix strands, resulting in the denaturation of the tertiary structure of the protein and to the formation of lower molecular weight fragments. According to the production process, gelatin can present a varying distribution of molecular weights, with a corresponding variability in the rheological properties[55].

Gelatin is completely soluble in water at T > 50 °C, while it undergoes a *sol-gel* transition around 30 °C. Below this temperature, gelatin chains, that were in a random-coil conformation, start to associate in left-handed helices thanks to hydrogen bonding interactions between the amino acid residues and, at sufficiently high concentration, form a hydrogel[56]. Thanks to its biodegradability, biocompatibility, thermo-responsive character and rheological properties, gelatin hydrogels are widely employed in the food, pharmaceutical and cosmetic industry. However, for certain applications (*e.g.*, scaffolds for tissue engineering) the poor mechanical integrity of gelatin hydrogels (especially at human body temperature) is a serious problem. To overcome this, several reinforcing strategies have been implemented based on physical and chemical cross-linking[57,58]. Because of its identical composition, gelatin represent an ideal substitute for the extra-

cellular matrix in connective tissues and it is thus considered a valuable material in the field of tissue engineering[59–61].

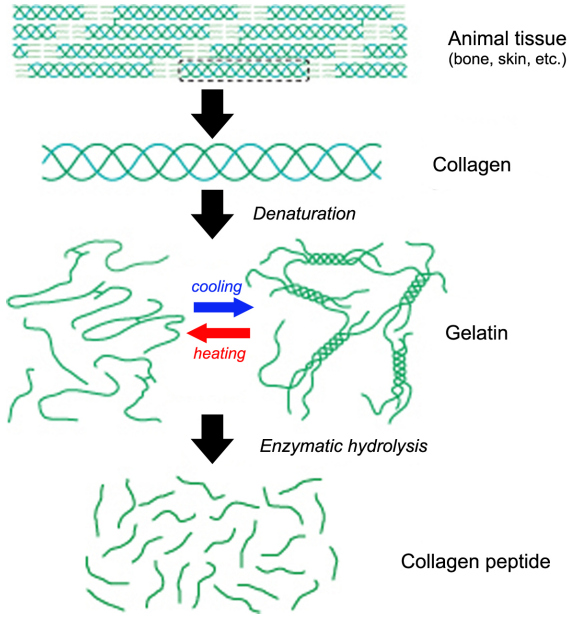

Figure 2.3 Schematic representation of the process to obtain gelatin from collagen, and of the temperature-induced *sol-gel* transition of gelatin.

2.4 Clay mineral nanotubes

The phyllosilicates, or sheet silicates, are an important class of minerals that includes the micas, chlorite, serpentine, talc and the clay minerals groups. The basic structure of phyllosilicates involves a stacked sequence of an interconnected six-member rings layer of SiO_4 tetrahedra, and an octahedral gibbsite-like ($AlOH_3$) or brucite-like ($MgOH_3$) layer (Figure 2.4). Depending on the ratio of tetrahedral to octahedral sheets in the crystalline unit cell (1:1 or 2:1), the layer-stacking sequences and the presence of interlayer materials, different phyllosilicates species can be classified. The two sheets are connected via the apical oxygen atoms of tetrahedra and the (OH) ions located at the center of the six-member rings formed by the SiO_4 layer. In the case of kaolinite ($Al_2Si_2O_5(OH)_4$), for instance, the SiO_4 tetrahedral sheet has unit cell parameters of a=5.02 Å and b=9.164 Å, while the values for gibbsite are a=5.066 Å and b=8.655 Å[62]. This lateral misfit induces a strain in the crystalline structure that can be compensated for either by rotation of adjacent tetrahedra in opposite directions around the silicate ring, or by the bending of the aluminosilicate layer to form spheroidal or tubular structures. Resulting tubular alluminosilicates are characterized by: a high aspect ratio (they can reach several micrometers in length and have a nano-sized diameter) and large surface area; the presence of a hollow lumen; the presence of two surfaces with different properties originating from the diverse composition and curvature of the inner and outer surfaces. All these peculiarities, together with their economic viability and environmental benefits compared to synthetic tubular materials, have boosted the scientific research on and the application of clay nanotubes in the field of nanotechnology, polymer nanocomposites and biomedicine.

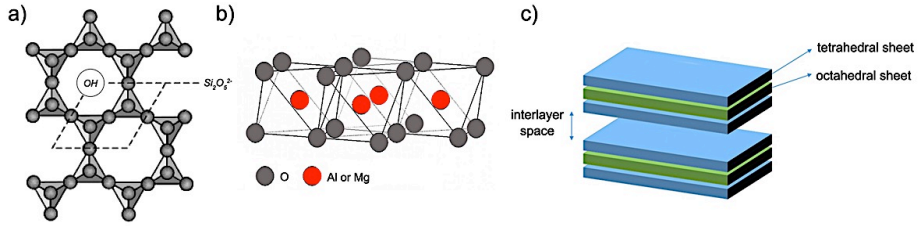

Figure 2.4 Schematic representation of a SiO_4 tetrahedra layer **(A)**, side view of a gibbsite-like layer of AlO_6 octahedra **(B)**, and layer stacking sequence of a 2:1 aluminosilicate **(C)**.

2.4.1 Halloysite

Halloysite is a naturally occurring kaolin mineral with the same chemical composition of kaolinite, except for higher water content. Halloysite can be described on the basis of hydration state of the interlayer and resulting *c*-cell axial length: halloysite (10 Å) is the more hydrated form with unit cell parameters of *a*~5.1, *b*~8.9, *c*~10.25 Å and chemical formula $Al_2Si_2O_5(OH)_4 \cdot 2H_2O$, while halloysite (7 Å) has unit cell parameters of *a*~5.1, *b*~8.9, *c*~7.3 Å and chemical formula $Al_2Si_2O_5(OH)_4$. Halloysite may occur in a number of morphologies (platy, spheroidal, prismatic), but the tubular structure is the most common and results from the wrapping of the clay layers, driven by the presence of interlayer water and by the mismatch in the periodicity between the tetrahedral SiO_4 sheets and adjacent octahedral AlO_6 sheets in the 1:1 layer[63].

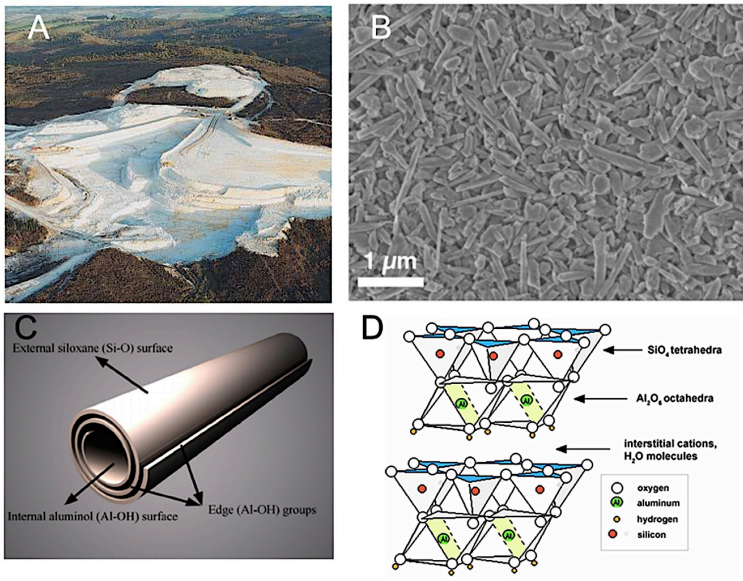

Figure 2.5 Halloysite mine in Matauri Bay, New Zealand **(A)**, SEM micrograph of the halloysite batch described in the following chapters **(B)**, schematic structure of a halloysite nanotube **(C)**, crystalline structure of halloysite **(D)**.

In other clays, the mismatch is corrected by rotation of alternate tetrahedral in opposite directions, while in halloysite the rotation is blocked due to the presence of interlayer water molecules. Halloysite morphology is related to crystallization conditions, *i.e.* geological

occurrence, and chemical composition. For instance, the amount of Fe^{3+} found in the mineral is inversely correlated to layer curvature. As the ionic radius of Fe^{3+} is larger than that of Al^{3+}, the size of the halloysite octahedra increases by ~6% when Fe^{3+} replaces Al^{3+} and the resultant increase in overall size of the octahedral sheet lessens the dimensional misfit between the sheets, allowing the layers to adopt a planar, short-tubular, or spheroidal shape[64]. As for most natural materials, the size of halloysite particles depend on their origin, with typical lengths ranging from ~800 nm to more than 10 μm, typical diameters ranging from 10 to 150 nm, and specific surface area of ~50 m^2/g. Due to their dimensions and characteristics, the term "halloysite nanotubes" (HNT, to cut short) is commonly accepted and will be used throughout the text.

2.4.1.1 Halloysite physico-chemical properties and reactivity

Since almost all halloysite tubules possess a hollow structure with an internal nano-sized lumen, the presence of two surfaces with different composition and surface charge allows, in principle, for selective adsorption and chemical functionalization strategies. Halloysite forms relatively stable colloids in water thanks to its negative ξ-potential, reaching -50 mV at pH>6. The external surface is negatively charged above pH ~2.5, dictating the electrostatic colloidal stabilization of the clay, and the internal lumen is positively charged over a wide pH range (from ~2.5 to ~8.5)[65]. This property of halloysite can thus be exploited to load negatively charged molecules into the lumen and, correspondingly, to adsorb positively charged species onto the external surface. An example of a biochemically relevant cation (Sr^{2+}) adsorbed on HNT surface will be discussed in detail in **Chapter 2**. Cation exchange capacity is a well-known property of halloysite and clay minerals in general. Cation exchange can occur at the broken bonds around the crystal edges, as substitution within the lattice and by replacing the hydrogen of exposed surface hydroxyls[66]; depending on the cation nature and concentration of the exchanging solution, intercalation complexes may also occur, leading to an increase of the basal spacing of the mineral[67]. Halloysite is more reactive than its flat analogue, kaolinite, towards several polar compounds (*e.g.*, hydrazine, potassium acetate, formamide, ethylene glycol), forming intercalation

complexes that can be reversed by the addition of water. Molecular species able to establish van der Waals, hydrogen bonding, electron-transfer and electrostatic interactions can also be adsorbed onto HNT outer surface. Unsaturated acids[68,69] (*e.g.*, sorbic and methacrylic acid), conjugated organic compounds[70] (*e.g.*, 2,5-bis(2-benzoxazolyl)thiophene), and quaternary ammonium salts[71] (*e.g.*, cetyl trimethyl ammonium chloride) are reported to adsorb onto HNT outer surface and to enhance the compatibility with different polymer matrices. Metal and metal oxide nanoparticles (Au, Ag, TiO_2, Fe_3O_4, etc.) have also been adsorbed onto HNT surface by in-situ reduction of inorganic precursors or by hydrothermal methods. Cao *et al.* [72], for instance, decorated HNT surface, previously functionalized with APTES, with Au nanoparticles synthesized by the Turkevich method (*i.e.*, citrate reduction of $HAuCl_4$) for electrochemical sensing applications. Immobilization of the nanoparticles was attributed to electrostatic interactions between positively charged amino groups of the APTES-grafted halloysite surface, and negatively charged Au nanoparticles.

The relatively low amount of reactive hydroxyl groups (*i.e.*, syloxane groups) on the halloysite outer surface allows for an efficient dispersibility (generally up to 3-5 %wt) and separation form aggregates, as a result of low interfacial interactions. On the other hand, the low reactivity of HNT outer surface due to the modest amount of SiOH groups may decrease their interaction with grafting agents and polymer matrices, generally resulting in a low functionalization degree. Nevertheless, in order to insert specific functionalities onto halloysite surface, several strategies have been successfully carried out, most of them involving, at least as a first step, hydrolysis-condensation reactions of silanes with proper composition. Yuan *et al.* [73], in one of the first report on this topic, followed a procedure generally applied for the grafting of silica-based materials to functionalize halloysite surface with (3-aminopropyl)triethoxysilane (APTES), by simply adding the silane to a suspension of halloysite in toluene, and refluxing the reaction mixture at 120 °C for 20 hours. Grafting of APTES occurred between hydrolyzed APTES molecules and surface hydroxyl groups, including the aluminol groups at the lumen surface and the aluminol/silanol groups at the edges or external surface defects. The quantity of available hydroxyl groups, which determines the content of grafted APTES results to be strongly dependent on the clay's

morphological parameters (length, external and internal diameter, wall thickness, number of defects) and on the chemical (e.g., NaOH) or thermal pretreatment steps.

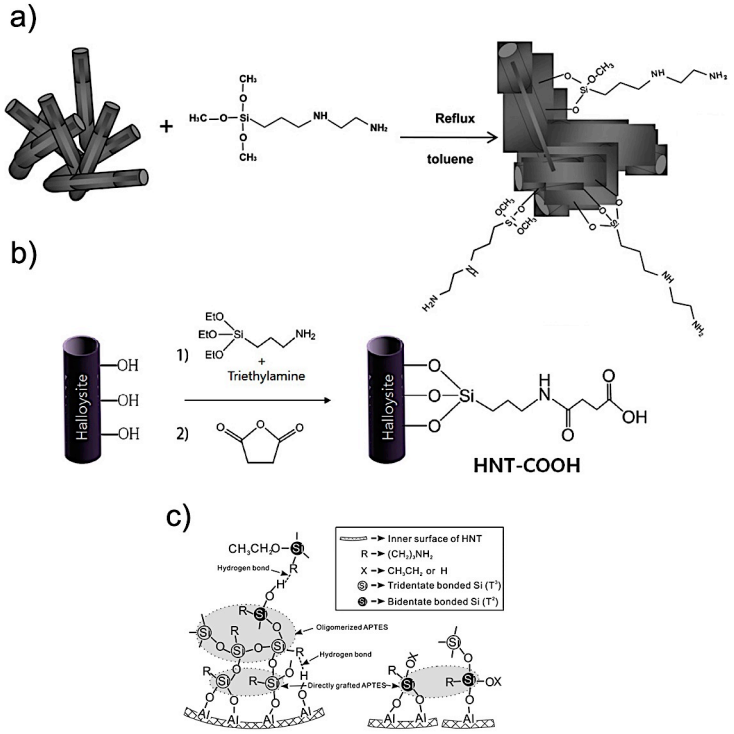

Figure 2.6 Scheme showing the grafting of 3-(2-aminoethyl)aminopropyltrimethoxysilane onto halloysite nanotubes[74] **(A)**, the modification of pristine HNT to carboxylic acid functionalized HNT-COOH[75] **(B)**, the mechanism for the formation of cross-linked APTES network on HNT surface (left) and for the grafting between bidentate bonded Si and AlOH groups (right)[73] **(C)**.

An analogous synthetic route has been adopted by Barrientos-Ramirez *et al.* to graft diamino- and triamino-silanes onto halloysite external surface in order to produce a novel catalyst support for atom-transfer-radical-polymerization (ATRP) reactions[74]. Massaro *et al.*[76] reported on the modification of halloysite with (3-mercatopropyl)trimethoxysilane by the classical wet procedure and by solvent-free microwave irradiation. Microwave-assisted synthesis and solvent-free conditions, not only

represent eco-friendly synthetic strategies, but also improved significantly the grafting of the organosilane, with respect to the traditional method. Joo *et al.* [75] started from APTES-functionalized halloysite, obtained by adding APTES and triethylamine to a suspension of HNT in toluene and mixing for 1 day at 80 °C, to insert carboxylic groups on the outer surface of the clay, by reaction of succinic anhydride in dimethylformamide. The obtained COOH-HNT exhibited pH-dependent aggregation/dispersion properties, as a result of electrostatic stabilization driven by surface charges (especially at basic pH), and hydrogen bonding interactions between pendant chains and the halloysite surface.

2.4.1.2 Halloysite-based nanocomposites

Halloysite nanotubes have been extensively studied in the field of nanocomposites, primarily because of their favorable mechanical properties. HNT mechanical properties of halloysite have been theoretically and experimentally studied: the Young's moduli for zigzag and armchair single-walled nanotubes have been calculated in the range of 230–340 GPa, while the averaged experimental value measured in a three-point bending mode is 140 GPa, being larger for tubules of smaller diameter[66]. In HNT-polymer composites, mechanical modulus, impact strength, ductility, tensile and flexural properties result improved thanks to an effective load transference from the polymer matrix to HNT via strong interfacial interactions, or thanks to the effect of the filler on the crystallization behavior of the polymer matrix. Embedding halloysite nanotubes in polymer matrices, such as polypropylene, can also increase thermal stability and induce flame retardancy. For instance, Du *et al.* [77] reported on a 30 °C increase in the temperature of 5% weight loss, with respect to pristine polypropylene, in nanocomposites with a moderate HNT loading and on a marked flame retardancy due to HNT barrier effect on heat and mass transfer. Halloysite nanotubes can also have an influence on the wettability properties of polymers, as they can tailor the surface microstructure of the nanocomposite as a consequence. For example, superhydrophobicity with a maximum water contact angle of nearly 170 degrees and sliding angle of about 2 degrees, was seen in halloysite-polypropylene nanocomposites, due to the rough surfaces

arising from the halloysite-induced heterogeneous nucleation of polypropylene[78].

Melt blending of clay particles with thermoplastic polymers or solution mixing in polar solvents often produces good nanocomposites, even though at high loading of HNT agglomerates are likely to form. A huge amount of literature is present, covering most of the commercially relevant polymers, such as polypropylene, polyethylene, polyvinylchloride, polystyrene, starch, styrene-butadiene rubber, and many more[79–83]. The influence of HNT on the mechanical and physico-chemical properties of the composite has been thoroughly investigated as a function of halloysite loading, processing method, presence of compatibilizers and surfactants, chemical functionalization of the clay surface. A fine tuning of the interfacial interactions is crucial to obtain a homogenous dispersion of the inorganic filler inside the polymer matrix, and thus a better performance of the final material[84]. For instance, Du *et al.* exploited the formation of amide bonds between APTES-functionalized halloysite (exposing amino groups) and maleic anhydride grafted polypropylene to increase the interfacial adhesion between the clay and the polymer, thus obtaining a composite with higher mechanical properties compared to the pristine polypropylene and to the simply mixed system[85]. In-situ controlled polymerization starting from functionalized HNT surface could represent an elegant, and often effective, way to obtain nanocomposite materials. In fact, with a properly designed "bottom-up" synthesis, specific functionalities (*e.g.*, responsive character) can be inserted in a controlled way, allowing for the obtainment of smart hybrid materials. Hou *et al.*[86] covalently attached amphiphilic brushes of polystyrene and poly(4-vinylpyridine) onto HNT surface *via* a reversible addition−fragmentation chain transfer (RAFT) polymerization. In the preliminary step, a chain transfer agent is grafted to the hallosyite surface via a silanization reaction, and then polymerization is started with the addition of an initiator, by increasing temperature. The obtained system was used as a Pickering emulsification agent, showing that the emulsification performance is dependent on the microstructure of amphiphilic brushes, as well as on the hydrophilic/hydrophobic segment size and sequence.

.

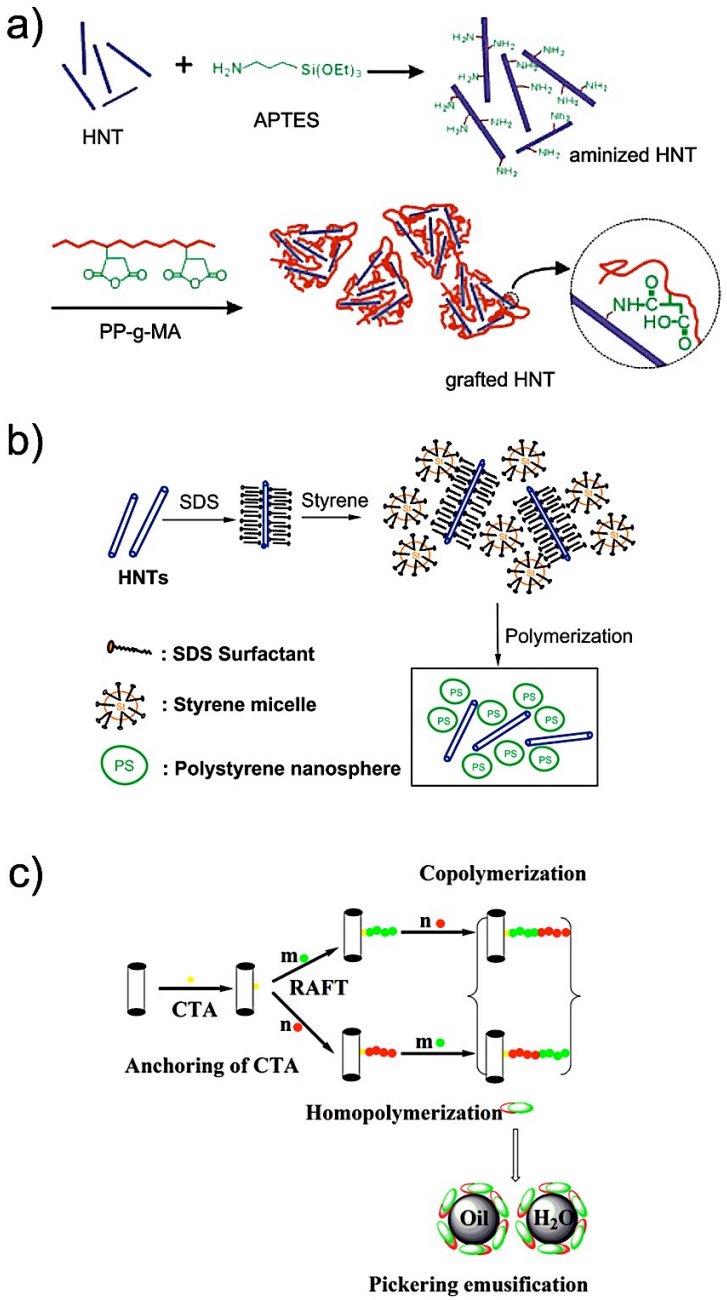

Figure 2.7 Schematic picture showing examples of the use of HNT in nanocomposites: silanized HNT integrated with maleic anhydride grafted polypropylene[85] **(A)**, in situ polymerization of styrene in the presence of HNT[81] **(B)**, the process of grafting amphiphilic brushes onto HNT *via* RAFT polymerization and their use as Pickering emulsification agents[86] **(C)**.

Li *et al.* [87] reported on the synthesis of a halloysite-polystyrene nanocomposite via a surface-initiated ATRP onto halloysite nanotubes. Halloysite was first functionalized with APTES, and then the silanized halloysite was further reacted with 2-bromoisobutyryl bromide to immobilize the initiator. Afterwards, grafting polystyrene produced the core–shell nanocomposite.

Specific physico-chemical interactions (*e.g.*, hydrogen bonding, electrostatic and van der Waals interactions) between the outer HNT surface and polymer functional groups can also be exploited to build-up nanocomposites. Chao *et al.*[88], for instance, reported on the modification of halloysite surface with dopamine, and used a model enzyme to elucidate the enzyme-immobilizing ability of dopamine-modified halloysite nanotubes. HNT were immersed in an alkaline aqueous solution of dopamine, and after several hours an adhesive polydopamine film is formed on the clay surface thanks to physisorption and subsequent self-polymerization of dopamine. Another example of non-covalent modification of halloysite outer surface is represented by the chitosan/halloysite nanocomposite, formed by taking advantage of electrostatic interactions between protonated chitosan and negatively charged HNT outer surface. A particular application of halloysite-chitosan nanocomposites in the field of controlled release will be discussed in detail in **Chapter 3**

2.4.1.3 Modification of Hallosyite internal lumen for advanced applications

Selective modification between silica-based and alumina-based surfaces in halloysite is a challenging task, and using organosilanes often results in silane bonding at both inner and outer surfaces. Organophosphorous compounds, that are known to possess a high affinity towards metal oxide surfaces, represent a possible solution. Yah *et al.*[89] used octadecylphosphonic acid to selectively modify the internal surface of halloysite and build a system with enhanced loading capacity for hydrophobic molecules. The clay and the alkylphosphonic acid were added to 4:1 vol ethanol-water mixture (adjusted to pH=4) and mixed at room temperature for one week. Vacuum was applied to the reaction mixture in order to remove all the air entrapped in the halloysite lumen and to ensure that the reactant solution effectively come in contact with the alumina surface. A detailed NMR and XPS analysis revealed the absence of any ocatedcylphosphonic acid bonding with the outer siloxane surface, and the presence of strong bidentate and tridentate Al-O-P bonds on the internal surface. The same authors also reported on the selective modification of HNT internal surface with 2-bromo-N-[2-(3,4-dihydroxyphenyl)ethyl]-isobutyryl amide (Dopa), used as an initiator for the surface initiated-ATRP to graft a layer of PMMA brush in the lumen. The selectivity of Dopa coating for halloysite lumen was ascribed to the high affinity of the catechol group of Dopa for metal oxides located at the tube inner surface and to weaker catechol−silica bonding interactions[90].

The structural characteristics of the halloysite internal lumen make it a very promising platform for controlled release applications. Moreover, halloysite natural abundance, its low extraction cost and the ease of the loading process represent further advantages over other nanotubular systems. In most cases, where hydrophilic compounds are used, halloysite is simply mixed as a dry powder with a concentrated solution of the desired active in water, ethanol, acetone or other polar solvents, and exposed to vacuum to release the air entrapped in the HNT lumen. HNT have been used for the uploading and subsequent release of different drugs, such as dexamethasone, furosemide, nifedipine[91], tetracycline, khellin, nicotinamide adenine dinucleotide[92,93]. Larger macromolecules can

also be loaded on halloysite, as long as they are able to fit the cross-sectional area of the internal lumen: globular proteins of different size and surface charge have been tested, showing a slower, and charge-dependent, release compared to lower molecular weight drugs[94].

Apart form drugs and pharmaceuticals, HNT can also act as a nano-scale container for different kind of actives, such as corrosion inhibitors for the production of self-healing coatings[95]. The loading of water-soluble benzotriazole inside the HNT lumen, and the incorporation of the modified clay into a ZrO_2-SiO_2 sol-gel coating deposited onto an Al alloy, demonstrated that the sustained release of the benzotriazole is effective in protecting the metal against corrosion. The coating without HNT showed the development of a corrosion defect during immersion in NaCl solution, while the sample coated with the film doped by benzotriazole-loaded halloysite exhibited no evidence of corrosion current and corrosion propagation. The function of benzotriazole-doped HNT is to provide slow release of the inhibitor agent, blocking the initial corrosion processes and healing micro-scale defects in the coating. The HNT container protects benzotriazole from leaching, thereby preventing the interaction with the matrix and deactivation of the inhibitor. The presence of a hollow lumen with nanometric size also suggests the use of HNT as, nanoreactors, nanotemplates and sorbents for contaminants[96]. For example, halloysite tubules were employed as hollow enzymatic nanoreactors for the urease-catalyzed mineralization of $CaCO_3$ from an aqueous solution of $CaCl_2$. The negative charge of urease enhanced its adsorption inside the positively charged halloysite lumen, and as a consequence, $CaCO_3$ was synthesized exclusively inside the hollow tubular lumen[97].

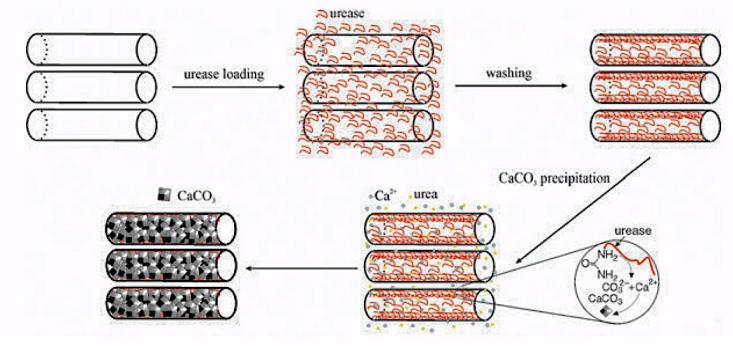

Figure 2.8 Schematic illustration of the urease-catalyzed synthesis of $CaCO_3$ inside halloysite nanotubes[97].

2.4.1.4 Biocompatibility and biomedical applications of Halloysite

Composition and structural characteristics of halloysite nanotubes has driven an increasing number of researchers to investigate their applicative potential in the biomedical field. Even though fibrous materials with micrometer length are often dangerous for human health (*e.g.*, asbestos fibers are well known to induce lung, pleural and peritoneal cancer and fibrosis), several studies have demonstrated that halloysite is well tolerated by cells, at low concentrations, and do not cause significant health issues. Tests have been carried out with HT-29 colon epithelial cells[98], MCF-7 and HeLa cancer cells[65], human dermal fibroblasts[99], providing strong evidences that HNT are biocompatible. In the case of lung epithelial cells, studies demonstrated the ability of nano-sized clays to pass the cell membrane and to accumulate in the intracellular space near the nucleus. A dose- dependent decrease in cell viability is observed for halloysite, with a strong correlation with specific surface area. However, HNT showed better compatibility with respect to platelet particles[100].

Of course, due to the large variability and complexity of the biochemical processes in a living organism, a universally accepted declaration of safety for HNT does not exist, and toxicity effects need to be evaluated on a case-by-case basis. However, halloysite is not biodegradable (at least in physiological conditions) and is suitable only for particular applications. For instance, intravenous injection of HNT, as well as other clay minerals, should be avoided as they can induce blood coagulation in a dose-dependent manner[101]. The cylindrical structure of the nanotube seems to cause more blood clotting with respect to nanospheres, suggesting a shape-specific effect on the activation and aggregation of blood platelets[102]. Application fields such as wound healing, medication of skin diseases, bone implants, dental fillers and tissue engineering, are indeed particularly indicated for halloysite nanotubes. Halloysite has been recently employed, for instance, in combination with polycaprolactone[103], poly(lactic-co-glycolic acid)[104], poly(vinyl alcohol)[105], poly(methyl methacrylate)[106], and chitosan[107] to fabricate composites with enhanced mechanical and bioactive properties. In this context, the possibility to include actives of different nature within the inorganic material and to control their release, together with the great mechanical performances induced by the presence

of HNT in polymer-based nanocomposites, is recognized as a great benefit for the production of novel and efficient biomedical devices[108].

2.4.2 Imogolite

Imogolite (IMO) is a poorly crystalline, tubular aluminosilicate composed of gibbsite-like sheets ($Al(OH)_3$), where the inner hydroxyl surface of the gibbsite is substituted by (SiO_3)OH tetrahedra. The chemical formula is $(OH)_3Al_2O_3SiOH$, which corresponds to the sequence of atoms encountered on passing from the outer to the inner surface. Imoglite thus possess an opposite arrangement of tetrahedral and octahedral sheets with respect to hallosyite, and expose an alumina-based surface (Figure 2.9).
Imogolite is a naturally occurring mineral, first discovered in volcanic soils deposits (Kyushu Island, Japan) by Yoshinaga and Aomine in 1962[109], but can also be synthesized from inorganic precursors. Farmer *et al.* [110] firstly reported on the synthesis of imogolite nanotubes starting from aluminum salt and $Si(OH)_4$ after heat treatment in acidic conditions. Several alternative synthetic path- ways have been proposed ever since, and much progress has been made to optimize the yield and purity of the obtained imogolite. The main chemical recipes for the synthesis of imogolite involve 1) the neutralization, by slow addition of hydroxyls, of an acidic aluminum salt solution in the presence of a Si source; 2) the neutralization of an acidic aluminum salt by a sodium silicate solution, that acts as a source of both Si and OH; 3) the use of organic precursors for both Si and Al in acidic conditions. For instance, Koenderink *et al.* [111] reported on the synthesis of imogolite starting from tetraethyl orthosilicate and aluminum-tri-*sec*-butoxide, mixed in a dilute $HClO_4$ solution. The solution was kept at 70 °C during 5 hours under continuous stirring, and then refluxed at 100 °C for 3 days. Several experimental parameters need to be carefully controlled to achieve an effective and reproducible synthesis of imogolite nanotubes. For example, the Si:Al ratio should be kept slightly higher than the stoichiometric 0.5 value (typical Si/Al ratios are between 0.5 and 0.66) to prevent the formation of aluminum hydroxide and other side minerals; total concentration of reagents is another critical parameter strongly connected to the imogolite growth kinetics[112]; the pH must be carefully controlled in order to have a well defined Al:OH ratio in the solution and

to avoid polymerization of Si in amorphous silica; temperature strongly affects both growth kinetics and stability of the aluminosilicate phases formed at early stages (generally T is kept below 100°C); agitation and ageing time are also critical parameters in determining imogolite final size. The general mechanism for the formation of imogolite nanotube has been the subject of numerous studies, and is now well accepted[66] (Figure 2.9-b). In the early stages of the reaction, the self-assembly of polynuclear species formed by hydrolyzed Al^{3+} and SiO_4^{2-} ions gives an amorphous precipitate of hydroxyaluminosilicate ions having an ideal Si/Al ratio of 0.5 and a structure predominantly constituted by Si–O–Al linkages. Internal restructuring during ageing, or at the beginning of the heating stage, leads to the formation of proto-imogolites. These are non-amorphous small fragments (~5 nm) of imogolite nanotubes and, as early reported by Farmer "can be presumed to incorporate orthosilicate groups attached to fragments of gibbsite-like sheets of aluminum hydroxide". Their average size, the presence of complexing anions and their mutual interactions are very important in determining the final IMO nanostructure. Finally, in proper conditions (low concentration, low pH, low salinity, and an Si/Al ratio between 0.5 and 0.6), nanotubes are obtained at the expense of proto-imogolites, upon heating. The dimensions of the natural nanotubes are ~1 nm for the inner diameter, 2.3-2.7 nm for the outer diameter, and length of more than 100 nm. Internal and external diameters of synthetic samples are typically 10-15 % greater, and imogolite length can be markedly increased (up to few microns) by increasing the reaction time. Synthetic imogolite nanotubes display a high specific surface area, typically ranging from 300 to 400 m^2g^{-1}, and multi-scale porosity resulting from internal pores (diameter of ~1 nm, corresponding to tube's lumen), intertubular pores (0.3-0.4 nm, corresponding to cavities formed by alignment of three nanotubes, and not accessible to water), and interbundle pores (disordered meso-pores resulting from bundle agglomeration). The porous inorganic structure and the high surface area imply that imogolite could adsorb a significant amount of gases and hydrogen bonded liquid, even though at high temperature (T>400°C) structural dehydroxylation results in a partial pore collapse. IMO presents indeed a significant water and moisture uptake (~30 g of water per 100g of IMO at 85 % relative humidity), mostly located in the hydrophilic nano-

sized lumen (confined water) and in the intertubular voids as bulk water. Adsorption of water on the external surface is poor, as the outer aluminum hydroxide layer is quite "hydrophobic". Such "hydrophobic" character of external IMO surface could also be invoked to explain its strong ability to form bundles and its strong interaction with natural organic matter in soils.

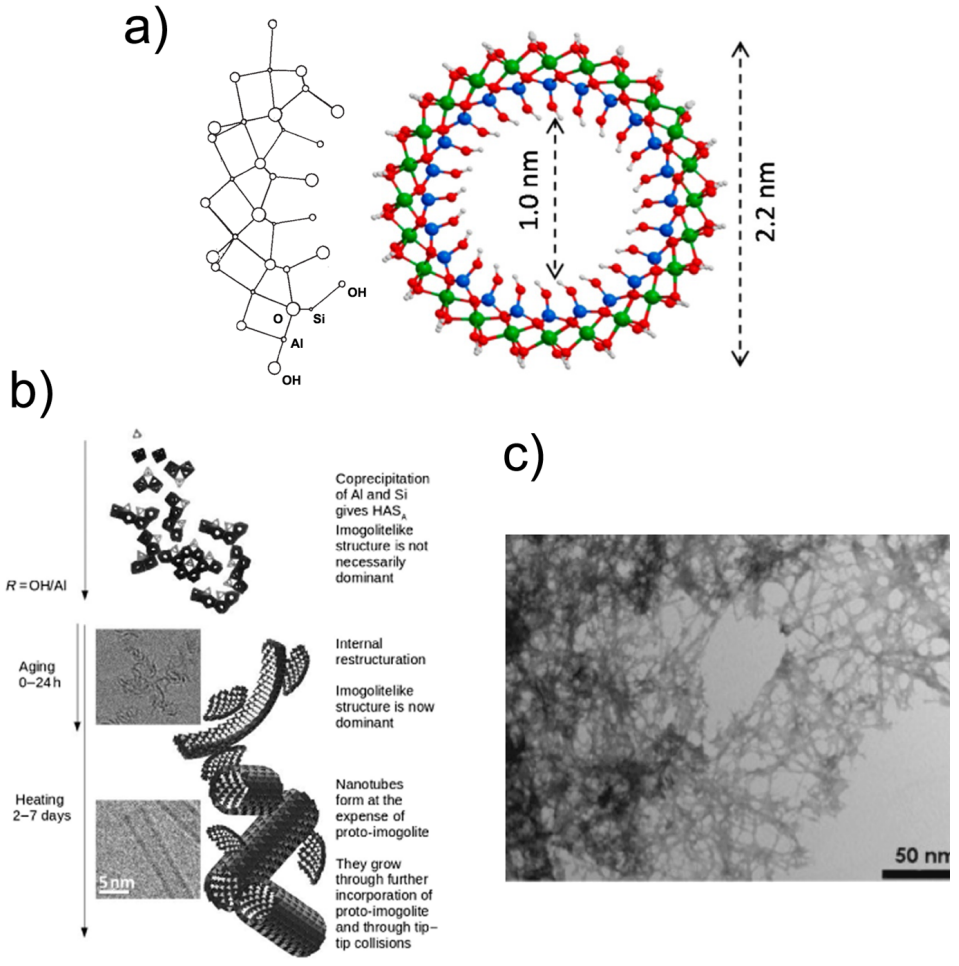

Figure 2.9 Schematic representation of imogolite structure **(A)**, schematic reaction pathway to obtain imogolite[66] **(B)**, TEM image of synthesized imogolite (see **Chapter 4** and **Chapter 6**) showing bundles of nanotubes **(C)**.

2.4.2.1 Imogolite physico-chemical properties

The stability of imogolite nanotubes and the properties arising from their unique structure have been the subject of experimental and theoretical research. As already discussed, the mismatch of the bond lengths between tetrahedral and octahedral sheets, in certain conditions, lead to the curvature of the gibbsite layer and to the formation of the tubular structure. Unlike other nanotubes for which the strain energy necessary to roll a monolayer into a tube monotonically decreases with increasing tube radius, there is an optimal curvature, which leads to the minimum strain in the structure for imogolite. Imogolite is composed of nonsymmetrical aluminosilicate layer and a difference in the surface tension of outer and inner tube surfaces must be additionally taken into account to successfully model the trend of strain energy versus tubule radius. The surface energy can support a negative curvature, decreasing the strain energy and introducing a minimum into the $E_{str}(R)$ curve (see Figure 2.10). This explains, for instance, why imogolite is monodisperse (in diameter) with very well-defined geometrical parameters and symmetry[113]. Partial or total substitution of Si with Ge in the tetrahedral sheet can be achieved by using germanium precursors during the synthesis. The outside diameter of the nanotube increases to more than 3 nm with complete Ge substitution, in accord with its greater size compared to Si and to the better fit between the O_3GeOH tetrahedra and the gibbsite layer[113]. Interestingly, Ge-rich imogolite can adopt a double-walled structure[114].

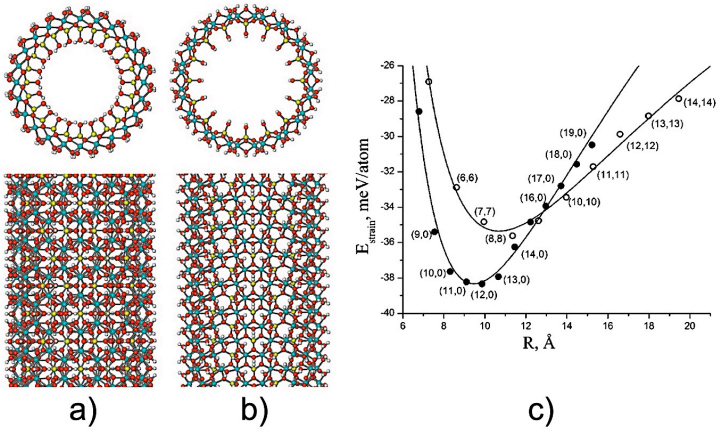

Figure 2.10 Optimized structures of *zigzag* (12,0) **(A)** and *armchair* (8,8) **(B)** imogolite nanotubes, and calculated strain energies as a function of the radius R for *zigzag* (filled dots) and *armchair* (empty dots) imogolite nanotubes **(C)**[115].

The presence of amphoteric aluminol and silanol groups located on the outer and inner surfaces of imogolite, respectively, is responsible for the build-up, in water, of permanent surface charges via pH-dependent equilibria:

$$Al\text{-}(OH)\text{-}Al + H^+ \rightleftharpoons Al\text{-}(OH_2)^+\text{-}Al \quad (i)$$

$$SiO\text{-}H \rightleftharpoons Si\text{-}O^- + H^+ \quad (ii)$$

Permanent charges in clay minerals can also be originated from Si/Al isomorphic substitution with ions of different charges. In spite of the lack of isomorphic substitutions in natural imogolite, Gustafsson[116] proposed that a weak positive surface charge is present in the outer IMO surface, based on the observation that IMO has the to ability to strongly adsorb anions. The lack of a precise structural characterization of imogolite at that time prevented from further testing the hypothesis, and the adsorption properties of IMO were justified by taking in to account the presence of defects and ill-coordinated atoms at the tube ends. Guimaraes *et al.*[115] confirmed the hypothesis of Gustaffson using DFT calculations. The imogolite charge is originated from steric effects related to the curved structure that induce a non-symmetric distribution of the electronic density around Si^{4+} and Al^{3+} cations, with longer Al–O bond lengths at the external surface of the gibbsite-like layer. Another structural feature that could lead to a net permanent charge is the presence of point defects, *i.e.* vacancies in the crystalline lattice. Surface charge of imogolite nanotubes is at the basis of their electrophoretic mobility and of the colloidal stability of IMO dispersions in water. IMO point of zero charge is around pH 10÷11, depending on the origin, and its evolution with time can also be used to assess the quality of synthesized imogolite from inorganic precursors[117]. At pH values lower than the point of zero charge of IMO, equilibrium (i) is shifted to the right, leading to an increased positive charge of the outer surface. On the other hand, at pH values higher than the point of zero charge, equilibrium (i) is shifted to the left and the external surface of IMO progressively becomes neutral. Equilibrium (ii) accounts for the internal charge of IMO, having a negligible effect on the overall surface charge and on colloidal stability of IMO dispersions.

Thanks to the high aspect ratio and rigid structure, imogolite nanotubes possess unique features when dispersed in water. A recent study on single walled and double-walled imogolite dispersions reported on the characterization of liquid crystalline phases in the low-concentration regime (volume fraction < 0.7 %), by means of polarized optical microscopy, small-angle and wide-angle X-ray scattering[118]. Imogolite suspensions exhibited a phase separation at very low volume fractions, with the appearance of an isotropic phase and a denser, birefringent nematic phase. At slightly larger volume fractions, another columnar hexagonal liquid-crystalline phase is formed, in which the rods organize on a hexagonal lattice perpendicular to the IMOs average direction. The remarkable positional ordering of the charged IMO is a strong evidence of the large intensity of the electrostatic repulsions between charged linear objects, which stabilize the columnar phase down to very low volume fractions.

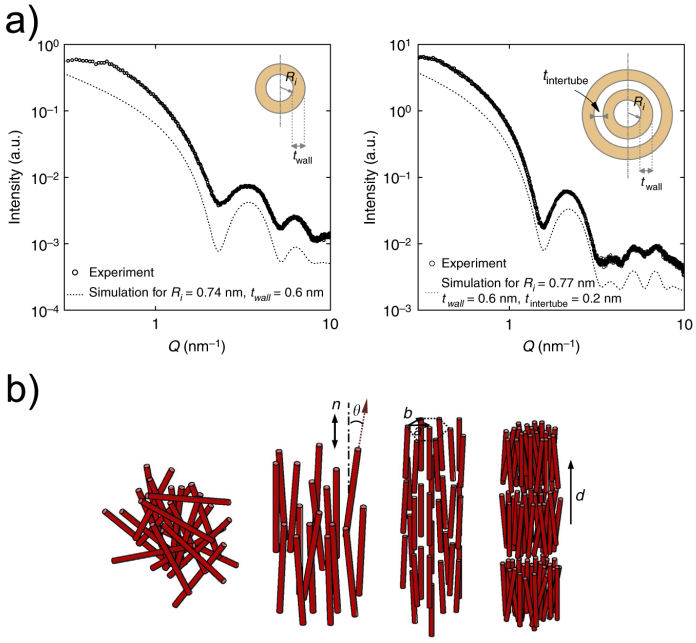

Figure 2.11 Experimental (black dots) and calculated (dotted line) wide-angle X-ray scattering curves for single-walled and double-walled imogolite nanotubes **(A)**, and schematic representation of liquid crystal phases in imogolite suspensions (from left to right: isotropic, nematic, columnar, smectic liquid phases) **(B)**[118].

2.4.2.2 Chemical modifications of Imogolite

Similar to halloysite, the tubular structure, the nano-sized dimensions and the different surface chemistry of the inner and outer sheets of imogolite make it a captivating platform for fundamental physico-chemical studies and advanced applications in the materials science. Modification of imogolite surface can be achieved either by direct synthesis methods, which is based on the replacement of the silicon precursors in the reaction mixture, or by post-synthetic functionalization. Typical examples of the first method involve the use of Ge precursors[119], or the substitution of hydroxyl groups of Si-precursors with hydrophobic moieties. One of the first successful examples of direct synthesis of organic-substituted imogolite nanotubes involved the use of methyltriethoxysilane (MTES) for producing a hydrophobic, methyl-functionalized surface[120]. The incorporation of methyl groups in the aluminosilicate structure has effects on dimensions, aggregation behavior, porosity and specific surface area. Differences have been ascribed to the electronic and steric effect of methyl groups that could lead to a shift in the energy minimum towards larger tube radii, or to a change in the external charges that could lead to an increased distance between tubes and to larger cell parameters. The change in the external charges due to the presence of methyl groups has been also related to the observed wider domains of aligned fibers, compared to bare imogolite. In fact, the absence of silanols could hinder electrostatic interactions between imogolite nanotubes, leading to fibers more loosely bound and freer to assume a close packed configuration. The behavior of modified imogolite nanotubes towards methane adsorption was studied, showing a 2.5-fold increase in capacity thanks to both hydrophobization of the lumen surface, and to a larger pore volume. Kang *et al.* [121] described the synthesis of a single-walled imogolite, in which ~15% of the interior Si-OH groups are substituted by Si-CH_2NH_2 groups, via the use of aminomethyltriethoxysilane (AMTES) as a Si-precursor. Morphology and crystallinity of the functionalized nanotube result slightly altered with respect to the bare imogolite, displaying smaller average lengths, a lower pore volume and broader diffraction peaks of specific basal reflections. The amine-functionalized nanotubes show a dramatic improvement in CO_2/CH_4 and CO_2/N_2 adsorptive selectivity compared to the bare nanotubes, and the selectivity increases with increasing

temperature and pressure. The presence of isolated amine sites as well as amine groups in close proximity to each other is considered the key factor for the observed reduction in affinity and the increased selectivity for CO_2. Amara *et al.* [122] explored the possibility to synthesize methyl modified imogolite nanotubes and to tune the Si/Ge ratio by using a mixture of methyltriethoxysilane (MTES) and methyltriethoxygermanate (MTEG). Similar to bare imogolite, a dependence of the inner cavity diameter on the substitution of Si by Ge is demonstrated, by means of SAXS, FT-IR and TEM analysis, also for methyl-modified clay nanotubes. The fine control of the size and hydrophobicity of the imogolite nano-channels allows for capturing organic molecules (*e.g.*, 3-bromo-1-propanol) from water solutions, conferring to the material a wide range of potential applications.
Post-synthetic functionalization methods can be applied both to the external and internal surface of imogolite, exploiting the chemical reactivity of AlOH and SiOH layers, respectively. In the case of internal modification, a dehydration step is always needed in order to remove physisorbed water (of course preserving the nanotube structure), ensuring an effective contact between lumen surface and reactants. Kang *et al.* [123], for instance, applied a heat treatment under vacuum (250-300 °C, 15 mTorr) before modifying the interior of imogolite nanotubes with three model compounds, namely acetyl chloride, methyltrimethoxysilane, trichlorosilane. As a reaction mixture the authors used a dispersion of imogolite in hexane, allowed to stir under nitrogen for 24 h after the addition of the organic reactant. Nitrogen physisorption measurements provided evidences that the surface modification mainly takes place in the interior of the imogolite nanotube (modified nanotubes possess significantly lower pore volumes and total surface areas, whereas no statistically significant variation in the external surface areas is observed). XRD measurements further revealed that nanotubular structure and bundling characteristics remain unchanged after the surface modification, while thermogravimetry was used to estimate the organic content in the modified imogolite, going from ~8 % using trichlorosilane, to ~9 % using methyltrimethoxysilane, to ~13 % using acetyl chloride. Finally, a significant decrease (up to 70 %) in water adsorption capacity of functionalized imogolite nanotubes demonstrate that all the surface modifications yield a lower hydrophilicity in the nanotube lumen.

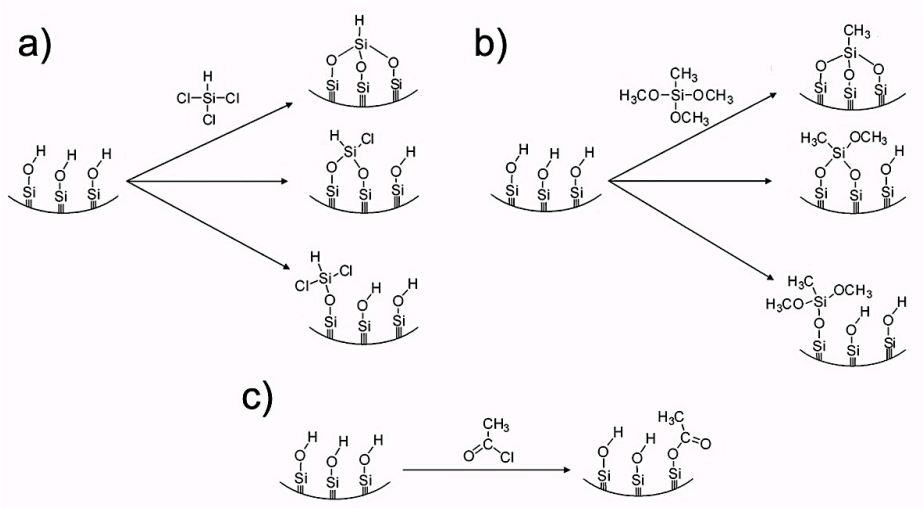

Figure 2.12 Reactions of trichlorosilane **(A)**, methyltrimethoxysilane **(B)**, and acetyl chloride **(C)** at the IMO internal surface[123].

Zanzottera *et al.*[124] described the preparation and characterization of a hybrid nanotube material, obtained by post-synthesis grafting with (3-aminopropyl)triethoxysilane (APTES) of a methyl-functionalized imogolite, previously synthesized using methyltriethoxysilane as a Si precursor. Under the adopted conditions, the functionalization reaction is complete and a variety of mono-, bi-, and tri-dentate species is obtained, with an average of two anchoring points per each unit.

NMR and FT-IR analysis further revealed that the reaction mainly takes place at the outer Al surface and, to a limited extent, on the nanotube's edges. Silane grafting in organic medium represent quite a significant improvement of the classical synthetic procedure, firstly reported by Pinnavia and coworkers, in which an aqueous APTES solution (*i.e.*, hydrolyzed APTES) was added to an imogolite water dispersion[125,126]. By using acidic conditions, a well-dispersed imogolite phase was obtained in water and the silane complete polymerization was hindered, thus ensuring the presence of mainly APTES monomers and dimers in the reaction mixture. However, there was a poor control of the grafting reaction, and the resulting APTES-modified imogolite nanotubes were not stable against hydrolysis. Another successful strategy to modify imogolite external surface is to exploit the higher reactivity of outer Al–OH–Al groups

towards phosphonic acids. For instance, Park *et al.*[127] used octadecyl phosphonic acid and tetradecyl phosphonic acid to functionalize bare imogolite, by simply mixing the reactants in water, at room temperature for 2 days. The hydrophobic nature of the modified IMO surface allowed the dispersion in organic solvents (*e.g.*, toluene, chloroform, hexane), with imogolite nanotubes aligning themselves at the air/water interface. Transferring the monolayer onto conductive surfaces and subsequent annealing, allowed for the first time to visualize by STM the structure of single, unbundled imogolite fibers.

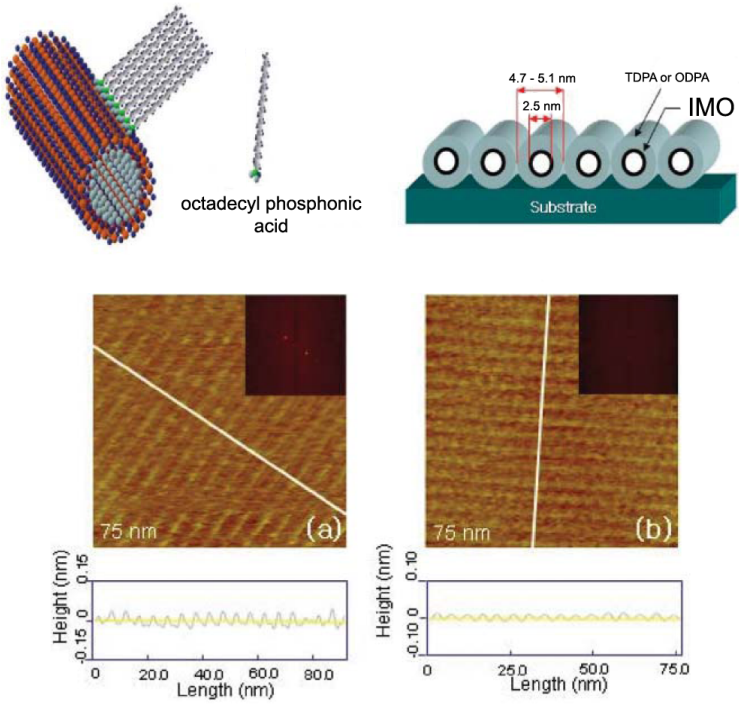

Figure 2.13 Chemical structure of octadecyl phosphonic acid modified imogolite adsorbed on a solid surface (top), and STM image of modified imogolite transferred onto graphite by the Langmuir-Blodgett method (bottom)[127].

2.4.2.3 Imogolite-based nanocomposites

As a general remark it is worth noting that, compared to the more famous carbon nanotubes, IMO-derived nanotubes can be functionalized under mild conditions. Physico-chemical properties of both the inner and the outer surface can be varied, as well as hydrophilicity, porosity, and thermal

stability. Moreover, surface functionalization often represents a determining step in the fabrication of imogolite-based nanocomposites thanks to the improved colloidal stability that ensures a homogenous distribution of nanotubes inside polymer matrices, and to the possibility of increasing the affinity towards hydrophobic polymer matrices.

The group of Takahara[128] was the first to report on the preparation of a nanocomposite made of hydrophobic polymer and surface-functionalized imogolite. The polymer/imogolite hybrid was obtained by free radical polymerization of methyl methacrylate in the presence of imogolite, modified with a phosphonic acid bearing a polymerizable methacrylate group. Poly(methyl methacrylate) (PMMA) grafting from imogolite surface results in a nanocomposite with a homogenous distribution of nanotubes, with peculiar optical and mechanical properties. The transparency of the material is similar to PMMA and significantly higher than the corresponding IMO/PMMA blended system. The dynamic storage modulus, tensile modulus and ultimate strength of the composite resulted to be approximately 1.5 times as high as that of pristine PMMA and blended PMMA/IMO system. However, the lack of interfacial defects between PMMA-grafted imogolite and PMMA matrix resulted in a decreased elongation at break, with respect to pristine PMMA and blended PMMA/IMO system. As expected, PMMA-grafted imogolite nanotubes also display very different interfacial properties with respect to bare imogolite.

Authors from the same group[129] also prepared a ternary imogolite-based nanocomposite, in which two different polymers are used: one is grafted on the imogolite surface (PMMA) via a surface-initiated ATRP, and the other is employed as the bulk polymer matrix (PVC). Interestingly, the interfacial adhesion between the PMMA-*grafted*-imogolite and the PVC matrix may be weak or strong with respect to the cohesive energy of the matrix, depending on temperature. In accordance with the interfacial performance, the nanohybrid shows inferior tensile performance at room temperature, but shows superior tensile performance at 90 °C, compared to pristine PVC in the same conditions. Kang *et al.* [130] used a hydrophilic poly(vinyl alcohol) (PVA) matrix to prepare a nanocomposite membrane without modifying the imogolite surface, and used the obtained membrane for evaporation of an ethanol/water mixture. The hydrophilic nature of

the polymer and the favorable interactions between hydroxyl groups of PVA and bridging hydroxyl groups on the outer surface of the imogolite nanotubes, result in good adhesion properties between the two materials and near-ideal dispersion of the nanotubes even at high loading (> 20 %wt). The authors compared two processing methods for the production of the nanocomposite. In one case IMO powder was simply added to a PVA solution under agitation; in the other case a IMO gel was firstly prepared by adding ammonia solution to a IMO aqueous suspension, dried and grinded to get a solid material, and finally added to a PVA solution. The membranes were obtained by casting the PVA/IMO mixture at 60 °C, and subsequent cross-linking with glutaraldehyde. SEM, EDX and XRD analysis provided evidences that in the case of membranes prepared starting from the IMO-gel the nanotubes are dispersed in the PVA matrix as isolated objects. The PVA chains may effectively penetrate the loosely coordinated network of IMO-water bonds existing in the gel, but are not likely able to penetrate the interstices between imogolite nanotubes in the powder. Permeation results indicated that the properties of membranes made from aggregated IMO powders are strongly affected by the occurrence of defects such as interfacial voids, while in the case of membranes made from IMO-gel enhanced water permeability was observed. However, the microstructural change of the PVA matrix upon incorporation of IMO nanotubes (*i.e.*, the reduction of PVA crystallinity and the higher mobility of polymer chains) led to a moderate reduction of the water/ethanol selectivity.

Imogolite-PVA nanocomposites have been also prepared by *in situ* synthesis of imogolite nanotubes inside a PVA solution, following the procedure reported by Farmer [131]. The average length of the synthesized imogolite fibers in the composite prepared by the in situ method is smaller than that of typical natural and synthesized imogolite nanofibers, while no fiber formation is observed below an IMO:PVA weight ratio of 1:50. The reason for this effect was ascribed to the adsorption of PVA molecules on the proto-imogolite structures and to the subsequent inhibition of their growth. The strong intermolecular interaction between IMO and PVA, also leading to a decrease in the crystallinity and crystallite size of PVA, as well as the good dispersibility of IMO in the polymer matrix are reflected

in the optical, mechanical and thermal properties of the final nanocomposite.

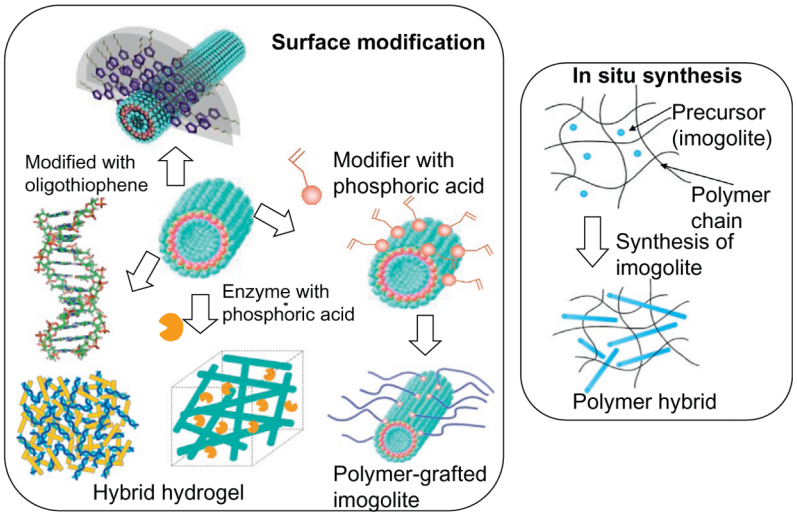

Figure 2.14 Some examples of imogolite-based composites produced by surface modification and *in-situ* synthesis[66].

2.4.2.4 Biocompatibility and biomedical applications of Imogolite

Imogolite unique structural and physico-chemical properties, together with the recent advances in their surface functionalization, make them a very promising material for the design of biomedical scaffolds and devices. In this respect, toxicity concerns on the use of imogolite nanotubes are essentially identical to those of halloysite and other high aspect ratio materials of similar composition. However, in a recent work it has been pointed out that imogolite nanotubes present mild, if any, toxic responses in a variety of cell models and tests, supporting the feasibility of their possible applications in nanomedicine[132].

Aluminum oxide/hydroxide surfaces find use in a wide range of biotechnological applications. Porous aluminum oxide and alumina membranes are used for size selective cell separation, cell growth and in the fabrication of scaffolds for tissue engineering. Alumina particles have also found use as carriers for enzyme immobilization, while adjuvants based on aluminum compounds are commonly used in vaccines to boost the immune response against infectious agents[133,134]. The use of imogolite

nanotubes, therefore, can combine the potential of alumina-based surface with the properties of 1D nanostructured materials. As a nanoscale support, 1D nanostructures could represent interesting materials for enzyme immobilization. Enzymes have been successfully immobilized onto carbon nanotubes *via* covalent and non-covalent interactions. However, water-insolubility of carbon nanotubes poses severe limitations for biotechnological applications, since almost all enzymatic reactions in cells occur in water or hydrophilic fluids. In this respect, imogolite nanotubes represent a viable alternative, since they possess high surface area, chemical stability, water solubility, and better biocompatibility. Furthermore, the three-dimensional hydrogel network of imogolite formed in aqueous solution could act as an efficient scaffold with high loading capacity, and much more controlled enzymatic activity. Inoue *et al.* [135] reported on the immobilization of pepsin onto imogolite, by exploiting the strong interaction between phosphoric acid groups of the enzyme with the Al-OH groups of the clay outer surface. Non-covalent interactions between pepsin and imogolite are strongly preferred with respect to covalent linkage, as in the latter case the possible alterations of the chemical and conformational structure could drastically reduce the enzymatic activity. Most likely, the strong electrostatic interaction between positively charged IMO and negatively charged pepsin is the driving force for the immobilization of the enzyme. The maximum amount of immobilized pepsin was found to be 1.8 mg per 1 mg of imogolite, higher than that of mesoporous silica, corresponding to an estimated surface coverage of ~70 %. The catalytic activity of the imogolite/pepsin resulted 25% lower than that of free pepsin, as evaluated by testing peptic hydrolysis of a hemoglobin solution. The pore created by the imogolite/pepsin hydrogel may not be large enough to allow rapid diffusion of hemoglobin to the active site of pepsin, so that only enzyme molecules located at the external surface of the IMO-gel network and those leached from the network could interact with hemoglobin. However, the imogolite/pepsin hybrid hydrogel displayed satisfactory characteristics, since it retained most of its enzymatic activity up to three-four catalytic cycles.

The high affinity of aluminols on the outer IMO surface towards phosphonic acid groups has been also exploited for the adsorption and

binding of nucleic acid. DNA-clay mineral adducts have attracted great interest because they can provide an effective protection against degradation, maintaining at the same time their biological activity, *e.g.* gene delivery. Furthermore, this hybridization can be performed with a very simple procedure and no need for surface functionalization. The group of Takahara[136] described the synthesis of hybrid gels of imogolite and DNA, prepared by simply mixing the two components in water at acidic pH (pH=4). When the DNA feed content was lower than 50 %wt, all DNA molecules were immobilized on imogolite to form the hybrid gels, while at higher feed content the amount of unbound DNA started to increase sharply. The incomplete loading of DNA was ascribed to electrostatic repulsion generated by the excessive negative charges of the nucleic acid that hindered the formation of the hybrid gel. The different amount of DNA in the hybrid gels strongly influenced their viscosity and physico chemical properties (*e.g.*, swelling degree, resistance to pH, resistance to salinity). For example, at higher imogolite content, the entanglement of clay nanotubes and DNA molecules led to highly viscous gels, while at higher DNA content, coverage of imogolite−DNA network surface by DNA molecules induced repulsion between small aggregations and led to low viscous liquid-like gels. The stability of the hybrid gels was tested at different pH, and in the presence of salt. Interestingly, the release of DNA was only 12% even at pH 11, suggesting a very strong interaction between DNA and imogolite surface. Opposite to the typical salt-induced desorption of DNA complexes with polycations, the amount of DNA released from the hybrid IMO-gel decreased with salt concentration. Most likely, the added salt dissociate surface charge around the hybrid gel instead of attacking the gel, indicating that the presence of imogolite protected DNA from attack of salt ions.

The incorporation of inorganic fillers, together with the use of cross-linking agents, is an effective strategy to reinforce gelatin hydrogels, as already reported in the literature. Yadav *et al.*[137], for instance, described the preparation of hybrid gelatin-hydroxyapatite hydrogels reinforced by multi-walled carbon nanotubes, for artificial bone grafting applications. Inspired by this approach, Teramoto *et al.* [138] reported on the preparation and characterization of a photocrosslinkable imogolite-gelatin nanocomposite. Gelatin was firstly modified with a methacrylate group,

then mixed with imogolite (previously dispersed in water at acidic pH), and then subjected to UV irradiation in the presence of a radical photoinitiator. After irradiation with UV, a semi-transparent self-standing hydrogel was obtained and then subjected to morphological and mechanical characterization. SEM/TEM analysis revealed a highly porous structure, with a partial aggregation of imogolite fibers at 2 %wt loading. In spite of the non-ideal distribution of clay nanotubes within the gelatin matrix, the compression strength of the nanocomposite hydrogel was remarkably improved, suggesting its use as a load-bearing biomaterial.

An example of the use of imogolite and gelatin to build a scaffold for bone tissue engineering is reported in **Chapter 5**.

3 Case study #1: design of a bioactive nanocomposite coating for bone tissue regeneration

Materials for bone tissue engineering should guide and promote the regeneration of bone tissue, acting as temporary substitutes for the extracellular matrix. Some of the prerequisites for an efficient bone tissue-engineering scaffold include: biocompatibility, well-suited mechanical properties, a percolative structure with properly sized interconnected pores to promote tissue integration and vascularization, and time- and space-controlled biodegradability and bioactivity [139]. Several materials have already been proposed as promising candidates, including bioceramics, bioglasses, and hydroxyapatite particles embedded in polymeric scaffolds [140–145]. Nevertheless, synthetic scaffolds still display limitations, boosting the search for materials integrating both osteoconductive and osteoinductive properties, *i.e.* able to support the growth of new bone tissue, and to stimulate osteogenesis.

Osteoporosis, literally "porous bone", is a condition in which the bone mineral density is reduced, the microarchitecture deteriorates, and the amount and variety of proteins in bone tissue are altered, leading to an increased risk of fracture. For instance, in Europe in the year 2010, 22 millions women and 5.5 millions men were estimated to be affected by osteoporosis, and the total projected health care cost is expected to exceed 46 billions € in 2025[146]. Therefore, the research in the bone medication field and in the development of new and efficient strategies for the cure of bone diseases is crucial. Thanks to its bioactivity, strontium(II) is effective in the treatment of osteoporosis. Strontium promotes the deposition of new bone thanks to the stimulation of calcium(II) receptors and differentiation of pre-osteoblasts to osteoblasts; at the same time, it hampers bone resorption through the stimulation of the osteoprotegerin secretion, so inhibiting the formation of osteoclasts from pre-osteoclasts[147] Strontium-based drugs have been widely prescribed over the last decades (*e.g.*, strontium ranelate marketed as Protelos or Osseor), but when Sr(II) is orally administered at high doses (*i.e.*, > 4 g/L), it could also produce detrimental effects on the bone metabolism [148]and increase the risk of

heart attack. For these reasons, the European Medicines Agency has severely restricted its use[149]. However, several studies demonstrated that synthetic grafts doped with strontium(II) display an enhanced osteoblast proliferation, resulting in higher bone mineral density. It is therefore crucial to deliver strontium(II) at the treatment site, so that its bioactivity could be locally exploited, without the collateral effects associated to its systemic administration. Based on these considerations, we designed a hybrid material made of Sr(II)-loaded halloysite nanotubes included within a biopolymer (3-polyhydroxybutyrate-co-3-hydroxyvalerate) (PHBV) matrix, aiming at addressing multiple tasks in the field of bone regeneration. In particular, the inorganic scaffold is intended to provide mechanical resistance, multi-scale porosity, and to favor the in-situ regeneration of bone tissue thanks to its biocompatibility and bioactivity; the interaction with the physiological environment is mediated by the biopolymer coating, which acts as a binder and as a diffusional barrier to the Sr(II) release; the degradation of the polymer progressively leads to the exposure of the inorganic scaffold, tuning its interaction with osteogenic cells.

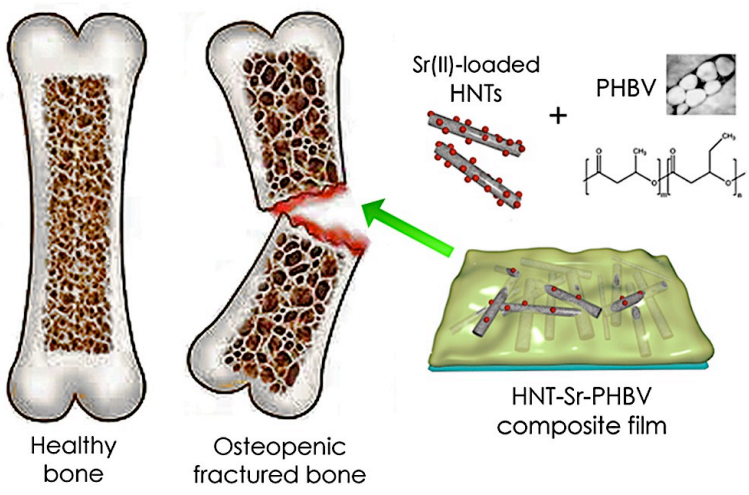

Figure 3.1 Schematic representation of the designed nanocomposite and its field of application.

3.1 Halloysite characterization

The halloysite (HNT) batch used in this work (actually it is the batch used in all the works reported in this thesis) was extracted from a natural deposit in the Kerikeri-Matauri Bay area of Northland, New Zealand and was kindly provided by Imerys Ltd. Figure 3.2-A shows a representative SEM image taken on a halloysite sample deposited onto an aluminum stub from an aqueous suspension at 2 %wt, and subsequently vacuum-dried at room temperature. The sample appears homogenous, with a clear predominance of cylindrical structures composed of thick wrapped tubules with lengths ranging from ~200 nm to ~1 μm. Longer structures are quite rare and this is a favorable characteristic in terms of safety, since 2 μm is generally taken as the upper size limit for silica fibers to be considered safe for human health[65,150].

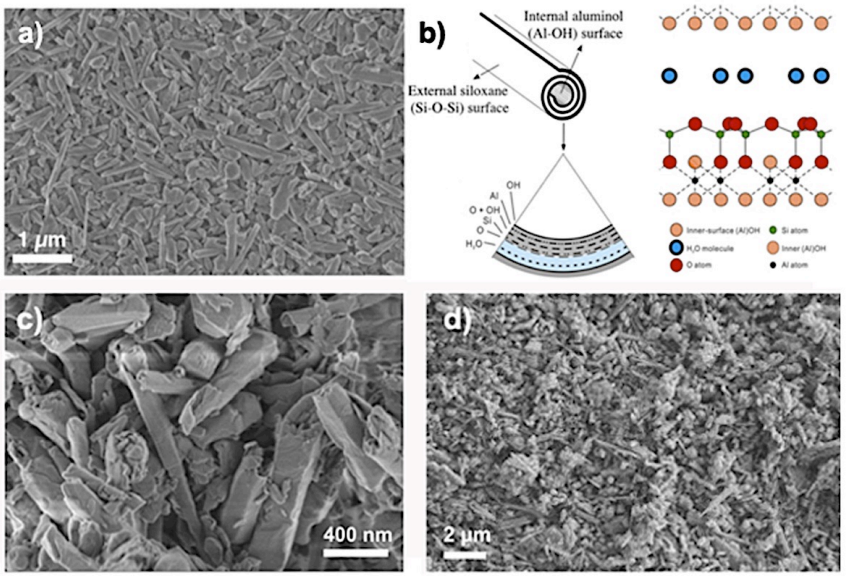

Figure 3.2 SEM micrograph of halloysite **(A)**, schematic representation of halloysite structure **(B)**, SEM micrograph of halloysite at higher magnification **(C)**, SEM micrograph of halloysite deposited *via* spin coating **(D)**.

Figure 3.2 also shows a sketch of the hallosyite structure, which has been already discussed in **Chapter 1**. The multilamellar, wrapped structure of the halloysite nanotubes is evident by looking at the higher magnified image in Figure 3.2-C: the tubular cross section is in the order of 50 nm,

while bigger irregular structures seems to be due to aggregates of smaller structures. In the case of samples prepared *via* drop casting, a big amount of material is deposited and aggregation of halloysite nanotubes is not prevented. A quite different situation occurs when halloysite is deposited *via* spin-coating: in fact, most of the material is removed during the spinning process and a thin layer is obtained, showing a less aggregated structure, with nanotubes partially oriented along the centrifugal force lines (Figure 3.2-D).

One of the distinctive structural features of halloysite is the spacing between aluminosilicate layers that can be assessed by X-ray diffraction (XRD) analysis. The basal reflection peak occurs at an angle corresponding to 7 Å (or 10 Å in the case of hydrated halloysite), but the precise position and width of the peak depends on several factors such as geological source, crystal size, interstratification of layers with different hydration states, temperature, presence of intercalated salts and so on. The observed XRD peak at $2\theta = 12.1°$ (Figure 3.3) corresponds to a 7.4 Å basal spacing, in good agreement with literature data for similar samples (7.2 Å - 7.6 Å). A Rietveld analysis of the XRD pattern of the halloysite batch, revealed that the sample also contains kaolin and, in a minor amount, quartz, both of which are already employed in composites for biomedical applications[151,152]. Furthermore, kaolin has the same chemical composition of halloysite, while quartz displays the same composition of its outer surface. We decided therefore not to purify the commercial batch, especially to demonstrate that no time and money consuming procedures are required to achieve the desired characteristics in the final material.

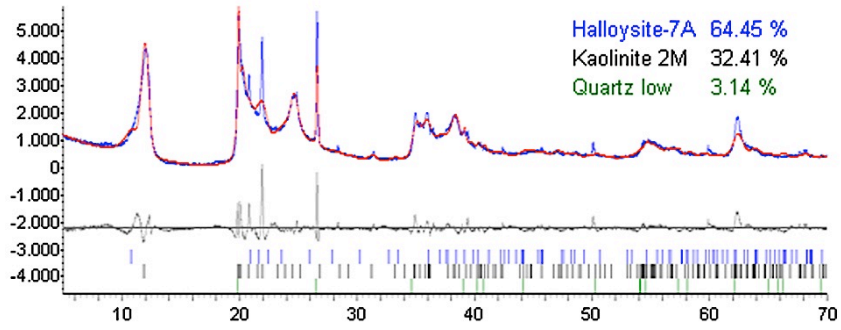

Figure 3.3 Rietveld analysis of the XRD spectrum of HNT, together with the relative abundances of halloysite, kaolinite and quartz.

Nitrogen adsorption isotherms, coupled with BET[c] and BJH[d] calculations, were used to characterize the surface area and porosity of the halloysite sample. Total BET surface area is around 20 m^2/g, a value that is consistent with the co-presence of non porous material. Several values of HNT surface area are reported in the literature, roughly ranging from 20 to 100 m^2/g, this variability being due to the origin of the deposit and especially to solvent treatments of the initial powder[155]. The nitrogen adsorption isotherm (Figure 3.4) shows a hysteresis loop associated with a capillary condensation in mesoporous cavities[154]. Total pore volume results to be ~0.18 ml/g, with a pore size distribution ranging from few to few tens of nm. Most of the pores are in the 20-80 nm range, consistent with the presence of inter-tubular and intra-particle pores. Halloysite does not show significant microporosity, indicating that the 0.7 nm spacing between layers in the nanotube walls is not accessible for nitrogen molecules.

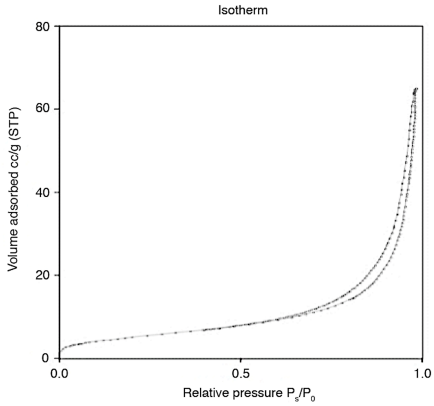

Pore Dia. Range(nm)	Pore Volume (ml/g)	%
Under 6	0.00630	3.45
6 - 8	0.00326	1.78
8 - 10	0.00326	1.79
10 - 12	0.00401	2.19
12 - 16	0.00671	3.67
16 - 20	0.00844	4.62
20 - 80	0.07260	39.72
Over 80	0.07821	42.79
BJH Total	0.18279	100.00

Figure 3.4 Adsorption isotherm and pore size distribution obtained with BJH calculation of a HNT sample.

[c] Brunauer-Emmet-Teller[153]

[d] Barrett-Joyner-Halenda[154]

3.1.1 Halloysite modification: APTES functionalization and Sr(II) uploading

HNT surface was functionalized with (3-aminopropyl)triethoxysilane (APTES) by mixing the powder (2.5 %wt) and the silane in ethanol, at room temperature for 24h. Few drops of NH_4OH were added to the reaction mixture to favor the silanization reaction. The amount of silane was chosen to cover about 20% of the HNT external surface, taking into account a silane cross section[156] of 50 $Å^2$ and half of the HNT surface area obtained from BET. The functionalization with APTES was conceived to increase the dispersibility of halloysite, *i.e.* by lowering interfacial interactions between nanotubes, and to enhance its chemical affinity with the PHBV biocompatible scaffold through hydrogen bonding between the exposed amine groups and the polymer carboxylic moieties. The successful modification of HNT surface with APTES was confirmed by ATR-FTIR analysis (Figure 3.5-A). Distinctive features of pristine halloysite spectra are the Al_2OH-stretching at 3693 and 3620 cm^{-1}, corresponding to OH being linked to two Al atoms, the Si-O-Si stretching at 1000 cm^{-1} and the weak absorption peak at 1646 cm^{-1} that can be attributed to the "scissor" bending mode of physisorbed water molecules[63,157,158]. Functionalized halloysite displays an additional band in the 3300-3500 cm^{-1} region, that can be attributed to the N-H stretching of APTES molecules. Furthermore, APTES-functionalized HNT suspensions in water display a marked increase in their stability with respect to pristine clay nanotubes, as shown in Figure 3.5-B.

To upload Sr(II), 100 mg of HNTs were mixed with 10 ml of a 100 mg/ml $SrCl_2 \cdot 6H_2O$ solution. The dispersion was vigorously mixed for 24 hours and then centrifuged. The solid was recollected, dried, and then used for the subsequent preparation of the nanocomposites. The use of Sr-loaded halloysite as the inorganic component of a nanocomposite scaffold could represent a significant advantage over the materials currently in use, since the modified nanotubes can improve the mechanical properties of the polymer matrix and, at the same time, deliver Sr(II) at the treatment site. The amount of uploaded strontium was determined by means of Inductively Coupled Plasma Atomic Emission Spectrometry (ICP-AES). Samples were dissolved by acidic attack in a small volume of boiling HNO_3. Each sample was then diluted to 5 mL with 0.1%

suprapure nitric acid, obtained by sub-boiling distillation, spiked with 0.32 ppm of Ge used as an internal standard, and analyzed. ICP-AES analysis indicated an average strontium content in the samples of 7.2 %wt. Functionalization of HNT with APTES and the loading with Sr(II) do not result in any significant variation in terms of surface area and porosity (data not shown).

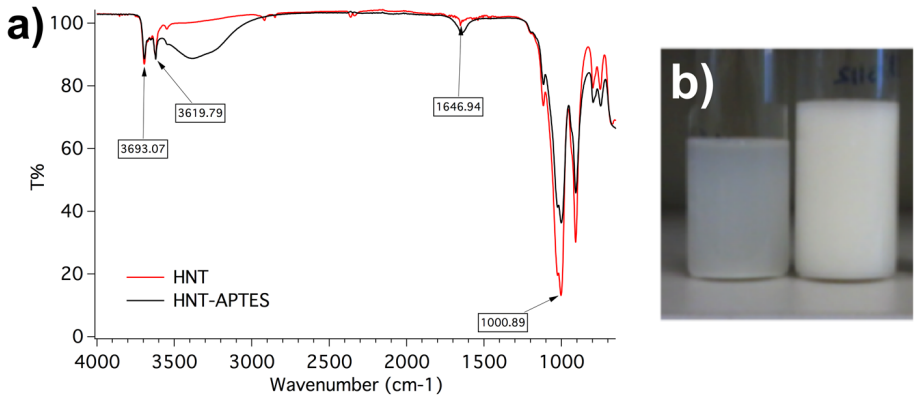

Figure 3.5 (A) ATR-FTIR spectra of Halloysite and APTES-functionalized Halloysite; **(B)** Halloysite (left) and APTES-functionalized Halloysite (right) water dispersions.

3.2 Preparation and characterization of HNT-Sr-PHBV nanocomposite

In order to simulate the application of the material as a coating onto synthetic bone grafts, we prepared the composites by spin-coating onto glass surfaces, whose chemical reactivity is similar to that of the ceramic materials commonly used in synthetic bone grafts. Clean glass slides were functionalized through incubation in a silane (TEOS or APTES) saturated atmosphere at 60 °C during 24 hours, and then used as substrates for the subsequent deposition steps. HNT dispersions (2 %wt) were spin coated onto the glass substrate, and then a PHBV chloroform solution (2 %wt) was spin coated on top of it. The coating process was carried out at room temperature in two stages at constant rotating speed (1500 and 2500 rpm), separated by an acceleration step.

SEM images of HNT-Sr-PHBV nanocomposite (Figure 3.6-A) revealed that PHBV almost completely embed the inorganic nanotubes in a quite homogenous and smooth film, with only few clay structures emerging from the polymer surface. In order to simulate the behavior and fate of an implant based on this composite, HNT-Sr-PHBV coupled on glass surface was exposed to para-physiological conditions (PBS buffer, 37 ºC) and analyzed by means of electron and atomic force microscopy to monitor the morphological evolution with time.

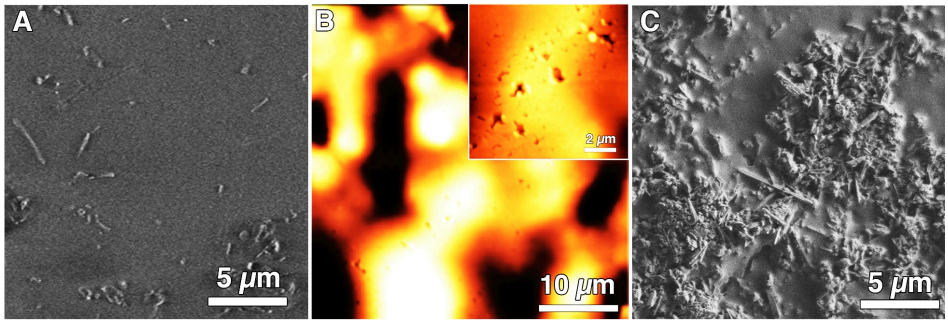

Figure 3.6 (A) SEM image of the freshly prepared nanocomposite; **(B)** Non Contact AFM image (Z-range: 800 nm) of a degraded (4 days) HNT-Sr-PHBV nanocomposite. The inset displays a zoom of a selected region (Z-range: 400 nm). **(C)** SEM image of the nanocomposite degraded during 28 days.

Figure 3.6-B reports the AFM topography of HNT-Sr-PHBV nanocomposite after 4 days of degradation. The surface displays a large number of voids resulting from the PHBV degradation. Insights on the mechanism can be inferred from the analysis of the inset in Figure 3.6-B, and from the evolution of the polymer surface roughness with time (Figure 3.7) that shows a random trend. The presence of irregularly shaped voids and semi-detached polymer fragments in their proximity indicates that the polymer degrades through a random bulk hydrolysis[159]. After 28 days of degradation the inorganic scaffold is exposed to the environment, as evident from the significant number of HNT tubules visible in the SEM image (Figure 3.6-C).

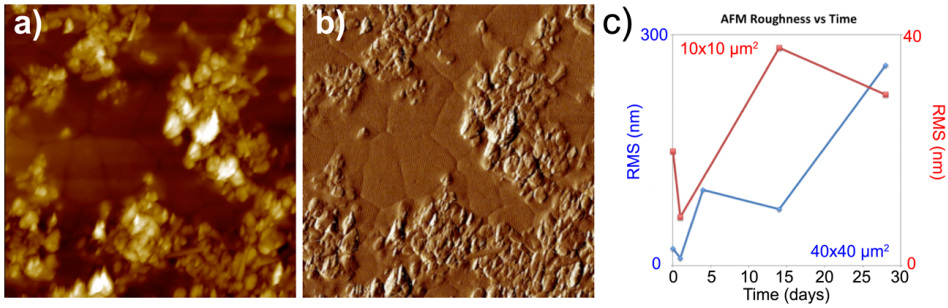

Figure 3.7 (A) AFM topography and **(B)** phase analysis images of HNT-Sr-PHBV nanocomposite after 24 hours of degradation in PBS at 37 °C (Z-range=500 nm, scan size=20 µm²); **(C)** root mean square roughness (RMS) evolution with time for PHBV film spin coated onto APTES-functionalized glass substrate (evaluated by AFM).

ICP-AES results indicate that halloysite nanotubes are able to retain a consistent amount of Sr(II), over 28 days of degradation (see the appendix). In particular, about 70% of the strontium uploaded is still available after one week, suggesting that once applied the bioactivity of the composite lasts long enough to allow the local regeneration of bone tissue. Furthermore, the presence of PHBV does not affect the release of strontium, simply modulating the exposure of HNT to the surrounding medium. This is consistent with a strong interaction between Sr(II) and HNT, much stronger than that between Sr(II) and PHBV. As a result, the release of Sr(II) to the environment is regulated by its affinity towards HNT.

The HNT-Sr-PHBV nanocomposite thickness and mechanical properties were evaluated through AFM nanoindentation experiments, *i.e.* by the analysis of AFM force-curve distances. Figure 3.8 shows a representative force *vs* displacement curve obtained during the nanoindentation test of a nanocomposite sample and the AFM image of the indented surface. The width of the plateau region indicates an average thickness of about 300 nm, while the maximum compression that the nanocomposite withstands is about 20 µN. Taking into account the area of contact resulting from the AFM probe curvature, a compressive strength of about 50 GPa can be estimated, mainly ascribable to the presence of the HNT[160].

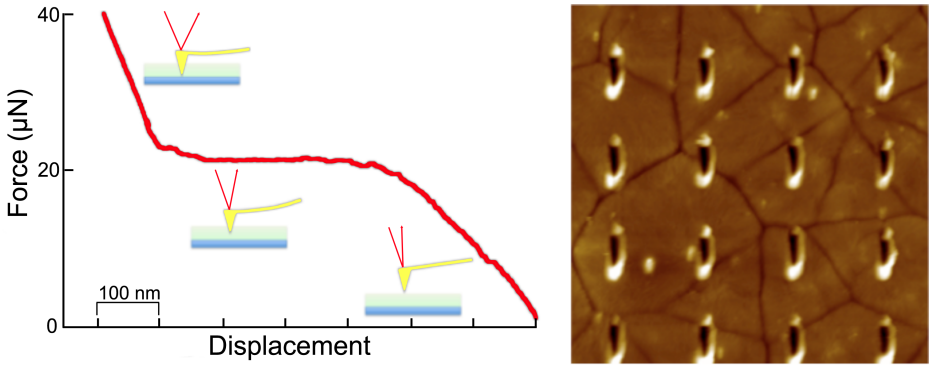

Figure 3.8 Representative Force *vs* Displacement curve obtained during the nanoindentation test of a HNT-Sr-PHBV nanocomposite (left), and corresponding AFM topography image of the indented sample.

To give a comparison, multi-walled carbon nanotubes that are frequently proposed as potential reinforcing agents in biomedical composites[161,162], display similar compressive strengths (around 100 GPa[163]) but present severe concerns from the toxicological point of view. On the other hand, the biocompatibility of halloysite nanotubes and their structural properties make HNT a very suitable platform for biomedical applications in the bone regeneration field, where mechanical resistance is a crucial prerequisite.

The *in vitro* biocompatibility of the nanocomposite was assessed by a direct contact method using mouse fibroblasts cell line L929, already employed in the past to evaluate carbon nanotube cytotoxicity[164,165]. The cell viability after incubation in the presence of HNT, HNT-PHBV, HNT-Sr and HNT-Sr-PHBV was measured by evaluation of functional state of mitochondria (MTT assay) and cellular membrane integrity (Trypan Blue assay). Moreover the proliferative capacity of the cells exposed to HNT was evaluated by incorporation of BrdU during cell replication. All these cell culture methods are highly reproducible, quantitative, and they have been already employed to assess the biocompatibility of diverse nanostructures and polymeric materials[166–169]. Figure 3.9 and Figure 3.10 summarize cytotoxicity data obtained with MTT and Trypan Blue assays, respectively.

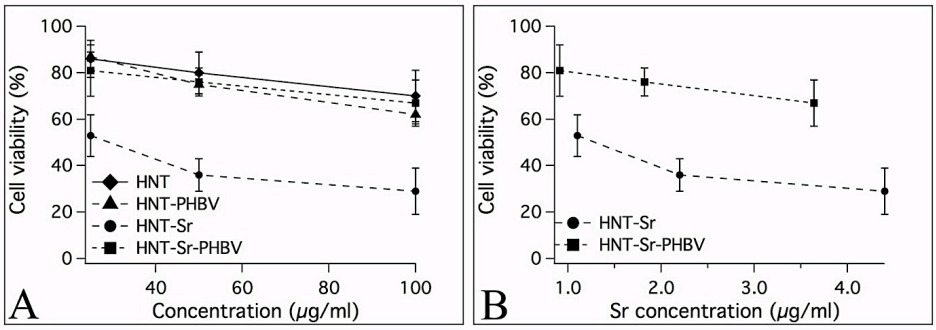

Figure 3.9 Comparative cytotoxicity of HNT, HNT-Sr, HNT-PHBV and HNT-Sr-PHBV obtained with MTT assay, after exposure of L929 cells for 72 hours. The percentage of cell viability was calculated versus control medium without composites (taken as 100%). Results are given as a function of **(A)** composite concentration and **(B)** Sr concentration.

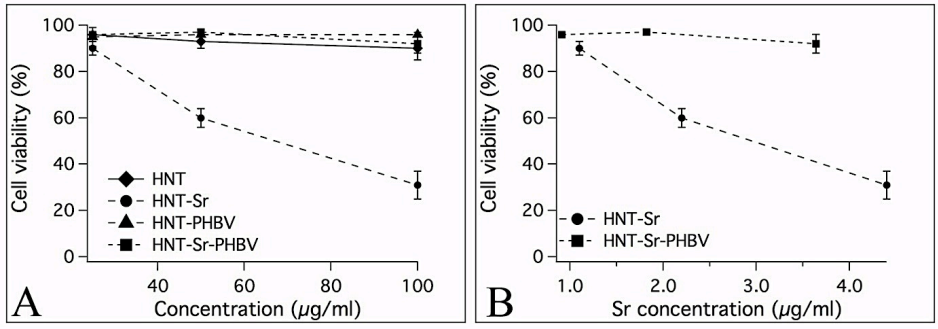

Figure 3.10 Comparative cytotoxicity of HNT, HNT-Sr, HNT-PHBV and HNT-Sr-PHBV obtained with Trypan Blue assay, after exposure of L929 cells for 72 hours. The number of viable cells was calculated as percentage of total cells for each sample. Results are given as a function of **(A)** composite concentration and **(B)** Sr concentration.

All samples exhibited cell growth inhibition in a concentration dependent manner. The cell viability was preserved (ca. 70% of cells survived) up to composite concentration of 100 μg/mL for HNT and for the composites HNT-PHBV and HNT-Sr-PHBV. For the HNT-Sr sample there is a clear decrease in cell viability (only 30% of cells survived at 100 μg/mL). The toxicity data obtained by Trypan blue tests confirmed the MTT results, showing that cell viability after 72 hours of exposure is maintained at >80% for HNT, HNT-PHBV and for HNT-Sr-PHBV at all Sr(II)

concentrations studied, indicating high biocompatibility of Halloysite nanotubes and PHBV, up to 100 μg/mL. However, the "naked" HNT-Sr induces a significant vitality reduction already at 25 μg/mL, suggesting the need for a barrier to modulate its interaction with cells.

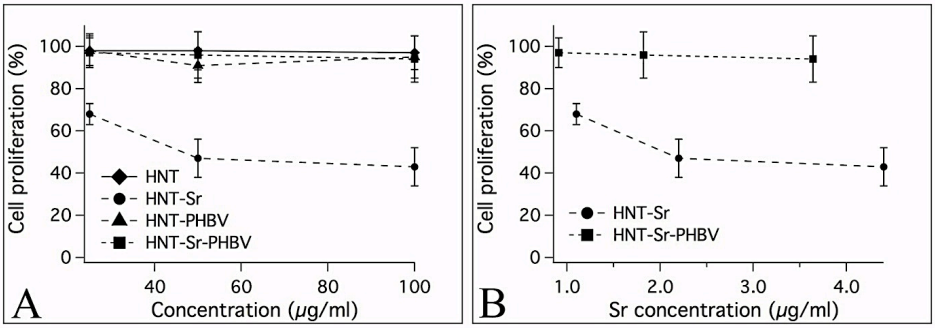

Figure 3.11 Comparative DNA synthesis measured as BrdU incorporation in L929 cells incubated with HNT, HNT-Sr, HNT-PHBV and HNT-Sr-PHBV for 48 hours. The percentage of cell proliferation was calculated versus control medium without composites (taken as 100%). Results are given as a function of **(A)** composite concentration and **(B)** Sr concentration.

The effectiveness of a biocompatible scaffold is also related to its ability to not affect the normal cellular proliferative capacity. The cell proliferation of L929 fibroblasts after 48 hours of incubation with different suspensions is reported in Figure 3.11 as the percentage with respect to the culture medium. Data show that cell proliferation in the presence of HNT, HNT-PHBV and HNT-Sr-PHBV is similar to control samples, while HNT-Sr induces a significant reduction at all analyzed concentrations. These data suggest that HNT and PHBV are well tolerated by L929 mouse fibroblasts, while the Sr contained in HNT showed a toxic effect on cells viability and growth due to their direct exposition to the cation. The coating of PHBV produces a biocompatible environment for the cells, even when high concentrations of Sr(II) are present within the composite. The biocompatible surface of PHBV thus acts as a tunable barrier for the interaction between fibroblasts and Sr-loaded HNT.

3.3 Concluding remarks

This case-study reports on the design and preparation of a biocompatible hybrid nanocomposite consisting of Sr(II)-loaded Halloysite nanotubes embedded within a biopolymer (PHBV) matrix. The nanotubular morphology of HNTs provides an inorganic scaffold with well-suited mechanical properties for bone replacement, especially in terms of lightness (hollow fiber) and high compressive strength. In particular, the chemical composition of HNT is identical to the widely adopted and biologically well-tolerated kaolin, introducing a significant advantage over other fibrous nanostructures in terms of safety and biocompatibility. Furthermore, thanks to the ability of halloysite to upload and dynamically exchange cations, we uploaded Sr(II) ions onto HNT in order to exploit the cation bioactivity at the local level, thus reducing the collateral effects associated to a systemic administration. The PHBV biopolymer embeds the inorganic scaffold, allowing for the progressive exposure of the nanotubes to the physiological environment, and the modulation of Sr(II) bioavailability.

The fabrication method described here to obtain the nanocomposite is highly versatile, and it could address different biomedical and physico-chemical needs. For example, the thermal characteristics of the composite (data reported in the appendix) make it easily processable and envisage its use as a filmable coating to enhance the bone regeneration capacity of synthetic bone grafts, or as a self-standing biomaterial. The reported experimental conditions (silanizing agents, concentration of solutions and dispersions, spin-coating parameters) were optimized in order to have i) an adequate coverage of the substrate surface, ii) adhesion between the HNT layer and the underlying glass substrate, iii) degradation of the biopolymer coating in a convenient time frame, but still they can be easily adjusted to meet specific needs. In particular, the amount of uploaded Sr(II) could be varied with proper HNT surface functionalization; the time before the bioactive inorganic scaffold is exposed to the physiological environment could be finely tuned by the thickness of the PHBV coating; the biopolymer matrix could also be used as a carrier for biochemical signals and drugs, opening the possibility to the design of multi-functional nanocomposite biomaterials.

4 Case study #2: engineered Halloysite and Imogolite nanotubes for the uploading/release of drug models

Tubular alluminosilicates, such as imogolite and halloysite, are characterized by a high aspect ratio, large surface area, a hollow nano-sized lumen and two surfaces with different reactivity. All these features are of great interest in various fields of nanotechnology and materials science. Furthermore, thanks to their economic viability, the environmental benefits associated to their use and composition similar to biologically relevant materials (*i.e.*, silica and alumina), halloysite and imogolite represent valuable platforms for biomedical applications. 1D tubular clays have already been proposed as nanoscale supports for enzymes and DNA, biomimetic nanoreactors, and drug-delivery vehicles[97,135,136,170]: biocompatibility and the ease of the functionalization/loading process represent decisive advantages over other nanotubular systems. In this chapter, two examples of the use of engineered nanotubular clays for the uploading and the controlled release of model drugs will be described.
In the first example, halloysite nanotubes were loaded with rhodamine 110 and carboxyfluorescein, used as models for opposite charged drugs, and their release capacity was assessed in the presence of a biocompatible polymer coating. In the second example, imogolite nanotubes were modified with a biodegradable surfactant bearing an amino acidic head group and an alkyl tail, and used in a proof-of-concept experiment for the uploading of a dye molecule. Both examples aim at demonstrating how novel drug-delivery systems based on clay nanotubes can be prepared by a smart design, and simple chemical functionalization routes.

4.1 Uploading of fluorescent compounds in the Halloysite lumen

The loading of the fluorescent compounds was achieved by suspending halloysite (HNT) powder (1 %wt) in 10 mg/l solutions of rhodamine110 (Rho10) or carboxyfluorescein (CF). These suspensions were placed under mild vacuum and under agitation, in order to force the solution to come in

contact with the nanometric cavity. The release of bubbles into the solution due to the leakage of air contained in the nanotube's lumen was taken as an evidence of the insertion of the solution inside the tubules. After 30 minutes, the solid material was recovered by centrifugation (10 min at 12500 g) and dried. The amount of dye retained by HNT was determined by the difference in the sample fluorescence before and after the loading procedure. In particular, HNT initially retained approximately 0.7 μg of CF and approximately 0.6 μg of Rho110 per mg of HNT. Loaded halloysite nanotubes were then used as the starting material for the preparation of the nanocomposites to be used in the release tests. In the case of the hyaluronan-based composites, the fluorescent dyes were loaded onto HNT silanized with (3-aminopropyl)trimethoxysilane (APTMS), following the same procedure (see below).

4.2 Halloysite/Chitosan and Halloysite/Hyaluronic Acid composites

HNT-chitosan nanocomposites (HNT-C) were prepared by taking advantage of the electrostatic attraction force between the negatively charged HNT external surface, and the positively charged polymer. 1 %wt of HNT and 1 %wt of chitosan were dispersed in water under vigorous agitation, then after the addition of acetic acid (to pH 5), a viscous, homogenous suspension was obtained. The suspension was centrifuged at 12500 g for 10 minutes to precipitate the composites and remove excess chitosan not physisorbed on the HNT surface. The amount of physisorbed polysaccharide did not change significantly by varying mixing time and decreasing the pH of the suspension. HNT-hyaluronan nanocomposites (HNT-H) were prepared by a covalent coupling between the inorganic and organic component. HNT surface were first functionalized with (3-aminopropyl)trimethoxysilane (APTMES) by mixing the silane with a 2 %wt HNT dispersion in ethanol, and adding few drops of NH_4OH to favor the silanization reaction. The amount of APTMS was chosen to obtain a 50 % coverage of the external surface, taking into account a silane cross section of 0.5 nm^2 [156]. The HNT silanization was confirmed by means of elemental analysis and spectroscopic measurements (Figure 4.1).

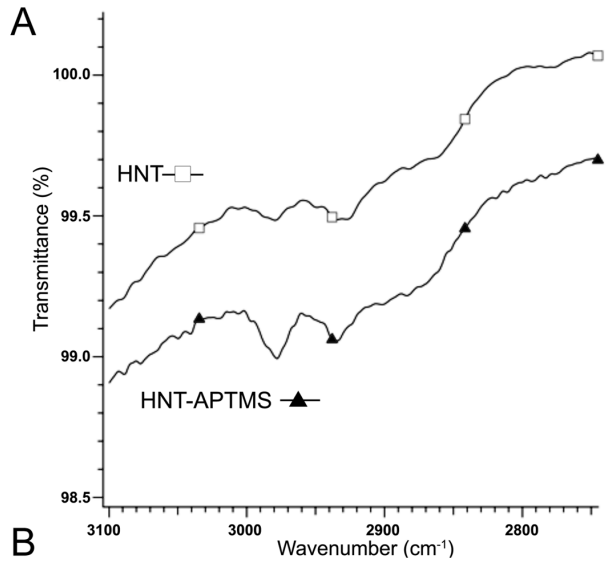

B

	N (%wt)	C (%wt)	H (%wt)	Est.surface coverage
HNT	0.00	0.09	1.70	-
HNT-APTMS 1	0.06	0.27	1.38	10 %
HNT-APTMS 2	0.09	0.39	1.71	25 %
HNT-APTMS 3	0.14	0.59	1.73	50 %

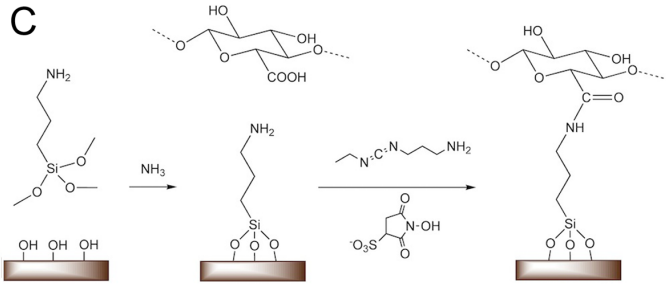

Figure 4.1 (A) Expanded view of the FTIR spectrum of silanized HNT. Due to the low amount of N and O in the samples, the characteristic adsorption peak of the APTMS amine group was not recognized clearly. However, in the 2870-2980 cm^{-1} region the silanized sample shows typical adsorption peaks attributable to alkyl C-H stretching. These signals are much weaker in the HNT sample, and in this case are due to some organic impurities; **(B)** CHN elemental analysis results confirm the presence of silane molecules bound to HNT, with both carbon and nitrogen weight percentage increasing with the amount of APTMS used during the silanization process. Estimated surface coverage corresponds to indicated percentages of total BET surface area (25 ± 4 m^2g^{-1}); **(C)** Scheme of the reaction route for the preparation of HNT-H nanocomposite.

Meanwhile, hyaluronic acid (1 %wt) was dissolved in 2-(N-morpholino)ethanesulfonic acid monohydrate (MES) buffer (pH 6) with stoichiometric amounts of N-(3-dimethylaminopropyl)-N′-ethylcarbodiimide hydrochloride (EDC) and N-hydroxysulfosuccinimide sodium salt (sulfo-NHS), and kept under agitation for 30 minutes. The pH was adjusted by adding a phosphate buffer saline (PBS) solution (pH 7.4), then 250 mg of silanized halloysite was added and the mixture was kept under agitation for 4 hours. The solid was finally recovered by centrifugation at 12500 g for 10 minutes, washed with water, and freeze-dried. A scheme of the reaction is reported in Figure 4.1-C

The obtained composites were characterized by means of FT-IR spectroscopy, TGA, TEM and ξ-potential measurements. Figure 4.2 shows the FT-IR spectrum of HNT-C and HNT-H, compared to the spectra of HNT, chitosan and hyaluronic acid in the 1300-1800 cm^{-1} spectral window. The FT-IR spectra of both nanocomposites show peaks arising from both the inorganic and organic constituents, confirming their presence in the composite material. The spectrum of HNT-C shows a band centered at 1650 cm^{-1} whose shape is due to the overlapping of the -OH bending of water physisorbed onto the HNT with the broad band of N-acetyl groups of chitosan at 1652 cm^{-1} [171]. The band at 1560 cm^{-1} in the nanocomposite is a further confirmation of the presence of N-acetyl groups owing to chitosan[172]. In the FT-IR spectra of HNT-H composite, the peak at 1560 cm^{-1} was attributed to bending vibrations of amide N-H groups[173], while the C=O stretching of deprotonated carboxylic groups appears as a weak peak at 1603 cm^{-1}.

The thermogravimetric profile of HNT-C (Figure 4.2) shows an initial weight loss due to water physisorbed onto HNT and weakly bound to chitosan, in the temperature range 25-150 ºC, and a signal due to the degradation of the organic component in the 150 – 350 °C range. The corresponding weight loss indicates that the polymer is about 6 % with respect to the total weight of dry sample. The thermogravimetric profile of HNT-H (Figure 4.2) shows a similar trend to that of HNT-C, with a few percentages of physisorbed water lost around 50 ºC, and the organic component, i.e. hyaluronic acid, degrading in two stages in the 150 – 350 ºC range. In this case, the amount of organic component is about 3% with respect to the total weight of dry sample.

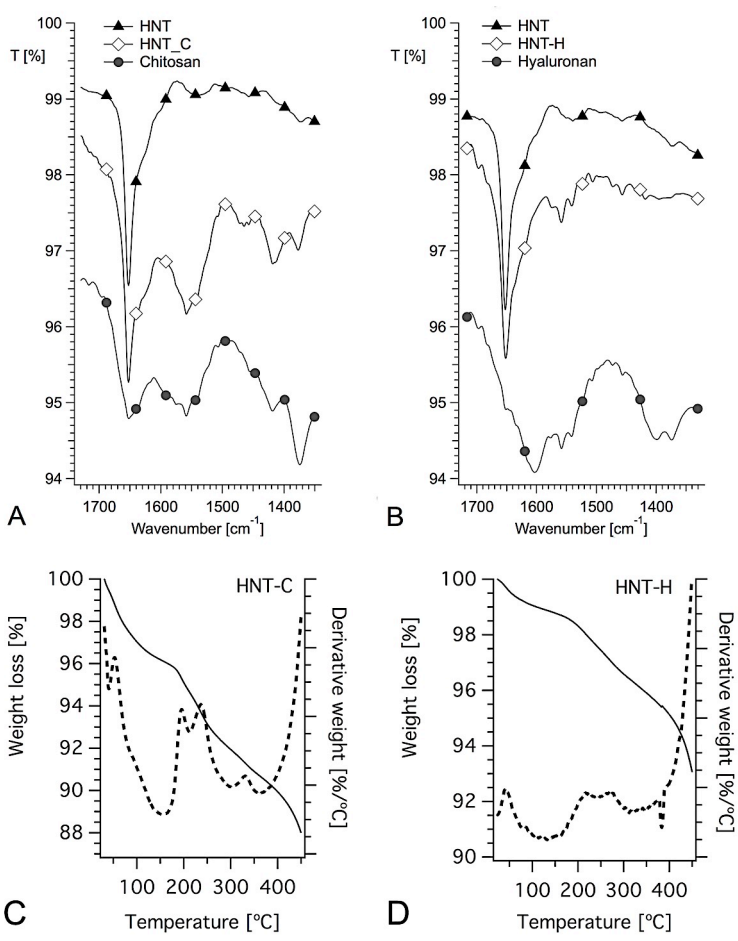

Figure 4.2 FT-IR spectra of HNT-chitosan composite **(A)** and HNT-hyaluronan composite **(B)** (each plot shows also the FTI-R spectrum of the correspondent polymer and of pure HNT; the curves are vertically shifted for the sake of clarity). Thermogravimetry and differential thermogravimetry profiles of HNT-chitosan **(C)** and HNT-hyaluronan nanocomposites **(D)**.

TEM images (Figure 4.3) give a clear indication of the presence of an organic, homogenous layer (indicated by arrows in the figures) covering halloysite nanotubes and clogging their extremities. The contrast in the TEM image is due to the difference in atomic numbers of the elements that constitutes the composite (mainly Al and Si for HNT, C and N for chitosan and hyaluronic acid), so the polymer film can be distinguished as a lighter coating covering the tubules. Additional evidence of the

interaction between the HNT and polysaccharides comes from ζ-potential measurements. As expected from electrostatic considerations, the HNT-C nanocomposites exhibit a positive charge (+33 ± 2 mV) in contrast to the ζ-potential of the native halloysite (-22 ± 1 mV). In the case of HNT-H nanocomposites, the ζ-potential decreased to -31 ± 2 mV, confirming that hyaluronan residues bearing negative charges are effectively linked to the inorganic surface. Chitosan and hyaluronan acid successfully imparted different charges to the surface of halloysite nanotubes, thus modulating their electrostatic interactions in solution.

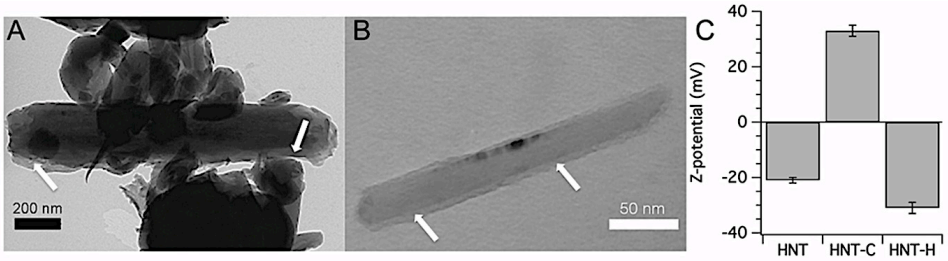

Figure 4.3 TEM images of **(A)** HNT-Chitosan and **(B)** HNT-Hyaluronan nanocomposites; ζ-potential measurements of halloysite (HNT), halloysite-chitosan (HNT-C) and halloysite-hyaluronan nanocomposites (HNT-H) **(C)**.

4.3 Release experiments and modeling of the release kinetics

A fixed amount (10 mg) of nanocomposite material loaded with the fluorescent dyes was placed in 5 ml of Milli-Q water and kept under agitation. At specific intervals of time and up to a period of 48 hours, 50 μl of the solution was collected and diluted 1:4. After any withdrawal the same amount of water was added to the sample to keep the volume constant throughout the experiment. To evaluate the concentration of the released probes, the maximum of the fluorescence intensity (at 514 nm for CF, at 519 nm for Rho110) of the sample solutions is evaluated at progressive intervals of time.

The release kinetics of chemicals loaded into HNT has been often modeled using the Ritger-Peppas[174,175] or related equations[91,93]. However, strong electrostatic interactions in the system, especially between the

polymer coating and the halloysite load, are expected to influence the release kinetics and cause deviations from a pure Fickian diffusion. Deviations from a diffusion-controlled release may also occur due to a broad particle size distribution, as in the case of commercial grade products. Recently, a new mechanistic model was proposed for the description of 5-amino salicylic acid released from halloysite[176]. The model is based on the adsorption-desorption equilibrium between the drug and HNT, and is comprised of two interface processes: a) desorption of the drug adsorbed on the external halloysite surface and/or inter-particle spaces (*i.e.*, fast release), and b) desorption of the drug molecules adsorbed into the tubular cavities of HNT (*i.e.*, slow release). The release profiles obtained in this work were fitted with an equation derived from this model. In particular, the adopted fitting equation is:

$$y = A + 100 \cdot \frac{C_e}{C_e^{max}} \left(1 - \exp(-k_D t / C_e)\right) \qquad \textbf{(1)}$$

where y represents the percentage of released dye over time (indicated with t in the model equation), A is the mass of dye released at t=0, C_e represents the equilibrium dye concentration released from the internal HNT surface, C_e^{max} is the maximum concentration of the released dye, and k_D represents the specific desorption rate of the dye. The parameter A is generally indicated as the "burst release" from a drug delivery system[177,178]. Figure 4.4 and Figure 4.5 show the release profiles for CF and Rho110 from chitosan-based and hyaluronan-based nanocomposites, together with the parameters extracted from the fitting. The release profile of "naked" halloysite is also reported for comparison (a detailed discussion of the fitting results is reported in the appendix).

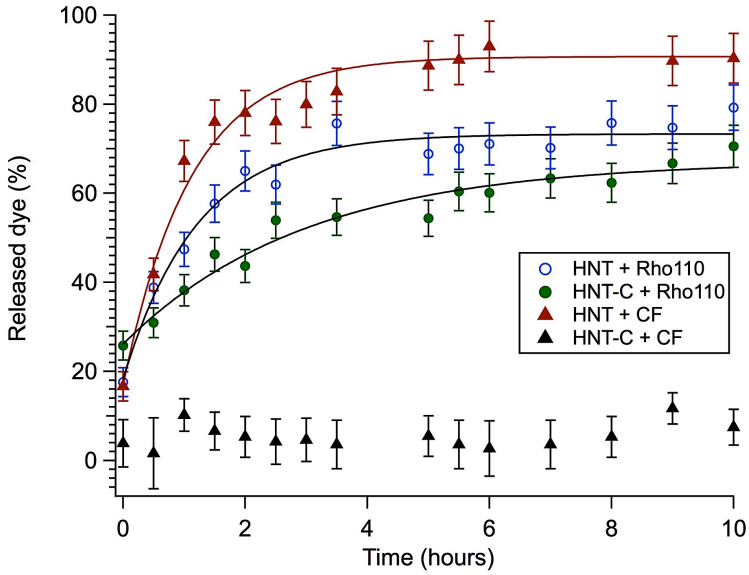

	C_e (%wt)	C_e^{max} (%wt)	k_D (1/h)	A (%wt)	X^2
HNT + CF	67 ± 3	90 ± 5	60 ± 8	17 ± 3	13.1
HNT-C + CF	-	8 ± 1	-	-	-
HNT + Rho110	44 ± 3	79 ± 4	36 ± 6	18 ± 3	6.2
HNT-C + Rho110	29 ± 3	71 ± 4	10 ± 2	26 ± 3	6.1

Figure 4.4 Release profiles of Rho110 and CF from HNT-Chitosan (HNT-C) composite and from pristine HNT (top), and parameters obtained from the fitting (bottom).

Results show that both the polymeric coatings altered the release process of the probes. In particular, the chitosan coating was able to completely hinder the release kinetic of the negative model drug (CF). On the other hand, the release of the positive dye (Rho110) from the inner part of the inorganic tubules was slowed down due to the electrostatic repulsive effect of the polymer coating. Due to the different strategy of preparation, it was observed that the negatively charged HNT-H composite did not inhibit the release of the positive dye. The reason is two-fold: (i) the amount of polymer on HNT is lower and (ii) some of the carboxylic moieties of the polymers were engaged in the bonding to the surface, reasonably leading to a weaker interaction with the positive probe. For the same reason, the hyaluronic acid coating decreased the release of the negative dye from the

inner lumen of the tubules, both in terms of total released amount and desorption rate, but it did not cause a remarkable burst release. The results show that the polymeric coatings were successful in modulating the charge of the halloysite surface and altering the release kinetics of the probes. In particular, the mathematical model adopted to fit the release kinetics well described the experimental data and indicated that both charge and coating composition play a key role in the desorption process. The model also provides a simple yet complete interpretation of desorption of charged model dyes from halloysite and halloysite-based composites.

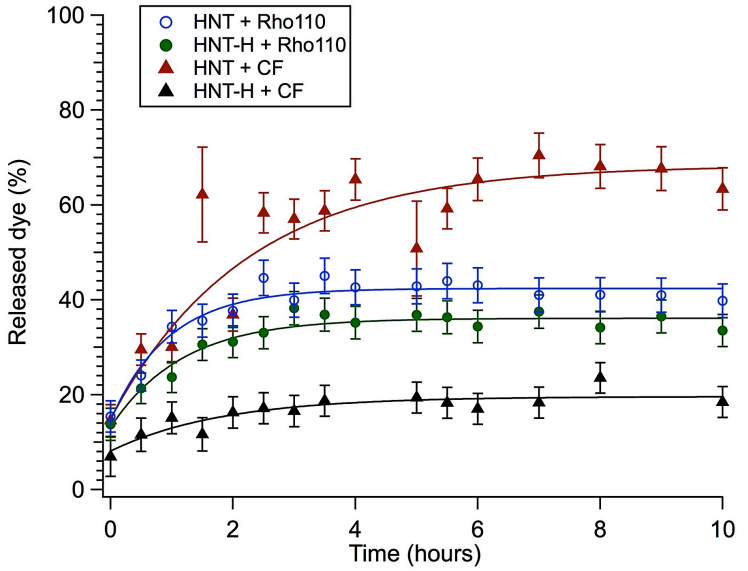

	C_e (%wt)	C_e^{max} (%wt)	k_D (1/h)	A (%wt)	X^2
HNT + CF	34 ± 2	63 ± 3	15 ± 3	15 ± 3	24.5
HNT-H + CF	2 ± 1	18 ± 1	2 ± 1	8 ± 3	3.7
HNT + Rho110	11 ± 1	40 ± 2	12 ± 3	15 ± 3	4.3
HNT-H + Rho110	8 ± 1	35 ± 2	13 ± 3	13 ± 3	3.7

Figure 4.5 Release profiles of Rho110 and CF from HNT-Hyaluronan (HNT-H) composite and from pristine HNT (top), and parameters obtained from the fitting (bottom).

4.4 Synthesis and characterization of imogolite nanotubes

Imogolite (IMO) nanotubes were synthesized following the procedure reported by Koenderink *et al.* [111]. 840 μl of tetraethyl orthosilicate and 1.90 g of Al-*sec*-butoxide were added to a 150 ml $HClO_4$ solution (0.025 M), pre-heated at 70 °C. The final Si:Al:$HClO_4$ molar ratios were 1:2:1. The dispersion was kept at 70 °C during 5 hours under continuous stirring, and then refluxed at 100 °C during 10 days. The reaction mixture was then cooled down, dialyzed against deionized water to remove unreacted reagents, and freeze-dried (-50 °C, $3 \cdot 10^{-2}$ mmHg).

A representative TEM micrograph of the synthesized imogolite nanotubes is reported in Figure 4.6.

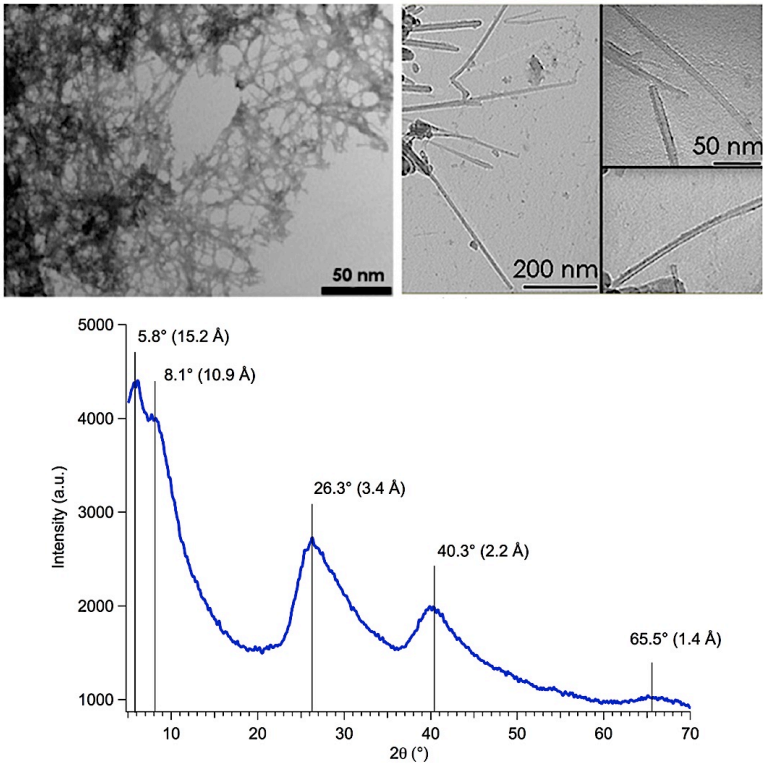

Figure 4.6 TEM micrographs (top) and XRD pattern (bottom) of synthesized imogolite nanotubes. All images are reproduced from the submitted paper *Adsorption of amino acids and glutamic acid-based surfactants on imogolite nanotubes* (see the appendix)

Consistently with the literature[179–181], imogolite shows a strong tendency to form bundles. The observed bundles of nanotubes have external diameters ranging from 5 to 15 nm, internal diameters ranging from 1 to 3 nm, and lengths of about 250-300 nm. The XRD pattern reported in Figure 4.6 confirms the successful preparation, showing a very good agreement with previous results[111,117] and with the pattern reported in the International Centre for Diffraction Data database (ICDD, PDF 38-0447). In particular, the first two peaks at $2\theta = 5.8°$ and $2\theta = 8.1°$ correspond to characteristic dimensions of ~15 Å and ~11 Å, respectively, which can be assigned to the regular distances resulting from hexagonal packing of nanotubes, while the peaks at higher angles can be assigned to bond distances between atoms composing the sample. For instance, the diagnostic peak at $2\theta = 26.3°$ corresponds to 3.4 Å and can be attributed to the Al-O-Si bond distance, *i.e.* the thickness of a tube wall (the sum of Al-O and Si-O bond distances gives 3.5 Å).

Nitrogen adsorption isotherm of imogolite sample (Figure 4.7) displays a Type I isotherm with a small hysteresis loops that is associated to slit-shaped mesopores, most likely deriving from aggregation of nanotubes into bundles[181,182]. The specific surface area of the synthesized imogolite sample is 317 ± 7 m^2/g, in good agreement with the typical values reported in the literature, ranging from 300 to 400 m^2/g. Thermogravimetric analysis (Figure 4.7) shows that IMO has a moisture content of ~23 %wt (calculated from the weight loss in the 25-150 °C range). The structural dehydroxylation of imogolite, *i.e.* loss of chemisorbed water, takes place in the 150-800 °C range producing a weight loss of ~20 %wt, consistent with the theoretical values obtained from the molecular formula $Al_2SiO_3(OH)_4$. Synthesized imogolite nanotubes were also characterized by ATR-FTIR spectroscopy. The spectrum (Figure 4.7) shows the characteristic peaks of aluminosilicate materials: the signals at 930 and 590 cm^{-1} are assigned to Si-O-Si stretching and O-Si-O bending, respectively[111]; the shoulder at 685 cm^{-1} corresponds to Al-O-Si stretching; the peak at ~1640 cm^{-1} is assigned to OH bending of physisorbed water[183], while the broad band around 3350 cm^{-1} is assigned to OH stretching of surface hydroxyl groups and physisorbed water. DLS analysis was also performed on imogolite aqueous dispersions, revealing the presence of two populations of scatterers. The most abundant

population consists of objects with hydrodynamic diameter of ~750 nm, while the second consists of large agglomerates. DLS results confirmed TEM observations, in which bundles of IMO nanotubes are always detected.

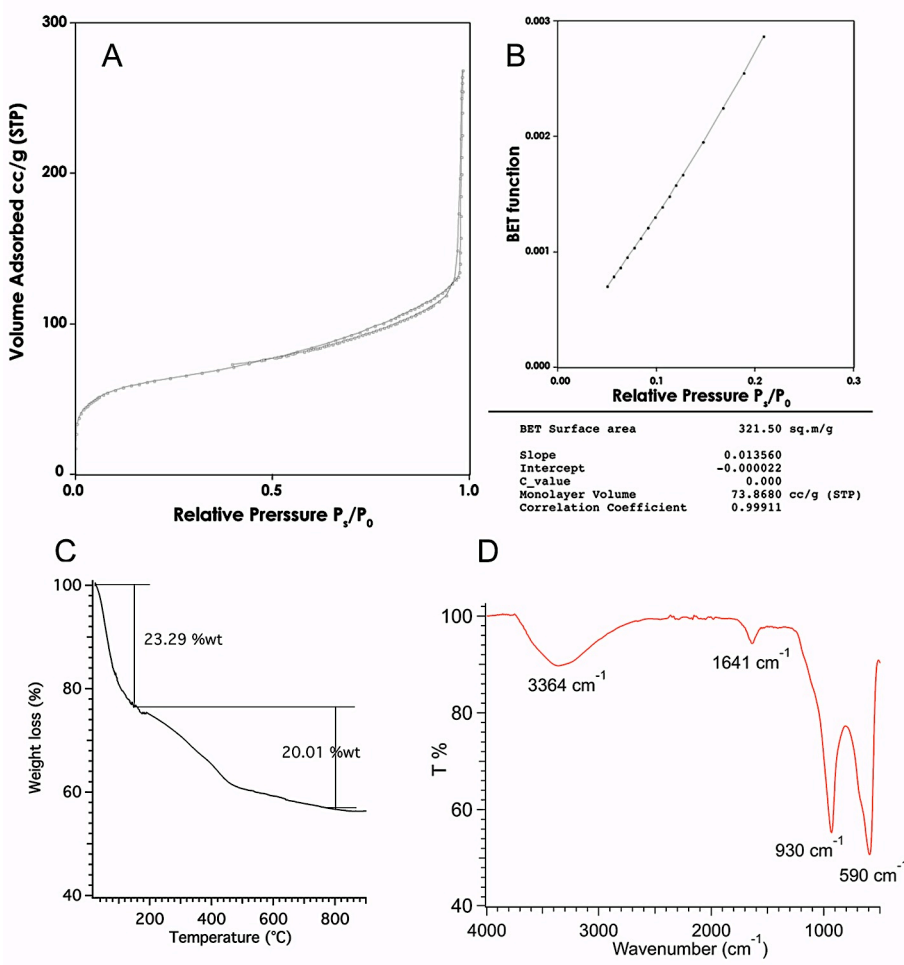

Figure 4.7 Nitrogen adsorption isotherm of imogolite sample, showing Type I isotherm with a small hysteresis loops that is associated to slit-shaped mesopores, most likely deriving from aggregation of nanotubes into bundles **(A)**. Example of BET surface area calculation on imogolite sample **(B)**. Thermogravimetry curve of imogolite sample in the 25-900 °C temperature range. Indicated weight losses correspond to the loss of physisorbed water (25-150 °C) and to structural dehydroxylation (150-800 °C) **(C)**. ATR FT-IR spectrum of synthesized imogolite in the 500-4000 cm^{-1} range **(D)**. All images are reproduced from the submitted paper *Adsorption of amino acids and glutamic acid-based surfactants on imogolite nanotubes* (see the appendix).

4.5 Amino acids as biocompatible building blocks

In the framework of bio-nanotechnology and bone tissue engineering, amino acids are of particular interest as they possess a broad spectrum of chemical reactivity and they are involved in many biochemical processes. For instance, negatively charged amino acids (*e.g.*, glutamic acid and phosphoserine) are highly expressed in non-collagenous proteins involved in the mineralization of bones[184] and they can either promote or inhibit hydroxyapatite formation, as well as alter its morphology and crystalline structure[185–187]. Furthermore, thanks to their chemical versatility and to the possibility of modulating their interactions with solid surfaces (e.g., by varying pH, ionic strength, etc.) amino acids could likely be used as biocompatible building blocks in the fabrication of hybrid nanostructures with tailored functionalities. For instance, amino acids have been employed as the polar head-group in the synthesis of amphiphilic compounds[188]. One of the most important properties of these surfactants is their easy biodegradability, which is a general prerequisite for most consumer and biomedical products in order to reduce the impact on the environment and the residence time in living organisms. All α-amino acids have a carboxyl group and a primary amino group, and a surfactant can be obtained by attaching a hydrophobic moiety (*i.e.*, an alkyl chain) at either of these sites, resulting in the formation of cationic, anionic or zwitterionic surfactants, depending on the synthetic procedure. If the starting amino acid contains an extra carboxyl group, as in the case of aspartic acid and glutamic acid, attaching a hydrophobic residue via the α-amino group results in the formation of dicarboxylic amino acid-based surfactants with chelating properties[189]. Besides their use as "green" solubilization or emulsification agents, the presence of a bioactive polar head-group allows for selective targeting of biological surfaces, and for the use of these biomimetic surfactants as carriers for actives and drugs.

4.6 Amino acid adsorption on imogolite nanotubes

Amino acids with different side chain functional groups were investigated: Arg and Lys, Glu, Gly, Ser were chosen as representative examples for basic, acidic, non-polar and polar amino acids, respectively. To adsorb

amino acids onto imogolite, 1 ml of an aqueous IMO dispersion (4 g/L) was mixed with a fixed amount of the selected compounds. The amount of amino acid was chosen to theoretically cover twice the surface area of the IMO in the sample: this value was calculated by taking into account the specific surface area of IMO resulting from porosimetry and considering a value of 0.2 nm^2 for the area occupied by the polar head of the amino acid[190]. Water was then added to reach a total volume of 5 mL. The final concentration of amino acid was 4 mM, while the final concentration of IMO was 0.8 g/L. A dispersion of IMO at the same concentration, without the amino acid, was prepared and used as a reference for the adsorption experiments. Experiments at different pHs were carried out by adding HCl 1M and NaOH 1M drop wise, and checking the final pH with a pH-meter. The adsorption experiments in saline physiological conditions were performed by making up the samples to the final volume with NaCl 0.9 %w/v. To evaluate the adsorption of amino acids onto IMO surface and to elucidate their effect on the colloidal stability of IMO dispersions in water, we extracted the coagulation rate from a linear regression of the turbidity curve in the early stage of the aggregation process (see the appendix for details). All results are summarized in Figure 4.8.

The kinetics of aggregation is differently affected by the presence of amino acids: basic amino acids, such as Arg and Lys, display a destabilizing effect on the IMO dispersions, while Glu, Ser and Gly slightly increase the stability. Two hypotheses can be drawn about the effect of amino acids on the surface charge of IMO. In the first, the physisorption of amino acids on the external surface of IMO takes place thanks to the affinity of the α-amino acid for the alumina surface. This will normally lead to a decrease of the IMO net charge, but if the amino acid contains an extra carboxyl group or an extra amino group, this functional group will be oriented towards water and may lead to an increase in the net charge. In the second hypothesis, amino acids with a pronounced acidic or basic character are able to change the pH of the system, thereby inducing changes in the surface charge of IMO by protonating or deprotonating aluminol and silanol groups (see **Chapter 1**).

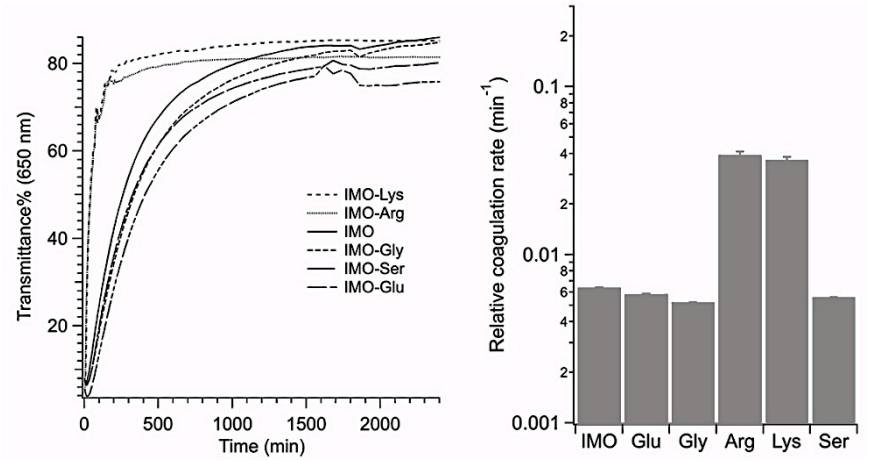

Figure 4.8 Transmittance @650 nm of the various IMO-amino acid dispersions as a function of time (an amino acid-free IMO dispersion is also shown for comparison) (left), and corresponding coagulation rates of IMO-amino acid dispersions (right). All images are reproduced from the submitted paper *Adsorption of amino acids and glutamic acid-based surfactants on imogolite nanotubes* (see the appendix).

By looking at the relative coagulation rates and the pH of IMO-AA dispersions (reported in Table 1, together with ξ-potential measurements), two general behaviors could be identified: (i) Arg and Lys produces pH values approaching the PZC of IMO, resulting in relative coagulation rates of the same order of magnitude as for IMO at pH = 10, (ii) the relative coagulation rates obtained with all the other tested amino acids are generally one order of magnitude smaller.

To further investigate the effect of pH and amino acids, Glu and Lys were selected as examples of the two general behaviors. Addition of Lys brings the pH to 9, which is one unit lower than the PZC of IMO, and results in a high coagulation rate, just below the one observed at pH = 10. On the other hand, the effect of Glu cannot be simply justified by the pH: in fact, the surface charge of IMO in the presence of Glu is very similar to that of IMO at the corresponding pH, but the coagulation rate in the presence of Glu is almost doubled. This peculiar behavior of Glu can be explained by taking into account its molecular structure, especially focusing on the presence of the two carboxyl groups. Two modes of chelation are suggested in the literature based on FT-IR data on glutamate adsorbed on γ-Al_2O_3 surface[191]: either both the carboxylate groups of Glu are involved

in bonding to surface Al atoms through covalent or hydrogen bonds, or only one of the two carboxylates (*i.e.*, the side chain COOH group) is bound to surface Al atoms. Since the external surface of IMO consists of alumina, it is reasonable to assume that glutamate physisorbs onto IMO similar to what happens in γ-Al_2O_3 crystals. As a result, the surface of the IMO particles will then expose the Glu amino group (which is protonated at pH = 4) and also one of the carboxylate groups in the case of a bidentate binuclear complex[191]. The increased aggregation rate of IMO-Glu compared to IMO without Glu at the same pH could thus be explained by invoking electrostatic attraction between protonated amino groups and carboxylate groups belonging to different particles.

Table 1 ξ -potential, pH values, and relative coagulation rate of IMO dispersions with and without addition of the amino acid (pH values of pure amino acid solutions are given within parentheses). The table is reproduced from the submitted paper *Adsorption of amino acids and glutamic acid-based surfactants on imogolite nanotubes* (see the appendix).

Sample	ξ -potential [mV]	pH	Rel. coagulation rate [1/min]
IMO pH 4.2	+46.7 ± 0.8	4.2	$3.33 \cdot 10^{-3}$
IMO	+34.1 ± 1.7	6.0	$6.35 \cdot 10^{-3}$
IMO-Glu	+48.5 ± 2.3	4.2 (3.5)	$5.80 \cdot 10^{-3}$
IMO-Gly	+32.8 ± 1.9	7.0 (6.3)	$5.20 \cdot 10^{-3}$
IMO-Ser	+33.7 ± 1.7	6.5 (6.2)	$5.60 \cdot 10^{-3}$
IMO-Arg	+11.7 ± 1.0	9.3 (10.1)	$3.92 \cdot 10^{-2}$
IMO-Lys	+12.1 ± 0.3	9.0 (9.8)	$3.67 \cdot 10^{-2}$
IMO pH 10	n.a.**	10.0	$5.91 \cdot 10^{-2}$

** Results not reliable, the error being larger than the experimental value.

The kinetics of aggregation of IMO dispersions was also evaluated under physiological conditions (data not shown, see the appendix). The results demonstrate that the increased ionic strength destabilizes all the samples with a leveling in the coagulation rates, as it is expected in dispersions where electrostatic stabilization plays a major role[192]. In the specific case of IMO-Glu, a ten-fold increase is observed (data not shown, see the appendix). To verify and quantify the adsorption of the amino acids on IMO nanotubes, IMO-amino acid dispersions were centrifuged; the resulting solid was collected and investigated by FT-IR spectroscopy and elemental analysis. FT-IR results (Figure 4.9) provide evidence that amino acids are adsorbed onto imogolite nanotubes, and that Glu is adsorbed in higher amount. The symmetric and asymmetric stretching of deprotonated carboxyl groups is observed at 1405 cm^{-1} and 1590 cm^{-1}, respectively. The absence of a peak above 1700 cm^{-1} supports the lack of protonated carboxyl groups and it is consistent with previous studies on the adsorption of amino acids on TiO_2 and γ-Al_2O_3 surfaces[193–195]. The signals at ~1460 and ~1350 cm^{-1} are attributed to CH_2 bending. The intense band centered at 1635 cm^{-1} (also present in the spectrum of pure imogolite, see Figure 4.7-D) is attributed to OH bending of physisorbed water.

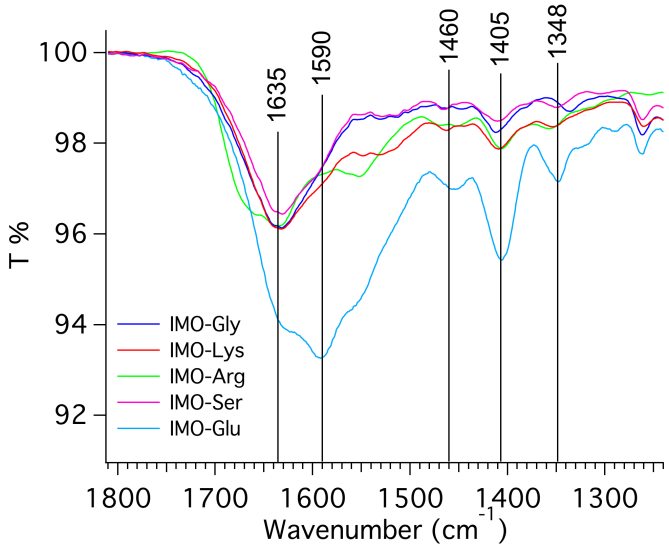

Figure 4.9 ATR FT-IR spectra of IMO-amino acid samples in the 1250-1800 cm^{-1} range. The image is reproduced from the submitted paper *Adsorption of amino acids and glutamic acid-based surfactants on imogolite nanotubes* (see the appendix).

Elemental analysis results indicate that a significant amount of carbon is detected in the case of IMO-Glu, corresponding to 11.6 %wt of Glu adsorbed onto IMO. Taking into account the specific surface area of the nanotubular clays and by assuming that the entire surface is available for the physisorption, we could then estimate an effective head group area of 0.33 nm^2 (see the appendix for details), a value which is ~1.5 times larger to what is found in tightly packed self-assembled monolayers formed by surfactants based on a carboxyl head group[190]. Even more interesting is the comparison with the head group area at the air-water interface found in Glu-derived surfactants (0.88 nm^2)[196]. These findings suggest a quite dense packing of Glu molecules onto the IMO surface, and inspired us to use glutamic acid as a building block in the design and fabrication of a hybrid material based on imogolites.

4.7 Imogolite-lauroyl glutamate nanocomposites

The marked affinity of glutamic acid for the IMO surface was exploited to prepare a composite material consisting of imogolite nanotubes coated with a Glu-based surfactant, able to upload a drug model. The surfactant chosen for this experiment was lauroyl glutamate (C_{12}Glu) in the disodium form[197], kindly provided by Prof. Krister Holmberg (Chalmers University, Göteborg, Sweden). This surfactant has already been shown to favorably adsorb on the surface of Al_2O_3, while no adsorption was detected on SiO_2. A value of about 285 ng/cm^2 was determined by means of a quartz crystal microbalance with monitoring of the dissipation (QCM-D) at the critical micelle concentration (cmc), in salt-free conditions. The adsorption of lauroyl glutamate onto IMO nanotubes was achieved by adding 3.7 mg of C_{12}Glu to 5 mL of a 0.8 g/L IMO dispersion, and allowing the system to equilibrate under constant stirring at room temperature. The mechanism of formation of the hybrid is sketched in Figure 4.10. The concentration of C_{12}Glu in the experiment was 2 mM; *i.e.*, well below the cmc (50 mM in salt-free conditions and 22 mM in NaCl 0.9%w/v) and also below the critical surface association concentration (csac), which is typically around 1/10 of the CMC[198]. At this level of concentration, one would expect that the adsorption of C_{12}Glu on IMO results in patches of micelle-covered surface separated by areas of naked surface. The micelle-covered surface

would be strongly anionic and the naked surface in-between would be cationic. Thus, with such an incomplete adsorption one would expect to have attraction between the particles, *i.e.*, fast aggregation (sometimes referred to as patchwise flocculation). This is actually the case in our experiment, where a precipitate is formed after just a few minutes (Figure 4.10).

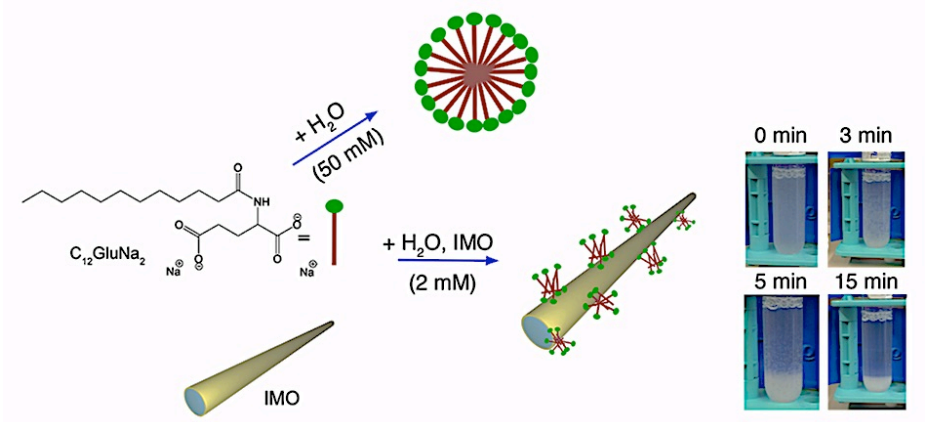

Figure 4.10 Schematic representation of the adsorption-uploading experiment performed with IMO-C_{12}Glu. The image is reproduced from the submitted paper *Adsorption of amino acids and glutamic acid-based surfactants on imogolite nanotubes* (see the appendix).

As a proof of concept, we performed an uploading experiment on the hybrid, using rhodamine B isothiocyanate (RHO) as a model for a drug. An aqueous solution of RHO (1 mL, 8 mg/L) was added to the dispersion of IMO-C_{12}Glu, left to equilibrate under constant stirring for 3 hours at room temperature, and then centrifuged for 40 min at 12500 g. To evaluate the effect of physiological saline conditions on the uploading process, IMO-C_{12}Glu was dispersed in a 0.9 %w/v NaCl solution and then the same procedure was followed. The supernatant solutions were collected, and UV-Vis spectra were acquired in order to quantify the residual amount of dye in solution. As a reference, a sample containing RHO and IMO, without disodium lauroyl glutamate, was used.
As shown in Figure 4.11, pristine IMO is able to adsorb a certain amount of dye, most reasonably through electrostatic and van der Waals interactions with the external surface: in fact, due to its molecular size, the access of the dye inside the lumen of IMO is limited by geometrical

constraints[199]. When the same experiment is performed in saline buffer solution (NaCl 0.9 %w/v), the uploaded amount is nearly unchanged. On the other hand, the amount of adsorbed dye drastically increases (nearly threefold) when C_{12}Glu is present, suggesting the direct role of the surfactant on the uploading process.

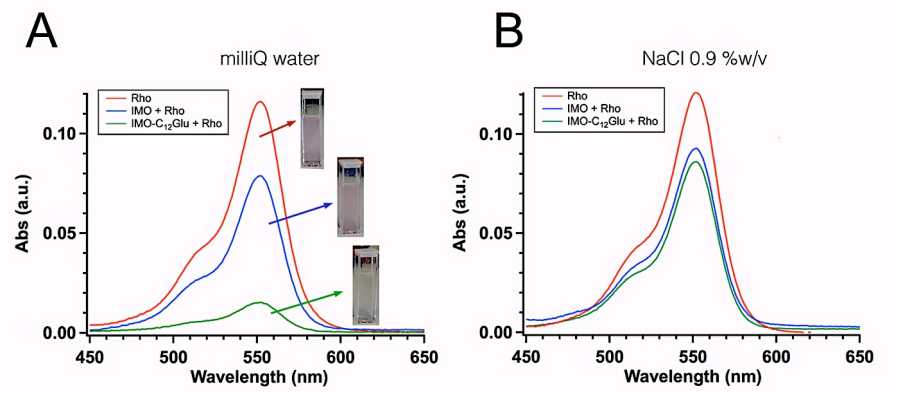

Figure 4.11 Adsorption spectra of Rhodamine B-ITC (RHO) and of IMO+RHO and IMO-C_{12}Glu+Rho supernatant solutions in Milli-Q water **(A)** and in physiological saline solution **(B)**. The image is reproduced from the submitted paper *Adsorption of amino acids and glutamic acid-based surfactants on imogolite nanotubes* (see the appendix).

When the adsorption of C_{12}Glu and RHO is carried out in physiological saline conditions (Figure 4.11-B), the amount of uploaded RHO is nearly the same as for pristine IMOs. This can be explained by taking into account the shielding effect of sodium chloride on the IMO surface charges, resulting in a decreased interaction between the C_{12}Glu polar head groups and the surface. This is also consistent with the relative coagulation rates in Table 1 showing that IMO nanotubes undergo a fast aggregation in the presence of NaCl, also in the presence of glutamate. All these results demonstrate that imogolite nanotubes represent flexible multifunctional platforms, thanks both to their nanotubular structure and to the exposed alumina surface, which dictates the interaction with amino acids bearing different side chain functional groups. Novel hybrid materials could be obtained by employing amino acids as molecular building blocks, fostering the use of imogolite clays in biotechnological applications.
Furthermore, the reported results are of particular interest since they could be generalized toward the adsorption of any Glu-containing surfactant on any aluminum oxide surface.

5 Case study #3: injectable nanocomposite hydrogel for the local treatment of bone defects

The scientific research in bone medication and in the development of new and efficient methodologies for the treatment of bone diseases is becoming more and more relevant, mainly because of the progressive ageing of the world population[200]. For instance, the total health care cost associated to traumatic and pathologic fractures, in Europe, is expected to exceed 46 billions € in 2025[146]. Any effective strategy to reduce those costs requires both a preventive action (typically achieved through a healthy life style) and the minimization of the post-surgery hospital stay. To this aim, minimal invasive surgery definitely represents a suitable strategy for the effective treatment of bone fractures and diseases[201]. In this perspective, the *in-situ* injection of properly designed biomaterials able to combine adequate mechanical properties with osteo-conductivity and osteo-inductivity can be of particular relevance. Materials integrating the rheological properties of biocompatible polymers with the mechanical properties of 1D inorganic nanostructures could represent, for instance, a valuable option.

Here it is described the preparation and characterization of an injectable nanocomposite made of Halloysite nanotubes (HNT) and carboxymethyl cellulose (CMC), conceived for the local treatment of bone defects. The choice of the polysaccharide matrix responds to the need of a biocompatible polymer with well-known rheological properties. In fact, CMC spontaneously forms a hydrogel and it is commonly adopted as a rheological modifier in several water-based formulations and as the polymer component of biomaterials[202]. The potential of Halloysite nanotubes in the biomedical field has been already described in **Chapters 1** and **2**. In addition to the described structural and physico-chemical properties, it is worth stressing that Halloysite nanotubes can be successfully employed to modify the rheology of polymer matrices[203], providing a stronger thickening power compared to spheroidal and platelet particles, thanks to their 1D shape[204].

5.1 Preparation of nanocomposite hydrogels

The Halloysite batch (see **Chapter 2**) was purified with a procedure derived from the work by Shchukin *et al.*[97]. In details, 5 g of HNT were suspended in 500 mL of water and mixed with a blender for 20 minutes. The suspension was then transferred to a beaker and left to sediment. After a fixed amount of time, the supernatant solution was discarded and the sediment was re-suspended in 500 mL of water. The suspension was mixed with the blender for another 20 minutes and left to sediment again. The procedure was repeated three times. At the end, the HNT suspension was centrifuged for 10 minutes at 7500 rpm and, finally, the precipitate was collected and dried at 60°C.

A crucial prerequisite to the reliable injection of the composite hydrogel is the homogeneous dispersion of Halloysite nanotubes (HNT) in the CMC matrix. To this aim, we followed the hydrazide-aldehyde protocol successfully introduced by Hoare for the coupling of polymers with inorganic nanostructures[205,206]. HNT surface was firstly modified by the reaction of the external silanol groups with maleic anhydride (MA): 10 g of clay and 10 g of anhydride were added to 100 ml of chloroform, previously bubbled with N_2, and kept at 37 °C under stirring, overnight. The solid product was recovered by centrifugation, washed with chloroform and dried. The functionalization of HNT with MA was confirmed by means of FT-IR spectroscopy (Figure 5.1) and ζ-potential measurements (Table 2) Comparing HNT to HNT-MA, both the appearance in the FT-IR spectrum of the C-H, C=O and C=C stretching and the change of the ζ-potential from -43 to -28 mV were taken as evidences for the occurred functionalization.

HNT-MA was further reacted with adipic acid dihydrazide (AAD) in order to introduce a hydrazine moiety on the clay surface. 1.5 g of AAD was added to a 0.5 %w/v water dispersion of HNT-MA, at room temperature. Then, 780 μl of (N-(3-dimethylaminopropyl)-N′-ethylcarbodiimide hydrochloride (EDC) were added and the reaction was allowed to run during 5 hours, checking and eventually adjusting the pH with HCl 0.1 M to remain constant (pH~4). After 5 hours the pH was adjusted to pH = 7 with NaOH, and the dispersion was dialyzed against milliQ water. The solid product was then recovered by centrifugation. The reaction between AAD and the carboxylic functions resulting from the functionalization of

HNT is confirmed by the change in the ξ-potential from -28 to -12 mV (Table 2), and takes to the exposition of hydrazine groups on the surface of functionalized HNT.

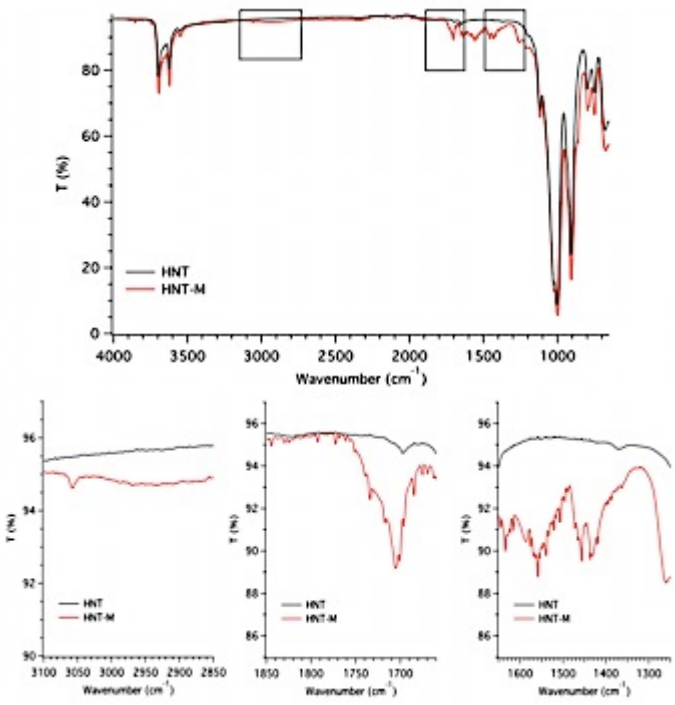

Figure 5.1 ATR FT-IR spectra of HNT-MA in the 650 - 4000 cm-1 range (the spectrum of pure HNT is also shown for comparison). In the HNT-MA spectrum signals attributable to saturated and unsaturated C-H stretching are detected at 2931 cm-1, corresponding to maleic residues. Carbonyl C=O stretching is observed around 1700 cm-1 and the signal corresponding to C=C stretching at ~1600 cm-1 is clearly observed.

Table 2 ξ -potential values of the products obtained from the functionalization of Halloysite nanotubes surface.

Sample	ξ-potential (mV)
HNT	-42.9 ± 1.1
HNT-MA	-27.6 ± 0.6
HNT-MA-AAD	-12.2 ± 0.3

Meanwhile, carboxymethyl cellulose was partially oxidized by adding 5.3 g of $NaIO_4$ to a 1% w/v CMC solution. After 2h of mixing at room temperature, ethylene glycol (2.7 ml) was added to quench the oxidation reaction. The short reaction time and the low concentration of oxidizing agent prevent a marked degradation of the polymer, as reported in the literature[207]. The polymer solution was dialyzed (membrane cut-off = 12.4 kDa) and the solvent was partially removed by rotavapor. The obtained oxidized CMC (oxCMC) was finally freeze-dried.

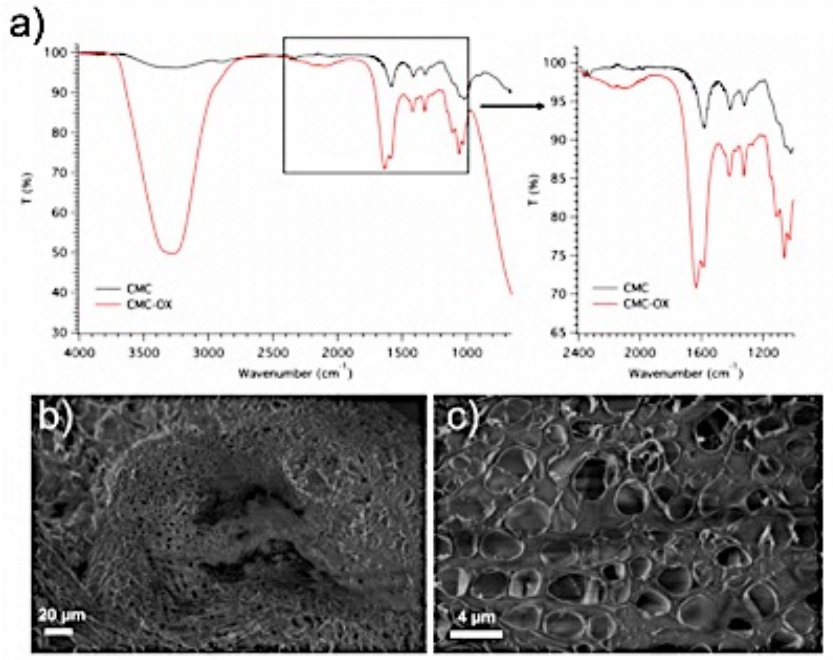

Figure 5.2 ATR FT-IR spectrum of oxidized CMC in the 650 – 4000 cm-1 range (the spectrum of pristine CMC is also shown for comparison) **(A)**; SEM images of freeze-dried samples of oxidized CMC in water at two different magnifications **(B, C)**.

Figure 5.2-A shows the FT-IR spectrum of oxidized CMC in the 650-4000 cm^{-1} range, together with that of pristine CMC. The appearance of a peak at ~1630 cm^{-1}, in addition to the carboxylate peak at ~1590 cm^{-1}, is taken as the evidence of CMC oxidation[208]. As can be deduced from the SEM image in Figure 5.2-B and Figure 5.2-C, oxCMC maintains the

ability to form the typical porous structure of pristine cellulose hydrogels, consistently with a modest level of CMC degradation.

In the last step, oxCMC was mixed with modified HNT in water, under mechanical stirring. The reaction between the aldehyde functions present in oxCMC and the hydrazine groups exposed by HNT-MA spontaneously takes to the formation of hydrazone bonds, resulting in a organic/inorganic composition of about 50 %w/w (see the appendix for details). The final concentration of both oxCMC and HNT-MA was 10 %wt. The nanocomposite hydrogel (NC-MA) was finally obtained by adding pristine CMC to a final concentration of 2 %wt, so to reach a viscosity suitable for injection purposes. A blank sample composed of 2 %wt CMC and 5 %wt oxCMC water solution was also prepared as a reference for the rheological and injectability tests. The amount of oxCMC was chosen to replicate the composition of NC-MA sample without the inorganic phase. The synthetic route followed for the preparation of the nanocomposite hydrogel is summarized in **Figure 5.3.**

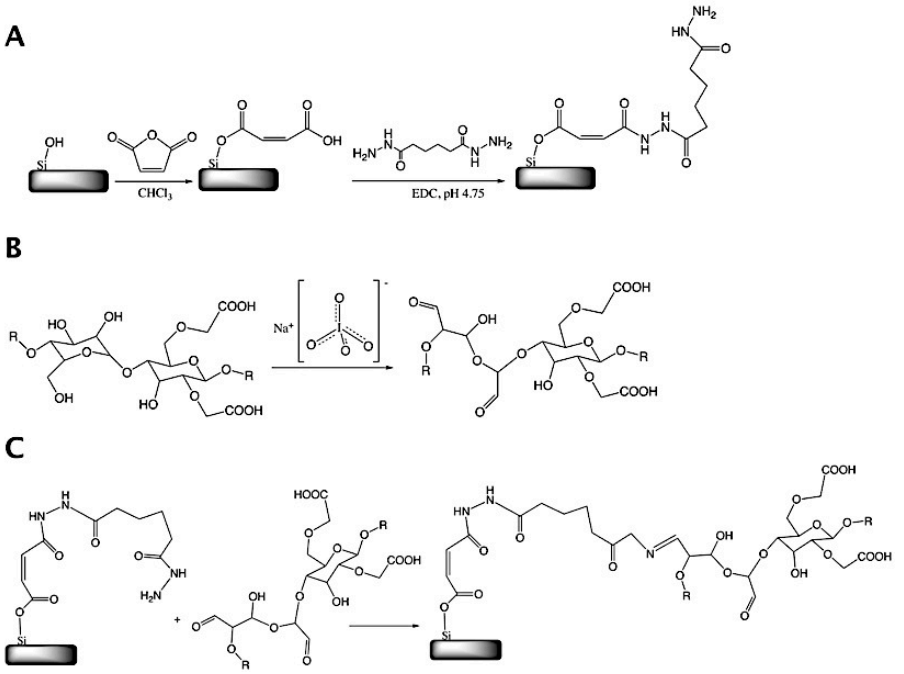

Figure 5.3 Synthetic route for the fabrication of NC-MA composite hydrogel.

5.2 Structural and rheological characterization

Representative SEM images of freeze-dried nanocomposites are shown in Figure 5.4, together with the CMC/oxCMC sample at the same magnifications. Composite hydrogel samples show a porous structure similar to that of CMC/oxCMC hydrogel. SEM results highlight that HNT are homogeneously distributed in the composite material and that the hydrogel-forming properties of CMC are retained.

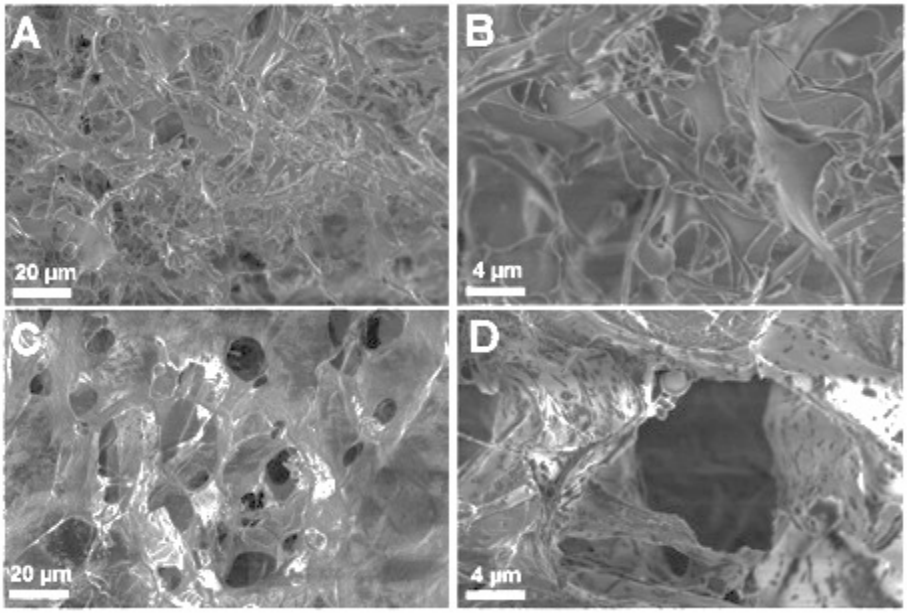

Figure 5.4 SEM images of freeze-dried CMC/oxCMC **(A, B)** and NC-MA **(C, D)** samples at different magnifications.

Figure 5.5-A shows the dynamic viscosity of the nanocomposite hydrogels (NC-MA) and of CMC/oxCMC reference sample, as a function of the shear rate. The CMC/oxCMC sample shows a very short Newtonian region (up to about 0.1 s^{-1}) at very low shear rates, followed by an extended shear-thinning region. This behavior can be ascribed to the disentanglement of the polymeric network, held together by hydrogen bonds, upon application of a certain stress. After the samples are stressed to high shear rates (about 50 s^{-1}), a hysteresis effect is observed upon the application of a decreasing shear rate ramp. This feature is typical of CMC

concentrated solutions[209] that are characterized by a rheopectic behavior, whose magnitude increases upon lowering the applied shear stress.

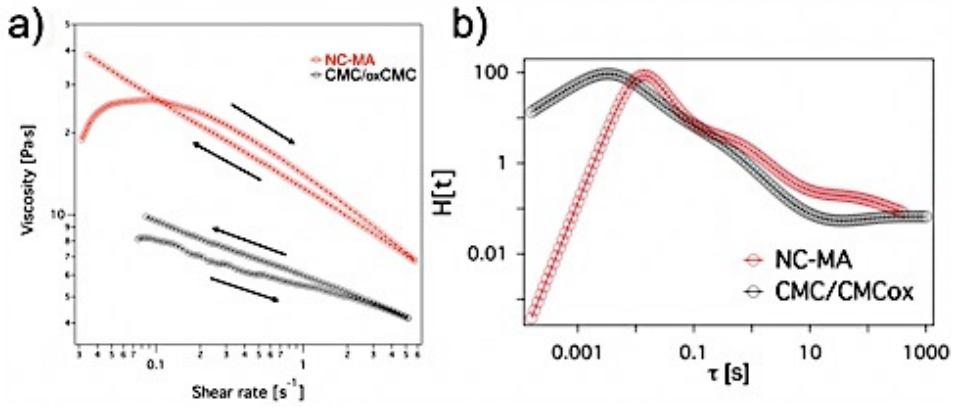

Figure 5.5 (A) Flow curves of CMC/oxCMC and NC-MA hydrogels (arrows indicate the shear rate ramp) and **(B)** continuous relaxation spectra *H[t]* of the CMC/oxCMC water based system before (black) and after (red) the loading of NC-MA composite. The spectra *H[t]* have been obtained from the frequency sweep curves of the two systems collected in the linear viscoelastic regime[210], since the dynamic of the two systems cannot be described by a single-element Maxwell model.

The introduction of HNT substantially modifies the rheological behavior of the system, making it significantly more viscous (at least twice as much) in the entire range of shear rates explored. Below 0.05 s^{-1} the sample displays a steep shear-thickening effect followed by a pseudo-Newtonian behavior up to about 0.1 s^{-1}, and then by a shear-thinning region as in the case of CMC/oxCMC. Similar to what has been observed in polymeric composites filled with fumed silica nanoparticles[211], the trend in the viscosity reflects the flow-induced aggregation of particles (shear-thickening regime), followed by the movement of aggregates along the flow direction (shear-thinning regime). The transition occurs at the so-called elasto-hydrodynamic lubrication limit of shear thickening, corresponding to a shear rate of about 0.2 s^{-1}. The nanocomposite also displays thixotropy at shear rates higher than 0.1 s^{-1}, while at lower shear rates the effect of the polymer matrix prevails and an anti-thixotropic behavior is observed. The presence of HNT is also reflected in the relaxation spectrum of the nanocomposite, which shows a shift toward higher *t* values of the main relaxation time (Figure 5.5-B).

5.3 Injectability of nanocomposite hydrogels

Injectable composites are typically complex and non-Newtonian fluids, such as hydrogels, gels, pastes, concentrated suspensions and so on. Among them, shear thinning and thixotropic materials are especially appealing to minimal invasive surgery, since their viscosity decreases during the injection, while they eventually recover their initial rheological state at the injection site, when the stress is relieved. As a result, the material is able to conform and eventually adhere to the site thanks to chemical affinity and microscopic interlocking[212]. A number of studies have already suggested the use of injectable composites in supporting the growth of damaged tissues, such as in bone tissue engineering, treatment of hemorrhage, and wound healing[213–215]. Such a broad range of applications highlights the need for new materials with tunable rheological properties that could be injected with needles of different gauges. The injectability of a material through a needle is typically assessed by evaluating the minimum pressure required for its injection, the evenness of its flow and the absence of clogging[216]. However, a detailed investigation of the material's properties during injection and a correlation between structure and rheology are often neglected.

The nanocomposite hydrogel NC-MA was investigated by means of injectability tests through two different needle gauges (G21: D = 12 mm; d = 0.51 mm; l = 40 mm and G29: D = 4.7 mm; d = 0.18 mm; l = 20 mm), which are commonly employed for intramuscular and subcutaneous injections, respectively. The tests were performed by applying controlled loads on the plunger of a syringe loaded with the composite, and by measuring the corresponding flow. Taking into account the geometrical parameters of the syringe and the needle, an apparent viscosity can be estimated from the Poiseuille law:

$$F = \frac{32D^2 lQ\eta}{d^4} \qquad \textbf{(2)}$$

where F is the force applied to the syringe plunger, D is the syringe plunger diameter, d and l are the inner diameter and the length of the needle, respectively, and Q is the flow rate.

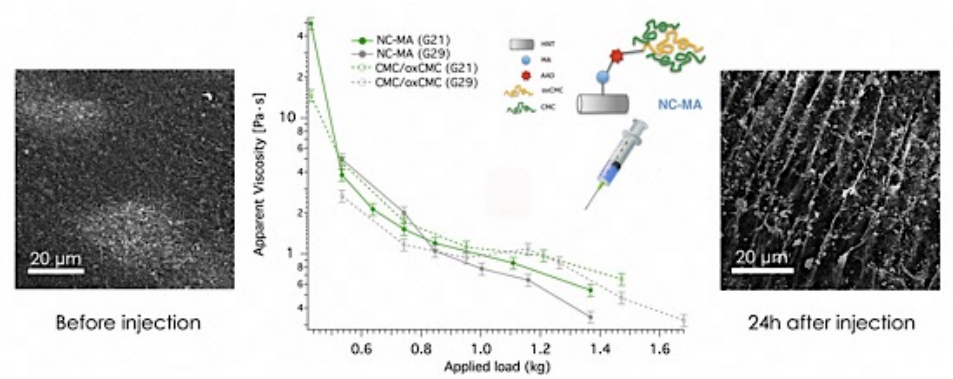

Figure 5.6 Injectability tests of NC-MA and CMC/oxCMC hydrogels, expressed as apparent viscosity *vs* applied load, performed on G21 and G29 needle gauges (in the middle); SEM images of NC-MA lyophilized hydrogel before the injection through a G21 needle (left) and 24 hours after the injection (right).

Injectability results are reported in Figure 5.6, together with representative SEM images of the nanocomposite before and after injection. Results show that the apparent viscosity exponentially increases when the load is reduced, and that our composite material can be easily injected through G21 and G29 needles under loads well below 1 kg. To make the (qualitative) comparison with the rotational rheology experiments one could calculate the wall shear rate in the injectability experiments considering a Newtonian fluid flowing within a pipe. The resulting flow curves in terms of apparent viscosity *vs* wall shear rate clearly indicate that the injection process takes place within the shear-thinning region (see the appendix for details). The lowest load producing a homogeneous flow with G21 was as small as about 0.4 kg (about 0.55 kg with G29). In spite of the presence of inorganic nanostructures that could in principle aggregate and obstruct the orifice, the injectability is mostly dictated by the CMC/oxCMC matrix, as no major difference was observed between the composite and the reference hydrogel. This was attributed to the peculiar 1D structure of Halloysite nanotubes, which tend to align with the direction of the flow, and was confirmed by the SEM images in Figure 5.6, showing that the injection produces a strong change in the structure of the polymer matrix at the microscale: in fact, once injected under lower loads, the material was not any longer injectable, unless the load was increased.

5.4 Concluding remarks

Combining the mechanical properties of Halloysite nanotubes with the rheology and biocompatibility of carboxymethyl cellulose results in the formation of a nanocomposite hydrogel that could represent a suitable platform for the supported growth of bone tissue. Moreover, the ability of both components to upload and release actives (such as drugs, proteins, genes, and living cells) and the biodegradable hydrazone coupling between the polymer and the clay, represent useful characteristics in the design of multi-functional biomaterials. Injectability tests provided a quantitative evaluation of the performances in practical conditions. The composite was successfully injected through needles with inner diameters spanning from 510 to 180 μm, without any clogging also at very low applied loads (*i.e.,* less than 1 kg). The injection takes to the structuring of the material, resulting in an increase of its viscosity at low shear rates. This is especially interesting in the framework of using the composite in minimal invasive surgery, since such structural effect would reduce the spreading of the material around the injection site. Together with the very small size of the needles and the low flow achievable, this could result in the possibility to robotically apply the described composite at the damaged site with a high spatial resolution. Further studies are needed to validate the *in-vivo* application of our materials, but still these results could represent a significant contribution to extend the use of composite hydrogels to minimal invasive surgery.

6 Case study #4: mineralization properties of macroporous Gelatin/Imogolite hydrogels

Hydroxyapatite ($Ca_{10}(PO_4)_6(OH)_2$) composes the main mineral fraction of human bones and teeth. In bones, it is found as non-stoichiometric, calcium-deficient apatite, containing carbonate and impurities such as sodium and magnesium ions[217,218]. The presence of these inclusions, especially carbonate, contributes to the unique features of bone in terms of mechanical and biological properties[20]. A great effort has been recently devoted to rationalize hydroxyapatite formation and crystallization in organic matrices[219], in the attempt of unraveling the process of bone tissue formation and remodeling. This is of particular interest in the fields of bone and dental tissue engineering, where synthetic scaffolds are designed to support and promote the growth of new tissue, including hydroxyapatite crystals with tunable composition and structural properties[220,221]. Among the various matrices investigated to this purpose, hydrogels represent a valuable example since they possess several favorable characteristics. Hydrogels can upload a high amount of water thus producing an environment suitable for cellular growth, and many biocompatible polymers are able to form 3-dimensional networks in water. Furthermore, hydrogels are easily endowed with the right features required in the design of a scaffold for bone tissue engineering: for instance, interconnected macro-porous structures (pores with diameter of at least 100 μm are needed to allow penetration by cells and adequate diffusion of nutrients) can be generated by freezing the water inside the hydrogel matrix and let it sublimate, *i.e.*, cryogenic pore formation.

Gelatin (Gel) is one of the hydrogel-forming materials mostly investigated in bone tissue engineering applications[222]. Unfortunately, its application is limited because of its fast dissolution rate in physiological conditions, making it necessary to increase stability of gelatin-based material[223,224]. Possible strategies include the introduction of covalent cross-linking sites that can be obtained by using ionizing radiation such as electrons or gamma rays[225], by fabricating composite materials[226], or by employing chemical cross-linking agents that react with the functional groups of gelatin. Bis-epoxy molecules, such as glycerol diglycidyl ether (GDE) and ethylene glycol diglycidyl ether (EGDE), have been reported to enhance

the stability of gelatin hydrogels[58], as the epoxide ring could be opened by the gelatin nucleophilic functional groups (*i.e.*, amine, hydroxyl and carboxyl groups) forming a cross-linked network. In the perspective of a biomedical application, the cross-linker toxicity is a parameter to take into account, since unreacted molecules can affect the final biocompatibility. Bis-epoxy cross-linking agents display a lower toxicity compared to glutaraldehyde and EDC, and represent thus an improved alternative to typical gelatin cross-linkers[227]. Another successful strategy to enhance the mechanical properties and the stability of polymer hydrogels is the integration with inorganic nano-sized fillers, to produce nanocomposite materials. Among the various fillers reported in the literature, Imogolite nanotubes (IMO) are an extraordinary example, as they possess unique structural and physico-chemical properties[228–230] (see **Chapter 2** for a general description of Imogolite properties and applications). Imogolite (IMO nanotubes are also very promising as components of biomaterials, since they display a reduced cyto- and geno-toxicity with respect to other synthetic nanotubes, *e.g.* carbon nanotubes[132]. Furthermore, the presence of Imo has been also demonstrated to enhance osteoblastic proliferation and differentiation[231].

In order to fully exploit the characteristics of gelatin and Imogolite nanotubes in the field of bone tissue engineering, in the following pages is described the preparation of a gelatin scaffold whose dissolution rate at physiological temperature is slowed down by means of the synergistic effect of an organic cross-linker (GDE) and Imo nanotubes. By means of cryogenic formation, macropores were generated in the hydrogel network, matching the proper dimensions for the permeation of cells. Mineralization experiments were performed following a well-accepted protocol, and a detailed characterization of the mineralized phases was conducted by means of X-ray crystallography, electron and optical microscopy, thermogravimetry and dissolution tests, demonstrating that the Gel/IMO system is able to support and enhance the formation of apatites.

6.1 Mineralization protocol

Hydroxyapatite (HA) has been synthetized according to a method reported in the literature[232] and schematized in Figure 6.1. The reaction was performed at 37 °C to simulate the physiological temperature. Imogolite nanotubes were added to calcium hydroxide suspension (5 mL, 0.5 M) before adding H_3PO_4. The concentration of Imo samples was chosen so to be 5 %wt and 10 %wt with respect to the calculated weight of precipitated HA. According to the literature, the slow addition of H_3PO_4 enables to obtain crystalline HA with nanometric size (~50 nm): for this reason H_3PO_4 solution (5 mL, 0.3 M) was added in aliquots of 200 µl every 5 minutes, during 2 hours. The suspensions were maintained under stirring at 37 °C for 15 hours, and then at room temperature for three days. During this time a gelatinous product gradually precipitated from the initially white suspension. The obtained products were collected by centrifugation and dried in oven at 120 °C during three days.

In the case of the hydrogel samples the same synthetic procedure for HA formation was followed: a portion of the freeze-dried Gel_{GDE} and Gel_{GDE}-IMO (see below) was cut and each portion was soaked in $Ca(OH)_2$ suspension (2.5 mL, 0.5 M) at 37 °C. A solution of H_3PO_4 (2.5 mL, 0.3 M) was added in aliquots of 105 µl every 5 minutes. At the end of the experiment, gels were recovered and dried in air.

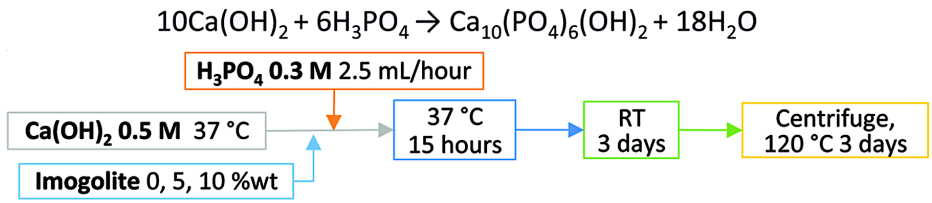

Figure 6.1 Precipitation reaction of hydroxyapatite and scheme of the experimental conditions. The image is reproduced from the submitted paper *Enhanced formation of hydroxyapatite in imogolite-reinforced macroporous hydrogels* (see the appendix).

6.2 Hydroxyapatite formation in the presence of Imogolite

The characterization of the products of the precipitation reactions highlights that the presence of IMO does not inhibit the formation of HA: Figure 6.2 shows that the morphology of the HA obtained in water without and in the presence of 10 %wt of IMO does not significantly change. It is worth noting that TEM images of HA-IMO sample do not reveal the characteristic nanotubular morphology of Imo, suggesting that HA nucleates on the surface of these structures, and that the nanotubes are included in the final HA crystals. Their XRD patterns (Figure 6.2-C) are nearly unaffected by the presence of Imo, apart from a hump at low angles in the diffractogram of HA-Imo sample, due to the presence of Imo. The XRD peaks were compared to the patterns in the ICDD database and clearly indicate the formation of hydroxyapatite [PDF 03-0747]. The Field Emission Scanning Electron Microscopy (FE-SEM) investigation of HA and HA-IMO samples shows the same homogeneous morphology (see the appendix for details). The homogeneous distribution of aluminum and silicon obtained from Energy Dispersive X-ray (EDX) analysis of HA-IMO (data not shown, see the appendix for details) further confirms that IMO is well distributed all over the sample.

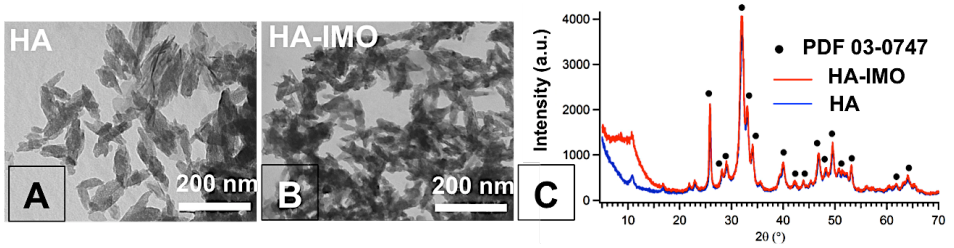

Figure 6.2 TEM image of HA obtained without IMO **(A)** and in the presence of IMO **(B)**; XRD patterns of HA and HA-IMO samples **(C)**. The image is reproduced from the submitted paper *Enhanced formation of hydroxyapatite in imogolite-reinforced macroporous hydrogels* (see the appendix).

6.3 Preparation and characterization of Gelatin/Imogolite hydrogels

To prepare the hydrogels, the amount of gelatin necessary to reach the concentration of 5 %wt was dissolved in milliQ water (0.5 g of gelatin in 9.5 g of water) and heated at 50 °C under magnetic stirring. After complete dissolution, the appropriate amount of imogolite nanotubes and/or GDE cross-linker was added to the gelatin solution, which was stirred for about 10 minutes. The amounts of reactant used and the respective %wt are summarized in Table 3. After homogenization, the hot dispersions were poured in polyethylene cylindrical molds (diameter 1 cm, height 1 cm) and were allowed to gel at room temperature. The formation of macropores was obtained by means of a cryogenic formation procedure: the hydrogels were cooled overnight in a freezer to -18 °C (cooling rate 1 °C/min) and then freeze-dried at -50 °C and 30 mTorr for two days.

Table 3 Composition and dissolution behavior of hydrogels.

Sample	Gelatin [g]	Water [g]	GDE [g]	IMO [g]	GDE %wt[f]	IMO %wt[g]	Dissolution Time[h]
Gel	0.5	9.5	/	/	/	/	~ 2 hours
Gel_{GDE}	0.5	9.5	0.025	/	5	/	~ 2 days
Gel_{GDE}-IMO	0.5	9.5	0.025	0.0525	5	10	~ 3 days
Gel-IMO5	0.5	9.5	/	0.0250	/	5	~ 6 hours
Gel-IMO10	0.5	9.5	/	0.0500	/	10	~ 6 hours
Gel_{GDE5}-IMO5	0.5	9.5	0.025	0.0262	5	5	~ 3 days
Gel_{GDE10}-IMO5	0.5	9.5	0.050	0.0275	10	5	> 5 days
Gel_{GDE10}-IMO10	0.5	9.5	0.050	0.0550	10	10	> 5 days

[f] %wt with respect to gelatin

[g] %wt with respect to organic content (gelatin+GDE)

[h] time required to observe full dissolution in water at 37 °C

The effects of GDE and IMO on the stability toward dissolution of the scaffolds (obtained by freeze-drying the hydrogels) was evaluated by placing them in an excess of water and checking the time needed before their full dissolution at 37 °C. The results are summarized in the last column of Table 3, showing that the concentration of GDE strongly affects the behavior of the hydrogel. Imo nanotubes are also effective in enhancing the stability against dissolution, but to a much smaller extent. These results highlight the possibility to control the dissolution rate by introducing different amounts of GDE and IMO, allowing the mineralization process to take place before the dissolution of the scaffold. Based on their intermediate dissolution behavior, we selected as a case of study the samples identified as Gel_{GDE}, and Gel_{GDE}-Imo (see Table 3).

Figure 6.3-B, Figure 6.3-C and Figure 6.3-D show FE-SEM micrographs and optical microscopy images of Gel, Gel_{GDE} and Gel_{GDE}-IMO, respectively. All the samples display a macroporous structure, with interconnected pores whose dimensions range from tens to hundreds of microns. The cryo-formation procedure adopted in the preparation of the porous hydrogels leads to a macroscopic deformation of the gel structure, clearly visible in the photos of Figure 6.3. Nevertheless, the formation of macropores, which is one of the key parameters to take into account when designing a scaffold for tissue engineering[233], is successfully obtained.

The presence of the cross-linker, as well as imogolite integration in the polymeric matrix, does not significantly alter gelatin microstructure. The inorganic fillers appear homogeneously dispersed in gelatin matrix, since no imogolite bundle can be observed in Gel_{GDE}-IMO FE-SEM micrograph (Figure 6.3-D).

The nanostructure of the hydrogels was investigated by means of small angle X-rays scattering (SAXS), in order to evaluate the influence of both cross-linker and imogolites on the nanostructure of the gels. SAXS curves were fitted using the Ornstein-Zernike function, an equation commonly adopted to describe polymers in a semi-dilute regime[234]:

$$I(q) = \frac{I_0}{1+\xi^2 q^2} \qquad \textbf{(3)}$$

in which I_0 is the scattered intensity at q=0, and ξ is the correlation length of the polymer. Additional fittings were performed with power law

functions to obtain information about the fractal nature of the scattering objects:

$$I(q) \propto q^{-p} \quad \textbf{(4)}$$

with p being the fractal dimension, that is 1 for 1D objects and 3 for full solid materials[235].

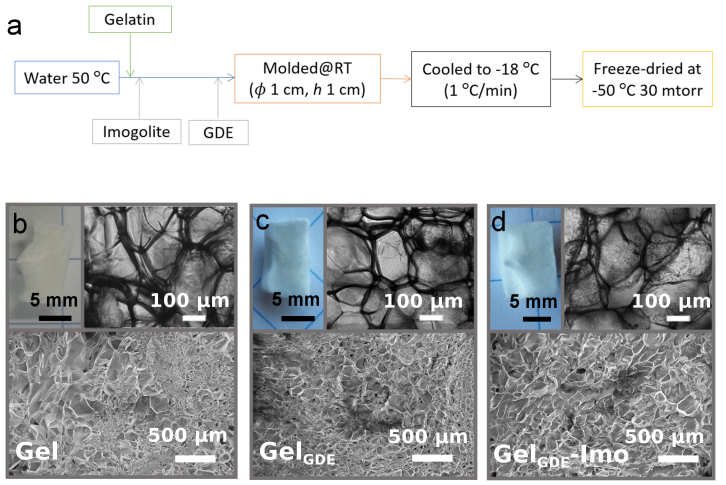

Figure 6.3 Block diagram summarizing hydrogels preparation **(A)**; photograph, optical microscopy image and SEM micrograph of Gel **(B)**, Gel$_{GDE}$ **(C)** and Gel$_{GDE}$-IMO **(D)**. The image is reproduced from the submitted paper *Enhanced formation of hydroxyapatite in imogolite-reinforced macroporous hydrogels* (see the appendix).

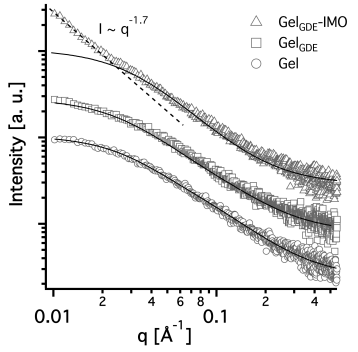

Figure 6.4 SAXS curves of Gel, Gel$_{GDE}$ and Gel$_{GDE}$-IMO fitted with Equation 3 (solid line) and 4 (dotted line). The curves are offset for display purposes. The image is reproduced from the submitted paper *Enhanced formation of hydroxyapatite in imogolite-reinforced macroporous hydrogels* (see the appendix).

The SAXS curves shown in Figure 6.4 are almost superimposable in the mid-to-high q range ($0.03 \leq q \leq 0.5$ Å^{-1}) and the correlation lengths obtained from the fittings of the curves according to the Ornstein-Zernike equation are 27 ± 1 Å, 28 ±1 Å, and 32 ± 2 Å for Gel, Gel_{GDE}, and Gel_{GDE}-IMO, respectively. This is a strong indication that the main contribution to the scattering profiles in this region is due to the polymer matrix and that the modifications of GDE and/or IMO to the gel network are negligible. The increase in the scattered intensity in the low q region ($0.009 \leq q < 0.3$ Å^{-1}) in Gel_{GDE}-IMO SAXS curve is a consequence of the presence of Imo in the gel, as it is not present in the other two profiles. Power-law fitting results in a mass fractal dimension of 1.7 that is typical of aggregated rod-like structures[236].

6.4 Hydroxyapatite formation onto Gelatin/Imogolite scaffold

Figure 6.5-A reports a FE-SEM image of the xerogel obtained after the HA synthesis (Gel_{GDE}-CaP), clearly showing that the gel phase is homogeneously filled with sub-micrometric particles with the typical platelet shape, having lateral size in the order of 100-200 nm and thickness of few tens of nm. The EDX spectrum (Figure 6.5-C) confirms the presence of Ca and P, together with the signals corresponding to the elements present in gelatin. XRD analysis (Figure 6.5-E) further demonstrates that the mineral phase effectively consists of HA. We can therefore conclude that the hydrogel scaffold does not hinder the formation of hydroxyapatite, as the crystal size, shape composition and phase obtained in the hydrogel is nearly identical to that obtained in the HA reference synthesis (see Figure 6.5 and the appendix for more details).
The effect of Imo, embedded in the hydrogel, on the HA formation was also evaluated (sample Gel_{GDE}-IMO-CaP). The FE-SEM micrographs evidence that the morphology of the mineralized sample containing Imo (see Figure 6.5-B) does not show the well-defined platelets typical of HA that are visible in Gel_{GDE}-CaP (Figure 6.5-A). This suggests that Imo is able to template the growth of HA particles also in the hydrogel system. The EDX spectrum (reported in Figure 6.5-D) confirms the presence of all the expected elements, while the XRD pattern (Figure 6.5-C) confirms

the occurred formation of HA. To understand if the presence of Imo is not only able to support the nucleation of HA, but also enhances its formation, we evaluated by means of Thermogravimetric Analysis (TGA) the amount of mineral phase formed (Figure 6.5-F). The results are normalized by equilibrating the samples at 130 ºC (*i.e.*, to remove water) and then corrected to take into account the loss of weight in the investigated range of temperature associated to pure HA and IMO. Very interestingly, we found that the inorganic fraction (after mineralization) is 10.4 %wt in the Gel_{GDE} sample, while it increases up to 21.3 %wt in Gel_{GDE}-IMO.

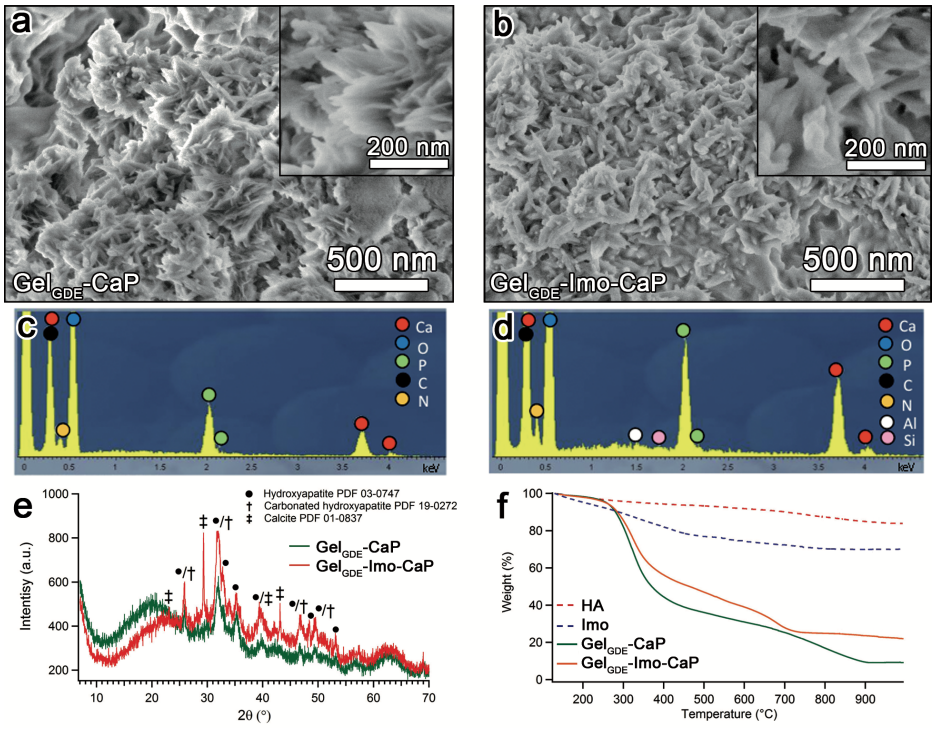

Figure 6.5 SEM images of Gel_{GDE}-CaP **(A)** and Gel_{GDE}-IMO-CaP **(B)**; EDX spectra of Gel_{GDE}-CaP **(C)** and Gel_{GDE}-IMO-CaP **(D)**; XRD patterns of Gel_{GDE}-CaP and Gel_{GDE}-IMO-CaP, together with the peak assignments according to HA, carbonated HA and calcite data **(E)**; TGA profiles of Gel_{GDE}-CaP and Gel_{GDE}-IMO-CaP, together with pure HA and IMO **(F)**. The image is reproduced from the submitted paper *Enhanced formation of hydroxyapatite in imogolite-reinforced macroporous hydrogels* (see the appendix).

The presence of IMO not only affects the amount of mineral, but also which crystal phase is formed. The XRD spectra were analyzed according to the Rietveld method and we compared the results obtained both as a function of the presence of IMO and of the hydrogel scaffold. We found that Imo promotes the carbonation of hydroxyapatite both in solution and in the scaffold: in HA and HA-IMO samples, carbonated hydroxyapatite (CHA) is present in the amounts of 18 % and 39 %, respectively (see the appendix for details), together with HA. On the other hand, in the hydrogel matrix the percentage of carbonation is even higher (CHA= 34 % in Gel_{GDE}-CaP vs 65 % in Gel_{GDE}-IMO-CaP), and a small amount of calcite (4 %) is also observed. These results are especially important recalling the beneficial effect of carbonate on both the mechanical and osteoconductive/osteoinductive properties in bones[232].

6.5 Concluding remarks

The reported results demonstrate that imogolite nanotubes could be effectively employed as fillers in macroporous gelatin-based hydrogels to be potentially used in bone tissue engineering applications. In particular, the presence of Imo produces two beneficial effects. First, the inclusion of nanotubes synergistically enhances the effect of a chemical cross-linker (GDE) in improving the hydrogel stabilization against dissolution. Most importantly, imogolite nanotubes are also shown to promote the formation of hydroxyapatite and carbonated hydroxyapatite, both when dispersed in water and when included in the macroporous scaffold.

7 Conclusions

This work of thesis describes the preparation and the physico-chemical characterization of nanostructured polymer-based systems. Clay nanotubes, namely imogolite and Halloysite, have been extensively investigated throughout this work and proposed as inorganic fillers for biodegradable polymer matrices with potential biomedical applications, especially in the bone medication field. Bone medication is not only a major issue from a clinical, economic and social perspective, but it represents an exemplary field for the study and development of new materials. The complexity of bone tissue and the large number of physical and chemical requisites that an efficient biomaterial should satisfy pose intriguing synthetic and formulative challenges, and require a detailed investigation of several physico-chemical properties. In fact, the design of efficacious devices for biomedical applications is an elaborated and multidisciplinary task, in which the role of chemists is central in the selection and proper modification of the constituent materials, in the formulation/realization of the product at the lab-scale, and in the physico-chemical characterization during the pre-clinical stages.

Material's design and properties are intimately connected, and ultimately drive the applicative potential of the final system. Starting from the careful selection of materials and their chemical modification, I prepared and characterized different nanocomposite systems, focusing each time on specific physico chemical aspects, such as stability and degradation in physiological conditions, mechanical properties, rheology, nano and microstructure, release/uploading properties.

In the first case of study reported, a bioactive hybrid film made of Halloysite nanotubes embedded within a biopolymer matrix was successfully prepared and characterized. Halloysite nanotubes introduce mechanical resistance (*i.e.*, resistance to compression evaluated by means of AFM nanoindentation experiments) in the composite, as well as providing Sr(II) uploading properties. The biodegradability of the polymer matrix is a key parameter, as the composite is able to progressively expose the Sr(II)-loaded inorganic scaffold, exploiting its bioactivity towards osteogenic cells at the local level and potentially limiting the collateral effects associated to a systemic Sr(II) administration. The *in vitro*

biocompatibility of the composite was finally demonstrated through cytotoxicity tests on fibroblast cells, highlighting the crucial role of the biopolymer film in acting both as a binder and a diffusional barrier to the Sr(II) release. Furthermore, the fabrication method used to obtain the nanocomposite is highly versatile, and it could address different biomedical and physico-chemical needs. In particular, the amount of uploaded Sr(II) could be easily adjusted by varying the surface functionalization of HNT, and the time before the bioactive inorganic scaffold is exposed to the physiological environment could be tuned by the thickness of the biopolymer coating.

In another case study, a nanocomposite material made of Halloysite nanotubes and carboxymethyl cellulose was prepared and characterized from a structural and rheological perspective. Chemical modification of the clay surface, followed by an hydrazide-aldehyde coupling protocol with partially oxidized cellulose, successfully produced a nanocomposite in which the inorganic nanotubes are homogeneously distributed, that is able to form a hydrogel when dispersed in water. Rheological properties of the composite are driven by chemical and structural design, with nanotubular fillers playing a crucial role as rheo-modifiers. In view of the application of the hybrid in minimally invasive surgery, its injectability through needles of different gauges was carefully evaluated. In spite of the presence of inorganic nanostructures that could in principle aggregate and obstruct the orifice, the injectability was mostly dictated by the cellulose matrix, with 1D clays tending to align with the direction of the flow. Injection (*i.e.* high stress) finally produces a strong change in the structure of the polymer matrix at the microscale and this was reflected in the rheological properties of the material.

Nanotubular clays have been already proposed as drug-delivery vehicles, with biocompatibility and ease of the functionalization/loading process being recognized as decisive advantages over other nanotubular systems. In this context, during my doctorate work, engineered Halloysite and imogolite nanotubes have been investigated for the uploading and release of drug models.

In a first example, Halloysite nanotubes were loaded with charged model drugs (namely rhodamine 110 and carboxyfluorescein) and coated with chitosan and hyaluronic acid to obtain hybrid nanocomposites with

opposing charges. In the case of chitosan, the preparation of the nanocomposite was carried out exploiting the electrostatic interaction between the polymer and Halloysite in water, while a covalent functionalization strategy was employed to couple the polymer and the clay in the case of hyaluronic acid. Results showed that the polymeric coatings were successful in modulating the charge of the halloysite surface and altering the release kinetics of the probes from the clay lumen. In particular, the model adopted to fit the release kinetics described very well the experimental data, indicating that both charge and coating composition play a key role in the desorption process from halloysite-based composites.

In a second example, imogolite nanotubes were modified by the adsorption of a surfactant bearing an alkyl chain and a glutamate head group (lauroyl glutamate), obtaining a hybrid material that was used in a proof of concept experiment for the upload of a model drug (namely rhodamine B isothiocyanate). The amount of uploaded drug drastically increases when lauroyl gluatamate is present, highlighting the crucial role of the surfactant's alkyl chains as hydrophobic pockets. The obtained results strongly point out towards the possibility of using glutamate-based surfactants and imogolite nanotubes for the design of hybrid systems for biomedical applications. Furthermore, the interaction of glutamate with imogolite surface could be exploited for modulating the chemical affinity between polymers bearing glutamate-based functionalities and the nanotube wall, paving the way to a more extended use of imogolite in the fabrication of nanocomposites.

In the last example, I reported on the preparation and characterization of a macroporous gelatin-based hydrogels of interest in the field of bone tissue engineering. The obtained results demonstrated that imogolite nanotubes could be effectively employed as fillers, since their presence produced two main beneficial effects: first, the inclusion of nanotubes synergistically enhances the effect of a chemical cross-linker (namely, GDE) in improving the hydrogel stabilization against dissolution; second, imogolite nanotubes are shown to promote and enhance the formation of hydroxyapatite and carbonated hydroxyapatite, both when dispersed in water and when included in the macroporous scaffold. These findings clearly highlight the potentials of imogolite when introduced in the design

of hydrogel-based scaffolds, especially thanks to the combination of their nanotubular shape and their affinity towards apatite mineral phases.

In conclusion, all the work done during my PhD course clearly demonstrate that clay minerals and biodegradable polymers could be effectively combined to give novel materials, representing valuable platforms for biomedical and fundamental studies. In particular, Halloysite and imogolite proved to be very interesting materials, thanks to their unique structural and physico-chemical characteristics, as well as their peculiar chemical reactivity.
The work described in this thesis has no claim to be exhaustive, as a lot of research still needs to be done for a comprehensive understanding and prediction of biomaterials properties and performances. However, this work could still represent a significant step forward in bringing the technology applied to bio-inspired nanocomposites closer to a widespread and reliable application.

Bibliography

(1) Chen, G.-Q.; Patel, M. K. Plastics Derived from Biological Sources: Present and Future: A Technical and Environmental Review. *Chem. Rev.* **2012**, *112* (4), 2082–2099.

(2) Derraik, J. G. The Pollution of the Marine Environment by Plastic Debris: A Review. *Mar. Pollut. Bull.* **2002**, *44* (9), 842–852.

(3) Vert, M.; Doi, Y.; Hellwich, K.-H.; Hess, M.; Hodge, P.; Kubisa, P.; Rinaudo, M.; Schué, F. Terminology for Biorelated Polymers and Applications (IUPAC Recommendations 2012). *Pure Appl. Chem.* **2012**, *84* (2).

(4) Bari, S. S.; Chatterjee, A.; Mishra, S. Biodegradable Polymer Nanocomposites: An Overview. *Polym. Rev.* **2016**, *56* (2), 287–328.

(5) Cao, G.; Wang, Y. *Nanostructures and Nanomaterials: Synthesis, Properties, and Applications*, 2. ed.; World scientific series in nanoscience and technology; World Scientific: Hackensack, NJ, 2011.

(6) Podsiadlo, P.; Kaushik, A. K.; Arruda, E. M.; Waas, A. M.; Shim, B. S.; Xu, J.; Nandivada, H.; Pumplin, B. G.; Lahann, J.; Ramamoorthy, A.; et al. Ultrastrong and Stiff Layered Polymer Nanocomposites. *Science* **2007**, *318* (5847), 80–83.

(7) Balachandran, M.; Bhagawan, S. S. Mechanical, Thermal, and Transport Properties of Nitrile Rubber-Nanocalcium Carbonate Composites. *J. Appl. Polym. Sci.* **2012**, *126* (6), 1983–1992.

(8) Zhao, X.; Zhang, Q.; Chen, D.; Lu, P. Enhanced Mechanical Properties of Graphene-Based Poly(vinyl Alcohol) Composites. *Macromolecules* **2010**, *43* (5), 2357–2363.

(9) Arinstein, A.; Zussman, E. Electrospun Polymer Nanofibers: Mechanical and Thermodynamic Perspectives. *J. Polym. Sci. Part B Polym. Phys.* **2011**, *49* (10), 691–707.

(10) Lee, L.; Zeng, C.; Cao, X.; Han, X.; Shen, J.; Xu, G. Polymer Nanocomposite Foams. *Compos. Sci. Technol.* **2005**, *65* (15-16), 2344–2363.

(11) Sanchez, C.; Lebeau, B.; Chaput, F.; Boilot, J.-P. Optical Properties of Functional Hybrid Organic–Inorganic Nanocomposites. *Adv. Mater.* **2003**, *15* (23), 1969–1994.

(12) Srivastava, S.; Kotov, N. A. Composite Layer-by-Layer (LBL) Assembly with Inorganic Nanoparticles and Nanowires. *Acc. Chem. Res.* **2008**, *41* (12), 1831–1841.

(13) Nair, L. S.; Laurencin, C. T. Biodegradable Polymers as Biomaterials. *Prog. Polym. Sci.* **2007**, *32* (8-9), 762–798.

(14) Fratzl, P. Biomimetic Materials Research: What Can We Really Learn from Nature's Structural Materials? *J. R. Soc. Interface* **2007**, *4* (15), 637–642.

(15) Wegst, U. G. K.; Bai, H.; Saiz, E.; Tomsia, A. P.; Ritchie, R. O. Bioinspired Structural Materials. *Nat. Mater.* **2014**, *14* (1), 23–36.

(16) Darder, M.; Aranda, P.; Ruiz-Hitzky, E. Bionanocomposites: A New Concept of Ecological, Bioinspired, and Functional Hybrid Materials. *Adv. Mater.* **2007**, *19* (10), 1309–1319.

(17) Fox, J. D.; Capadona, J. R.; Marasco, P. D.; Rowan, S. J. Bioinspired Water-Enhanced Mechanical Gradient Nanocomposite Films That Mimic the Architecture and Properties of the Squid Beak. *J. Am. Chem. Soc.* **2013**, *135* (13), 5167–5174.

(18) Lee, J. E.; Lee, N.; Kim, T.; Kim, J.; Hyeon, T. Multifunctional Mesoporous Silica Nanocomposite Nanoparticles for Theranostic Applications. *Acc. Chem. Res.* **2011**, *44* (10), 893–902.
(19) Purnendu, P.; Ramanan, A.; Ray, A. R. Nanocrystalline Powders of Alkaline-Earth Phosphates as Precursors for Bioceramics. *Am. J. Biochem. Biotechnol.* **2006**, *2* (2), 61–65.
(20) Rho, J.-Y.; Kuhn-Spearing, L.; Zioupos, P. Mechanical Properties and the Hierarchical Structure of Bone. *Med. Eng. Phys.* **1998**, *20* (2), 92–102.
(21) Shepherd, J. H.; Shepherd, D. V.; Best, S. M. Substituted Hydroxyapatites for Bone Repair. *J. Mater. Sci. Mater. Med.* **2012**, *23* (10), 2335–2347.
(22) Liu, Y.; Luo, D.; Wang, T. Hierarchical Structures of Bone and Bioinspired Bone Tissue Engineering. *Small* **2016**, *12* (34), 4611–4632.
(23) Nair, A. K.; Gautieri, A.; Chang, S.-W.; Buehler, M. J. Molecular Mechanics of Mineralized Collagen Fibrils in Bone. *Nat. Commun.* **2013**, *4*, 1724.
(24) Ritchie, R. O. The Conflicts between Strength and Toughness. *Nat. Mater.* **2011**, *10* (11), 817–822.
(25) Hollister, S. J. Scaffold Design and Manufacturing: From Concept to Clinic. *Adv. Mater.* **2009**, *21* (32-33), 3330–3342.
(26) Pina, S.; Oliveira, J. M.; Reis, R. L. Natural-Based Nanocomposites for Bone Tissue Engineering and Regenerative Medicine: A Review. *Adv. Mater.* **2015**, *27* (7), 1143–1169.
(27) Vallés-Lluch, A.; Poveda-Reyes, S.; Amorós, P.; Beltrán, D.; Monleón Pradas, M. Hyaluronic Acid–Silica Nanohybrid Gels. *Biomacromolecules* **2013**, *14* (12), 4217–4225.
(28) Berthold, A.; Cremer, K.; Kreuter, J. Preparation and Characterization of Chitosan Microspheres as Drug Carrier for Prednisolone Sodium Phosphate as Model for Anti-Inflammatory Drugs. *J. Controlled Release* **1996**, *39* (1), 17–25.
(29) Ha, D. I.; Lee, S. B.; Chong, M. S.; Lee, Y. M.; Kim, S. Y.; Park, Y. H. Preparation of Thermo-Responsive and Injectable Hydrogels Based on Hyaluronic Acid and poly(N-Isopropylacrylamide) and Their Drug Release Behaviors. *Macromol. Res.* **2006**, *14* (1), 87–93.
(30) Agnihotri, S. A.; Mallikarjuna, N. N.; Aminabhavi, T. M. Recent Advances on Chitosan-Based Micro- and Nanoparticles in Drug Delivery. *J. Controlled Release* **2004**, *100* (1), 5–28.
(31) Burdick, J. A.; Prestwich, G. D. Hyaluronic Acid Hydrogels for Biomedical Applications. *Adv. Mater.* **2011**, *23* (12), H41–H56.
(32) Falcone, S. J.; Berg, R. A. Crosslinked Hyaluronic Acid Dermal Fillers: A Comparison of Rheological Properties. *J. Biomed. Mater. Res. A* **2008**, *87* (1), 264–271.
(33) Roig-Roig, F.; Solans, C.; Esquena, J.; García-Celma, M. J. Preparation, Characterization, and Release Properties of Hydrogels Based on Hyaluronan for Pharmaceutical and Biomedical Use. *J. Appl. Polym. Sci.* **2013**, *130* (2), 1377–1382.
(34) Collins, M. N.; Birkinshaw, C. Hyaluronic Acid Based Scaffolds for Tissue engineering—A Review. *Carbohydr. Polym.* **2013**, *92* (2), 1262–1279.
(35) Berger, J.; Reist, M.; Mayer, J. M.; Felt, O.; Peppas, N. A.; Gurny, R. Structure and Interactions in Covalently and Ionically Crosslinked Chitosan Hydrogels for Biomedical Applications. *Eur. J. Pharm. Biopharm.* **2004**, *57* (1), 19–34.
(36) Croisier, F.; Jérôme, C. Chitosan-Based Biomaterials for Tissue Engineering. *Eur. Polym. J.* **2013**, *49* (4), 780–792.

(37) Khan, F.; Tare, R. S.; Oreffo, R. O. C.; Bradley, M. Versatile Biocompatible Polymer Hydrogels: Scaffolds for Cell Growth. *Angew. Chem. Int. Ed.* **2009**, *48* (5), 978–982.
(38) Koosha, M.; Mirzadeh, H.; Shokrgozar, M. A.; Farokhi, M. Nanoclay-Reinforced Electrospun chitosan/PVA Nanocomposite Nanofibers for Biomedical Applications. *RSC Adv* **2015**, *5* (14), 10479–10487.
(39) Zuo, P.-P.; Feng, H.-F.; Xu, Z.-Z.; Zhang, L.-F.; Zhang, Y.-L.; Xia, W.; Zhang, W.-Q. Fabrication of Biocompatible and Mechanically Reinforced Graphene Oxide-Chitosan Nanocomposite Films. *Chem. Cent. J.* **2013**, *7* (1), 39.
(40) Sobhana, S. S. L.; Sundaraseelan, J.; Sekar, S.; Sastry, T. P.; Mandal, A. B. Gelatin–Chitosan Composite Capped Gold Nanoparticles: A Matrix for the Growth of Hydroxyapatite. *J. Nanoparticle Res.* **2009**, *11* (2), 333–340.
(41) Ten, E.; Turtle, J.; Bahr, D.; Jiang, L.; Wolcott, M. Thermal and Mechanical Properties of poly(3-Hydroxybutyrate-Co-3-Hydroxyvalerate)/cellulose Nanowhiskers Composites. *Polymer* **2010**, *51* (12), 2652–2660.
(42) George, J.; Siddaramaiah. High Performance Edible Nanocomposite Films Containing Bacterial Cellulose Nanocrystals. *Carbohydr. Polym.* **2012**, *87* (3), 2031–2037.
(43) Perioli, L.; Nocchetti, M.; Giannelli, P.; Pagano, C.; Bastianini, M. Hydrotalcite Composites for an Effective Fluoride Buccal Administration: A New Technological Approach. *Int. J. Pharm.* **2013**, *454* (1), 259–268.
(44) Hudson, S. P.; Langer, R.; Fink, G. R.; Kohane, D. S. Injectable in Situ Cross-Linking Hydrogels for Local Antifungal Therapy. *Biomaterials* **2010**, *31* (6), 1444–1452.
(45) Sivakumar, B.; Aswathy, R. G.; Nagaoka, Y.; Suzuki, M.; Fukuda, T.; Yoshida, Y.; Maekawa, T.; Sakthikumar, D. N. Multifunctional Carboxymethyl Cellulose-Based Magnetic Nanovector as a Theragnostic System for Folate Receptor Targeted Chemotherapy, Imaging, and Hyperthermia against Cancer. *Langmuir* **2013**, *29* (10), 3453–3466.
(46) Camerlo, A.; Vebert-Nardin, C.; Rossi, R. M.; Popa, A.-M. Fragrance Encapsulation in Polymeric Matrices by Emulsion Electrospinning. *Eur. Polym. J.* **2013**, *49* (12), 3806–3813.
(47) Velasco, M. V. R.; Vieira, R. P.; Fernandes, A. R.; Dario, M. F.; Pinto, C. A. S. O.; Pedriali, C. A.; Kaneko, T. M.; Baby, A. R. Short-Term Clinical of Peel-off Facial Mask Moisturizers. *Int. J. Cosmet. Sci.* **2014**, *36* (4), 355–360.
(48) Vuddanda, P. R.; Mathew, A. P.; Velaga, S. Electrospun Nanofiber Mats for Ultrafast Release of Ondansetron. *React. Funct. Polym.* **2016**, *99*, 65–72.
(49) Baker, M. I.; Walsh, S. P.; Schwartz, Z.; Boyan, B. D. A Review of Polyvinyl Alcohol and Its Uses in Cartilage and Orthopedic Applications. *J. Biomed. Mater. Res. B Appl. Biomater.* **2012**, *100B* (5), 1451–1457.
(50) El-Hadi, A.; Schnabel, R.; Straube, E.; Müller, G.; Henning, S. Correlation between Degree of Crystallinity, Morphology, Glass Temperature, Mechanical Properties and Biodegradation of Poly (3-Hydroxyalkanoate) PHAs and Their Blends. *Polym. Test.* **2002**, *21* (6), 665–674.
(51) Philip, S.; Keshavarz, T.; Roy, I. Polyhydroxyalkanoates: Biodegradable Polymers with a Range of Applications. *J. Chem. Technol. Biotechnol.* **2007**, *82* (3), 233–247.
(52) Chen, G.-Q.; Wu, Q. The Application of Polyhydroxyalkanoates as Tissue Engineering Materials. *Biomaterials* **2005**, *26* (33), 6565–6578.

(53) Huang, W.; Wang, Y.; Ren, L.; Du, C.; Shi, X. A Novel PHBV/HA Microsphere Releasing System Loaded with Alendronate. *Mater. Sci. Eng. C* **2009**, *29* (7), 2221–2225.
(54) Jack, K. S.; Velayudhan, S.; Luckman, P.; Trau, M.; Grøndahl, L.; Cooper-White, J. The Fabrication and Characterization of Biodegradable HA/PHBV Nanoparticle–polymer Composite Scaffolds. *Acta Biomater.* **2009**, *5* (7), 2657–2667.
(55) Bigi, A. Relationship between Triple-Helix Content and Mechanical Properties of Gelatin Films. *Biomaterials* **2004**, *25* (25), 5675–5680.
(56) Guo, L.; Colby, R. H.; Lusignan, C. P.; Whitesides, T. H. Kinetics of Triple Helix Formation in Semidilute Gelatin Solutions. *Macromolecules* **2003**, *36* (26), 9999–10008.
(57) Chaibi, S.; Benachour, D.; Merbah, M.; Esperanza Cagiao, M.; Baltá Calleja, F. J. The Role of Crosslinking on the Physical Properties of Gelatin Based Films. *Colloid Polym. Sci.* **2015**, *293* (10), 2741–2752.
(58) Vargas, G.; Acevedo, J. L.; López, J.; Romero, J. Study of Cross-Linking of Gelatin by Ethylene Glycol Diglycidyl Ether. *Mater. Lett.* **2008**, *62* (21-22), 3656–3658.
(59) Lu, Y.; Jiang, H.; Tu, K.; Wang, L. Mild Immobilization of Diverse Macromolecular Bioactive Agents onto Multifunctional Fibrous Membranes Prepared by Coaxial Electrospinning. *Acta Biomater.* **2009**, *5* (5), 1562–1574.
(60) Shen, H.; Hu, X.; Yang, F.; Bei, J.; Wang, S. Combining Oxygen Plasma Treatment with Anchorage of Cationized Gelatin for Enhancing Cell Affinity of Poly(lactide-Co-Glycolide). *Biomaterials* **2007**, *28* (29), 4219–4230.
(61) Chen, J.-P.; Su, C.-H. Surface Modification of Electrospun PLLA Nanofibers by Plasma Treatment and Cationized Gelatin Immobilization for Cartilage Tissue Engineering. *Acta Biomater.* **2011**, *7* (1), 234–243.
(62) Singh, B. Why Does Halloysite Roll?–A New Model. *Clays Clay Miner.* **1996**, *44* (2), 191–196.
(63) Joussein, E.; Petit, S.; Churchman, J.; Theng, B.; Righi, D.; Delvaux, B. Halloysite Clay Minerals — a Review. *Clay Miner.* **2005**, *40* (4), 383–426.
(64) Bailey, S. W. Halloysite - a Critical Assessment. *Sci. Geol. Memoires* **1990**, *86*, 89–98.
(65) Vergaro, V.; Abdullayev, E.; Lvov, Y. M.; Zeitoun, A.; Cingolani, R.; Rinaldi, R.; Leporatti, S. Cytocompatibility and Uptake of Halloysite Clay Nanotubes. *Biomacromolecules* **2010**, *11* (3), 820–826.
(66) *Nanosized Tubular Clay Minerals: Halloysite and Imogolite*; Yuan, P., Thill, A., Bergaya, F., Eds.; Developments in clay science; Elsevier: Amsterdam Boston Heidelberg London New York Oxford Paris San Diego San Francisco Singapore Sydney Tokyo, 2016.
(67) Garrett, W. G. The Cation-Exchange Capacity of Hydrated Halloysite and the Formation of Halloysite-Salt Complexes*. *Clay Miner.* **1959**, *4* (22), 75–80.
(68) Guo, B.; Chen, F.; Lei, Y.; Liu, X.; Wan, J.; Jia, D. Styrene-Butadiene Rubber/halloysite Nanotubes Nanocomposites Modified by Sorbic Acid. *Appl. Surf. Sci.* **2009**, *255* (16), 7329–7336.
(69) Guo, B.; Lei, Y.; Chen, F.; Liu, X.; Du, M.; Jia, D. Styrene–butadiene Rubber/halloysite Nanotubes Nanocomposites Modified by Methacrylic Acid. *Appl. Surf. Sci.* **2008**, *255* (5), 2715–2722.
(70) Liu, M.; Guo, B.; Zou, Q.; Du, M.; Jia, D. Interactions between Halloysite Nanotubes and 2,5-bis(2-Benzoxazolyl) Thiophene and Their Effects on Reinforcement of Polypropylene/halloysite Nanocomposites. *Nanotechnology* **2008**, *19* (20), 205709.

(71) Deng, S.; Zhang, J.; Ye, L. Halloysite–epoxy Nanocomposites with Improved Particle Dispersion through Ball Mill Homogenisation and Chemical Treatments. *Compos. Sci. Technol.* **2009**, *69* (14), 2497–2505.
(72) Cao, H.; Sun, X.; Zhang, Y.; Jia, N. Electrochemical Sensing Based on Gold Nanoparticle-Decorated Halloysite Nanotube Composites. *Anal. Biochem.* **2012**, *430* (2), 111–115.
(73) Yuan, P.; Southon, P. D.; Liu, Z.; Green, M. E. R.; Hook, J. M.; Antill, S. J.; Kepert, C. J. Functionalization of Halloysite Clay Nanotubes by Grafting with γ-Aminopropyltriethoxysilane. *J. Phys. Chem. C* **2008**, *112* (40), 15742–15751.
(74) Barrientos-Ramírez, S.; Oca-Ramírez, G. M. de; Ramos-Fernández, E. V.; Sepúlveda-Escribano, A.; Pastor-Blas, M. M.; González-Montiel, A. Surface Modification of Natural Halloysite Clay Nanotubes with Aminosilanes. Application as Catalyst Supports in the Atom Transfer Radical Polymerization of Methyl Methacrylate. *Appl. Catal. Gen.* **2011**, *406* (1-2), 22–33.
(75) Joo, Y.; Jeon, Y.; Lee, S. U.; Sim, J. H.; Ryu, J.; Lee, S.; Lee, H.; Sohn, D. Aggregation and Stabilization of Carboxylic Acid Functionalized Halloysite Nanotubes (HNT-COOH). *J. Phys. Chem. C* **2012**, *116* (34), 18230–18235.
(76) Massaro, M.; Riela, S.; Cavallaro, G.; Gruttadauria, M.; Milioto, S.; Noto, R.; Lazzara, G. Eco-Friendly Functionalization of Natural Halloysite Clay Nanotube with Ionic Liquids by Microwave Irradiation for Suzuki Coupling Reaction. *J. Organomet. Chem.* **2014**, *749*, 410–415.
(77) Du, M.; Guo, B.; Jia, D. Thermal Stability and Flame Retardant Effects of Halloysite Nanotubes on Poly(propylene). *Eur. Polym. J.* **2006**, *42* (6), 1362–1369.
(78) Liu, M.; Jia, Z.; Liu, F.; Jia, D.; Guo, B. Tailoring the Wettability of Polypropylene Surfaces with Halloysite Nanotubes. *J. Colloid Interface Sci.* **2010**, *350* (1), 186–193.
(79) Singh, V. P.; Vimal, K. K.; Kapur, G. S.; Sharma, S.; Choudhary, V. High-Density Polyethylene/halloysite Nanocomposites: Morphology and Rheological Behaviour under Extensional and Shear Flow. *J. Polym. Res.* **2016**, *23* (3).
(80) Liu, C.; Luo, Y.; Jia, Z.; Li, S.; Guo, B.; Jia, D. Structure and Properties of Poly(vinyl chloride)/Halloysite Nanotubes Nanocomposites. *J. Macromol. Sci. Part B* **2012**, *51* (5), 968–981.
(81) Lin, Y.; Ng, K. M.; Chan, C.-M.; Sun, G.; Wu, J. High-Impact Polystyrene/halloysite Nanocomposites Prepared by Emulsion Polymerization Using Sodium Dodecyl Sulfate as Surfactant. *J. Colloid Interface Sci.* **2011**, *358* (2), 423–429.
(82) He, Y.; Kong, W.; Wang, W.; Liu, T.; Liu, Y.; Gong, Q.; Gao, J. Modified Natural Halloysite/potato Starch Composite Films. *Carbohydr. Polym.* **2012**, *87* (4), 2706–2711.
(83) Fu, Y.; Zhao, D.; Yao, P.; Wang, W.; Zhang, L.; Lvov, Y. Highly Aging-Resistant Elastomers Doped with Antioxidant-Loaded Clay Nanotubes. *ACS Appl. Mater. Interfaces* **2015**, *7* (15), 8156–8165.
(84) Carli, L. N.; Daitx, T. S.; Soares, G. V.; Crespo, J. S.; Mauler, R. S. The Effects of Silane Coupling Agents on the Properties of PHBV/halloysite Nanocomposites. *Appl. Clay Sci.* **2014**, *87*, 311–319.
(85) Du, M.; Guo, B.; Liu, M.; Jia, D. Preparation and Characterization of Polypropylene Grafted Halloysite and Their Compatibility Effect to Polypropylene/Halloysite Composite. *Polym. J.* **2006**, *38* (11), 1198–1204.
(86) Hou, Y.; Jiang, J.; Li, K.; Zhang, Y.; Liu, J. Grafting Amphiphilic Brushes onto Halloysite Nanotubes via a Living RAFT Polymerization and Their Pickering Emulsification Behavior. *J. Phys. Chem. B* **2014**, *118* (7), 1962–1967.

(87) Li, C.; Liu, J.; Qu, X.; Guo, B.; Yang, Z. Polymer-Modified Halloysite Composite Nanotubes. *J. Appl. Polym. Sci.* **2008**, *110* (6), 3638–3646.
(88) Chao, C.; Liu, J.; Wang, J.; Zhang, Y.; Zhang, B.; Zhang, Y.; Xiang, X.; Chen, R. Surface Modification of Halloysite Nanotubes with Dopamine for Enzyme Immobilization. *ACS Appl. Mater. Interfaces* **2013**, *5* (21), 10559–10564.
(89) Yah, W. O.; Takahara, A.; Lvov, Y. M. Selective Modification of Halloysite Lumen with Octadecylphosphonic Acid: New Inorganic Tubular Micelle. *J. Am. Chem. Soc.* **2012**, *134* (3), 1853–1859.
(90) Yah, W. O.; Xu, H.; Soejima, H.; Ma, W.; Lvov, Y.; Takahara, A. Biomimetic Dopamine Derivative for Selective Polymer Modification of Halloysite Nanotube Lumen. *J. Am. Chem. Soc.* **2012**, *134* (29), 12134–12137.
(91) Veerabadran, N. G.; Price, R. R.; Lvov, Y. M. Clay Nanotubes for Encapsulation and Sustained Release of Drugs. *Nano* **2007**, *2* (02), 115–120.
(92) Price, R. R.; Gaber, B. P.; Lvov, Y. In-Vitro Release Characteristics of Tetracycline HCl, Khellin and Nicotinamide Adenine Dineculeotide from Halloysite; a Cylindrical Mineral. *J. Microencapsul.* **2001**, *18* (6), 713–722.
(93) Ward, C. J.; Song, S.; Davis, E. W. Controlled Release of Tetracycline-HCl from Halloysite-Polymer Composite Films. *J. Nanosci. Nanotechnol.* **2010**, *10* (10), 6641–6649.
(94) Lvov, Y. M.; Shchukin, D. G.; Mőhwald, H.; Price, R. R. Halloysite Clay Nanotubes for Controlled Release of Protective Agents. *ACS Nano* **2008**, *2* (5), 814–820.
(95) Shchukin, D. G.; Möhwald, H. Surface-Engineered Nanocontainers for Entrapment of Corrosion Inhibitors. *Adv. Funct. Mater.* **2007**, *17* (9), 1451–1458.
(96) Du, M.; Guo, B.; Jia, D. Newly Emerging Applications of Halloysite Nanotubes: A Review. *Polym. Int.* **2010**, *59* (5), 574–582.
(97) Shchukin, D. G.; Sukhorukov, G. B.; Price, R. R.; Lvov, Y. M. Halloysite Nanotubes as Biomimetic Nanoreactors. *Small* **2005**, *1* (5), 510–513.
(98) Lai, X.; Agarwal, M.; Lvov, Y. M.; Pachpande, C.; Varahramyan, K.; Witzmann, F. A. Proteomic Profiling of Halloysite Clay Nanotube Exposure in Intestinal Cell Co-Culture: Intestinal Cell Proteomics after Exposure to Halloysite Nanoclay. *J. Appl. Toxicol.* **2013**, n/a – n/a.
(99) Kommireddy, D. S.; Ichinose, I.; Lvov, Y. M.; Mills, D. K. Nanoparticle Multilayers: Surface Modification for Cell Attachment and Growth. *J. Biomed. Nanotechnol.* **2005**, *1* (3), 286–290.
(100) Verma, N. K.; Moore, E.; Blau, W.; Volkov, Y.; Babu, P. R. Cytotoxicity Evaluation of Nanoclays in Human Epithelial Cell Line A549 Using High Content Screening and Real-Time Impedance Analysis. *J. Nanoparticle Res.* **2012**, *14* (9), 1–11.
(101) Heimark, R. L.; Kurachi, K.; Fujikawa, K.; Davie, E. W. Surface Activation of Blood Coagulation, Fibrinolysis and Kinin Formation. *Nature* **1980**, *286* (5772), 456–460.
(102) Liu, H.-Y.; Du, L.; Zhao, Y.-T.; Tian, W.-Q. In Vitro Hemocompatibility and Cytotoxicity Evaluation of Halloysite Nanotubes for Biomedical Application. *J. Nanomater.* **2015**, *2015*, 1–9.
(103) Lvov, Y.; Abdullayev, E. Functional Polymer–clay Nanotube Composites with Sustained Release of Chemical Agents. *Prog. Polym. Sci.* **2013**, *38* (10-11), 1690–1719.
(104) Qi, R.; Guo, R.; Shen, M.; Cao, X.; Zhang, L.; Xu, J.; Yu, J.; Shi, X. Electrospun Poly(lactic-Co-Glycolic Acid)/halloysite Nanotube Composite Nanofibers for Drug Encapsulation and Sustained Release. *J. Mater. Chem.* **2010**, *20* (47), 10622.

(105) Zhou, W. Y.; Guo, B.; Liu, M.; Liao, R.; Rabie, A. B. M.; Jia, D. Poly(vinyl Alcohol)/halloysite Nanotubes Bionanocomposite Films: Properties and in Vitro Osteoblasts and Fibroblasts Response. *J. Biomed. Mater. Res. A* **2009**, n/a – n/a.
(106) Wei, W.; Abdullayev, E.; Hollister, A.; Mills, D.; Lvov, Y. M. Clay Nanotube/Poly(methyl Methacrylate) Bone Cement Composites with Sustained Antibiotic Release. *Macromol. Mater. Eng.* **2012**, *297* (7), 645–653.
(107) Liu, M.; Wu, C.; Jiao, Y.; Xiong, S.; Zhou, C. Chitosan–halloysite Nanotubes Nanocomposite Scaffolds for Tissue Engineering. *J. Mater. Chem. B* **2013**, *1* (15), 2078.
(108) Abdullayev, E.; Lvov, Y. Halloysite Clay Nanotubes as a Ceramic "skeleton" for Functional Biopolymer Composites with Sustained Drug Release. *J. Mater. Chem. B* **2013**, *1* (23), 2894–2903.
(109) Yoshinaga, N.; Aomine, S. Imogolite in Some Ando Soils. *Soil Sci. Plant Nutr.* **1962**, *8* (3), 22–29.
(110) Farmer, V. C.; Fraser, A. R.; Tait, J. M. Synthesis of Imogolite: A Tubular Aluminium Silicate Polymer. *J. Chem. Soc. Chem. Commun.* **1977**, No. 13, 462.
(111) Koenderink, G. H.; Kluijtmans, S. G. J. .; Philipse, A. P. On the Synthesis of Colloidal Imogolite Fibers. *J. Colloid Interface Sci.* **1999**, *216* (2), 429–431.
(112) Levard, C.; Masion, A.; Rose, J.; Doelsch, E.; Borschneck, D.; Dominici, C.; Ziarelli, F.; Bottero, J.-Y. Synthesis of Imogolite Fibers from Decimolar Concentration at Low Temperature and Ambient Pressure: A Promising Route for Inexpensive Nanotubes. *J. Am. Chem. Soc.* **2009**, *131* (47), 17080–17081.
(113) Duarte, H. A.; P., M.; Heine, T.; Guimares, L. Clay Mineral Nanotubes: Stability, Structure and Properties. In *Stoichiometry and Materials Science - When Numbers Matter*; Innocenti, A., Ed.; InTech, 2012.
(114) Maillet, P.; Levard, C.; Larquet, E.; Mariet, C.; Spalla, O.; Menguy, N.; Masion, A.; Doelsch, E.; Rose, J.; Thill, A. Evidence of Double-Walled Al−Ge Imogolite-Like Nanotubes. A Cryo-TEM and SAXS Investigation. *J. Am. Chem. Soc.* **2010**, *132* (4), 1208–1209.
(115) Guimarães, L.; Enyashin, A. N.; Frenzel, J.; Heine, T.; Duarte, H. A.; Seifert, G. Imogolite Nanotubes: Stability, Electronic, and Mechanical Properties. *ACS Nano* **2007**, *1* (4), 362–368.
(116) Gustafsson, J. P. The Surface Chemistry of Imogolite. *Clays Clay Miner.* **2001**, *49* (1), 73–80.
(117) Arancibia-Miranda, N.; Escudey, M.; Molina, M.; García-González, M. T. Use of Isoelectric Point and pH to Evaluate the Synthesis of a Nanotubular Aluminosilicate. *J. Non-Cryst. Solids* **2011**, *357* (7), 1750–1756.
(118) Paineau, E.; Krapf, M.-E. M.; Amara, M.-S.; Matskova, N. V.; Dozov, I.; Rouzière, S.; Thill, A.; Launois, P.; Davidson, P. A Liquid-Crystalline Hexagonal Columnar Phase in Highly-Dilute Suspensions of Imogolite Nanotubes. *Nat. Commun.* **2016**, *7*, 10271.
(119) Amara, M.-S.; Paineau, E.; Bacia-Verloop, M.; Krapf, M.-E. M.; Davidson, P.; Belloni, L.; Levard, C.; Rose, J.; Launois, P.; Thill, A. Single-Step Formation of Micron Long (OH)3Al2O3Ge(OH) Imogolite-like Nanotubes. *Chem. Commun.* **2013**, *49* (96), 11284.
(120) Bottero, I.; Bonelli, B.; Ashbrook, S. E.; Wright, P. A.; Zhou, W.; Tagliabue, M.; Armandi, M.; Garrone, E. Synthesis and Characterization of Hybrid Organic/inorganic Nanotubes of the Imogolite Type and Their Behaviour towards Methane Adsorption. *Phys Chem Chem Phys* **2011**, *13* (2), 744–750.

(121) Kang, D.-Y.; Brunelli, N. A.; Yucelen, G. I.; Venkatasubramanian, A.; Zang, J.; Leisen, J.; Hesketh, P. J.; Jones, C. W.; Nair, S. Direct Synthesis of Single-Walled Aminoaluminosilicate Nanotubes with Enhanced Molecular Adsorption Selectivity. *Nat. Commun.* **2014**, *5*.
(122) Amara, M. S.; Paineau, E.; Rouzière, S.; Guiose, B.; Krapf, M.-E. M.; Taché, O.; Launois, P.; Thill, A. Hybrid, Tunable-Diameter, Metal Oxide Nanotubes for Trapping of Organic Molecules. *Chem. Mater.* **2015**, *27* (5), 1488–1494.
(123) Kang, D.-Y.; Zang, J.; Jones, C. W.; Nair, S. Single-Walled Aluminosilicate Nanotubes with Organic-Modified Interiors. *J. Phys. Chem. C* **2011**, *115* (15), 7676–7685.
(124) Zanzottera, C.; Vicente, A.; Celasco, E.; Fernandez, C.; Garrone, E.; Bonelli, B. Physico-Chemical Properties of Imogolite Nanotubes Functionalized on Both External and Internal Surfaces. *J. Phys. Chem. C* **2012**, *116* (13), 7499–7506.
(125) Johnson, L. M.; Pinnavaia, T. J. Silylation of a Tubular Aluminosilicate Polymer (imogolite) by Reaction with Hydrolyzed (.gamma.-Aminopropyl)triethoxysilane. *Langmuir* **1990**, *6* (2), 307–311.
(126) Johnson, L. M.; Pinnavaia, T. J. Hydrolysis of (.gamma.-Aminopropyl)triethoxysilane-Silylated Imogolite and Formation of a Silylated Tubular Silicate-Layered Silicate Nanocomposite. *Langmuir* **1991**, *7* (11), 2636–2641.
(127) Park, S.; Lee, Y.; Kim, B.; Lee, J.; Jeong, Y.; Noh, J.; Takahara, A.; Sohn, D. Two-Dimensional Alignment of Imogolite on a Solid Surface. *Chem. Commun.* **2007**, No. 28, 2917.
(128) Yamamoto, K.; Otsuka, H.; Wada, S.-I.; Sohn, D.; Takahara, A. Preparation and Properties of [poly(methyl Methacrylate)/imogolite] Hybrid via Surface Modification Using Phosphoric Acid Ester. *Polymer* **2005**, *46* (26), 12386–12392.
(129) Ma, W.; Yah, W. O.; Otsuka, H.; Takahara, A. Application of Imogolite Clay Nanotubes in Organic–inorganic Nanohybrid Materials. *J. Mater. Chem.* **2012**, *22* (24), 11887–11892.
(130) Kang, D.-Y.; Tong, H. M.; Zang, J.; Choudhury, R. P.; Sholl, D. S.; Beckham, H. W.; Jones, C. W.; Nair, S. Single-Walled Aluminosilicate Nanotube/Poly(vinyl Alcohol) Nanocomposite Membranes. *ACS Appl. Mater. Interfaces* **2012**, *4* (2), 965–976.
(131) Yamamoto, K.; Otsuka, H.; Wada, S.-I.; Sohn, D.; Takahara, A. Transparent Polymer Nanohybrid Prepared by in Situ Synthesis of Aluminosilicate Nanofibers in Poly(vinyl Alcohol) Solution. *Soft Matter* **2005**, *1* (5), 372–377.
(132) Rotoli, B. M.; Guidi, P.; Bonelli, B.; Bernardeschi, M.; Bianchi, M. G.; Esposito, S.; Frenzilli, G.; Lucchesi, P.; Nigro, M.; Scarcelli, V.; et al. Imogolite: An Aluminosilicate Nanotube Endowed with Low Cytotoxicity and Genotoxicity. *Chem. Res. Toxicol.* **2014**, *27* (7), 1142–1154.
(133) Ingham, C. J.; ter Maat, J.; de Vos, W. M. Where Bio Meets Nano: The Many Uses for Nanoporous Aluminum Oxide in Biotechnology. *Biotechnol. Adv.* **2012**, *30* (5), 1089–1099.
(134) He, P.; Zou, Y.; Hu, Z. Advances in Aluminum Hydroxide-Based Adjuvant Research and Its Mechanism. *Hum. Vaccines Immunother.* **2015**, *11* (2), 477–488.
(135) Inoue, N.; Otsuka, H.; Wada, S.-I.; Takahara, A. (Inorganic Nanofiber/enzyme) Hybrid Hydrogel: Preparation, Characterization, and Enzymatic Activity of Imogolite/pepsin Conjugate. *Chem. Lett.* **2006**, *35* (2), 194–195.

(136) Jiravanichanun, N.; Yamamoto, K.; Kato, K.; Kim, J.; Horiuchi, S.; Yah, W.-O.; Otsuka, H.; Takahara, A. Preparation and Characterization of Imogolite/DNA Hybrid Hydrogels. *Biomacromolecules* **2012**, *13* (1), 276–281.
(137) Yadav, S. K.; Bera, T.; Saxena, P. S.; Maurya, A. K.; Garbyal, R. S.; Vajtai, R.; Ramachandrarao, P.; Srivastava, A. MWCNTs as Reinforcing Agent to the Hap-Gel Nanocomposite for Artificial Bone Grafting. *J. Biomed. Mater. Res. A* **2009**, *9999A*, NA – NA.
(138) Teramoto, N.; Hayashi, A.; Yamanaka, K.; Sakiyama, A.; Nakano, A.; Shibata, M. Preparation and Mechanical Properties of Photo-Crosslinked Fish Gelatin/Imogolite Nanofiber Composite Hydrogel. *Materials* **2012**, *5* (12), 2573–2585.
(139) Amini, A. R.; Laurencin, C. T.; Nukavarapu, S. P. Bone Tissue Engineering: Recent Advances and Challenges. *Crit. Rev. Biomed. Eng.* **2012**, *40* (5).
(140) Greenspan, D. C. Bioactive Ceramic Implant Materials. *Curr. Opin. Solid State Mater. Sci.* **1999**, *4* (4), 389–393.
(141) Xynos, I. D.; Hukkanen, M. V. J.; Batten, J. J.; Buttery, L. D.; Hench, L. L.; Polak, J. M. Bioglass ®45S5 Stimulates Osteoblast Turnover and Enhances Bone Formation In Vitro: Implications and Applications for Bone Tissue Engineering. *Calcif. Tissue Int.* **2000**, *67* (4), 321–329.
(142) Hollister, S. J. Porous Scaffold Design for Tissue Engineering. *Nat. Mater.* **2005**, *4* (7), 518–524.
(143) Fu, S.; Wang, X.; Guo, G.; Shi, S.; Liang, H.; Luo, F.; Wei, Y.; Qian, Z. Preparation and Characterization of Nano-Hydroxyapatite/Poly(ε-caprolactone)−Poly(ethylene glycol)−Poly(ε-Caprolactone) Composite Fibers for Tissue Engineering. *J. Phys. Chem. C* **2010**, *114* (43), 18372–18378.
(144) Shepherd, J. H.; Shepherd, D. V.; Best, S. M. Substituted Hydroxyapatites for Bone Repair. *J. Mater. Sci. Mater. Med.* **2012**, *23* (10), 2335–2347.
(145) Moore, W. R.; Graves, S. E.; Bain, G. I. Synthetic Bone Graft Substitutes. *ANZ J. Surg.* **2001**, *71* (6), 354–361.
(146) Svedbom, A.; Ivergård, M.; Compston, J.; Cooper, C.; Stenmark, J.; McCloskey, E. V.; Jönsson, B.; Kanis, J. A. Osteoporosis in the European Union: A Compendium of Country-Specific Reports. *Arch. Osteoporos.* **2013**, *8* (1-2).
(147) Bonnelye, E.; Chabadel, A.; Saltel, F.; Jurdic, P. Dual Effect of Strontium Ranelate: Stimulation of Osteoblast Differentiation and Inhibition of Osteoclast Formation and Resorption in Vitro. *Bone* **2008**, *42* (1), 129–138.
(148) Cabrera, W. E.; Schrooten, I.; De Broe, M. E.; D'Haese, P. C. Strontium and Bone. *J. Bone Miner. Res.* **1999**, *14* (5), 661–668.
(149) European Medicines Agency - News and Events - Recommendation to restrict the use of Protelos / Osseor (strontium ranelate) http://www.ema.europa.eu/ema/index.jsp?curl=pages/news_and_events/news/2013/04/news_detail_001774.jsp&mid=WC0b01ac058004d5c1 (accessed Aug 30, 2013).
(150) Georgia A. Hart; Thomas W. Hesterberg. In Vitro Toxicity of Respirable-Size Particles of Diatomaceous Earth and Crystalline Silica Compared With Asbestos and Titanium Dioxide. *J. Occup. Environ. Med.* **1998**, *40* (1), 29–42.
(151) Wanna, D.; Alam, C.; Toivola, D. M.; Alam, P. Bacterial Cellulose–kaolin Nanocomposites for Application as Biomedical Wound Healing Materials. *Adv. Nat. Sci. Nanosci. Nanotechnol.* **2013**, *4* (4), 045002.

(152) Santerre, J. P.; Shajii, L.; Leung, B. W. Relation of Dental Composite Formulations To Their Degradation and the Release of Hydrolyzed Polymeric-Resin-Derived Products. *Crit. Rev. Oral Biol. Med.* **2001**, *12* (2), 136–151.
(153) Brunauer, S.; Emmett, P. H.; Teller, E. Adsorption of Gases in Multimolecular Layers. *J. Am. Chem. Soc.* **1938**, *60* (2), 309–319.
(154) Barrett, E. P.; Joyner, L. G.; Halenda, P. P. The Determination of Pore Volume and Area Distributions in Porous Substances. I. Computations from Nitrogen Isotherms. *J. Am. Chem. Soc.* **1951**, *73* (1), 373–380.
(155) White, R. D.; Bavykin, D. V.; Walsh, F. C. The Stability of Halloysite Nanotubes in Acidic and Alkaline Aqueous Suspensions. *Nanotechnology* **2012**, *23* (6), 065705.
(156) Abdelmouleh, M.; Boufi, S.; ben Salah, A.; Belgacem, M. N.; Gandini, A. Interaction of Silane Coupling Agents with Cellulose. *Langmuir* **2002**, *18* (8), 3203–3208.
(157) Finocchio, E.; Macis, E.; Raiteri, R.; Busca, G. Adsorption of Trimethoxysilane and of 3-Mercaptopropyltrimethoxysilane on Silica and on Silicon Wafers from Vapor Phase: An IR Study. *Langmuir* **2007**, *23* (5), 2505–2509.
(158) Xu, J.; Li, L.; Yan, Y.; Wang, H.; Wang, X.; Fu, X.; Li, G. Synthesis and Photoluminescence of Well-Dispersible Anatase TiO2 Nanoparticles. *J. Colloid Interface Sci.* **2008**, *318* (1), 29–34.
(159) Göpferich, A. Mechanisms of Polymer Degradation and Erosion. *Biomaterials* **1996**, *17* (2), 103–114.
(160) Lecouvet, B.; Horion, J.; D'Haese, C.; Bailly, C.; Nysten, B. Elastic Modulus of Halloysite Nanotubes. *Nanotechnology* **2013**, *24* (10), 105704.
(161) Saito, N.; Usui, Y.; Aoki, K.; Narita, N.; Shimizu, M.; Ogiwara, N.; Nakamura, K.; Ishigaki, N.; Kato, H.; Taruta, S.; et al. Carbon Nanotubes for Biomaterials in Contact with Bone. *Curr. Med. Chem.* **2008**, *15* (5), 523–527.
(162) Polizu, S.; Savadogo, O.; Poulin, P.; Yahia, L. Applications of Carbon Nanotubes-Based Biomaterials in Biomedical Nanotechnology. *J. Nanosci. Nanotechnol.* **2006**, *6* (7), 1883–1904.
(163) Yu, M. Strength and Breaking Mechanism of Multiwalled Carbon Nanotubes Under Tensile Load. *Science* **2000**, *287* (5453), 637–640.
(164) Gonçalves, G.; Portolés, M.-T.; Ramírez-Santillán, C.; Vallet-Regí, M.; Serro, A. P.; Grácio, J.; Marques, P. A. A. P. Evaluation of the in Vitro Biocompatibility of PMMA/high-Load HA/carbon Nanostructures Bone Cement Formulations. *J. Mater. Sci. Mater. Med.* **2013**, *24* (12), 2787–2796.
(165) Meng, Z. X.; Zheng, W.; Ding, M. H.; Zhou, H. M.; Chen, X. Q.; Chen, J. C.; Liu, M. K.; Zheng, Y. F. Fabrication and Characterization of Elastomeric Polyester/Carbon Nanotubes Nanocomposites for Biomedical Application. *J. Nanosci. Nanotechnol.* **2011**, *11* (4), 3126–3133.
(166) Lanone, S.; Rogerieux, F.; Geys, J.; Dupont, A.; Maillot-Marechal, E.; Boczkowski, J.; Lacroix, G.; Hoet, P. Comparative Toxicity of 24 Manufactured Nanoparticles in Human Alveolar Epithelial and Macrophage Cell Lines. *Part. Fibre Toxicol.* **2009**, *6* (1), 14.
(167) Coccini, T.; Manzo, L.; Roda, E. Safety Evaluation of Engineered Nanomaterials for Health Risk Assessment: An Experimental Tiered Testing Approach Using Pristine and Functionalized Carbon Nanotubes. *ISRN Toxicol.* **2013**, *2013*, 1–13.
(168) Thomas, V.; Halloran, B. A.; Ambalavanan, N.; Catledge, S. A.; Vohra, Y. K. In Vitro Studies on the Effect of Particle Size on Macrophage Responses to Nanodiamond Wear Debris. *Acta Biomater.* **2012**, *8* (5), 1939–1947.

(169) Briganti, E.; Losi, P.; Raffi, A.; Scoccianti, M.; Munaò, A.; Soldani, G. Silicone Based Polyurethane Materials: A Promising Biocompatible Elastomeric Formulation for Cardiovascular Applications. *J. Mater. Sci. Mater. Med.* **2006**, *17* (3), 259–266.
(170) Ghebaur, A.; Garea, S. A.; Iovu, H. New Polymer–halloysite Hybrid Materials—potential Controlled Drug Release System. *Int. J. Pharm.* **2012**, *436* (1-2), 568–573.
(171) Ruiz-Hitzky, E.; Van Meerbeek, A. Chapter 10.3 Clay Mineral– and Organoclay–Polymer Nanocomposite. In *Developments in Clay Science*; Faïza Bergaya, B. K. G. T. and G. L., Ed.; Handbook of Clay Science; Elsevier, 2006; Vol. Volume 1, pp 583–621.
(172) Sudina, M. L.; R.C., C.; V.L., M.; M.O., C.; H., L.; L., E. Application of Infrared Spectroscopy to Analysis of Chitosan/Clay Nanocomposites. In *Infrared Spectroscopy - Materials Science, Engineering and Technology*; Theophile, T., Ed.; InTech, 2012.
(173) Haxaire, K.; Mar[illegible]chal, Y.; Milas, M.; Rinaudo, M. Hydration of Polysaccharide Hyaluronan Observed by IR Spectrometry. I. Preliminary Experiments and Band Assignments. *Biopolymers* **2003**, *72* (1), 10–20.
(174) Ritger, P. L.; Peppas, N. A. A Simple Equation for Description of Solute Release I. Fickian and Non-Fickian Release from Non-Swellable Devices in the Form of Slabs, Spheres, Cylinders or Discs. *J. Controlled Release* **1987**, *5* (1), 23–36.
(175) Ritger, P. L.; Peppas, N. A. A Simple Equation for Description of Solute Release II. Fickian and Anomalous Release from Swellable Devices. *J. Controlled Release* **1987**, *5* (1), 37–42.
(176) Aguzzi, C.; Viseras, C.; Cerezo, P.; Salcedo, I.; Sánchez-Espejo, R.; Valenzuela, C. Release Kinetics of 5-Aminosalicylic Acid from Halloysite. *Colloids Surf. B Biointerfaces* **2013**, *105*, 75–80.
(177) Bariana, M.; Aw, M. S.; Kurkuri, M.; Losic, D. Tuning Drug Loading and Release Properties of Diatom Silica Microparticles by Surface Modifications. *Int. J. Pharm.* **2013**, *443* (1-2), 230–241.
(178) Horcajada, P.; Chalati, T.; Serre, C.; Gillet, B.; Sebrie, C.; Baati, T.; Eubank, J. F.; Heurtaux, D.; Clayette, P.; Kreuz, C.; et al. Porous Metal-Organic-Framework Nanoscale Carriers as a Potential Platform for Drug Delivery and Imaging. *Nat. Mater.* **2010**, *9* (2), 172–178.
(179) Farmer, V. C.; Adams, M. J.; Fraser, A. R.; Palmieri, F. Synthetic Imogolite: Properties, Synthesis, and Possible Applications. *Clay Min.* **1983**, *18*, 459–472.
(180) Yah, W. O.; Yamamoto, K.; Jiravanichanun, N.; Otsuka, H.; Takahara, A. Imogolite Reinforced Nanocomposites: Multifaceted Green Materials. *Materials* **2010**, *3* (3), 1709–1745.
(181) Bonelli, B.; Bottero, I.; Ballarini, N.; Passeri, S.; Cavani, F.; Garrone, E. IR Spectroscopic and Catalytic Characterization of the Acidity of Imogolite-Based Systems. *J. Catal.* **2009**, *264* (1), 15–30.
(182) Pierotti, R. A.; Rouquerol, J. Reporting Physisorption Data for Gas/solid Systems with Special Reference to the Determination of Surface Area and Porosity. *Pure Appl Chem* **1985**, *57* (4), 603–619.
(183) Johnston, C. T.; Sposito, G.; Erickson, C. Vibrational Probe Studies of Water Interactions with Montmorillonite. *Clays Clay Miner.* **1992**, *40* (6), 722–730.
(184) Jahromi, M. T.; Yao, G.; Cerruti, M. The Importance of Amino Acid Interactions in the Crystallization of Hydroxyapatite. *J. R. Soc. Interface* **2013**, *10* (80), 20120906.

(185) Sugino, A.; Miyazaki, T.; Ohtsuki, C. Apatite-Forming Ability of Polyglutamic Acid Hydrogels in a Body-Simulating Environment. *J. Mater. Sci. Mater. Med.* **2008**, *19* (6), 2269–2274.
(186) Koutsopoulos, S.; Kontogeorgou, A.; Dalas, E.; Petroheilos, J. Calcification of Porcine and Human Cardiac Valves: Testing of Various Inhibitors for Antimineralization. *J. Mater. Sci. Mater. Med.* **1998**, *9* (7), 421–424.
(187) Eiden-Aßmann, S.; Viertelhaus, M.; Heiß, A.; Hoetzer, K. A.; Felsche, J. The Influence of Amino Acids on the Biomineralization of Hydroxyapatite in Gelatin. *J. Inorg. Biochem.* **2002**, *91* (3), 481–486.
(188) Lu, J. R.; Zhao, X. B.; Yaseen, M. Biomimetic Amphiphiles: Biosurfactants. *Curr. Opin. Colloid Interface Sci.* **2007**, *12* (2), 60–67.
(189) Bordes, R.; Holmberg, K. Amino Acid-Based Surfactants – Do They Deserve More Attention? *Adv. Colloid Interface Sci.* **2015**, *222*, 79–91.
(190) Kim, K. S.; Moller, M. A.; Tildesley, D. J.; Quirke, N. Molecular Dynamics Simulations of Langmuir-Blodgett Monolayers with Explicit Head-Group Interactions. *Mol. Simul.* **1994**, *13* (2), 77–99.
(191) Greiner, E.; Kumar, K.; Sumit, M.; Giuffre, A.; Zhao, W.; Pedersen, J.; Sahai, N. Adsorption of L-Glutamic Acid and L-Aspartic Acid to γ-Al2O3. *Geochim. Cosmochim. Acta* **2014**, *133*, 142–155.
(192) Israelachvili, J. N. Chapter 14 - Electrostatic Forces between Surfaces in Liquids. In *Intermolecular and Surface Forces (Third Edition)*; Israelachvili, J. N., Ed.; Academic Press: San Diego, 2011; pp 291–340.
(193) Greiner, E.; Kumar, K.; Sumit, M.; Giuffre, A.; Zhao, W.; Pedersen, J.; Sahai, N. Adsorption of L-Glutamic Acid and L-Aspartic Acid to γ-Al2O3. *Geochim. Cosmochim. Acta* **2014**, *133*, 142–155.
(194) Roddick-Lanzilotta, A. D.; Connor, P. A.; McQuillan, A. J. An In Situ Infrared Spectroscopic Study of the Adsorption of Lysine to TiO_2 from an Aqueous Solution. *Langmuir* **1998**, *14* (22), 6479–6484.
(195) Roddick-Lanzilotta, A. D.; McQuillan, A. J. An in Situ Infrared Spectroscopic Study of Glutamic Acid and of Aspartic Acid Adsorbed on TiO2: Implications for the Biocompatibility of Titanium. *J. Colloid Interface Sci.* **2000**, *227* (1), 48–54.
(196) Bordes, R.; Holmberg, K. Physical Chemical Characteristics of Dicarboxylic Amino Acid-Based Surfactants. *Colloids Surf. Physicochem. Eng. Asp.* **2011**, *391* (1–3), 32–41.
(197) Bordes, R.; Tropsch, J.; Holmberg, K. Adsorption of Dianionic Surfactants Based on Amino Acids at Different Surfaces Studied by QCM-D and SPR. *Langmuir* **2010**, *26* (13), 10935–10942.
(198) Kronberg, B.; Holmberg, K.; Lindman, B. *Surface Chemistry of Surfactants and Polymers*; John Wiley & Sons, Inc: Chichester, West Sussex, 2014.
(199) Guo, Y.; Zhao, J.; Zhang, H.; Yang, S.; Qi, J.; Wang, Z.; Xu, H. Use of Rice Husk-Based Porous Carbon for Adsorption of Rhodamine B from Aqueous Solutions. *Dyes Pigments* **2005**, *66* (2), 123–128.
(200) Raftery, A. E.; Li, N.; Ševčíková, H.; Gerland, P.; Heilig, G. K. Bayesian Probabilistic Population Projections for All Countries. *Proc. Natl. Acad. Sci.* **2012**, *109* (35), 13915–13921.
(201) Dimick JB; Ryan AM. TAking a Broader Perspective on the Benefits of Minimally Invasive Surgery. *JAMA Surg.* **2013**, *148* (7), 648–648.
(202) Sannino, A.; Demitri, C.; Madaghiele, M. Biodegradable Cellulose-Based Hydrogels: Design and Applications. *Materials* **2009**, *2* (2), 353–373.

(203) Handge, U. A.; Hedicke-Höchstötter, K.; Altstädt, V. Composites of Polyamide 6 and Silicate Nanotubes of the Mineral Halloysite: Influence of Molecular Weight on Thermal, Mechanical and Rheological Properties. *Polymer* **2010**, *51* (12), 2690–2699.
(204) Yuan, J.; Murray, H. H. The Importance of Crystal Morphology on the Viscosity of Concentrated Suspensions of Kaolins. *Appl. Clay Sci.* **1997**, *12* (3), 209–219.
(205) Campbell, S. B.; Patenaude, M.; Hoare, T. Injectable Superparamagnets: Highly Elastic and Degradable Poly(*N* -isopropylacrylamide)–Superparamagnetic Iron Oxide Nanoparticle (SPION) Composite Hydrogels. *Biomacromolecules* **2013**, *14* (3), 644–653.
(206) Patenaude, M.; Hoare, T. Injectable, Mixed Natural-Synthetic Polymer Hydrogels with Modular Properties. *Biomacromolecules* **2012**, *13* (2), 369–378.
(207) Li, H.; Wu, B.; Mu, C.; Lin, W. Concomitant Degradation in Periodate Oxidation of Carboxymethyl Cellulose. *Carbohydr. Polym.* **2011**, *84* (3), 881–886.
(208) Biswas, A.; Kim, S.; Selling, G. W.; Cheng, H. N. Conversion of Agricultural Residues to Carboxymethylcellulose and Carboxymethylcellulose Acetate. *Ind. Crops Prod.* **2014**, *60*, 259–265.
(209) Edali, M.; Esmail, M. N.; Vatistas, G. H. Rheological Properties of High Concentrations of Carboxymethyl Cellulose Solutions. *J. Appl. Polym. Sci.* **2001**, *79* (10), 1787–1801.
(210) Honerkamp, J.; Weese, J. A Nonlinear Regularization Method for the Calculation of Relaxation Spectra. *Rheol. Acta* **1993**, *32* (1), 65–73.
(211) Ding, J.; Tian, T.; Meng, Q.; Guo, Z.; Li, W.; Zhang, P.; Ciacchi, F. T.; Huang, J.; Yang, W. Smart Multifunctional Fluids for Lithium Ion Batteries: Enhanced Rate Performance and Intrinsic Mechanical Protection. *Sci. Rep.* **2013**, *3*.
(212) Vernon, B. *Injectable Biomaterials: Science and Applications*; Ed.; Woodhead Publishing in materials; Woodhead Pub: Oxford ; Philadelphia, 2011.
(213) Arun Kumar, R.; Sivashanmugam, A.; Deepthi, S.; Iseki, S.; Chennazhi, K. P.; Nair, S. V.; Jayakumar, R. Injectable Chitin-Poly(ε-caprolactone)/Nanohydroxyapatite Composite Microgels Prepared by Simple Regeneration Technique for Bone Tissue Engineering. *ACS Appl. Mater. Interfaces* **2015**, *7* (18), 9399–9409.
(214) Gaharwar, A. K.; Avery, R. K.; Assmann, A.; Paul, A.; McKinley, G. H.; Khademhosseini, A.; Olsen, B. D. Shear-Thinning Nanocomposite Hydrogels for the Treatment of Hemorrhage. *ACS Nano* **2014**, *8* (10), 9833–9842.
(215) Tran, N. Q.; Joung, Y. K.; Lih, E.; Park, K. D. In Situ Forming and Rutin-Releasing Chitosan Hydrogels As Injectable Dressings for Dermal Wound Healing. *Biomacromolecules* **2011**, *12* (8), 2872–2880.
(216) Cilurzo, F.; Selmin, F.; Minghetti, P.; Adami, M.; Bertoni, E.; Lauria, S.; Montanari, L. Injectability Evaluation: An Open Issue. *AAPS PharmSciTech* **2011**, *12* (2), 604–609.
(217) Olszta, M. J.; Cheng, X.; Jee, S. S.; Kumar, R.; Kim, Y.-Y.; Kaufman, M. J.; Douglas, E. P.; Gower, L. B. Bone Structure and Formation: A New Perspective. *Mater. Sci. Eng. R Rep.* **2007**, *58* (3-5), 77–116.
(218) Dorozhkin, S. V. Calcium Orthophosphates (CaPO4): Occurrence and Properties. *Prog. Biomater.* **2016**, *5* (1), 9–70.
(219) Ridi, F.; Meazzini, I.; Castroflorio, B.; Bonini, M.; Berti, D.; Baglioni, P. Functional Calcium Phosphate Composites in Nanomedicine. *Adv. Colloid Interface Sci.* **2016**.
(220) Kim, T. G.; Shin, H.; Lim, D. W. Biomimetic Scaffolds for Tissue Engineering. *Adv. Funct. Mater.* **2012**, *22* (12), 2446–2468.

(221) Moioli, E. K.; Clark, P. A.; Xin, X.; Lal, S.; Mao, J. J. Matrices and Scaffolds for Drug Delivery in Dental, Oral and Craniofacial Tissue Engineering. *Adv. Drug Deliv. Rev.* **2007**, *59* (4-5), 308–324.
(222) Van Vlierberghe, S.; Dubruel, P.; Schacht, E. Biopolymer-Based Hydrogels As Scaffolds for Tissue Engineering Applications: A Review. *Biomacromolecules* **2011**, *12* (5), 1387–1408.
(223) Buwalda, S. J.; Boere, K. W. M.; Dijkstra, P. J.; Feijen, J.; Vermonden, T.; Hennink, W. E. Hydrogels in a Historical Perspective: From Simple Networks to Smart Materials. *J. Controlled Release* **2014**, *190*, 254–273.
(224) Santoro, M.; Tatara, A. M.; Mikos, A. G. Gelatin Carriers for Drug and Cell Delivery in Tissue Engineering. *J. Controlled Release* **2014**, *190*, 210–218.
(225) Wisotzki, E. I.; Hennes, M.; Schuldt, C.; Engert, F.; Knolle, W.; Decker, U.; Käs, J. A.; Zink, M.; Mayr, S. G. Tailoring the Material Properties of Gelatin Hydrogels by High Energy Electron Irradiation. *J Mater Chem B* **2014**, *2* (27), 4297–4309.
(226) Tatini, D.; Tempesti, P.; Ridi, F.; Fratini, E.; Bonini, M.; Baglioni, P. Pluronic/gelatin Composites for Controlled Release of Actives. *Colloids Surf. B Biointerfaces* **2015**, *135*, 400–407.
(227) Nishi, C.; Nakajima, N.; Ikada, Y. In Vitro Evaluation of Cytotoxicity of Diepoxy Compounds Used for Biomaterial Modification. *J. Biomed. Mater. Res.* **1995**, *29* (7), 829–834.
(228) Teramoto, N.; Hayashi, A.; Yamanaka, K.; Sakiyama, A.; Nakano, A.; Shibata, M. Preparation and Mechanical Properties of Photo-Crosslinked Fish Gelatin/Imogolite Nanofiber Composite Hydrogel. *Materials* **2012**, *5* (12), 2573–2585.
(229) Yamamoto, K.; Otsuka, H.; Wada, S.-I.; Sohn, D.; Takahara, A. Transparent Polymer Nanohybrid Prepared by in Situ Synthesis of Aluminosilicate Nanofibers in Poly(vinyl Alcohol) Solution. *Soft Matter* **2005**, *1* (5), 372.
(230) Yamamoto, K.; Otsuka, H.; Wada, S.-I.; Sohn, D.; Takahara, A. Preparation and Properties of [poly(methyl Methacrylate)/imogolite] Hybrid via Surface Modification Using Phosphoric Acid Ester. *Polymer* **2005**, *46* (26), 12386–12392.
(231) Ishikawa, K.; Akasaka, T.; Abe, S.; Yawaka, Y.; Suzuki, M.; Watari, F. Application of Imogolite, Alumino-Silicate Nanotube, as Scaffold for the Mineralization of Osteoblasts. *Bioceram. Dev. Appl.* **2010**, *1*, 1–3.
(232) Morgan, E. F.; Yetkinler, D. N.; Constantz, B. R.; Dauskardt, R. H. Mechanical Properties of Carbonated Apatite Bone Mineral Substitute: Strength, Fracture and Fatigue Behaviour. *J. Mater. Sci. Mater. Med.* **1997**, *8* (9), 559–570.
(233) Van Vlierberghe, S.; Cnudde, V.; Dubruel, P.; Masschaele, B.; Cosijns, A.; De Paepe, I.; Jacobs, P. J. S.; Van Hoorebeke, L.; Remon, J. P.; Schacht, E. Porous Gelatin Hydrogels: 1. Cryogenic Formation and Structure Analysis. *Biomacromolecules* **2007**, *8* (2), 331–337.
(234) Shibayama, M. Structure-Mechanical Property Relationship of Tough Hydrogels. *Soft Matter* **2012**, *8* (31), 8030.
(235) Schaefer, D. W. Fractal Models and the Structure of Materials. *MRS Bull.* **1988**, *13* (02), 22–27.
(236) Wang, H.; Zhou, W.; Ho, D. L.; Winey, K. I.; Fischer, J. E.; Glinka, C. J.; Hobbie, E. K. Dispersing Single-Walled Carbon Nanotubes with Surfactants: A Small Angle Neutron Scattering Study. *Nano Lett.* **2004**, *4* (9), 1789–1793.

Appendix

List of publications

1. **Design and characterization of a composite material based on Sr(II)-loaded clay nanotubes included within a biopolymer matrix**

Reprinted from Journal of Colloid and Interface Science (2015), 448, 501-507, with permission from Elsevier
doi: 10.1016/j.jcis.2015.02.043

Stefano Del Buffa[a,b], Massimo Bonini[a,b], Francesca Ridi[a,b], Mirko Severi[a], Paola Losi[c], Silvia Volpi[c], Tamer Al Kayal[c], Giorgio Soldani[c] and Piero Baglioni[a,b]

[a]Department of Chemistry "Ugo Schiff", University of Florence, via della Lastruccia 3, Sesto Fiorentino, 50019 Florence, Italy; [b]CSGI Consortium, via della Lastruccia 3, Sesto Fiorentino, 50019 Florence, Italy; [c]Laboratory of Biomaterials & Graft Technology, Institute of Clinical Physiology, National Research Council, Via Aurelia Sud, 54100 Massa, Italy

A layman summary of the work entitled "**Clay nanotubes loaded with Sr(II) could help in designing composite scaffolds for bone regeneration**" was selected for publication on Atlas Of Science (www.atlasofscience.org), on February 18th 2016.

2. **The effect of charge on the release kinetics from polysaccharide–nanoclay composites**

Reprinted from Journal of Nanoparticle Research (2015), 17:146, with permission of Springer
doi 10.1007/s11051-015-2947-z

Stefano Del Buffa, Emanule Grifoni, Francesca Ridi and Piero Baglioni

Department of Chemistry "Ugo Schiff" and CSGI consortium, University of Florence, via della Lastruccia 3, Sesto Fiorentino, 50019 Florence, Italy

3. **Injectable composites *via* functionalization of 1D nanoclays and biodegradable coupling with a polysaccharide hydrogel**
Reprinted from Colloids and Surfaces B: Biointerfaces (2016), 145, 562-566, with permission from Elsevier
doi: 10.1016/j.colsurfb.2016.05.056

Stefano Del Buffa, Elia Rinaldi, Emiliano Carretti, Francesca Ridi, Massimo Bonini and Piero Baglioni

Department of Chemistry "Ugo Schiff" and CSGI consortium, University of Florence, via della Lastruccia 3, Sesto Fiorentino, 50019 Florence, Italy

A layman summary of the work entitled "**Injectable composite made of nano tubular clays and a polysaccharide matrix**" was selected for publication on Atlas Of Science (www.atlasofscience.org), on December, 18th 2016

4. **Adsorption of amino acids and glutamic acid-based surfactants on imogolite nanotubes**
Manuscript submitted to Langmuir (under revision, Jan 2017)

Francesca Ridi[a], Alessio Gabbani[a], Stefano Del Buffa[a], Romain Bordes[b,c], Massimo Bonini[a], Krister Holmberg[b] and Piero Baglioni[a]

[a]Department of Chemistry "Ugo Schiff" and CSGI consortium, University of Florence, via della Lastruccia 3, Sesto Fiorentino, 50019 Florence, Italy; [b]Department of Chemistry and Chemical Engineering, Chalmers University of Technology, 41296 Göteborg, Sweden; [c]Vinn Excellence Center SuMo Biomaterials, Chalmers University of Technology, 41296 Göteborg, Sweden

5. **Enhanced formation of hydroxyapatite in imogolite-reinforced macroporous hydrogels**
Manuscript submitted to Materials and Design (Jan 2017)

Rita Gelli, Stefano Del Buffa, Paolo Tempesti, Massimo Bonini, Francesca Ridi and Piero Baglioni

Department of Chemistry "Ugo Schiff" and CSGI consortium, University of Florence, via della Lastruccia 3, Sesto Fiorentino, 50019 Florence, Italy

6. State of water in hydrating tricalcium silicate pastes: the effect of a cellulose ether

Reprinted with permission from The Journal of Physical Chemistry C, 120, 14, 7612-7620. Doi: 10.1021/acs.jpcc.6b00691

Stefano Del Buffa[a], Emiliano Fratini[a], Francesca Ridi[a], Antonio Faraone[b,c] and Piero Baglioni[a]

[a]Department of Chemistry "Ugo Schiff" and CSGI consortium, University of Florence, via della Lastruccia 3, Sesto Fiorentino, 50019 Florence, Italy; [b]NIST Center for Neutron Research, 100 Bureau Drive, Gaithersburg, Maryland 20899-6102, United States; [c]Department of Materials Science and Engineering, University of Maryland, College Park, Maryland 20742, United States

Manuscript reprints

In the following pages a reprint of all the manuscripts published, and submitted for publication, during the period of my PhD is reported. At the end of each paper, a section with all the supplementary information related to each work is also reported.
All the papers are reprinted with permission from the publisher, as specified in the previous section.

Journal of Colloid and Interface Science 448 (2015) 501–507

Contents lists available at ScienceDirect

Journal of Colloid and Interface Science

www.elsevier.com/locate/jcis

Design and characterization of a composite material based on Sr(II)-loaded clay nanotubes included within a biopolymer matrix

Stefano Del Buffa [a,b], Massimo Bonini [a,b], Francesca Ridi [a,b], Mirko Severi [a], Paola Losi [c], Silvia Volpi [c], Tamer Al Kayal [c], Giorgio Soldani [c], Piero Baglioni [a,b,*]

[a] Department of Chemistry "Ugo Schiff", University of Florence, via della Lastruccia 3, Sesto Fiorentino, 50019 Florence, Italy
[b] CSGI Consortium, via della Lastruccia 3, Sesto Fiorentino, 50019 Florence, Italy
[c] Laboratory of Biomaterials & Graft Technology, Institute of Clinical Physiology, National Research Council, via Aurelia Sud, 54100 Massa, Italy

GRAPHICAL ABSTRACT

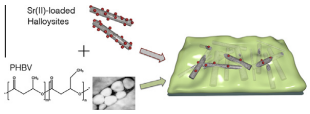

ARTICLE INFO

Article history:
Received 30 December 2014
Accepted 13 February 2015
Available online 23 February 2015

Keywords:
Nanocomposite
Biopolymers
Halloysite
Polyhydroxybutyric acid
In vitro cytotoxicity
Bone regeneration
Strontium

ABSTRACT

This paper reports on the preparation, characterization, and cytotoxicity of a hybrid nanocomposite material made of Sr(II)-loaded Halloysite nanotubes included within a biopolymer (3-polyhydroxybutyrate-co-3-hydroxyvalerate) matrix. The Sr(II)-loaded inorganic scaffold is intended to provide mechanical resistance, multi-scale porosity, and to favor the in-situ regeneration of bone tissue thanks to its biocompatibility and bioactivity. The interaction of the hybrid system with the physiological environment is mediated by the biopolymer coating, which acts as a binder, as well as a diffusional barrier to the Sr(II) release. The degradation of the polymer progressively leads to the exposure of the Sr(II)-loaded Halloysite scaffold, tuning its interaction with osteogenic cells. The *in vitro* biocompatibility of the composite was demonstrated by cytotoxicity tests on L929 fibroblast cells. The results indicate that this composite material could be of interest for multiple strategies in the field of bone tissue engineering.

1. Introduction

Materials for bone tissue engineering should guide and promote the regeneration of bone tissue. Various biocompatible and biodegradable porous scaffolds have been recently designed, aiming at providing a temporary substitute for the extracellular matrix of bone [1], which mimic the structural materials present in nature [2]. Prerequisites for an efficient biomaterial are its biocompatibility, well-suited mechanical properties (both in terms of resistance and lightness), a percolative structure with properly sized interconnected pores to promote tissue integration and vascularization, and finally time and space controlled biodegradability and bioactivity [3]. Several materials have been recently suggested in the

Abbreviations: HNT, Halloysite nanotubes; PHBV, 3-polyhydroxybutyrate-co-3-hydroxyvalerate; HNT-Sr, Halloysite nanotubes loaded with Sr^{2+}; HNT–PHBV, nanocomposite material made of Halloysite nanotubes and 3-polyhydroxybutyrate-co-3-hydroxyvalerate; HNT-Sr-PHBV, nanocomposite material made of Halloysite nanotubes loaded with Sr^{2+} and 3-polyhydroxybutyrate-co-3-hydroxyvalerate; PBS, Phosphate buffer solution; APTES, 3-aminopropyl-triethoxysylane; TEOS, tetraethyl orthosilicate; MTT, mitochondrial succinate dehydrogenase activity test; BrdU, 5-bromo-2′-deoxyuridine; SEM, scanning electron microscope; AFM, atomic force microscopy; BET, Brunauer Emmett Teller; BJH, Barrett Joyner, Halenda; ICP-AES, inductively coupled plasma-atomic emission spectroscopy; ATR–FTIR, attenuated total reflectance-Fourier transform infrared spectroscopy; TGA, thermogravimetry analysis; DSC, differential scanning calorimetry; OD, optical density; SD, standard deviation.

* Corresponding author at: Department of Chemistry "Ugo Schiff" and CSGI, University of Florence, via della Lastruccia 3, Sesto Fiorentino, 50019 Florence, Italy. Fax: +39 0554573032.
E-mail address: piero.baglioni@unifi.it (P. Baglioni).

http://dx.doi.org/10.1016/j.jcis.2015.02.043
0021-9797/

literature as promising candidates [4], including bioceramics [5], bioglasses [6], and hydroxyapatite particles embedded in polymeric scaffolds [7–9]. Nevertheless, synthetic grafts still display many limitations, boosting the search for materials integrating both osteoconductive and osteoinductive properties [10,11].

Several studies demonstrated that doping with strontium(II) enhances the osteoblast proliferation onto the graft and finally results in higher bone mineral density. Thanks of its bioactivity, Sr(II) is also effective in the treatment of osteoporosis [12–14]. In osteopenic bones, as the mineral density is reduced, the microarchitecture deteriorates and the amount and variety of embedded proteins are altered, leading to an increased risk of fracture. Strontium-based drugs have been widely prescribed over the last decades [15], aiming at restoring the optimal equilibrium between bone resorption and formation through a dual mechanism [16]. Strontium(II) promotes the deposition of new bone thanks to the stimulation of calcium(II) receptors and differentiation of pre-osteoblasts to osteoblasts. At the same time, it hampers bone resorption through the stimulation of the osteoprotegerin secretion, so inhibiting the formation of osteoclasts from pre-osteoclasts [17]. Strontium is naturally present in the human body (about 4.6 mg/kg), the vast majority of which is localized within bone tissues. Unfortunately, when orally administered at high doses (*i.e.*, >4 g/L), it could also produce detrimental effects [18] on the bone metabolism and increase the risk of heart attack. For these reasons the European Medicines Agency has severely restricted the use of Protelos/Osseor® [19]. Rather than through its systemic administration, it is therefore crucial to deliver strontium(II) at the treatment site, so that its bioactivity could be locally exploited without the collateral effects that have restricted its use. In this framework, a possible carrier for Sr(II) is represented by the synthetic graft matrix. In particular, filling the matrix with particles able to improve the mechanical properties and to upload and deliver Sr(II) at the treatment site could represent a significant advantage over the materials currently in use.

Halloysites are a class of natural clays with the same chemical composition as kaolinite ($Al_2(OH)_4Si_2O_5{\cdot}nH_2O$) and a tubular morphology, resulting from the wrapping of the clay layers [20]. Their lengths range from ~100 nm to several μm, while the inner diameter is within 15 and 100 nm, depending on their provenance. The potentials of HNT as carriers for drugs [21,22] and substrates for proliferation of cells [23,24] have been recently highlighted. Their hollow fiber-like shape suggests also their use as an inorganic scaffold with the required mechanical properties (especially lightness and compressive strength) for bone replacement: in fact, HNT structure closely resembles that of multi-walled carbon nanotubes, whose use as reinforcing agents in biomaterials is limited because of toxicity concerns [25]. Furthermore, due to their hydroxylated outer surface and the high surface area, HNT are well known to upload and dynamically exchange a variety of cations, including Sr(II) [26]. In a recent work, the potential use of HNTs in composite biomaterials for the regeneration of bone tissues was demonstrated through their co-formulation with polyvinylalcohol, showing to favor the *in vitro* adhesion and growth of fibroblast and osteoblast cell lines [27].

In this study we formulated a new biomaterial for tissue engineering that integrates the structural properties of HNT and the bioactivity of Sr(II) into a biocompatible and biodegradable matrix made of a biopolymer. In particular, we chose 3-polyhydroxybutyrate-co-3-hydroxyvalerate (PHBV), a polyhydroxyalcanoate produced through microbial synthesis. PHBV is biodegradable, biocompatible and easy to process, being the main reasons for its use in a variety of biomedical applications [28–30]. In our design, the biopolymer is intended both as a biocompatible binder and a diffusional barrier to contain the effect of Sr(II) within the treatment region. The progressive degradation in physiological conditions leads to the progressive exposure of HNT to the environment, as well as that of Sr(II), so promoting the growth of new bone tissue. Most of the strontium cations are expected not to be released from the treatment site, but to promote the adhesion and growth of cells, eventually being integrated in the final bone tissue.

2. Materials and methods

2.1. Materials

Halloysite nanotube (HNT) powder was provided by Imerys Minerals Ltd (Auckland, New Zealand) and it was used as-received, without further purification. PHBV was purchased from Good Fellow (England, UK). The biopolymer has a composition of 88% polyhydroxybutyrate and 12% polyhydroxyvalerate. Tetraethylorthosilicate (TEOS, 97%) and 3-aminopropyl-triethoxysylane (APTES, 97%) were obtained from Fluka (Milan, Italy). Strontium chloride hexahydrate were purchased from Riedel-de Haen (Milan, Italy). Phosphate buffer solution (PBS) was prepared in accordance to Dulbecco's formulation [31], NaCl was purchased from Sigma Aldrich (Milan, Italy), $Na_2HPO_4{\cdot}2H_2O$ and KH_2PO_4 from Merck (Milan, Italy) and KCl from Fluka (Milan, Italy). HNO_3 (65%, RPE-ISO) was purchased from Carlo Erba (Milan, Italy). NH_4OH (30% v/v) was purchased from Sigma Aldrich (Milan, Italy). Ethanol (99.8% v/v) was purchased from Fluka (Milan, Italy).

2.2. Preparation of nanocomposites

In order to simulate the application of the material as a coating onto synthetic bone grafts, we prepared the composites by spin-coating onto glass surfaces, whose chemical reactivity is similar to that of the ceramic materials commonly used in synthetic bone grafts. In order to remove organic residues and to activate the silanol groups, glass slides were sequentially cleaned by sonicating them in a detergent solution, in ethanol, and finally treated with ozone (PSD-UV, Novascan Technologies, Ames, USA). Glass substrates were then functionalized through incubation in a silane (TEOS or APTES) saturated atmosphere at 60 °C during 24 h. HNT surface was functionalized with a solution of APTES in ethanol (2.5 %wt). The amount of silane was chosen to cover about 20% of the HNT external surface, taking into account a silane cross section [32] of 50 $Å^2$ and the HNT surface area obtained from BET. To upload Sr(II), 100 mg of HNTs were mixed with 10 ml of a 100 mg/ml $SrCl_2{\cdot}6H_2O$ solution. The dispersion was vigorously mixed for 24 h and then centrifuged. The solid was recollected, dried, and then used for the subsequent preparation of the nanocomposites. HNT dispersions were spin coated by means of a P6700 spin coater of Specialty Coating Systems Inc. (Indianapolis, IN, USA) onto the glass substrate, and then a PHBV chloroform solution (2 %wt) was spin coated on top of it. The coating process was carried out at room temperature in two stages at constant rotating speed (1500 and 2500 rpm), separated by an acceleration step.

2.3. Nanocomposite degradation

Nanocomposites were exposed to PBS solution at 37 °C and observed during 28 days to address morphological and structural changes.

2.4. Microscopy

Scanning Electron Microscopy was performed on non-metallized samples using a ΣIGMA Field Emission SEM (Carl Zeiss Microscopy GmbH, Germany). Atomic Force Microscopy

(in non-contact mode) and nanoindentation experiments were performed by means of a XE-100 microscope (Park Instruments, Korea) equipped with NCHR probes.

2.5. ICP-AES

The concentration of strontium and silicon in the samples was determined in triplicate by means of a Varian 720-ES Inductively Coupled Plasma Atomic Emission Spectrometer (ICP-AES). The samples were diluted to 5 mL with 0.1% suprapure nitric acid obtained by sub-boiling distillation, spiked with 0.32 ppm of Ge used as an internal standard, and analyzed. Calibration standards were prepared by gravimetric serial dilution from commercial stock standard solutions of Sr and Si at 1000 mg L^{-1}. Wavelengths used for Sr determination were 421.552 and 407.771 nm, those used for Si analysis were 185.005, 251.432, 250.690, 288.158 and 251.611 nm whereas for Ge was used the line at 209.426 nm. The operating conditions were optimized to obtain maximum signal intensity, and between each sample, a rinse solution constituted by 2% v/v HNO_3 was used.

2.6. Infrared spectroscopy

ATR–FTIR measurements were performed on a Nexus 870 spectrometer (Nicolet, Madison, WI, USA), equipped with a liquid N_2-cooled mercury cadmium telluride (MCT) detector in the 400–4000 cm^{-1} range with a resolution of 2 cm^{-1}.

2.7. Thermal analysis

Thermogravimetric analysis (TGA) was carried out on a SDT Q600 (TA Instruments, Philadelphia, PA, USA) from RT to 1000 °C at 10 °C/min. Differential Scanning Calorimetry (DSC) was performed by means of a DSC-Q2000 by TA Instruments (Philadelphia, PA, USA), in the −20/200 °C range at 10 °C/min. Measurements were conducted in N_2 atmosphere, flow rate 50 ml/min.

2.8. Surface area and pore analysis

Surface area and porosity of the samples were determined with a Beckmann-Coulter SA 3100 analyzer, utilizing BET [33] and BJH [34] calculations, respectively.

2.9. Cytotoxicity testing

The cytotoxicity of HNT samples was determined using a standard method for measurement of mitochondrial succinate dehydrogenase activity (MTT assay) and the Trypan blue exclusion assay for integrity cell membrane evaluation. All the samples were prepared in the form of films by solvent casting and then grinded and suspended in distilled water with the help of a Ultra-Turrax® T25 Basic mechanical homogenizer (IKA-Werke GmbH & Co, Staufen, Germany) working at 24,000 rpm. Suspension concentrations were adjusted to 1 mg/ml, thereafter were placed in glass ampoules and autoclaved for 20 min at 121 °C (ASAL 760, Milan, Italy). The initial concentrations were kept by addition of sterile H_2O. Samples were then stored at 4 °C until use.

2.10. MTT assay

Mouse fibroblasts L929 (see Supplementary Information) were seeded into 96-well plates at a density of 4×10^3 cells per well. After 24 h, the medium was replaced with 200 µl per well of HNT suspension samples or complete culture medium. The Halloysite suspensions at different concentration (25, 50 and 100 µg/mL) were diluted with complete culture medium. After 72 h of incubation, MTT solution (0.5 mg/mL final concentration) was added to each well and incubated for 3 h at 37 °C. The resulting formazan crystals were solubilized with 100 µL/well of dimethylsulfoxide (DMSO, Sigma Aldrich). The optical densities (ODs) were measured in a microplate reader (Spectrafluor Plus; TECAN, Austria GmbH) at 550 nm. The results were expressed as the percentage of OD compared to medium without HNT.

2.11. Trypan blue assay

L929 were seeded and treated as described for the MTT assay. After 72 h of exposure, cell monolayers were rinsed twice with PBS and re-suspended with trypsin–EDTA. An aliquot of the cells was stained with 0.4% Trypan blue, and the number of viable cells was determined using a hemocytometer and light microscopy. The number of viable cells was calculated as percentage of total cells.

2.12. Proliferation assay

The pyrimidine analogue 5-bromo-2′-deoxyuridine (BrdU) incorporation assay is a suitable method for the quantitative measurement of cell proliferation based on BrdU incorporation instead of thymidine into newly synthesized DNA. In the present study a commercially available BrdU-based enzyme-linked immunoassay was used (Roche Molecular Biochemicals, Mannheim, Germany). L929 fibroblasts (4×10^3 cells per well) were plated into 96-well plates and incubated for 24 h. After that, the medium was replaced by HNT suspension at the same concentration of cytotoxicity tests or complete medium. After 48 h of exposure, BrdU reagent was added and incubated for 4 h. The assay was performed following the procedure prescription. The ODs were measured at 450 nm by the microplate reader. The proliferation activity in presence of HNT was reported in percentages respect to cell growth in medium without HNT.

2.13. Statistical analysis

The viability and proliferation tests were performed in three independent experiments. The results are expressed as mean value ± standard deviation (SD) of four replicates wells for each HNT concentration and control medium. Data were evaluated statistically by StatView™ 5.0 software (SAS Institute, Cary, NC, USA). The various means were compared by the independent Student's *t*-test. A value of $p < 0.05$ was considered statistically significant.

3. Results and discussion

HNT are versatile mesoporous materials with a tubular structure. The different chemical composition of the inner (aluminol) and outer (siloxane) surfaces allows for the selective functionalization of the lumen/exterior, making this material very well suited for the design of composites for biomedical applications. Furthermore the peculiar hollow fiber shape of HNT is ideal for the inclusion of small molecules and for the assembly of a light and resistant composite, providing at the same time preferential diffusion pathways.

A representative SEM micrograph of the HNT commercial batch used throughout this work is given in Fig. 1, together with the schematic structure of a single tube. Different morphologies are visible, the nanotubular (length ranging from 100 nm to few µm) being the most represented. As suggested by XRD Rietveld analysis, the batch contains also kaolin and, in a minor amount, quartz (See Supplementary Information, Fig. SI-1), both of which are already employed in composites for biomedical applications [33,34]. Furthermore, kaolin has the same chemical composition

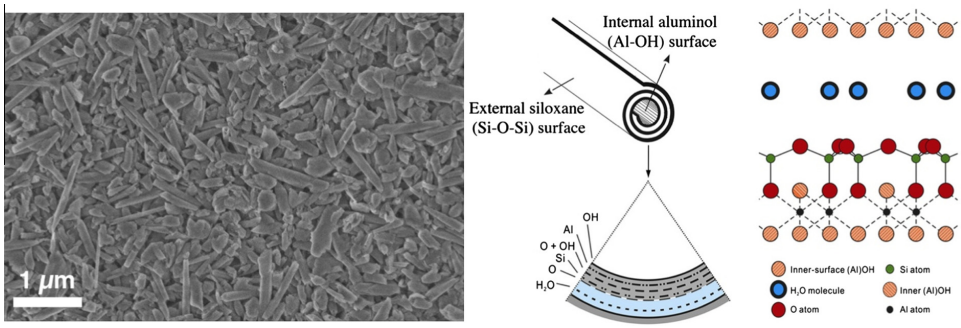

Fig. 1. Scanning electron microscopy image of a HNT sample (*left*), schematic representation of HNT structure (*middle*), and HNT crystallographic structure (*right*).

of Halloysite, while quartz (present in minor amounts) displays the same composition of its exterior. We decided therefore not to purify the commercial material, especially to demonstrate that no time and money consuming procedures are required to achieve optimal characteristics in the final material.

The BET analysis reveals that the pore size distribution ranges from few to few tens of nm, consistent with the presence of inter-tubular and intra-particle pores. In particular, nitrogen adsorption isotherm on HNT samples (see Fig. SI-2A in Supplementary Information) shows a hysteresis loop associated with a capillary condensation in mesoporous cavities [35]. The analysis of the hysteresis curve reveals that most of the pores are in the 20–80 nm range. Total BET surface area is 18 ± 1 m^2/g, while total pore volume is found to be 0.17 ± 0.01 ml/g. Several values of HNT surface area are reported in the literature, roughly ranging from 20 to 100 m^2/g, this variability being due to the origin of the deposit and especially to solvent treatments of the initial powder [36]. The relatively low value found for our powder further confirms the co-presence of non porous material. Functionalization of HNT with APTES and the loading with Sr^{2+} do not result in any significant variation in terms of surface area and porosity.

The cation-exchange capacity of the HNT batch versus Sr(II) was evaluated after mixing the powder material during 24 h in a saturated $SrCl_2$ solution. ICP-AES analysis indicated a strontium content of about 7 %wt.

Previous studies reported that the functionalization with APTES enhances the biocompatibility of several nanomaterials [37–39]. In our study, HNT surface was functionalized with APTES to enhance the chemical affinity of HNT with the PHBV biocompatible scaffold through hydrogen bonding between the amine groups and the polymer carboxylic moieties. The successful modification of HNT surface with APTES was confirmed by the presence of the N–H stretching band in the 3300–3500 cm^{-1} region of the ATR–FTIR spectrum shown in Fig. SI-3. Furthermore, APTES-functionalized HNT suspensions display a marked increase in their stability with respect to pristine clay nanotubes (Fig. SI-4).

SEM image of nanocomposites (HNT-Sr-PHBV) in Fig. 2A shows that the PHBV matrix almost completely embed the inorganic nanotubes in a quite homogenous and smooth film, with only few clay structures emerging from the polymer surface.

The HNT-Sr-PHBV nanocomposite thickness and mechanical properties were evaluated through AFM nanoindentation experiments [40,41] (see Fig. SI-5), resulting in an average thickness of the film of about 300 nm. The maximum compression that the nanocomposite withstands is about 20 μN. Taking into account the area of contact resulting from the AFM probe curvature, a compressive strength of about 50 GPa can be estimated, mainly ascribable to the presence of the Halloysite nanotubes [42]. Multi-walled carbon nanotubes that are frequently reported as potential reinforcing agents in biomedical composites [43,44] display compressive strengths of ~100 GPa [45] but present severe concerns from the toxicological point of view. The structural properties of Halloysite nanotubes make them very suitable for biomedical applications in the bone regeneration field, where mechanical resistance is a crucial prerequisite.

The thermal behavior of the composite was studied by means of thermogravimetry and differential scanning calorimetry in order to assess both its stability and processability features. Fig. 3A shows the weight losses of HNT, PHBV and HNT–PHBV composite. The thermogravimetry profile of the composite results from the combination of those of PHBV and HNT. The PHBV polymer is thermally stable up to 220 °C, while the weight of HNT is constant

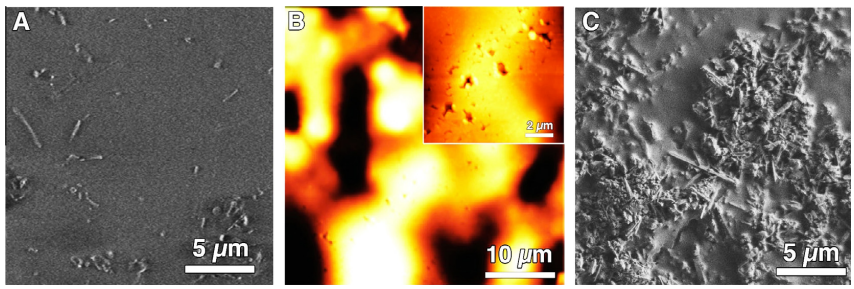

Fig. 2. (A) SEM image of the freshly prepared nanocomposite. (B) Non contact AFM image of a degraded (4 days) HNT–PHBV nanocomposite (*Z*-range: 800 nm). The inset displays a zoom of a selected region (*Z*-range: 400 nm). (C) SEM image of the nanocomposite degraded during 28 days.

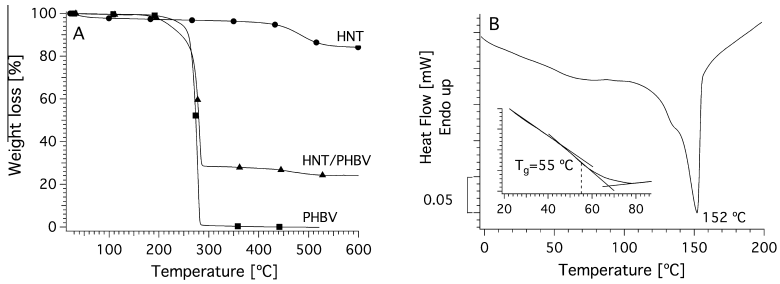

Fig. 3. (A) Thermogravimetry of HNT, PHBV and HNT–PHBV composite; (B) DSC thermogram of a PHBV sample. In the inset the temperature range 20–80 °C is enlarged, showing the glass transition of the polymer.

up to ~400 °C (aside from an initial weight loss due to physisorbed water). From the weight loss profile, the composition of the nanocomposite was found to be 28 %wt HNT and 72 %wt PHBV. The DSC analysis (Fig. 3B) shows that the polymer undergoes a glass transition at about 55 °C (see the inset) and has a relatively low melting temperature (~150 °C). These thermal properties open the way to the direct compounding [46] of inorganic fillers in a PHBV matrix, and confer also a high processability to the resulting composite. For instance, properly functionalized Halloysite can be mixed directly with molten PHBV and extruded to form a self-standing scaffold.

In order to simulate the behavior and fate of an implant based on this composite, HNT-Sr-PHBV coupled on glass surface were exposed to para-physiological conditions (PBS buffer, 37 °C) and analyzed by means of electron and atomic force microscopy to monitor the morphological and mechanical evolution, as well as their adhesion properties. Fig. 2B reports the AFM topography of HNT-Sr-PHBV nanocomposite after 4 days of degradation. The surface displays a large number of voids resulting from the PHBV degradation. Insights on the mechanism can be inferred from the analysis of the inset in Fig. 2B (as well as from Figs. SI-6) and from the evolution of the polymer surface roughness with time (Fig. SI-7) that shows a random trend. The presence of irregularly shaped voids and semi-detached polymer fragments in their proximity indicates that the polymer degrades through a random bulk hydrolysis [47]. After 28 days of degradation the inorganic scaffold is exposed to the environment, as evident from the significant number of HNT tubules visible in the SEM image (Fig. 2C).

The amount of Sr(II) dispersed in the medium was evaluated by means of ICP-AES. Fig. 4 shows that more that 60% of the initially loaded Sr(II) is retained after 28 days of degradation: results demonstrate that the HNTs are able to retain a consistent amount of Sr(II) over time. In details, about 70% of the strontium uploaded is still available after one week, suggesting that its bioactivity lasts long enough to allow the local regeneration of bone tissue. Furthermore, the presence of PHBV does not affect the release of strontium, simply modulating the exposure of HNTs to the surrounding medium. This is consistent with a strong interaction between Sr(II) and HNT, much stronger than that between Sr(II) and PHBV. As a result, the release of Sr(II) to the environment is regulated by its affinity towards HNTs. Finally, the small amount of strontium released also minimizes the toxicity concerns.

The *in vitro* HNT biocompatibility was assessed by a direct contact method using mouse fibroblasts cell line (L929), previously employed to evaluate carbon nanotube cytotoxicity [48,49]. The cell viability after incubation in the presence of HNT, HNT–PHBV, HNT-Sr and HNT-Sr-PHBV was measured by evaluation of functional state of mitochondria (MTT assay) and cellular membrane integrity (Trypan Blue assay). Moreover the proliferative capacity

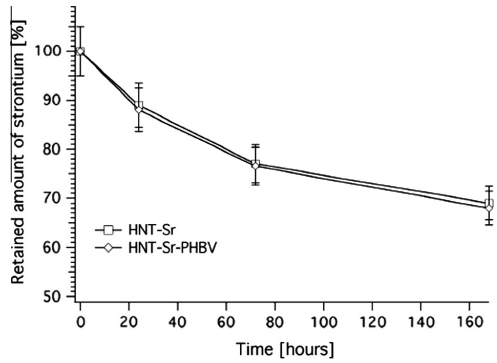

Fig. 4. Retained amount of strontium over time in para-physiological conditions in the case of HNTs and HNT–PHBV composite.

of the cells exposed to HNT was evaluated by incorporation of BrdU during cell replication. All these cell culture methods are highly reproducible, quantitative, and they have been already employed to assess the biocompatibility of diverse nanostructures [50–52] and polymeric materials [53].

Fig. 5 summarizes cytotoxicity data. MTT test was performed after 72 h of exposure at different composite concentrations (25, 50 and 100 μg/mL, Fig. 5a). To highlight the specific effect of Sr(II) concentration on cytotoxicity, results are also given as a function of the cation concentration in each sample (Fig. 5b). All samples exhibited cell growth inhibition in a concentration dependent manner. The cell viability was preserved (ca. 70% of cells survived) up to composite concentration of 100 μg/mL for HNT and for the composites HNT–PHBV and HNT-Sr-PHBV. For the HNT-Sr sample there is a clear decrease in cell viability (only 30% of cells survived at 100 μg/mL).

The toxicity data obtained by Trypan blue tests (Fig. 6) confirmed the MTT results. These data show that cell viability after 72 h of exposure is maintained at >80% for HNT, HNT–PHBV and for HNT-Sr-PHBV at all Sr(II) concentrations studied, indicating high biocompatibility of Halloysite nanotubes and PHBV, up to 100 μg/mL. However, the "naked" HNT-Sr induces a significant vitality reduction already at 25 μg/mL, suggesting the need for a barrier to modulate its interaction with cells.

The effectiveness of a biocompatible scaffold is also related to its ability to not lessen the normal cellular proliferative capacity. The cell proliferation of L929 fibroblasts after 48 h of incubation with different suspensions is reported in Fig. 7 as the percentage with respect to the culture medium. The data show that cell

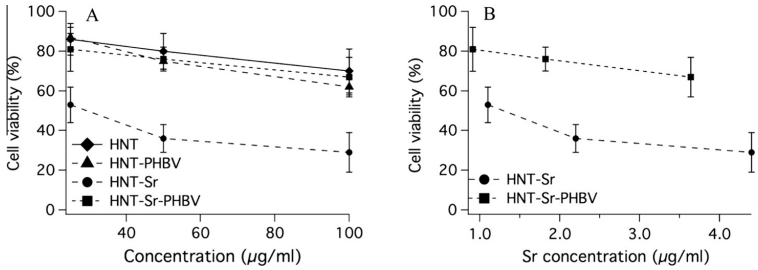

Fig. 5. Comparative cytotoxicity of HNT, HNT-Sr, HNT–PHBV and HNT-Sr-PHBV obtained with MTT assay, after exposure of L929 cells for 72 h. The percentage of cell viability was calculated versus control medium without composites (taken as 100%). Results are given as a function of (A) composite concentration; (B) Sr concentration.

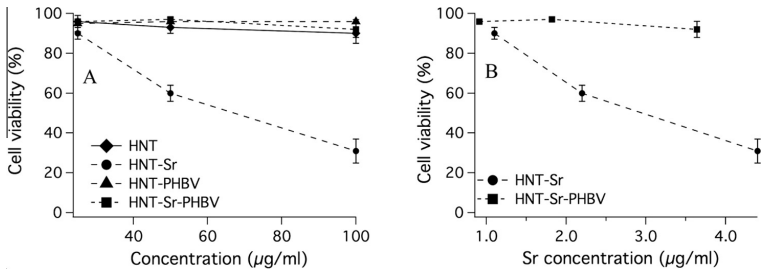

Fig. 6. Comparative cytotoxicity of HNT, HNT-Sr, HNT–PHBV and HNT-Sr-PHBV obtained with Trypan blue assay, after exposure of L929 cells for 72 h. The number of viable cells was calculated as percentage of total cells for each sample. Results are given as a function of (A) composite concentration; (B) Sr concentration.

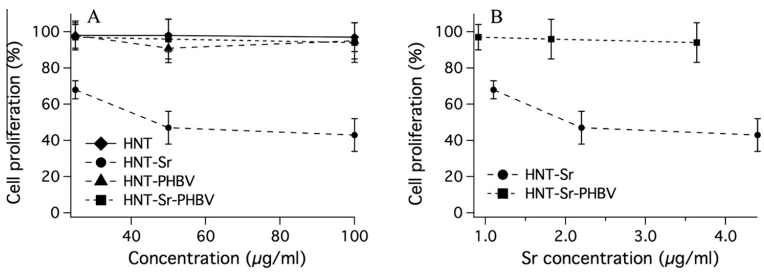

Fig. 7. Comparative DNA synthesis measured as BrdU incorporation in L929 cells incubated with HNT, HNT-Sr, HNT–PHBV and HNT-Sr-PHBV for 48 h. The percentage of cell proliferation was calculated versus control medium without composites (taken as 100%). Results are given as a function of (A) composite concentration; (B) Sr concentration.

proliferation in the presence of HNT, HNT–PHBV and HNT-Sr-PHBV is similar to control samples, while HNT-Sr induces a significant reduction at all analyzed concentrations. These data suggest that HNT and PHBV are well tolerated by L929 mouse fibroblasts, while the Sr contained in HNT showed a toxic effect on cells viability and growth due to their direct exposition to the cation. The coating of PHBV produces a biocompatible environment for the cells, even when high concentrations of strontium are present within the composite. The biocompatible surface of PHBV thus acts as a tunable barrier for the interaction between fibroblasts and Sr-loaded HNT.

4. Conclusions

This paper reports on a biocompatible hybrid nanocomposite consisting of Sr(II)-loaded Halloysite nanotubes embedded within a biopolymer (PHBV) matrix. The nanotubular morphology of HNTs provides an inorganic scaffold with well-suited mechanical properties for bone replacement, especially in terms of lightness (hollow fiber) and high compressive strength. Thanks to the ability of Halloysites to upload and dynamically exchange cations [26], we prepared for the first time a HNT–PHBV composite capable of effectively uploading and carrying high doses of Sr(II). The biopolymer embeds the inorganic scaffold, allowing for the progressive exposure of the nanotubes to the physiological environment, and the modulation of Sr(II) bioavailability. In our design, the bioactive role of Sr(II) [12,14] could be fully exploited at the local level, as it is significantly retained on the scaffold during the first month of exposure to phosphate buffer, thus avoiding the collateral effects associated with Sr(II) systemic administration [19]. The thermal characteristics of our composite make it easily processable and envisage its use in several treatments of bone defects or diseases. For example, it could be applied as a filmable coating to enhance the bone regeneration capacity of synthetic bone grafts or it could be fabricated as a self-standing biomaterial. The chemical composition of HNT is identical to the widely adopted and biologically

well-tolerated kaolin, introducing a significant advantage over other fibrous nanostructures. For instance, carbon nanotubes display comparable mechanical properties, but their use is not recommended due to toxicity issues [50]. The fabrication method described here to obtain the nanocomposite is highly versatile, and it could address different biomedical and physico-chemical needs. In particular, the amount of uploaded Sr(II) could be easily adjusted by varying the surface functionalization of HNT; the time before the bioactive inorganic scaffold is exposed to the physiological environment could be finely tuned by the thickness of the PHBV coating; the biopolymer matrix could also be used as a carrier for biochemical signals and drugs, opening the possibility to the design of multi-functional nanocomposite biomaterials.

Acknowledgments

Stefano Spezzani (Imerys Tiles Minerals Italia s.r.l.) for kindly providing HNT samples, CSGI for funding this research, and Professor Helmuth Moehwald for the stimulating discussions are gratefully acknowledged.

Appendix A. Supplementary material

Supplementary data associated with this article can be found, in the online version, at http://dx.doi.org/10.1016/j.jcis.2015.02.043.

References

[1] V. Guarino, A. Gloria, M.G. Raucci, R. De Santis, L. Ambrosio, Int. Mater. Rev. 57 (2012) 256–275, http://dx.doi.org/10.1179/0950660812Z.00000000021.
[2] P. Fratzl, J. R. Soc. Interface 4 (2007) 637–642, http://dx.doi.org/10.1098/rsif.2007.0218.
[3] A.R. Amini, C.T. Laurencin, S.P. Nukavarapu, CRC Crit. Rev. Bioeng. 40 (2012) 363–408, http://dx.doi.org/10.1615/CritRevBiomedEng.v40.i5.10.
[4] S.J. Hollister, Nat. Mater. 4 (2005) 518–524, http://dx.doi.org/10.1038/nmat1683.
[5] D.C. Greenspan, Curr. Opin. Solid State Mater. Sci. 4 (1999) 389–393, http://dx.doi.org/10.1016/S1359-0286(99)00021-2.
[6] I.D. Xynos, M.V.J. Hukkanen, J.J. Batten, L.D. Buttery, L.L. Hench, J.M. Polak, Calcif. Tissue Int. 67 (2000) 321–329, http://dx.doi.org/10.1007/s002230001134.
[7] J.H. Shepherd, D.V. Shepherd, S.M. Best, J. Mater. Sci.: Mater. Med. 23 (2012) 2335–2347, http://dx.doi.org/10.1007/s10856-012-4598-.
[8] S. Fu, X. Wang, G. Guo, S. Shi, H. Liang, F. Luo, Y. Wei, Z. Qian, J. Phys. Chem. C 114 (2010) 18372–18378, http://dx.doi.org/10.1021/jp106488t.
[9] W.R. Moore, S.E. Graves, G.I. Bain, Aust. N. Z. J. Surg. 71 (2001) 354–361, http://dx.doi.org/10.1046/j.1440-1622.2001.02128.x.
[10] R.E. McMahon, L. Wang, R. Skoracki, A.B. Mathur, J. Biomed. Mater. Res., Part B 101B (2013) 387–397, http://dx.doi.org/10.1002/jbm.b.32823.
[11] F. Peng, M.T. Shaw, J.R. Olson, M. Wei, J. Phys. Chem. C 115 (2011) 15743–15751, http://dx.doi.org/10.1021/jp201384q.
[12] E. Gentleman, Y.C. Fredholm, G. Jell, N. Lotfibakhshaiesh, M.D. O'Donnell, R.G. Hill, M.M. Stevens, Biomaterials 31 (2010) 3949–3956, http://dx.doi.org/10.1016/j.biomaterials.2010.01.121.
[13] P.J. Marie, Osteoporosis Int. 14 (2003) 9–12, http://dx.doi.org/10.1007/s00198-002-1344-5.
[14] P.J. Marie, Curr. Opin. Pharmacol. 5 (2005) 633–636, http://dx.doi.org/10.1016/j.coph.2005.05.005.
[15] S. O'Donnell, A. Cranney, G. Wells, J. Adachi, J. Reginster, Cochrane Library (2006) 4, http://dx.doi.org/10.1002/14651858.CD005326.pub3.
[16] E. Bonnelye, A. Chabadel, F. Saltel, P. Jurdic, Bone 42 (2008) 129–138, http://dx.doi.org/10.1016/j.bone.2007.08.043.
[17] P.J. Meunier, C. Roux, E. Seeman, S. Ortolani, J.E. Badurski, T.D. Spector, J. Cannata, A. Balogh, E.-M. Lemmel, S. Pors-Nielsen, et al., N. Engl. J. Med. 350 (2004) 459–468, http://dx.doi.org/10.1056/NEJMoa022436.
[18] W.E. Cabrera, I. Schrooten, M.E. De Broe, P.C. D'Haese, J. Bone Miner. Res. 14 (1999) 661–668, http://dx.doi.org/10.1359/jbmr.1999.14.5.661.
[19] European medicines agency – news and events – recommendation to restrict the use of Protelos/Osseor (strontium ranelate). <http://www.ema.europa.eu/ema/index.jsp?curl=pages/news_and_events/news/2013/04/news_detail_001774.jsp&mid=WC0b01ac058004d5c1> (accessed March, 2015).
[20] E. Joussein, S. Petit, J. Churchman, B. Theng, D. Righi, B. Delvaux, Clay Miner. 40 (2005) 383–426, http://dx.doi.org/10.1180/0009855054040180.
[21] V. Vergaro, Y.M. Lvov, S. Leporatti, Macromol. Biosci. 12 (2012) 1265–1271, http://dx.doi.org/10.1002/mabi.201200121.
[22] N.G. Veerabadran, R.R. Price, Y.M. Lvov, Nano 2 (2007) 115–120, http://dx.doi.org/10.1142/S1793292007000441.
[23] S.A. Konnova, I.R. Sharipova, T.A. Demina, Y.N. Osin, D.R. Yarullina, O.N. Ilinskaya, Y.M. Lvov, R.F. Fakhrullin, Chem. Commun. 49 (2013) 4208, http://dx.doi.org/10.1039/C2CC38254G.
[24] V. Vergaro, E. Abdullayev, Y.M. Lvov, A. Zeitoun, R. Cingolani, R. Rinaldi, S. Leporatti, Biomacromolecules 11 (2010) 820–826, http://dx.doi.org/10.1021/bm9014446.
[25] C.A. Poland, R. Duffin, I. Kinloch, A. Maynard, W.A.H. Wallace, A. Seaton, V. Stone, S. Brown, W. MacNee, K. Donaldson, Nat. Nanotechnol. 3 (2008) 423–428, http://dx.doi.org/10.1038/nnano.2008.111.
[26] D. Carroll, Geol. Soc. Am. Bull. 70 (1959) 749, http://dx.doi.org/10.1130/0016-7606(1959) 70[749:IEICAO]2.0.CO;2.
[27] W.Y. Zhou, B. Guo, M. Liu, R. Liao, A.B.M. Rabie, D. Jia, J. Biomed. Mater. Res., Part A 93A (2010) 1574–1587, http://dx.doi.org/10.1002/jbm.a.32656.
[28] A.P. Bonartsev, V.L. Myshkina, D.A. Nikolaeva, E.K. Furina, T.A. Makhina, V.A. Livshits, A.P. Boskhomdzhiev, E.A. Ivanov, A.L. Iordanskii, G.A. Bonartseva, in: A. Méndez-Vilas (Ed.), Communicating Current Research and Educational Topics and Trends in Applied Microbiology, Formatex, Badajoz, Spain, 2007, pp. 295.
[29] N. Sultana, T.H. Khan, J. Nanomater. 2012 (2012) 1–12, http://dx.doi.org/10.1155/2012/190950.
[30] X.-T. Li, Y. Zhang, G.-Q. Chen, Biomaterials 29 (2008) 3720–3728, http://dx.doi.org/10.1016/j.biomaterials.2008.06.004.
[31] R. Dulbecco, M. Vogt, J. Exp. Med. 99 (1954) 167–182, http://dx.doi.org/10.1084/jem.99.2.167.
[32] M. Abdelmouleh, S. Boufi, A. ben Salah, M.N. Belgacem, A. Gandini, Langmuir 18 (2002) 3203–3208, http://dx.doi.org/10.1021/la011657.
[33] D. Wanna, C. Alam, D.M. Toivola, P. Alam, Adv. Nat. Sci.: Nanosci. Nanotechnol. 4 (2013) 045002, http://dx.doi.org/10.1088/2043-6262/4/4/045002.
[34] J.P. Santerre, L. Shajii, B.W. Leung, Rev. Oral Biol. Med. 12 (2001) 136–151, http://dx.doi.org/10.1177/10454411010120020401.
[35] E.P. Barrett, L.G. Joyner, P.P. Halenda, J. Am. Chem. Soc. 73 (1951) 373–380, http://dx.doi.org/10.1021/ja01145a126.
[36] R.D. White, D.V. Bavykin, F.C. Walsh, Nanotechnology 23 (2012) 065705, http://dx.doi.org/10.1088/0957-4484/23/6/065705.
[37] M.-A. Neouze, U. Schubert, Monatsh. Chem. 139 (2008) 183–195, http://dx.doi.org/10.1007/s00706-007-0775-2.
[38] B. Tang, B. Tang, Cheang, S. Wang, Xu Pro, Int. J. Nanomed. (2012), http://dx.doi.org/10.2147/IJN.S28267. 1061.
[39] V.K.S. Hsiao, J.R. Waldeisen, Y. Zheng, P.F. Lloyd, T.J. Bunning, T.J. Huang, J. Mater. Chem. 17 (2007) 4896, http://dx.doi.org/10.1039/b711200a.
[40] Surface and Thin Film Analysis: Principles, Instrumentation, Applications, in: H. Bubert, H. Jenett (Eds.), Wiley-VCH: Weinheim, Germany, 2002.
[41] I. Natali, P. Tempesti, E. Carretti, M. Potenza, S. Sansoni, P. Baglioni, L. Dei, Langmuir 30 (2014) 660–668, http://dx.doi.org/10.1021/la404085v.
[42] B. Lecouvet, J. Horion, C. D'Haese, C. Bailly, B. Nysten, Nanotechnology 24 (2013) 105704, http://dx.doi.org/10.1088/0957-4484/24/10/105704.
[43] N. Saito, Y. Usui, K. Aoki, N. Narita, M. Shimizu, N. Ogiwara, K. Nakamura, N. Ishigaki, H. Kato, S. Taruta, et al., Curr. Med. Chem. 15 (2008) 523–527, http://dx.doi.org/10.2174/092986708783503140.
[44] S. Polizu, O. Savadogo, P. Poulin, L. Yahia, J. Nanosci. Nanotechnol. 6 (2006) 1883–1904, http://dx.doi.org/10.1166/jnn.2006.197.
[45] M.-F. Yu, O. Lourie, M.J. Dyer, K. Moloni, T.F. Kelly, R.S. Ruoff, Science 287 (2000) 637–640, http://dx.doi.org/10.1126/science.287.5453.637.
[46] F. Ridi, M. Bonini, P. Baglioni, Adv. Colloid Interface Sci. 207 (2013) 3–13, http://dx.doi.org/10.1016/j.cis.2013.09.006.
[47] A. Göpferich, Biomaterials 17 (1996) 103–114, http://dx.doi.org/10.1016/0142-9612(96)85755-3.
[48] G. Gonçalves, M.-T. Portolés, C. Ramírez-Santillán, M. Vallet-Regí, A.P. Serro, J. Grácio, P.A.A.P. Marques, J. Mater. Sci.: Mater. Med. 24 (2013) 2787–2796, http://dx.doi.org/10.1007/s10856-013-5030-.
[49] Z.X. Meng, W. Zheng, M.H. Ding, H.M. Zhou, X.Q. Chen, J.C. Chen, M.K. Liu, Y.F. Zheng, J. Nanosci. Nanotechnol. 11 (2011) 3126–3133, http://dx.doi.org/10.1166/jnn.2011.3761.
[50] S. Lanone, F. Rogerieux, J. Geys, A. Dupont, E. Maillot-Marechal, J. Boczkowski, G. Lacroix, P. Hoet, Part. Fibre Toxicol. 6 (2009) 14, http://dx.doi.org/10.1186/1743-8977-6-14.
[51] T. Coccini, L. Manzo, E. Roda, ISRN Toxicol. 2013 (2013) 1–13, http://dx.doi.org/10.1155/2013/825427.
[52] V. Thomas, B.A. Halloran, N. Ambalavanan, S.A. Catledge, Y.K. Vohra, Acta Biomater. 8 (2012) 1939–1947, http://dx.doi.org/10.1016/j.actbio.2012.01.033.
[53] E. Briganti, P. Losi, A. Raffi, M. Scoccianti, A. Munaò, G. Soldani, J. Mater. Sci.: Mater. Med. 17 (2006) 259–266, http://dx.doi.org/10.1007/s10856-006-7312-4.

Supplementary Material

Design and characterization of a composite material based on Sr(II)-loaded clay nanotubes included within a biopolymer matrix

Stefano Del Buffa [a,b], *Massimo Bonini* [a,b], *Francesca Ridi*[a,b], *Mirko Severi*[a], *Paola Losi*[c], *Silvia Volpi*[c], *Tamer Al Kayal*[c], *Giorgio Soldani*[c] *and Piero Baglioni*[a,b]*

[a] Department of Chemistry "Ugo Schiff", University of Florence, via della Lastruccia 3, Sesto Fiorentino, 50019 Florence, Italy.

[b] CSGI Consortium, via della Lastruccia 3, Sesto Fiorentino, 50019 Florence, Italy

[c] Laboratory of Biomaterials & Graft Technology, Institute of Clinical Physiology, National Research Council, Via Aurelia Sud, 54100 Massa, Italy

*corresponding author: Piero Baglioni. Fax: +39 0554573032 ; Tel: +39 0554573033; E-mail: piero.baglioni@unifi.it

Content. Rietveld analysis of XRD spectrum of HNT, Surface area and pore volume analysis of HNT, FT-IR and dispersion stability of functionalized HNT, nanoindentation tests, morphology, surface roughness evolution during degradation, details about cell cultures.

Rietveld analysis of XRD spectrum of HNT

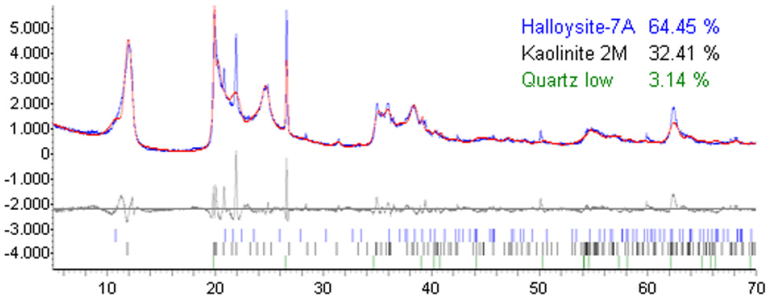

Figure SI-1. Rietveld analysis of the XRD spectrum of HNT, together with the relative abundances of Halloysite, Kaolinite and Quartz.

Surface area and pore volume analysis of HNT

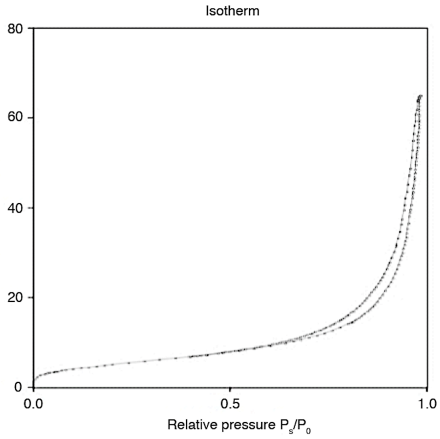

Pore Dia. Range(nm)	Pore Volume (ml/g)	%
Under 6	0.00630	3.45
6 - 8	0.00326	1.78
8 - 10	0.00326	1.79
10 - 12	0.00401	2.19
12 - 16	0.00671	3.67
16 - 20	0.00844	4.62
20 - 80	0.07260	39.72
Over 80	0.07821	42.79
BJH Total	0.18279	100.00

Figure SI2. Adsorption isotherm and pore size distribution obtained with BJH calculation of a HNT sample.

FT-IR and stability of functionalized HNT

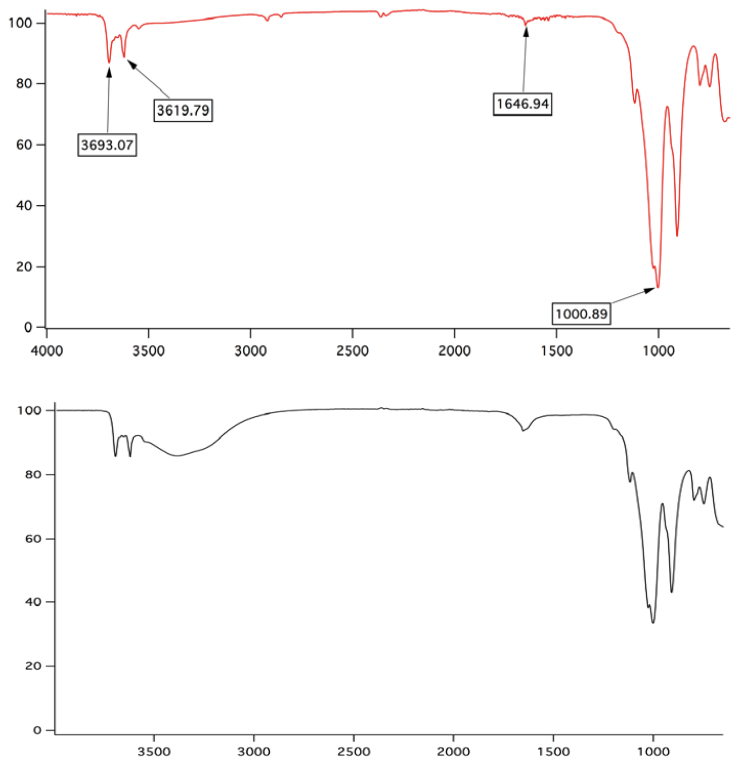

Figure SI-3. ATR-FTIR spectra of halloysite (top) and APTES-functionalized HNT (bottom). The successful functionalization is demonstrated by the broad absorption band around 3300 cm^{-1} corresponding to N-H stretching.

Figure SI-4. Halloysite water dispersion (left) and APTES-functionalized HNT water dispersion (right), clearly showing the improved dispersibility of the latter.

Nanoindentation tests

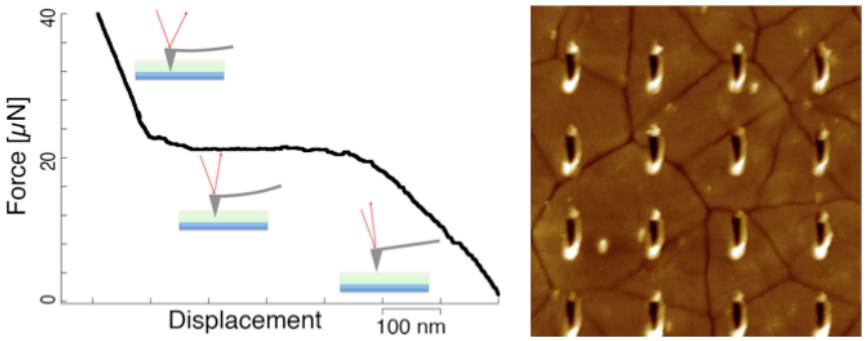

Figure SI-5. Left: Representative force versus displacement curve obtained during the nanoindentation test of a nanocomposite sample Right: AFM image of the indented sample.

Morphology

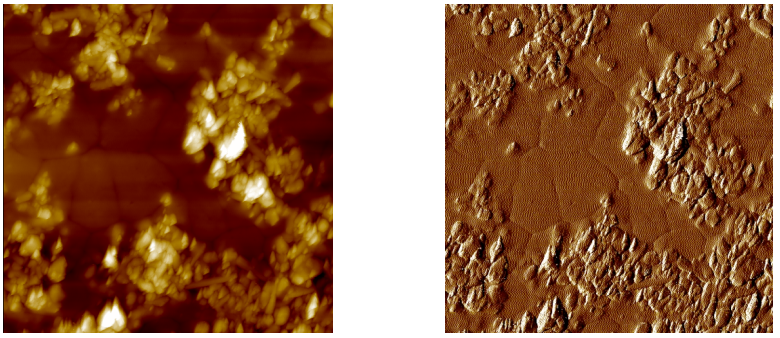

Figure SI-6. AFM topography (left) and phase analysis image (right) of HNT-PHBV nanocomposite after 24 hours of degradation in PBS at 37 °C. (Z-range=500 nm, scan size=20 μm^2)

Surface roughness evolution during degradation

Surface roughness is a measure of the texture of a surface and it is quantified by the root mean square (RMS) vertical deviations of a real surface from its ideal form (i.e. average value). Apart from the nonlinear RMS trend that is consistent with a random bulk hydrolysis mechanism of the polymer, the decrease in RMS roughness within the first 24 hours of degradation, can be taken as a qualitative assessment of the swelling capacity of PHBV.

Figure SI-7. RMS roughness evolution with time for PHBV film spin coated onto APTES-functionalized glass substrate.

Details about cell cultures.

Mouse fibroblasts (L929) from Interlab Cell Line Collection (ICLC ATL 95001) were cultured in RPMI supplemented with 10% FBS, 2 mM L-Glutamine, 100 µg/mL streptomycin and 100 U/mL penicillin. Cells were subcultured when at confluence (split ratio 1:3) by trypsinization (0.5% trypsin/0.02% EDTA). The cell cultures were kept at 37°C in a humidified atmosphere of 5% CO_2 in air. The medium was changed every three days and cell viability was routinely checked by vital staining with Trypan blue. Each experiment was performed on cells that demonstrated viability rates >95%. Culture media were supplied by BioWhittaker Europe, sera and all culture reagents were from Sigma Aldrich. Cell line was obtained from National Institute for Cancer Research of Genoa, Italy.

J Nanopart Res (2015) 17:146
DOI 10.1007/s11051-015-2947-z

RESEARCH PAPER

The effect of charge on the release kinetics from polysaccharide–nanoclay composites

Stefano Del Buffa · Emanuele Grifoni · Francesca Ridi · Piero Baglioni

Received: 31 October 2014 / Accepted: 4 March 2015 / Published online: 17 March 2015

Abstract The objective of this study was to integrate inorganic halloysite nanotubes (HNT) with chitosan and hyaluronic acid to obtain hybrid nanocomposites with opposing charges and to investigate their potential in the controlled release of drug model probes. Two oppositely charged polysaccharides, chitosan and hyaluronic acid, were selected for their biocompatibility and their importance in biomedical applications. The high surface area and the hollow nanometric-sized lumen of HNT allowed for the efficient loading of rhodamine 110 and carboxyfluorescein, used as models for oppositely charged drugs. In the case of chitosan, the preparation of the nanocomposite was carried out exploiting the electrostatic interaction between the polymer and HNT in water, while with hyaluronic acid, a covalent functionalization strategy was employed to couple the polymer with the clay. Nanocomposites were characterized with thermal, microscopic, and spectroscopic techniques, and the release kinetics of the model compounds was assessed by fluorescence measurements. The release curves were fitted with a model able to account for the desorption process from the external and the internal halloysite surfaces. The results show that both polymeric coatings alter the release of the probes, indicating a key role of both charge and coating composition on the initial and final amount of released dye, as well as on the rate of the desorption process.

Keywords Release kinetics · Nanocomposites · Halloysite · Chitosan · Hyaluronic acid

Guest Editor: Liudmyla Rieznichenko

This article is part of the topical collection on Engineered Bioinspired Nanomaterials

Electronic supplementary material The online version of this article (doi:10.1007/s11051-015-2947-z) contains supplementary material, which is available to authorized users.

S. Del Buffa · E. Grifoni · F. Ridi · P. Baglioni (✉)
Department of Chemistry "Ugo Schiff" and CSGI, University of Florence, via della Lastruccia 3, Sesto Fiorentino, 50019 Florence, Italy
e-mail: piero.baglioni@unifi.it
URL: http://www.csgi.unifi.it

F. Ridi
e-mail: francesca.ridi@unifi.it

Introduction

Polysaccharide-based composites have been the subject of numerous studies and have been proposed as favorable materials in a wide range of technological and bio-based applications (Ghorai et al. 2013; Travan et al. 2011; Pandey et al. 2013; Kulterer et al. 2012; Shingel and Marchessault 2006; Murugan and Ramakrishna 2004; Buchtová et al. 2013; Stodolak et al. 2009; Habibi and Dufresne 2008). Biocompatibility and biodegradability of starting materials, together with their large availability in nature, are added values for composites intended to perform medical and bio-

based functions. By virtue of straightforward chemical modifications (Ortona et al. 2008), introduction of properly designed inorganic nanostructures (Duarte et al. 2012; Ruiz-Hitzky et al. 2013), or adopting different fabrication procedures (Suh et al. 2000; Calvert 2001; Liu Tsang and Bhatia 2004; Ryan et al. 2006), material properties can be tailored to meet specific needs (Fox et al. 2013; Connell et al. 2014). Among polysaccharides, chitosan and hyaluronic acid have been extensively studied and adopted in the formulation of nano-hybrid hydrogels, composites, and drug carriers (Vallés-Lluch et al. 2013; Ha et al. 2006; Berthold et al. 1996; Agnihotri et al. 2004). Hyaluronic acid is a natural polysaccharide ubiquitous in the tissues of humans and other mammalians. It is an essential component of the extracellular matrix in which its structural and biological properties mediate cellular signaling, wound repair, morphogenesis, and matrix organization (Burdick and Prestwich 2011). Hyaluronic acid and its derivatives have been used as dermal fillers (Falcone and Berg 2008), therapeutic agents (Lee et al. 2008; Roig-Roig et al. 2013), as well as potential building blocks for the creation of new biomaterials for tissue engineering and regenerative medicine (Collins and Birkinshaw 2013). Subsequently, chitosan is prepared by the *N*-deacetylation of chitin, the major constituent in the exoskeleton of arthropods, and it has been demonstrated an invaluable material in the fields of biomedical engineering (Roldo and Fatouros 2011; Jayakumar et al. 2010a, b), biotechnology (Issa et al. 2005; Kaur and Dhillon 2014), cosmetics, and medical materials (Jayakumar et al. 2010b; Baldrick 2010; Gu et al. 2013), thanks to its wound healing effect in addition to good biocompatibility and biodegradability (Mi et al. 2002; Hejazi and Amiji 2003; Kean and Thanou 2010).

Recently, chitosan was used in combination with halloysite nanotubes (HNT) (Liu et al. 2012; Khoo et al. 2012; Abdullayev and Lvov 2013; Liu et al. 2013; Bai et al. 2014; Liu et al. 2014) while, to date, few studies have been concerned with halloysite–hyaluronic acid nanocomposites (Deen and Zhitomirsky 2014). HNTs are natural aluminosilicates with tubular morphology that show intriguing properties, thanks to their unique structure and composition (Joussein et al. 2005). HNT are generally well tolerated by cells (Vergaro et al. 2010; Verma et al. 2012; Zhao et al. 2013) and have the quality to expose two differently reactive surfaces (inner Al–OH and outer Si–OH, Fig. 1) to the environment, thus paving the way to a whole range of asymmetric functionalization strategies (Yuan et al. 2008; Chao et al. 2013; Marney et al. 2012; Massaro et al. 2014; Arcudi et al. 2014). The presence of a hollow lumen with nanometric size suggests the use of HNT as nanoreactors, nanotemplates, or sorbents for contaminants (Du et al. 2010), and HNT may also be exploited for the loading and release of chemicals and drugs (Price et al. 2001; Ward et al. 2010; Shchukin and Möhwald 2011). The use of organic hybrid composites is continuously increasing in the field of nanomedicine, and combining HNT with biocompatible polymers may result in the fabrication of novel and promising biomaterials. The objective of this study was to integrate HNT with chitosan and hyaluronic acid to obtain hybrid nanocomposites with opposing charges and to explore their potential in controlled drug release applications. HNT were loaded with two fluorescent probes commonly used as model for drugs (Chen et al. 2011; Forster et al. 2012) having similar molecular structure but opposite charges—rhodamine 110 (positively charged) and carboxyfluorescein (negatively charged) (see Fig. 1). By fitting the experimental release data with a recently developed mechanistic model, the effect of the probe–composite electrostatic interaction on the release process was elucidated, and general conclusions on the release of charged probes from halloysite-based polymeric nanocomposites were determined.

Materials and methods

Materials

Chitosan powder (deacetylation $\geq$ 75 %; viscosity at 1 wt% in 1 % acetic acid at 25 °C = 800–2000 cps), (3-aminopropyl)trimethoxysilane (APTMS, purity $\geq$ 97 %), rhodamine 110 chloride (Rho110, purity $\geq$ 99 %), 5(6)-carboxyfluorescein (CF, purity $\geq$ 95 %), *N*-(3-dimethylaminopropyl)-*N*′-ethylcarbodiimide hydrochloride (EDC, commercial grade), 2-(*N*-morpholino) ethanesulfonic acid monohydrate (MES, purity $\geq$ 99.5 %), *N*-hydroxysulfosuccinimide sodium salt (sulfo-NHS, purity $\geq$ 98 %), ethanol (puriss. p.a. grade), ammonium hydroxide (28.0–30.0 NH_3 basis), acetic acid (purity $\geq$ 99.7 %), and toluene (anhydrous, purity = 99.8 %) were purchased

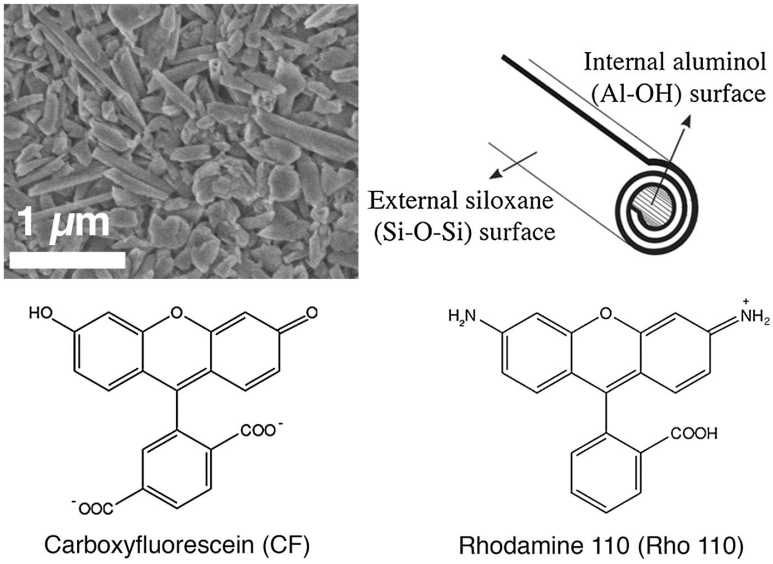

Fig. 1 Scanning electron microscopy image of a HNT sample (*upper left*), schematic representation of HNT structure (*upper right*), and molecular structure of carboxyfluorescein and rhodamine 110 (*bottom*)

from Sigma Aldrich (Milan, Italy) and used as received. Sodium hyaluronan (average MW = 80–100 kDa, intrinsic viscosity at 25 °C = 0.18–0.28 $m^3\ kg^{-1}$) was purchased from Altergon Italia srl (Avellino, Italy) and used without further purification. Halloysite powder was provided by Imerys Minerals Ltd (Auckland, New Zealand) and purified prior to use according to a procedure reported in the literature (Shchukin et al. 2005). (3-glycidoxypropyl)trimethoxysilane (GPTMS) was purchased by abcr GmbH & Co. KG (Karlsruhe, Germany) and used as received. Phosphate-buffered saline (PBS) solution was prepared in accordance to Dulbecco's formulation (Dulbecco and Vogt 1954). NaCl and KCl were purchased from Sigma Aldrich (Milan, Italy), and $Na_2HPO_4{\cdot}2H_2O$ and KH_2PO_4 were purchased from Merck (Darmstadt, Germany). The characterization of the halloysite sample (surface area, porosity, infrared spectrum, and thermogravimetry) was performed, and the data are supplied as supplementary material.

Methods

ATR-FTIR measurements were performed on a Nexus 870 spectrometer (Nicolet, Madison, WI, USA), equipped with a liquid N_2-cooled mercury cadmium telluride (MCT) detector (650–4000 cm^{-1} range, resolution 2 cm^{-1}). Thermogravimetric analysis (TGA) was conducted on a SDT Q600 (TA Instruments, Philadelphia, PA, USA) from ~25 to 1000 °C at 10 °C/min. Morphological characterization was conducted by means of scanning electron microscopy (ΣIGMA Field Emission SEM, Carl Zeiss Microscopy GmbH, Germany) and transmission electron microscopy (TEM—CM12 Philips, Eindhoven, Netherlands). Surface area and porosity of the samples were determined from N_2 adsorption isotherms with a SA 3100 analyzer (Beckmann-Coulter, Milano, Italy) utilizing BET (Brunauer et al. 1938) and BJH (Barrett et al. 1951) calculations. Zeta potential measurements were performed on a Z-PALS analyzer of Brookhaven Instruments (Holtsville, NY, USA). Elemental analysis was performed on solid samples with a CHN-S Flash E1112 analyzer (Thermo Finnigan, Milano, Italy). Fluorescence was measured with a LS50B spectrofluorimeter (Perkin Elmer, Italy) equipped with a Xe lamp and LC-240 FL detector, using QS cells with 1 cm path length (Hellma GmbH & Co. KG, Mulheim, Germany). Fluorescence was evaluated at 519 nm in the case of rhodamine 110 (λ_{exc} = 480 nm) and at 514 nm in the case of carboxyfluorescein (λ_{exc} = 460 nm).

Loading of fluorescent compounds

The loading of the fluorescent compounds was achieved by suspending halloysite powder (1 wt%)

in 10 mg/l solutions of Rho110 or CF. These suspensions were placed under vacuum and under agitation so the solutions were forced to enter the nanometric cavity. The release of bubbles into the solution due to the leakage of air contained in the lumen of the nanotubes was a clear evidence of the insertion of solution inside the tubules. After 30 min, the solid material was recovered by centrifugation (10 min at 12,500 *g*) and dried. The amount of dye retained by HNT was determined by the difference in the sample fluorescence before and after the loading procedure. In particular, HNT initially retained approximately 0.7 μg of CF and approximately 0.6 μg of Rho110 per mg of HNT. Loaded HNTs were then used as the starting material for the preparation of the nanocomposites to be used in the release tests. In the case of the hyaluronan-based composites, the fluorescent dyes were loaded onto HNT silanized with APTMES, following the same procedure.

Preparation of the composites

HNT/chitosan nanocomposites (HNT–C) were prepared by exploiting the electrostatic attraction force between the negatively charged HNT external surface and the positively charged polymer. 1 wt% of HNT and 1 wt% of chitosan were dispersed in Milli-Q water under vigorous agitation. After addition of acetic acid (to pH 5), a viscous, homogenous suspension was obtained. The suspension was centrifuged at 12,500 *g* for 10 min to precipitate the composites and remove excess chitosan not physisorbed on the HNT surface. The amount of physisorbed polysaccharide did not change significantly by varying mixing time and decreasing the pH of the suspension. HNT/hyaluronan nanocomposites (HNT–H) were prepared by covalent interaction between the inorganic and organic components, because the electrostatic repulsions prevent their direct interaction in aqueous medium. HNT surfaces were first functionalized with APTMS by mixing silane with 2 wt% HNT dispersion in ethanol and adding of NH_4OH to obtain a pH of 9. The amount of APTMS was chosen to obtain a specific value for the surface area coverage of HNT (50 % of total BET surface area, see supplementary material) by taking into account a silane cross section of 0.5 nm^2 (Abdelmouleh et al. 2002). The HNT silanization was verified by means of elemental analysis and spectroscopic measurements (supplementary material). Meanwhile, hyaluronic acid was dissolved in MES buffer (1 wt%, pH 6) with stoichiometric amounts of EDC and sulfo-NHS, and kept under agitation for 30 min. After introduction of PBS solution (pH 7.4), 250 mg of silanized halloysite was added and kept under agitation for 4 h. The solid was recovered by centrifugation at 12,500 *g* for 10 min, washed with water, and freeze-dried.

Release tests

A fixed amount (10 mg) of nanocomposite material loaded with the fluorescent dyes was placed in 5 ml of Milli-Q water and kept under agitation. At specific intervals of time and up to a period of 48 h (every 30 min for the first 6 h, every hour for the following 18 h, every 4 h until 48 h), 50 μl of the solution was collected and diluted 1:4. After any withdrawal, the same amount of water was added to the sample to keep the volume constant throughout the experiment. To evaluate the concentration of the released probes, the maximum of the fluorescence intensity (at 514 nm for CF, at 519 nm for Rho110) of sample solutions is evaluated at progressive intervals of time. The concentration of each sample was extrapolated from the corresponding calibration curve (supplementary material). Weight percentage of released dye (calculated as amount of release dye over the initial amount of loaded dye) was plotted against time.

Results and discussion

Characterization of the composites

Figure 2a shows the FTIR spectrum of HNT-C compared to the spectra of pure chitosan and HNT in the 1300–1800 cm^{-1} spectral window (the complete spectra in the 650–4000 cm^{-1} range are reported in the supplementary material). The spectra of both the nanocomposites show peaks arising from both the inorganic and organic constituents, confirming their presence in the composite material. In particular, the spectrum of HNT–C shows a band centered at 1650 cm^{-1} whose shape is due to the overlapping of the –OH bending of water physisorbed onto the HNT (Ruiz-Hitzky and Van Meerbeek 2006) with the broad band of *N*-acetyl groups of chitosan at 1652 cm^{-1}. The band at 1560 cm^{-1} in the nanocomposite sample is a further confirmation of the presence of *N*-acetyl

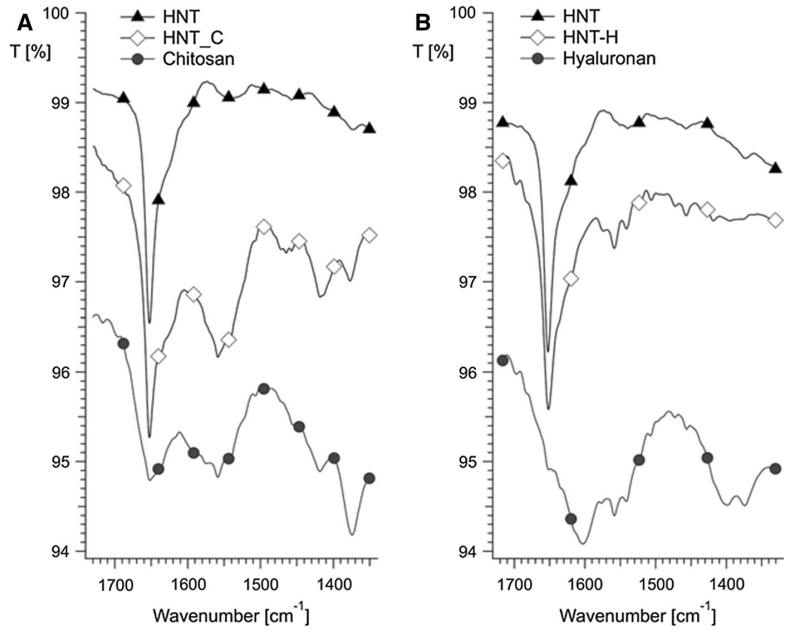

Fig. 2 FTIR spectra of (**A**) HNT-C composite and (**B**) HNT-H composite. Each plot shows also the FTIR spectrum of the correspondent polymer (chitosan and hyaluronic acid) and of pure HNT, for comparison. The curves are vertically shifted for the sake of clarity

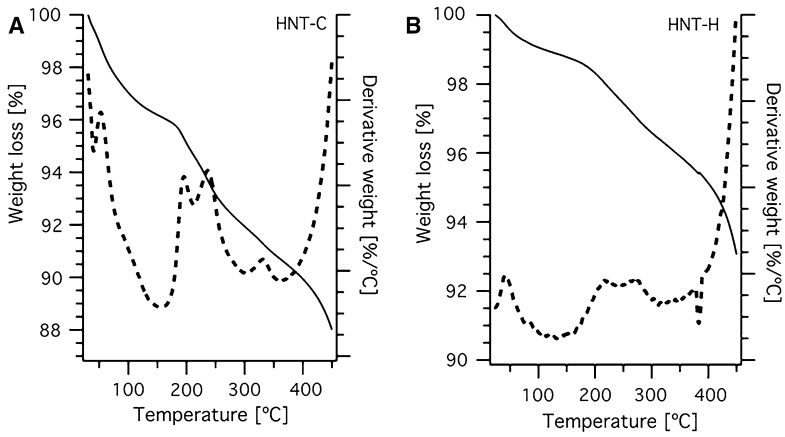

Fig. 3 Thermogravimetric and differential thermogravimetric profiles of the nanocomposites: (**A**) HNT–chitosan (HNT–C); (**B**) HNT–hyaluronan (HNT–H)

groups owing to chitosan (Sudina et al. 2012). In the FTIR spectra of HNT–H composite (reported in Fig. 2b), a peak at 1560 cm^{-1}, attributable to bending vibrations of amide N–H groups (Haxaire et al. 2003), can be observed; other characteristic peak of hyaluronan, correspondent to the C=O stretching of deprotonated carboxylic groups at 1603 cm^{-1} (Haxaire et al. 2003), appears as a shoulder in the spectra of the composite.

The thermogravimetric profile of HNT–C (Fig. 3A) shows an initial weight loss due to water physisorbed onto HNT and weakly bound to chitosan, in the temperature range of 25–150 °C, well shown in the derivative signal as a defined peak at 50 °C and a bump at 100 °C. In the range of 150–350 °C, the degradation of the organic component occurs in three stages, as clearly visible in the DTG signal, and the corresponding weight loss indicates that the polymer

is about 6 % with respect to the total weight of dry sample. At higher temperatures, HNT undergoes a structural dehydroxylation that corresponds to the loss of chemically bound water (see supplementary material). The thermogravimetric profile of HNT–H (Fig. 3B) shows a similar trend to that of HNT–C, with a few percentages of physisorbed water lost around 50 °C (see peak in the DTG profile), and the organic component, i.e., hyaluronic acid, degrading in two stages in the 150–350 °C range. In this case, the amount of organic component is about 3 % with respect to the total weight of dry sample.

TEM images (Fig. 4) give a clear indication of the presence of an organic, homogenous layer (indicated by arrows in the figures) covering HNTs and clogging their extremities. The contrast in the TEM image is due to the difference in atomic numbers of the elements that constitutes the composite (mainly Al and Si for HNT and C and N for chitosan), so the polymer film can be distinguished as a lighter coating covering the tubules. Additional evidence of the interaction between the HNT and polysaccharides comes from ζ-potential measurements reported in Fig. 5.

As expected from electrostatic considerations, the HNT–C nanocomposites exhibit a positive charge (+33 ± 2 mV) in contrast to the ζ-potential of the native halloysite (−22 ± 1 mV). In the case of HNT–H nanocomposites, the ζ-potential decreased to −31 ± 2 mV, confirming that hyaluronan residues bearing negative charges are effectively linked to the inorganic surface. Chitosan and hyaluronan acid successfully imparted different charges to the surface of HNTs, thus modulating their electrostatic interactions in solution. This property could be of great interest in biomedical applications and in fields requiring selective affinity between charged interfaces.

Release kinetics

The investigation in using HNTs as a drug delivery system (Levis and Deasy 2002) and the study of the release of chemicals, especially pharmaceuticals, from halloysite and halloysite-based polymeric composites has been tackled in the recent past (Levis and Deasy 2003; Lvov et al. 2008; Ghebaur et al. 2012; Wang et al. 2014). The release kinetics of chemicals loaded into HNT has been modeled thus far using the Ritger–Peppas (Ritger and Peppas 1987a, b) or related equations (Veerabadran et al. 2007; Ward et al. 2010). Previous authors succeeded in determining kinetic descriptors of the release process and in obtaining different release profiles by optimizing experimental conditions (solvent, pH, presence of polymeric coating, reticulation of the polymeric coating). However, as pointed out in some publications, strong electrostatic interactions in the system,

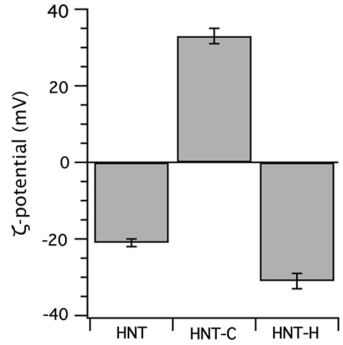

Fig. 5 ζ-potential measurements of halloysite (HNT), halloysite/chitosan nanocomposites (HNT–C), and halloysite/hyaluronan nanocomposites (HNT–H)

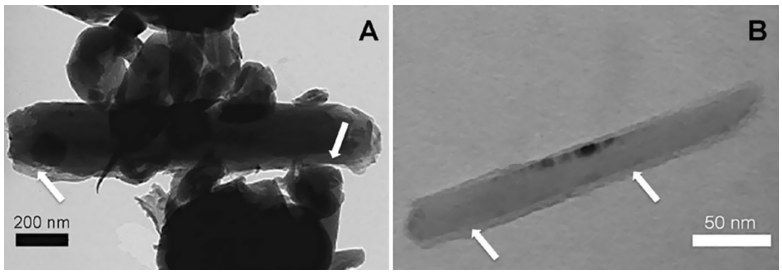

Fig. 4 TEM images of (**A**) HNT–C and (**B**) HNT–H nanocomposites

especially between the polymer coating and the halloysite load, are expected to influence the release kinetics and cause deviations from a pure Fickian diffusion. Deviations from a diffusion-controlled release may also occur due to a broad particle size distribution, as in the case of commercial grade products. Recently, a new mechanistic model was proposed for the description of 5-amino salicylic acid released from halloysite (Aguzzi et al. 2013). This model is based on the adsorption–desorption equilibrium between the drug and HNT and comprised two interface processes: (a) the desorption of the drug adsorbed on the external halloysite surface and/or inter-particle spaces and (b) the desorption of the drug molecules adsorbed into the tubular cavities of HNT. The release profiles obtained in this work were fitted with an equation derived from this model. In particular, the release model equation is:

$$y = A + 100 \cdot \frac{C_e}{C_e^{max}}(1-\exp(-(k_D t/C_e)),$$

where y represents the percentage of released dye over time (indicated with t in the equation) and A is the mass of dye (or drug) released at time zero and is associated to the amount of dye quickly released from the outer surface of halloysite. A is generally indicated (Bariana et al. 2013; Horcajada et al. 2010) as the burst release from a drug delivery system. C_e represents the equilibrium dye concentration for the slow process (desorption from the internal HNT surface) and C_e^{max} is the maximum concentration of released dye. k_D represents the specific desorption rate of the dye from the inside of HNTs.

Figures 6 and 7 report the release profiles for CF and Rho110 from chitosan- and hyaluronan-based nanocomposites, respectively. Dye release from pure halloysite is also shown for comparison. Only the first 10 h of the release profiles are shown since after this time lapse no significant variations took place and all the samples reached an equilibrium value, i.e., the maximum amount of dye released in that particular experimental condition. The kinetic parameters extracted from fitting the data to the release model equation are reported in Table 1 (chitosan-based composites) and Table 2 (hyaluronan-based composites). The analysis of the release profiles shows that the model well describes the experimental data. As seen in Fig. 6, the presence of the chitosan coating reduced the amount of dye released

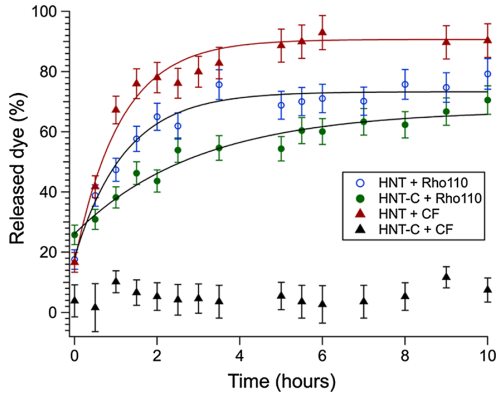

Fig. 6 Release kinetics of Rho110 and CF from HNT–C composite and from pristine HNT

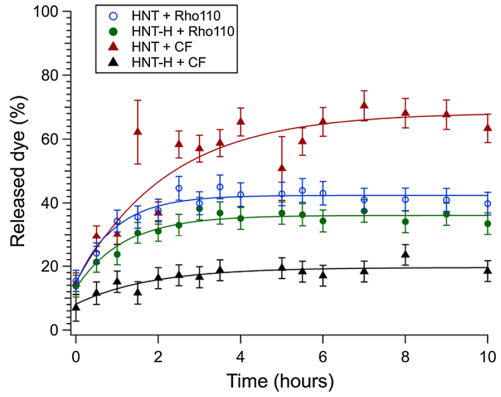

Fig. 7 Release kinetics of Rho110 and CF from HNT–H composite and from HNT-APTMES

after 10 h. The most noticeable effect is seen for the HNT–C nanocomposite loaded with CF. In this case, the negatively charged dye is almost completely retained in the composite, presumably because of favorable electrostatic interactions with the positively charged chitosan layer. Comparing this result with the release of CF from pure HNT, which shows the fastest release ($k_D = 60 \pm 8\ h^{-1}$) and the highest amount of dye release at 10 h ($C_e^{max} = 90.3$ wt%), the role of chitosan as a diffusional barrier is evident. In addition, the amount of CF quickly released from the outer HNT surface (parameter A in the model equation) is severely reduced in the presence of chitosan, going from 17 to 5 %. In the

Table 1 Parameters obtained from the fitting of the release kinetics of Rho110 and CF from HNT–C composite and from pristine HNT to the model release equation

	C_e (wt%)	C_e^{max} (wt%)	k_D (1/h)	A (wt%)	χ^2
HNT + CF	67 ± 3	90 ± 5	60 ± 8	17 ± 3	13.1
HNT–C + CF	–	–	–	–	–
HNT + Rho110	44 ± 3	79 ± 4	36 ± 6	18 ± 3	6.2
HNT–C + Rho110	29 ± 3	71 ± 4	10 ± 2	26 ± 3	6.1

χ^2 is defined as $\Sigma_i(y - y_i/\sigma_i)^2$, where y is the fitted value for a given point, y_i is the measured data value for the point, and σ_i is an estimate of the SD for y_i

Table 2 Parameters obtained from the fitting of the release kinetics of Rho110 and CF from HNT–H composites and from HNT-APTMES for the model release equation

	C_e (wt%)	C_e^{max} (wt%)	k_D (1/h)	A (wt%)	χ^2
HNT + CF	34 ± 2	63 ± 3	15 ± 3	15 ± 3	24.5
HNT–H + CF	2 ± 1	18 ± 1	2 ± 1	8 ± 3	3.7
HNT + Rho110	11 ± 1	40 ± 2	12 ± 3	15 ± 3	4.3
HNT–H + Rho110	8 ± 1	35 ± 2	13 ± 3	13 ± 3	3.7

χ^2 is defined as $\Sigma_i(y - y_i/\sigma_i)^2$, where y is the fitted value for a given point, y_i is the measured data value for the point, and σ_i is an estimate of the SD for y_i

case of the desorption of Rho110 from the HNT–C hybrid, the initial burst release from the outer surface is observed to be higher than that of the pristine HNT sample, while the desorption rate associated with the release process from the inner part ($k_D = 10 \pm 2\ h^{-1}$) is reduced with respect to the value found for the pure HNT clays ($k_D = 36 \pm 6\ h^{-1}$). However, the amount of Rho110 released after 10 h does not seem to be significantly altered by the presence of the chitosan coating. The behavior of the HNT–C/Rho110 system can be rationalized by taking into account the fact that the polymeric coating and the model drug have the same electrostatic charge. This implies that immediately after the dispersion of the system in water most of the Rho110 interacting with the external surface of the composite is quickly desorbed, causing a large burst release. On the other hand, the Rho110 trapped inside the HNT lumen has to pass the positively charged chitosan coating to exit in the solution, and this process is slower due to the electrostatic repulsive effect.

Figure 7 shows the kinetic profiles obtained for the release of the two dyes from HNT functionalized with APTMES and from the HNT–H nanocomposites. By comparing the release profiles from pure HNT (Fig. 6) and from HNT functionalized with APTMES (Fig. 7), it is evident that the presence of silane results in a smaller amount of dye being released regardless of its charge. In the case of CF, C_e^{max} is 90 wt% for pristine HNT and reduces to 63 wt% when the HNT surface is functionalized with the silane. An even more pronounced decrease is found for Rho110, with C_e^{max} passing from 79 to 40 wt% in the case of silanized HNT. As evidenced in Scheme 1, the functionalization of HNT-APTMES tubules with hyaluronic acid to obtain HNT–H composites produces a material where some of the carboxylic moieties of the polymers have reacted to form an amidic bond. However, the ζ-potential measurements indicate that the net charge of this composite is strongly negative, suggesting that most of the carboxylates are still free. The profiles reported in Fig. 7 show that the release of positively charged Rho110 from negatively charged HNT–H composites is not slowed down with respect to that of the uncoated HNT (see the comparison of the k_D values in Table 2), and the desorption is not completely inhibited as observed in the reverse system (HNT–C + CF). This behavior can be due to the fact that the electrostatic contribution in the HNT–H system is weaker. The reason for this is twofold: (i) the amount of polymer on HNT is small (roughly

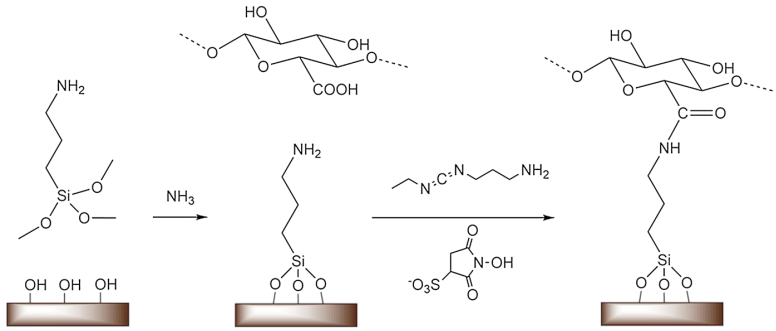

Scheme 1 Scheme of the reaction route for the preparation of HNT–H nanocomposites

halved with respect to the chitosan case, as shown by TGA) and (ii) part of the anionic carboxylic moieties of the polymers was engaged in the covalent bonding to the surface. The release of CF from HNT–H is decreased with respect to the HNT-APTMES sample. In particular, the final amount of released dye (C_e^{max} going from 63 to 18 wt%) and the rate of desorption from the inside of HNT (k_D, going from 15 to 8 h^{-1}) are significantly lowered. As the composite (HNT–H) and the dye (CF) both have the same (negative) charge, a behavior of the burst release similar to that found for the inverse system, HNT–C + Rho110, with increased initial release due to the repulsion between similar charges could have been expected. In this case, the CF desorbed immediately after the dispersion of the HNT–H composite in water (time = 0 h) is slightly lower than in the uncoated case (see *A* values in Table 2), and this behavior is likely due to the weak electrostatic effect of this composite, as discussed previously.

Conclusions

In this paper, nanocomposites based on HNTs and two highly biocompatible polysaccharides, chitosan and hyaluronic acid, were prepared. In the case of HNT–C composite, the electrostatic attraction between the negatively charged silanol surface of HNT and the positively charged polymer was exploited. The characterization of this composite showed that this simple strategy led to the formation of a positively charged, stable material made of inorganic tubules covered by a polymeric coating, whose amount was approximately 6 wt%. In the case of HNT/hyaluronic acid (HNT–H) composites, a chemical functionalization strategy was employed due to the unfavorable electrostatic interaction. The HNT surface was first silanized with APTMES, and then a covalent bond was formed between the carboxylic moiety of the polymer and the amine group exposed on the inorganic clays. This strategy produced a negatively charged composite containing approximately 3 wt% of polymer covering the inorganic tubules.

In order to address the effect of the relative charge of composites and drugs on the kinetics of release, two model dyes having similar structure but opposite net charge (rhodamine 110 and carboxyfluorescein) were loaded into the nanocomposites and their release kinetics in water were evaluated via fluorescence measurements. The curves were fitted with a model able to account for the desorption process from the external and the internal halloysite surfaces. The results showed that both the polymeric coatings altered the release process of the probes. In particular, the chitosan coating was able to completely hinder the release kinetic of the negative model drug. On the other hand, the release of the positive dye from the inner part of the inorganic tubules was slowed down due to the electrostatic repulsive effect of the polymer coating. Due to the different strategies of preparation, it was observed that the negatively charged HNT–H composite did not inhibit the release of the positive dye. The reason is twofold: (i) the amount of polymer on HNT is lower and (ii) some of the carboxylic moieties of the polymers were engaged in the covalent bonding to the surface, reasonably leading to a weaker interaction with the positive probe. For the same reason, the hyaluronic acid coating decreased the release of the negative dye from the inner lumen of the

tubules, both in terms of total released amount and desorption rate, but it did not cause a remarkable burst release. The results show that the polymeric coatings were successful in modulating the charge of the halloysite surface and altering the release kinetics of the probes. In particular, the mathematical model adopted to fit the release kinetics well described the experimental data and indicated that both charge and coating composition play a key role in the desorption process, and it provides a simple yet complete interpretation of the desorption of charged model dyes from halloysite and halloysite-based composites. Further studies have already been planned to investigate the release of oppositely charged model drugs in physiological conditions, where the high ionic strength and the presence of proteins may alter the process of release of charged molecules. The identification of models able to describe the delivery process also in complex matrices would constitute an important goal to properly tailor the characteristics of systems to be used in biomedical applications.

Acknowledgments CSGI is acknowledged for financial support. Stefano Spezzani (Imerys Tiles Minerals Italia s.r.l.) is acknowledged for kindly providing HNT samples.

Conflict of interest The authors declare that they have no conflict of interest.

Compliance with ethical standards This research did not involve human participants or animals.

References

Abdelmouleh M, Boufi S, ben Salah A et al (2002) Interaction of silane coupling agents with cellulose. Langmuir 18: 3203–3208

Abdullayev E, Lvov Y (2013) Halloysite clay nanotubes as a ceramic "skeleton" for functional biopolymer composites with sustained drug release. J Mater Chem B 1:2894–2903. doi:10.1039/C3TB20059K

Agnihotri SA, Mallikarjuna NN, Aminabhavi TM (2004) Recent advances on chitosan-based micro- and nanoparticles in drug delivery. J Control Release 100:5–28. doi:10.1016/j.jconrel.2004.08.010

Aguzzi C, Viseras C, Cerezo P et al (2013) Release kinetics of 5-aminosalicylic acid from halloysite. Colloids Surf B 105:75–80. doi:10.1016/j.colsurfb.2012.12.041

Arcudi F, Cavallaro G, Lazzara G et al (2014) Selective functionalization of halloysite cavity by click reaction: structured filler for enhancing mechanical properties of bionanocomposite films. J Phys Chem C 118:15095–15101. doi:10.1021/jp504388e

Bai H, Zhang H, He Y et al (2014) Enhanced proton conduction of chitosan membrane enabled by halloysite nanotubes bearing sulfonate polyelectrolyte brushes. J Membr Sci 454:220–232. doi:10.1016/j.memsci.2013.12.005

Baldrick P (2010) The safety of chitosan as a pharmaceutical excipient. Regul Toxicol Pharmacol 56:290–299. doi:10.1016/j.yrtph.2009.09.015

Bariana M, Aw MS, Kurkuri M, Losic D (2013) Tuning drug loading and release properties of diatom silica microparticles by surface modifications. Int J Pharm 443:230–241. doi:10.1016/j.ijpharm.2012.12.012

Barrett EP, Joyner LG, Halenda PP (1951) The determination of pore volume and area distributions in porous substances. I. Computations from nitrogen isotherms. J Am Chem Soc 73:373–380. doi:10.1021/ja01145a126

Berthold A, Cremer K, Kreuter J (1996) Preparation and characterization of chitosan microspheres as drug carrier for prednisolone sodium phosphate as model for anti-inflammatory drugs. J Control Release 39:17–25. doi:10.1016/0168-3659(95)00129-8

Brunauer S, Emmett PH, Teller E (1938) Adsorption of gases in multimolecular layers. J Am Chem Soc 60:309–319. doi:10.1021/ja01269a023

Buchtová N, Réthoré G, Boyer C et al (2013) Nanocomposite hydrogels for cartilage tissue engineering: mesoporous silica nanofibers interlinked with siloxane derived polysaccharide. J Mater Sci 24:1875–1884. doi:10.1007/s10856-013-4951-0

Burdick JA, Prestwich GD (2011) Hyaluronic acid hydrogels for biomedical applications. Adv Mater 23:H41–H56. doi:10.1002/adma.201003963

Calvert P (2001) Inkjet printing for materials and devices. Chem Mater 13:3299–3305. doi:10.1021/cm0101632

Chao C, Liu J, Wang J et al (2013) Surface modification of halloysite nanotubes with dopamine for enzyme immobilization. ACS Appl Mater Interfaces 5:10559–10564. doi:10.1021/am4022973

Chen M, Liu X, Fahr A (2011) Skin penetration and deposition of carboxyfluorescein and temoporfin from different lipid vesicular systems: in vitro study with finite and infinite dosage application. Int J Pharm 408:223–234. doi:10.1016/j.ijpharm.2011.02.006

Collins MN, Birkinshaw C (2013) Hyaluronic acid based scaffolds for tissue engineering—a review. Carbohydr Polym 92:1262–1279. doi:10.1016/j.carbpol.2012.10.028

Connell LS, Romer F, Suárez M et al (2014) Chemical characterisation and fabrication of chitosan–silica hybrid scaffolds with 3-glycidoxypropyl trimethoxysilane. J Mater Chem B 2:668. doi:10.1039/c3tb21507e

Deen I, Zhitomirsky I (2014) Electrophoretic deposition of composite halloysite nanotube–hydroxyapatite–hyaluronic acid films. J Alloys Compd 586(1):S531–S534. doi:10.1016/j.jallcom.2013.01.088

Du M, Guo B, Jia D (2010) Newly emerging applications of halloysite nanotubes: a review. Polym Int 59:574–582

Duarte HA, Lourenco MP, Heine T, Guimares L (2012) Clay mineral nanotubes: stability, structure and properties. INTECH Open Access Publisher, Rijeka

Dulbecco R, Vogt M (1954) Plaque formation and isolation of pure lines with poliomyelitis viruses. J Exp Med 99:167–182

Falcone SJ, Berg RA (2008) Crosslinked hyaluronic acid dermal fillers: a comparison of rheological properties. J Biomed Mater Res A 87:264–271. doi:10.1002/jbm.a.31675

Forster S, Thumser AE, Hood SR, Plant N (2012) Characterization of rhodamine-123 as a tracer dye for use in in vitro drug transport assays. PLoS ONE 7:e33253. doi:10.1371/journal.pone.0033253

Fox JD, Capadona JR, Marasco PD, Rowan SJ (2013) Bioinspired water-enhanced mechanical gradient nanocomposite films that mimic the architecture and properties of the squid beak. J Am Chem Soc 135:5167–5174. doi:10.1021/ja4002713

Ghebaur A, Garea SA, Iovu H (2012) New polymer–halloysite hybrid materials—potential controlled drug release system. Int J Pharm 436:568–573. doi:10.1016/j.ijpharm.2012.07.014

Ghorai S, Sarkar A, Panda AB, Pal S (2013) Evaluation of the flocculation characteristics of polyacrylamide grafted xanthan gum/silica hybrid nanocomposite. Ind Eng Chem Res 52:9731–9740. doi:10.1021/ie400550m

Gu BK, Park SJ, Kim MS et al (2013) Fabrication of sonicated chitosan nanofiber mat with enlarged porosity for use as hemostatic materials. Carbohydr Polym 97:65–73. doi:10.1016/j.carbpol.2013.04.060

Ha DI, Lee SB, Chong MS et al (2006) Preparation of thermoresponsive and injectable hydrogels based on hyaluronic acid and poly(*N*-isopropylacrylamide) and their drug release behaviors. Macromol Res 14:87–93. doi:10.1007/BF03219073

Habibi Y, Dufresne A (2008) Highly filled bionanocomposites from functionalized polysaccharide nanocrystals. Biomacromolecules 9:1974–1980. doi:10.1021/bm8001717

Haxaire K, Marechal Y, Milas M, Rinaudo M (2003) Hydration of polysaccharide hyaluronan observed by IR spectrometry. I. Preliminary experiments and band assignments. Biopolymers 72:10–20. doi:10.1002/bip.10245

Hejazi R, Amiji M (2003) Chitosan-based gastrointestinal delivery systems. J Control Release 89:151–165. doi:10.1016/S0168-3659(03)00126-3

Horcajada P, Chalati T, Serre C et al (2010) Porous metal-organic-framework nanoscale carriers as a potential platform for drug delivery and imaging. Nat Mater 9:172–178. doi:10.1038/nmat2608

Issa MM, Köping-Höggård M, Artursson P (2005) Chitosan and the mucosal delivery of biotechnology drugs. Drug Discov Today 2:1–6. doi:10.1016/j.ddtec.2005.05.008

Jayakumar R, Menon D, Manzoor K et al (2010a) Biomedical applications of chitin and chitosan based nanomaterials—a short review. Carbohydr Polym 82:227–232. doi:10.1016/j.carbpol.2010.04.074

Jayakumar R, Prabaharan M, Nair SV, Tamura H (2010b) Novel chitin and chitosan nanofibers in biomedical applications. Biotechnol Adv 28:142–150. doi:10.1016/j.biotechadv.2009.11.001

Joussein E, Petit S, Churchman J et al (2005) Halloysite clay minerals—a review. Clay Miner 40:383–426. doi:10.1180/0009855054040180

Kaur S, Dhillon GS (2014) The versatile biopolymer chitosan: potential sources, evaluation of extraction methods and applications. Crit Rev Microbiol 40:155–175. doi:10.3109/1040841X.2013.770385

Kean T, Thanou M (2010) Biodegradation, biodistribution and toxicity of chitosan. Adv Drug Deliv Rev 62:3–11. doi:10.1016/j.addr.2009.09.004

Khoo WS, Ismail H, Ariffin A (2012) Tensile, swelling, and oxidative degradation properties of crosslinked polyvinyl alcohol/chitosan/halloysite nanotube composites. Int J Polym Mater 62:390–396. doi:10.1080/00914037.2012.719133

Kulterer MR, Reichel VE, Kargl R et al (2012) Functional polysaccharide composite nanoparticles from cellulose acetate and potential applications. Adv Funct Mater 22:1749–1758. doi:10.1002/adfm.201102350

Lee H, Lee K, Park TG (2008) Hyaluronic acid–paclitaxel conjugate micelles: synthesis, characterization, and antitumor activity. Bioconjug Chem 19:1319–1325. doi:10.1021/bc8000485

Levis SR, Deasy PB (2002) Characterisation of halloysite for use as a microtubular drug delivery system. Int J Pharm 243:125–134

Levis SR, Deasy PB (2003) Use of coated microtubular halloysite for the sustained release of diltiazem hydrochloride and propranolol hydrochloride. Int J Pharm 253:145–157

Liu Tsang V, Bhatia SN (2004) Three-dimensional tissue fabrication. Adv Drug Deliv Rev 56:1635–1647. doi:10.1016/j.addr.2004.05.001

Liu M, Zhang Y, Wu C et al (2012) Chitosan/halloysite nanotubes bionanocomposites: structure, mechanical properties and biocompatibility. Int J Biol Macromol 51:566–575. doi:10.1016/j.ijbiomac.2012.06.022

Liu M, Wu C, Jiao Y et al (2013) Chitosan–halloysite nanotubes nanocomposite scaffolds for tissue engineering. J Mater Chem B 1:2078–2089. doi:10.1039/C3TB20084A

Liu M, Shen Y, Ao P et al (2014) The improvement of hemostatic and wound healing property of chitosan by halloysite nanotubes. RSC Adv 4:23540–23553. doi:10.1039/C4RA02189D

Lvov YM, Shchukin DG, Möhwald H, Price RR (2008) Halloysite clay nanotubes for controlled release of protective agents. ACS Nano 2:814–820

Marney DCO, Yang W, Russell LJ et al (2012) Phosphorus intercalation of halloysite nanotubes for enhanced fire properties of polyamide 6. Polym Adv Technol 23:1564–1571. doi:10.1002/pat.3030

Massaro M, Riela S, Cavallaro G et al (2014) Eco-friendly functionalization of natural halloysite clay nanotube with ionic liquids by microwave irradiation for Suzuki coupling reaction. J Organomet Chem 749:410–415. doi:10.1016/j.jorganchem.2013.10.044

Mi F-L, Tan Y-C, Liang H-F, Sung H-W (2002) In vivo biocompatibility and degradability of a novel injectable-chitosan-based implant. Biomaterials 23:181–191. doi:10.1016/S0142-9612(01)00094-1

Murugan R, Ramakrishna S (2004) Bioresorbable composite bone paste using polysaccharide based nano hydroxyapatite. Biomaterials 25:3829–3835. doi:10.1016/j.biomaterials.2003.10.016

Ortona O, D'Errico G, Mangiapia G, Ciccarelli D (2008) The aggregative behavior of hydrophobically modified chitosans with high substitution degree in aqueous solution.

Carbohydr Polym 74:16–22. doi:10.1016/j.carbpol.2008.01.009

Pandey S, Goswami GK, Nanda KK (2013) Green synthesis of polysaccharide/gold nanoparticle nanocomposite: an efficient ammonia sensor. Carbohydr Polym 94:229–234. doi:10.1016/j.carbpol.2013.01.009

Price R, Gaber BP, Lvov Y (2001) In-vitro release characteristics of tetracycline HCl, khellin and nicotinamide adenine dineculeotide from halloysite; a cylindrical mineral. J Microencapsul 18:713–722. doi:10.1080/02652040010019532

Ritger PL, Peppas NA (1987a) A simple equation for description of solute release I. Fickian and non-fickian release from non-swellable devices in the form of slabs, spheres, cylinders or discs. J Control Release 5:23–36. doi:10.1016/0168-3659(87)90034-4

Ritger PL, Peppas NA (1987b) A simple equation for description of solute release II. Fickian and anomalous release from swellable devices. J Control Release 5:37–42. doi:10.1016/0168-3659(87)90035-6

Roig-Roig F, Solans C, Esquena J, García-Celma MJ (2013) Preparation, characterization, and release properties of hydrogels based on hyaluronan for pharmaceutical and biomedical use. J Appl Polym Sci 130:1377–1382. doi:10.1002/app.39306

Roldo M, Fatouros DG (2011) Chitosan-derivative based hydrogels as drug delivery platforms: applications in drug delivery and tissue engineering. In: Zilberman M (ed) Act. Implants scaffolds tissue regen. Springer, Berlin, pp 351–376

Ruiz-Hitzky E, Van Meerbeek A (2006) Chapter 10.3 clay mineral- and organoclay-polymer nanocomposite. In: Bergaya F, Theng BKG, Lagaly G (eds) Developments in clay science. Elsevier, Amsterdam, pp 583–621

Ruiz-Hitzky E, Darder M, Fernandes FM et al (2013) Fibrous clays based bionanocomposites. Prog Polym Sci 38:1392–1414. doi:10.1016/j.progpolymsci.2013.05.004

Ryan G, Pandit A, Apatsidis DP (2006) Fabrication methods of porous metals for use in orthopaedic applications. Biomaterials 27:2651–2670. doi:10.1016/j.biomaterials.2005.12.002

Shchukin DG, Möhwald H (2011) Smart nanocontainers as depot media for feedback active coatings. Chem Commun 47:8730. doi:10.1039/c1cc13142g

Shchukin DG, Sukhorukov GB, Price RR, Lvov YM (2005) Halloysite nanotubes as biomimetic nanoreactors. Small 1:510–513

Shingel KI, Marchessault RH (2006) Iron-polysaccharide composites for pharmaceutical applications. Polysacch Drug Deliv Pharm Appl 934:271–287

Stodolak E, Paluszkiewicz C, Bogun M, Blazewicz M (2009) Nanocomposite fibres for medical applications. J Mol Struct 924–926:208–213. doi:10.1016/j.molstruc.2009.01.018

Sudina ML, Braga CRC, Marcus VL et al (2012) Application of infrared spectroscopy to analysis of chitosan/clay nanocomposites. InTech, Rijeka, pp 43–62

Suh DJ, Lim YT, Park OO (2000) The property and formation mechanism of unsaturated polyester–layered silicate nanocomposite depending on the fabrication methods. Polymer 41:8557–8563. doi:10.1016/S0032-3861(00)00216-0

Travan A, Marsich E, Donati I et al (2011) Silver–polysaccharide nanocomposite antimicrobial coatings for methacrylic thermosets. Acta Biomater 7:337–346. doi:10.1016/j.actbio.2010.07.024

Vallés-Lluch A, Poveda-Reyes S, Amorós P et al (2013) Hyaluronic acid-silica nanohybrid gels. Biomacromolecules 14:4217–4225. doi:10.1021/bm401041z

Veerabadran NG, Price RR, Lvov YM (2007) Clay nanotubes for encapsulation and sustained release of drugs. NANO 2:115–120

Vergaro V, Abdullayev E, Lvov YM et al (2010) Cytocompatibility and uptake of halloysite clay nanotubes. Biomacromolecules 11:820–826

Verma NK, Moore E, Blau W et al (2012) Cytotoxicity evaluation of nanoclays in human epithelial cell line A549 using high content screening and real-time impedance analysis. J Nanoparticle Res 14:1–11. doi:10.1007/s11051-012-1137-5

Wang Q, Zhang J, Zheng Y, Wang A (2014) Adsorption and release of ofloxacin from acid- and heat-treated halloysite. Colloids Surf B 113:51–58. doi:10.1016/j.colsurfb.2013.08.036

Ward CJ, Song S, Davis EW (2010) Controlled release of tetracycline-hcl from halloysite-polymer composite films. J Nanosci Nanotechnol 10:6641–6649. doi:10.1166/jnn.2010.2647

Yuan P, Southon PD, Liu Z et al (2008) Functionalization of halloysite clay nanotubes by grafting with γ-aminopropyltriethoxysilane. J Phys Chem C 112:15742–15751. doi:10.1021/jp805657t

Zhao Y, Wang S, Guo Q et al (2013) Hemocompatibility of electrospun halloysite nanotube- and carbon nanotube-doped composite poly(lactic-co-glycolic acid) nanofibers. J Appl Polym Sci 127:4825–4832. doi:10.1002/app.38054

Supplementary material

The effect of charge on the release kinetics from polysaccharide-nanoclay composites.

Stefano Del Buffa, Emanuele Grifoni, Francesca Ridi, Piero Baglioni

Department of Chemistry "Ugo Schiff" and CSGI, University of Florence, via della Lastruccia 3, Sesto Fiorentino, 50019 Florence, Italy.

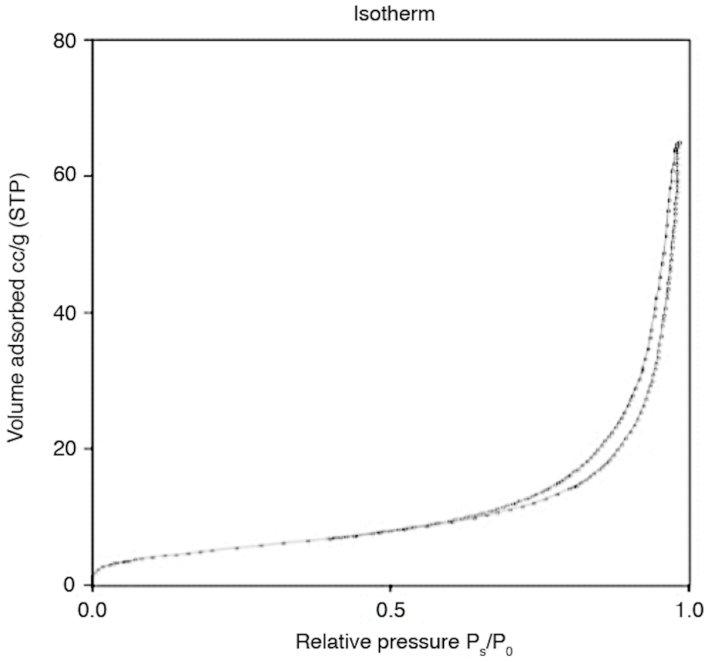

Figure S1. Typical N_2 adsorption-desorption isotherm of a halloysite sample showing a hysteresis loop associated to capillary condensation (Pierotti and Rouquerol 1985). BET surface area is found to be 25 ± 4 m^2g^{-1}.

Pore Dia. Range(nm)	Pore Volume (ml/g)	%
Under 6	0.00630	3.45
6 - 8	0.00326	1.78
8 - 10	0.00326	1.79
10 - 12	0.00401	2.19
12 - 16	0.00671	3.67
16 - 20	0.00844	4.62
20 - 80	0.07260	39.72
Over 80	0.07821	42.79
BJH Total	0.18279	100.00

Figure S2. Typical pore size distribution of a halloysite sample as obtained by BJH calculations.

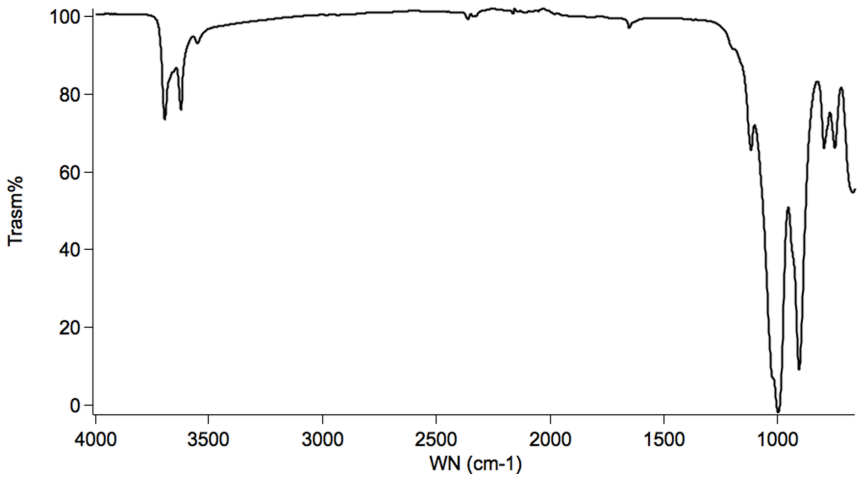

Figure S3. ATR-FTIR spectrum of halloysite powder. Characteristic signals that occurred at 3695 cm^{-1}, 3620 cm^{-1} and 1650 cm^{-1} are attributed to O-H stretching of inner surface hydroxyl groups, O-H stretching of inner hydroxyl groups and deformation of physisorbed water molecules, respectively (Zhu et al 2012). The intense band at 1000 cm^{-1} is attributed to Si-O-Si stretching (Finocchio et al 2007).

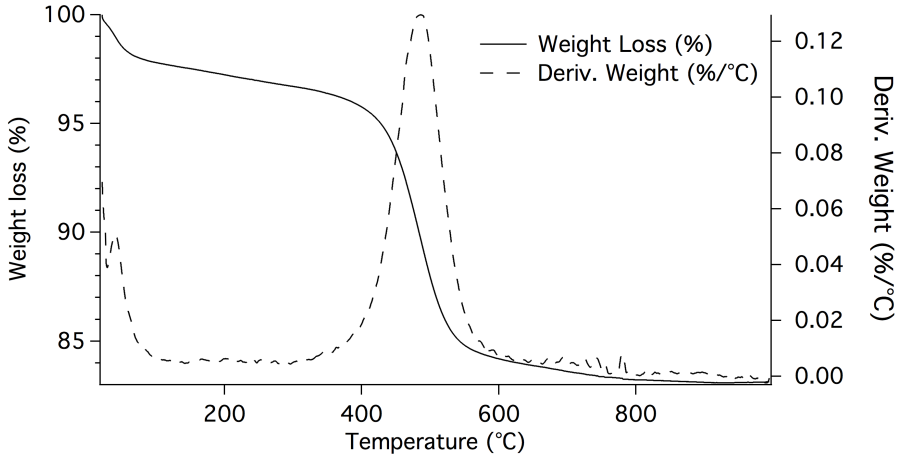

Figure S4. DTG curve of a halloysite sample. The initial weight loss (~2.5 %wt, RT-150°C) is due to physisorbed water molecules, while the second thermal events (large endothermic peak centered at 485 °C) corresponds to the structural dehydroxylation of halloysite, i.e. loss of chemically bound water (~14 %wt, 150-600 °C). At higher temperature (~650°C) a first order transition, identified by a change in the heat flow profile with no corresponding weight loss, is detected. This can be associated with the formation of crystalline γ-Al_2O_3 and mullite from the high temperature decomposition of dehydroxylated halloysite (Roy et al 1955)

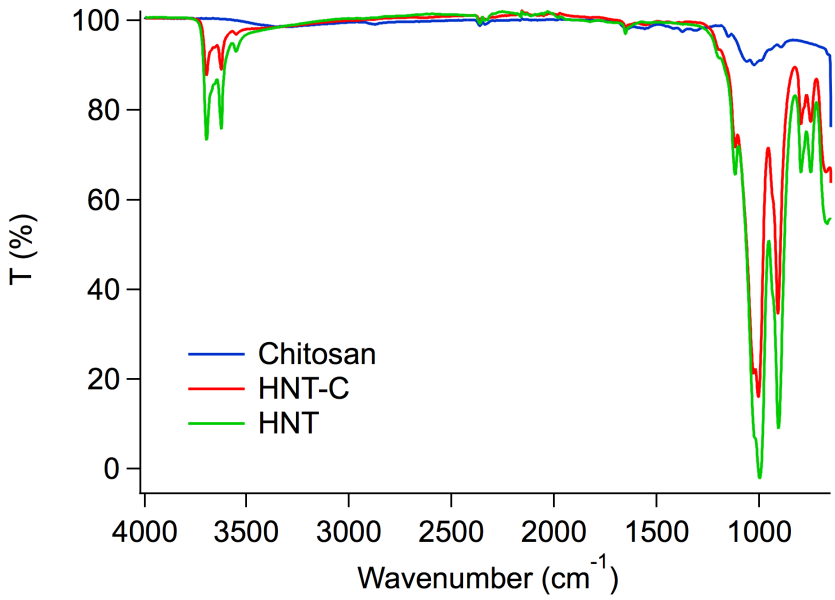

Figure S5. FTIR spectra of chitosan, halloysite nanotubes (HNT) and halloysite-chitosan nanocomposites. Chitosan characteristic signals (Silva et al 2012) are detected in the 3000-3570 cm^{-1} range (OH stretching), at 2875 cm^{-1} (methyl C-H stretching), at 1375 cm^{-1} (bending vibrations of methyl groups), in the 1680-1480 cm^{-1} range (vibrations of carbonyl bonds of amide group), and at 1150 cm^{-1} (asymmetric vibrations of CO in the oxygen bridge resulting from deacetylation of chitosan).

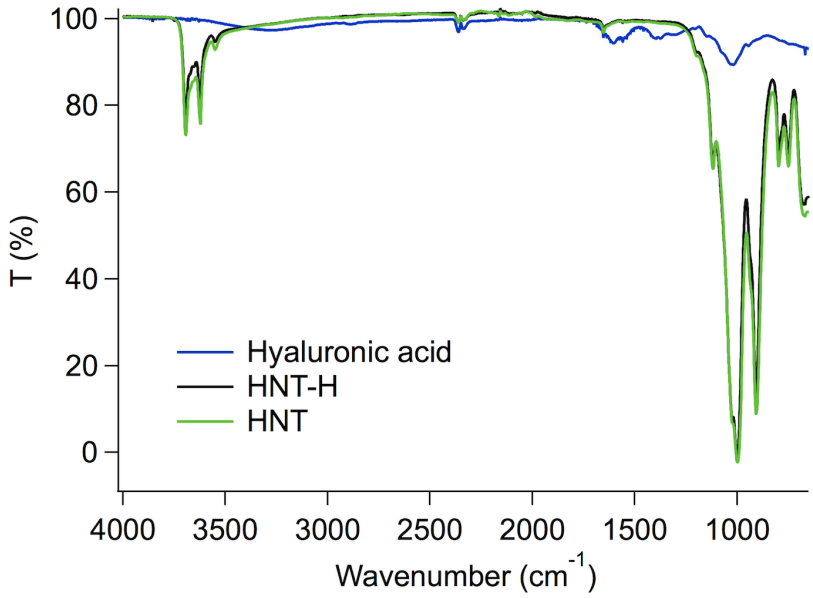

Figure S6. ATR-FTIR spectra of hyaluronan, halloysite nanotubes (HNT) and halloysite-hyaluronan nanocomposites. Hyaluronan characteristic signal (Haxaire et al 2003) are a broad band in the 3000-3300 cm^{-1} range (O-H and N-H stretching), a peak at 1600 cm^{-1} corresponding to C=O stretching of deprotonated carboxylic groups, a weak shoulder at 1145 cm^{-1} corresponding to antisymmetric C-O-C stretching of glycoside bonds, and a peak around 1010 cm^{-1} attributable to C-OH stretching.

Table S1. CHN elemental analysis performed on HNT and functionalized HNT.

	N (%wt)	C (%wt)	H (%wt)	Est.surface coverage
HNT	0.00	0.09	1.70	-
HNT+APTMS 1	0.06	0.27	1.38	10 %
HNT+APTMS 2	0.09	0.39	1.71	25 %
HNT+APTMS 3	0.14	0.59	1.73	50 %

Results confirm the presence of silane molecules bound to HNT, with both carbon and nitrogen weight percentage increasing with the amount of APTMS used during the silanization process. Estimated surface coverage corresponds to indicated percentages of total BET surface area (25 ± 4 m^2g^{-1}).

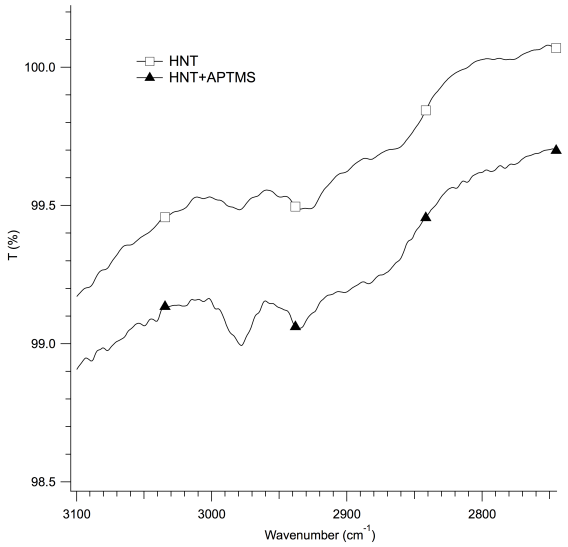

Figure S7. Expanded view of the FTIR spectrum of silanized HNT. Due to the low amount of N and O in the samples, the characteristic adsorption peak of the APTMS amine group was not recognized clearly. However, in the 2870-2980 cm^{-1} region the silanized sample shows typical adsorption peaks attributable to alkyl C-H stretching. These signals are much weaker in the HNT sample, and in this case are due to some organic impurities.

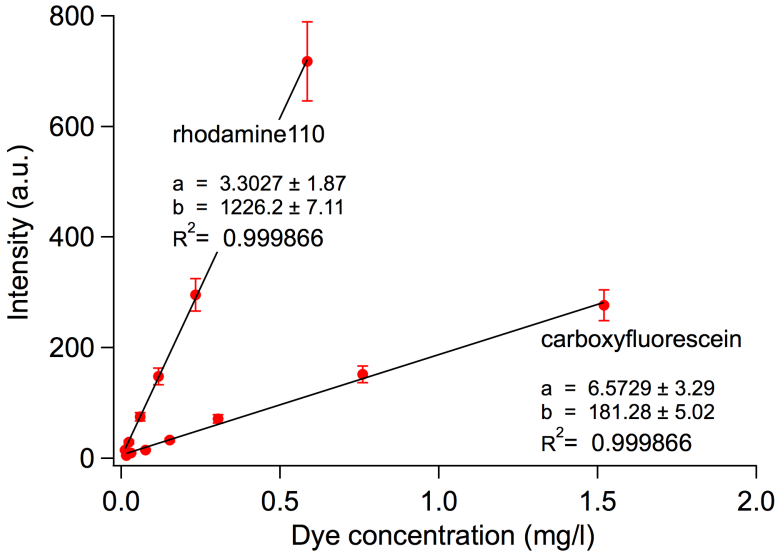

Figure S8. To evaluate the concentration of the released probes, the maximum of the fluorescence intensity (at 514 nm for CF, at 519 nm for Rho110) of sample solutions is evaluated at progressive intervals of time and the concentration is extrapolated from the corresponding calibration curve. From the comparison of the fluorescence intensity of the dye solution, before and after the addition of HNT, we found that the amount of loaded Rho110 and CF was 0.0595 %wt and 0.0678 %wt, respectively (percentages refer to total weight of HNT). The difference in loaded dye could be rationalized in terms of the more effective electrostatic interaction between negatively charged CF (at neutral pH) and the positively charged lumen of HNT.

Bibliography:

Finocchio E, Macis E, Raiteri R, Busca G (2007) Adsorption of Trimethoxysilane and of 3-Mercaptopropyltrimethoxysilane on Silica and on Silicon Wafers from Vapor Phase: An IR Study. Langmuir 23:2505–2509. doi: 10.1021/la062972b

Haxaire K, Marechal Y, Milas M, Rinaudo M (2003) Hydration of polysaccharide hyaluronan observed by IR spectrometry. I. Preliminary experiments and band assignments. Biopolymers 72:10–20. doi: 10.1002/bip.10245

Pierotti RA, Rouquerol J (1985) Reporting physisorption data for gas/solid systems with special reference to the determination of surface area and porosity. Pure Appl Chem 57:603–619.

Roy R, Roy DM, Francis EE (1955) New Data on Thermal Decomposition of Kaolinite and Halloysite. J Am Ceram Soc 38:198–205. doi: 10.1111/j.1151-2916.1955.tb14929.x

Silva SM, Braga CR, Fook MV, et al Application of Infrared Spectroscopy to Analysis of Chitosan/Clay Nanocomposites.

Zhu H, Du M, Zou M, et al (2012) Green synthesis of Au nanoparticles immobilized on halloysite nanotubes for surface-enhanced Raman scattering substrates. Dalton Trans 41:10465. doi: 10.1039/c2dt30998j

Colloids and Surfaces B: Biointerfaces 145 (2016) 562–566

Contents lists available at ScienceDirect

Colloids and Surfaces B: Biointerfaces

journal homepage: www.elsevier.com/locate/colsurfb

Short communication

Injectable composites *via* functionalization of 1D nanoclays and biodegradable coupling with a polysaccharide hydrogel

Stefano Del Buffa, Elia Rinaldi, Emiliano Carretti, Francesca Ridi, Massimo Bonini, Piero Baglioni*

Department of Chemistry "Ugo Schiff" and CSGI, University of Florence, via della Lastruccia 3, Sesto Fiorentino, 50019 Florence, Italy

ARTICLE INFO

Article history:
Received 12 November 2015
Received in revised form 6 April 2016
Accepted 18 May 2016
Available online 21 May 2016

Keywords:
Nanocomposite
Injectability
Hydrogel
Halloysite
Rheology
Carboxymethyl cellulose
Needle gauge

ABSTRACT

The use of injectable materials in minimally invasive surgical procedures could help in facing the bone diseases connected to the ageing of world population. To this aim, materials integrating the rheological properties of biocompatible polymers with the mechanical properties of 1D inorganic nanostructures represent promising scaffolds. Here we describe the preparation of hydrogel composites made of carboxymethyl cellulose (CMC) and halloysite nanotubes (HNT) as injectable materials for the local treatment of bone defects. The rheology and injectability of the materials reflects their structural properties, showing the possibility of successfully injecting the prepared composites over a large range of operative conditions.

1. Introduction

The scientific research in bone medication and in the development of new and efficient methodologies for the treatment of bone diseases is becoming more and more relevant, mainly because of the progressive ageing of the world population [1]. For instance, in Italy the population ageing over 50 years is estimated to grow from 24 millions in 2010 to more than 29 millions in 2025. The number of fractures (both traumatic and pathologic) in Europe is expected to increase by more than 28%, with a total projected health care cost exceeding 46 billions € [2]. Any effective strategy to reduce those costs requires both a preventive action (typically achieved through a healthy life style) and the minimization of the post-surgery hospital stay. To this aim, minimal invasive surgery definitely represents a suitable strategy for the effective treatment of bone fractures and diseases [3]. In this perspective, the *in-situ* injection of properly designed biomaterials able to combine adequate mechanical properties with osteo-conductivity and osteo-inductivity can be of particular relevance.

The injectability of a material through a needle is typically assessed by evaluating the minimum pressure required for its injection, the evenness of its flow and the absence of clogging [4]. In the case of injectable composite materials, which typically are complex and non-Newtonian fluids (*i.e.*, hydrogels, gels, pastes, concentrated suspensions), the complete understanding of their rheological properties is crucial. Among them, shear thinning materials are especially appealing to minimal invasive surgery. Their viscosity decreases during the injection, while they eventually recover their initial rheological state at the injection site when the stress is relieved. As a result, the material is able to conform and eventually adhere to the site thanks to chemical affinity and microscopic interlocking [5].

Injectable biodegradable hydrogels provide an effective and convenient way for the controlled administration of a wide variety of actives (such as drugs, proteins, genes, and living cells) and they can be cleared from the body after accomplishing their mission [6]. A number of studies have already suggested the use of injectable composites in supporting the growth of damaged tissues, such as in bone tissue engineering [7], treatment of hemorrhage [8], and wound healing application [9]. Such a broad range of applications highlights the need for new materials (with tunable rheological properties) that could be injected with needles of different gauges.

In this work, we report on the preparation and the characterization of an injectable composite material made of halloysite nanotubes (HNTs) and carboxymethyl cellulose (CMC) conceived for the local treatment of bone defects. The choice of a polysac-

* Corresponding author.
E-mail address: piero.baglioni@unifi.it (P. Baglioni).

http://dx.doi.org/10.1016/j.colsurfb.2016.05.056
0927-7765/

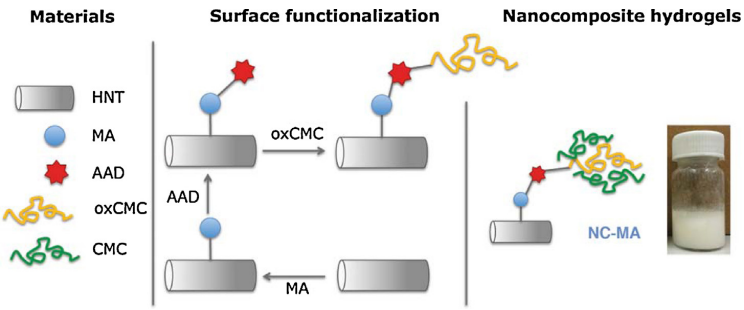

Fig. 1. Schematic representation of the HNT surface functionalization and of the formation of the nanocomposite hydrogels. The reaction scheme, including chemical structures, is given in the Supplementary material, Fig. S2.

charide matrix responds to the need of a biocompatible polymer with well-known rheological properties. CMC spontaneously forms a hydrogel and it is commonly adopted as a rheological modifier or additive in several water-based formulations in biomaterials and bio-based applications [10]. On the other hand, the use of nanotubular fillers introduces multiple advantages. HNTs are natural tubular aluminosilicates [11] which have been already proposed as reinforcing agents for composite materials in the field of bone medication thanks to their cytocompatibility [12], their mechanical properties [13], and their potentials as rheo-modifiers [14]. Compared to spheroidal and platelet particles, their 1D shape provides a stronger thickening power [15], while their hollow structure avoids a large increase in the density of the composite. Furthermore, their high surface area and the composition of the external surface allow for the adsorption of cations and positively charged species [16], while the presence of a hollow lumen of nanometric size can be exploited to accommodate and slowly release actives and drugs [17].

A crucial prerequisite to the reliable injection of our composite hydrogel through the needle gauges commonly employed in minimally invasive surgery is the homogeneous dispersion of HNTs in the CMC matrix. To this aim, we followed the hydrazide-aldehyde protocol successfully introduced by Hoare for the coupling of polymers and inorganic nanostructures [18,19]. HNTs were first functionalized with maleic anhydride and then reacted with adipic acid dihydrazide to obtain a hydrazide group. On the other hand, CMC was partially oxidized so to produce aldehyde groups. The two materials were finally mixed to spontaneously form a hydrazone bond.

2. Materials and methods

2.1. Materials

Halloysite nanotubes (HNT) were kindly provided by Imerys Minerals Ltd (Auckland, New Zealand). Sodium carboxymethyl cellulose (pre-hydrated TICALOSE® CMC 6000) was obtained from TIC Gums (Belcamp, MD, USA) and used as received. Adipic acid dihydrazide (AAD, purity ≥ 98%), (N-(3-dimethylaminopropyl)-N′-ethylcarbodiimide hydrochloride (EDC, commercial grade), ethanol (puriss grade), hydrochloric acid, sodium hydroxide, chloroform (purity ≥ 99.5%) were purchased from Sigma Aldrich (Sigma-Aldrich, Milan, Italy). Maleic anhydride (MA, purity 99%) and ethylene glycol (purity ≥ 99.5%) were purchased from Fluka (Buchs, Switzerland). Sodium periodate (purity 99.8%) was purchased from Merck (Darmstadt, Germany). MilliQ water (resistivity = 18.2 MΩ·cm) was used for the preparation of all the aqueous solutions and dispersions.

2.2. Purification of halloysites

The procedure for purifying the HNT batch used in this study was derived from the work by Shchukin et al. [20]. In details, 5 g of HNT were suspended in 500 ml of water and mixed with a blender for 20 min. The suspension was then transferred to a beaker and left to sediment. After a fixed amount of time, the supernatant solution was discarded and the sediment was re-suspended in 500 ml of water. The suspension was mixed with the blender for another 20 min and left to sediment again. The procedure was repeated three times. At the end, the HNT suspension was centrifuged for 10 min at 7500 rpm, and finally the precipitate was collected and dried in oven at 60 °C.

2.3. Methods

Surface area and porosity of HNTs were determined from N_2 adsorption isotherm with a SA 3100 analyzer (Beckmann-Coulter, Milan, Italy) utilizing BET and BJH calculations. ATR-FTIR measurements were performed on a Nexus 870 spectrometer (Nicolet, Madison, WI, USA), equipped with a liquid N_2-cooled mercury cadmium telluride (MCT) detector (650–4000 cm^{-1} range, resolution 2 cm^{-1}). Thermogravimetric analyses (TGA) was conducted on a SDT Q600 (TA Instruments, Newcastle, DE, USA) from room temperature to 1000 °C at 10 °C/min. Zeta potential (ζ, calculated according to the Smoluchowski model) was obtained with a 90Plus Particle Size Analyzer by Brookhaven Instruments Corporation. Morphological characterization was conducted by means of field emission scanning electron microscopy (ΣIGMA FE-SEM, Carl Zeiss Microscopy GmbH, Germany) on freeze-dried samples. Rotational shear measurements were carried out at 25 °C (Peltier temperature control system) on a Paar Physica UDS200 rheometer using a 2 cone and plate geometry (25 mm diameter) and working at controlled shear stress. After their loading, samples were equilibrated for 1 h at 25 °C prior to carrying out the experiments. Injectability tests were performed by means of a custom-made apparatus where controlled loads are applied to commercial syringes and the flow is evaluated from the amount of the composite which is injected over a known period of time. Apparent viscosity values (η) were calculated from the Poiseuille law (Eq. (1)) [21]:

$$F = \frac{32D^2 lQ\eta}{d^4} \quad (1)$$

where F is the force applied to the syringe plunger, D is the syringe plunger diameter, d and l are the inner diameter and the length of the needle, respectively, and Q is the flow rate.

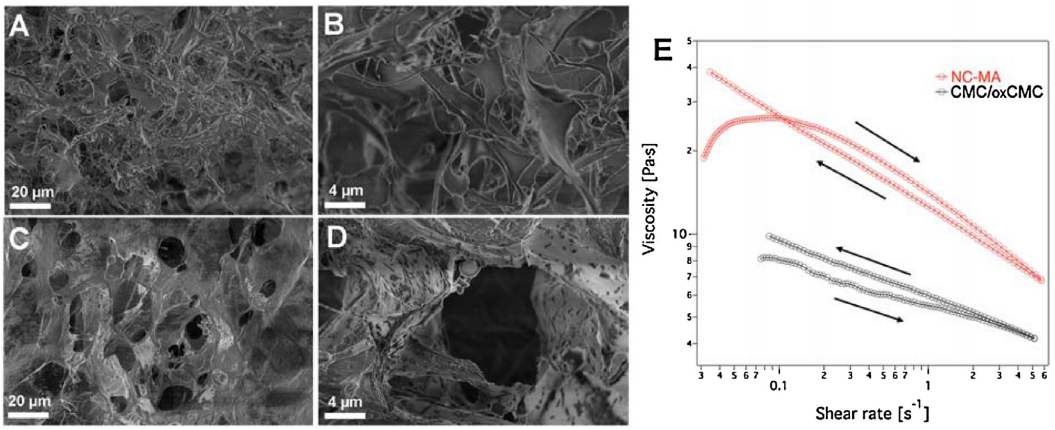

Fig. 2. SEM images of freeze-dried CMC/oxCMC (A, B) and NC-MA (C, D) samples at different magnifications, and flow curves (E) of CMC/oxCMC and NC-MA hydrogels (arrows indicate the shear rate ramp).

2.4. Preparation of composite hydrogels

HNT surface was firstly modified by the reaction of the external silanol groups with maleic anhydride (MA). 10 g of clay and 10 g of anhydride were added to 100 ml of chloroform, previously bubbled with N_2, and kept at 37 °C under stirring overnight. The solid product was recovered by centrifugation, washed with chloroform and dried. HNT-MA was further reacted with adipic acid dihydrazide (AAD) to introduce a hydrazine moiety on the clay surface. 1.5 g of AAD was added to a 0.5%w/v water dispersion of HNT-MA, at room temperature. Then, 780 μl of EDC were added (pH of the dispersion is about 4) and the reaction was allowed to run during 5 h, checking and eventually adjusting the pH with HCl 0.1 M to remain constant. After 5 h the pH was adjusted to pH = 7 with NaOH and the dispersion was dialyzed (membrane cut-off = 12.4 kDa) against milliQ water. The solid product was then recovered by centrifugation.

To partially oxidize carboxymethyl cellulose (CMC), 10 g of solid was dissolved in water (at a concentration of 1% w/v), then 5.3 g of sodium periodate were added and the solution was kept under agitation for two hours, at room temperature. Ethylene glycol (2.7 ml) was then added to quench the oxidation reaction. The polymer solution was dialyzed (membrane cut-off = 12.4 kDa) and the solvent was partially removed by rotavapor. The obtained oxidized CMC (oxCMC) was finally freeze-dried. The short reaction time and the low concentration of oxidizing agent prevent a marked degradation of the polymer [22].

In the last step, oxCMC was mixed with modified HNT in milliQ water under mechanical stirring. The final concentration of both oxCMC and HNT-MA was 10%wt. The NC-MA nanocomposite hydrogel was finally obtained by adding pristine CMC to a final concentration of 2%wt. A blank sample composed of 2%wt CMC and 5%wt oxCMC water solution was also prepared as a reference for the rheological and injectability tests. The amount of oxCMC was chosen to replicate the composition of NC-MA sample without the inorganic phase (see Supplementary material Fig. S6).

3. Results and discussions

CMC and HNT were chemically modified to be coupled *via* a biodegradable hydrazone bond. Hydrazone bonds are easily formed with no need of harsh chemical reactions and have been recently exploited to obtain cross-linked hydrogels [19] and superparamagnetic hybrids [18] for drug-release and *in-vivo* biomedical applications. The introduction of a biodegradable function is especially useful in view of the *in-vivo* application of a temporary scaffold able to support the growth of bone tissue and to be eventually resorbed by the organism. The nanocomposite hydrogels were prepared as sketched in Fig. 1 (details are given in the Supplementary material, Section 2, Fig. S2).

Maleic (MA) anhydride was used as grafting agent on the surface of HNT exploiting its reactivity towards inorganic nanoparticles [23–25]. The successful functionalization of HNT with MA was confirmed by means of FT-IR and Zeta Potential (see Supplementary material, sections 3 and 4). Comparing HNT to HNT-MA, both the appearance in the FT-IR spectrum of the C—H, C=O and C=C stretching and the change of the Zeta Potential from −43 to −28 mV confirm the successful functionalization.

Functionalized HNTs were reacted with adipic acid dihydrazide (AAD) and then mixed with oxidized CMC (oxCMC), which was previously obtained through the partial oxidation of CMC with sodium periodate. The reaction between AAD and the carboxylic functions resulting from the functionalization of HNTs is confirmed by the change in the Zeta potential from −28 to −12 mV and takes to the exposition of hydrazine groups on the surface of functionalized HNTs. Then, the reaction between the aldehyde functions present in oxCMC and the hydrazine groups exposed by HNT-MA spontaneously takes to the formation of hydrazone bonds, resulting in an organic/inorganic composition of about 50%w/w (see Supplementary material, Fig. S6).

The resulting hydrogels were added with pristine CMC so to reach a viscosity suitable for injection purposes (see Fig. 1 on the right). The concentrations of oxCMC/HNT-MA and CMC in the final NC-MA composites were 10%wt and 2%wt, respectively.

Representative SEM images of freeze-dried nanocomposites are shown in Fig. 2, together with the CMC/oxCMC sample at the same magnifications. Composite hydrogel sample (Fig. 2C and D) show a porous structure similar to that of CMC/oxCMC hydrogel (Fig. 2A and B). Furthermore, the results highlight that HNTs are homogeneously distributed in the composite material and that the hydrogel-forming properties of CMC are retained.

The dynamic viscosity of the CMC/oxCMC sample is reported in Fig. 2E as a function of the shear rate. A very short Newtonian region (up to about 0.1 s^{-1}) is observed at very low shear rates, followed by an extended shear-thinning region. This can be explained by the disentanglement of the polymeric network (held together

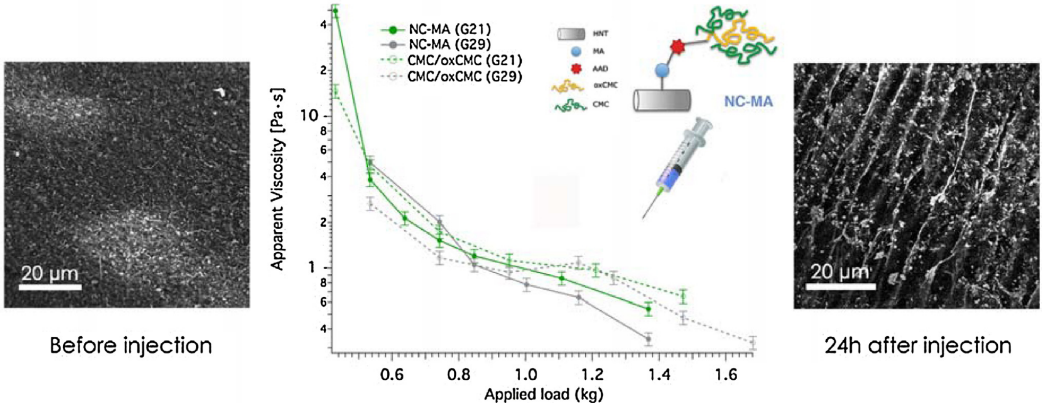

Fig. 3. *In the middle:* Injectability tests of NC-MA and CMC/oxCMC hydrogels, expressed as apparent viscosity *versus* applied load, performed on different needle gauges (G21, G29). *On the sides:* SEM images of NC-MA lyophilized hydrogel before the injection through a G21 needle (*left side*) and 24 h after the injection (*i.e.*, making sure the system has relaxed, *right side*) are shown.

by hydrogen bonds) upon application of a certain stress. After the samples are stressed to high shear rates (about 50 s^{-1}), a hysteresis effect is observed upon the application of a decreasing shear rate ramp. This is typical of CMC concentrated solutions [26], that are characterized by a rheopectic behavior whose magnitude increases upon lowering the applied shear stress.

The introduction of HNTs, due to their chemical functionalities favoring inter-chain interactions, substantially modifies the rheological behavior of the system, making it significantly more viscous (at least twice as much) in the entire range of shear rates explored. Below 0.05 s^{-1} the sample displays a steep shear-thickening effect, followed by a pseudo-Newtonian behavior up to about 0.1 s^{-1}, and then by a shear-thinning region similarly to CMC/oxCMC. The trend at very low shear rates strongly reminds the case of polymeric composites filled with fumed silica nanoparticles [27]. In that paper the authors ascribed the trend in the viscosity to the initial alignment of the particles along the flow direction, followed by their aggregation and the subsequent hindering of the flow. Once the applied stress overcomes the so-called elasto-hydrodynamic lubrication limit of shear thickening, the hydrodynamicity prevails and all the clusters are pushed in the flow direction favoring the transition from a shear thickening to a shear thinning regime.

Moreover, the composite displays thixotropy at shear rates higher than 0.1 s^{-1}, while at lower shear rates, the effect of the CMC/oxCMC network prevails and an anti-thixotropic behavior is observed. We explain this behavior based on the profile of the relaxation spectra (Fig. S7) that shift toward higher τ values upon the addition of HNTs, indicating an increase of the main relaxation time (given by the peak position).

The composite hydrogel was also investigated by means of injectability tests through two different needle gauges (G21: $D = 12$ mm; $d = 0.51$ mm; $l = 40$ mm and G29: $D = 4.7$ mm; $d = 0.18$ mm; $l = 20$ mm), which are commonly employed for intramuscular and subcutaneous injections, respectively. The tests were performed by applying controlled loads on the plunger of a syringe loaded with the composite, and by measuring the corresponding flow.

Taking into account the geometrical parameters of the syringe and the needle, an apparent viscosity can be estimated from the Poiseuille law (Eq. (1)). Injectability results on the NC-MA composite are reported in Fig. 3 (in the middle), together with the results on the CMC/oxCMC reference sample. The investigated range of applied loads was chosen so to cover the operative conditions commonly adopted in minimally invasive surgery, starting from the minimum value producing an even flow of our composites. As a reference, the load applied by an operator on a syringe plunger easily exceeds 1.5 kg.

Results show that the apparent viscosity exponentially increases when the load is reduced and that our composite material can be easily injected through G21 and G29 needles under loads well below 1 kg. To make the (qualitative) comparison with the rotational rheology experiments one could calculate the wall shear rate in the injectability experiments considering a Newtonian fluid flowing within a pipe (see Fig. S8). The resulting flow curves in terms of apparent viscosity *versus* wall shear rate clearly indicate that the injection process takes place within the shear thinning region (see Fig. S9).

The lowest load producing a homogeneous flow with G21 was as small as about 0.4 kg (about 0.55 kg with G29). In spite of the presence of inorganic nanostructures that could in principle aggregate and obstruct the orifice, the injectability is mostly dictated by the CMC/oxCMC matrix, as no major difference was observed between the composite and the reference hydrogels. This could be attributed to the peculiar 1D structure of Halloysite nanotubes, which tend to align with the direction of the flow. This is confirmed by the SEM images in Fig. 3 (before and after the injection), showing that the injection produces a strong change in the structure of the polymer matrix at the microscale. This change was also reflected in the injectability behavior: in fact, once injected under the lower loads, the material was not any longer injectable, unless the load was increased. This is especially interesting in the framework of using our material in minimal invasive surgery: in fact, once injected, the structuring of the material takes to an increase of its viscosity, eventually reducing its spreading from the injection site. Together with the very small size of the needles and the low flow achievable, this could result in the possibility to robotically apply our composite at the damaged site with a high spatial resolution.

4. Conclusions

In conclusion, we explored the injectability potentials of nanocomposite hydrogels made of 1D nanostructures embedded within a polysaccharide matrix, properly modified by simple chemical routes and coupled through a biodegradable hydrazone bond.

Thanks to the mechanical properties of halloysite nanotubes and carboxymethyl cellulose, their biocompatibility, and their ability to upload and release bio-actives, our materials could represent a versatile platform for the supported growth of bone tissue. An already known protocol based on the hydrazide-aldehyde coupling into a biodegradable hydrazone bond was employed to obtain a homogeneous composite. The injectability tests provided a quantitative evaluation of the performances in practical conditions. The composite was successfully injected through needles with inner diameters spanning from 510 to 180 μm, without any clogging also at very low applied loads (*i.e.*, less than 1 kg). The injection of the material takes to its structuring, resulting in an increase of its viscosity at low shear rates. We believe that these results could represent a significant contribution to extend the use of composite hydrogels to minimal invasive surgery. Further studies are needed to validate the *in-vivo* application of our materials and they must concern with the evaluation of their biodegradation, their toxicological effects, and their influence on the bio-mineralization process.

Acknowledgment

Consorzio per lo sviluppo dei sistemi a grande interfase, CSGI, is acknowledged for financially supporting this work.

Appendix A. Supplementary data

Supplementary data associated with this article can be found, in the online version, at http://dx.doi.org/10.1016/j.colsurfb.2016.05.056.

References

[1] A.E. Raftery, N. Li, H. Ševčíková, P. Gerland, G.K. Heilig, Bayesian probabilistic population projections for all countries, Proc. Natl. Acad. Sci. 109 (2012) 13915–13921, http://dx.doi.org/10.1073/pnas.1211452109.
[2] A. Svedbom, M. Ivergård, J. Compston, C. Cooper, J. Stenmark, E.V. McCloskey, et al., Osteoporosis in the European Union: a compendium of country-specific reports, Arch. Osteoporos. 8 (2013), http://dx.doi.org/10.1007/s11657-013-0137-0.
[3] J.B. Dimick, A.M. Ryan, TAking a broader perspective on the benefits of minimally invasive surgery, JAMA Surg. 148 (2013), http://dx.doi.org/10.1001/jamasurg.2013.160, 648–648.
[4] F. Cilurzo, F. Selmin, P. Minghetti, M. Adami, E. Bertoni, S. Lauria, et al., Injectability evaluation: an open issue, AAPS PharmSciTech. 12 (2011) 604–609, http://dx.doi.org/10.1208/s12249-011-9625-y.
[5] Injectable Biomaterials: Science and Applications, in: B. Vernon (Ed.), Woodhead Pub, Oxford; Philadelphia, 2011.
[6] S. Lü, C. Gao, X. Xu, X. Bai, H. Duan, N. Gao, et al., Injectable and self-healing carbohydrate-based hydrogel for cell encapsulation, ACS Appl. Mater. Interfaces 7 (2015) 13029–13037, http://dx.doi.org/10.1021/acsami.5b03143.
[7] R. Arun Kumar, A. Sivashanmugam, S. Deepthi, S. Iseki, K.P. Chennazhi, S.V. Nair, et al., Injectable chitin-poly(ε-caprolactone)/nanohydroxyapatite composite microgels prepared by simple regeneration technique for bone tissue engineering, ACS Appl. Mater. Interfaces 7 (2015) 9399–9409, http://dx.doi.org/10.1021/acsami.5b02685.
[8] A.K. Gaharwar, R.K. Avery, A. Assmann, A. Paul, G.H. McKinley, A. Khademhosseini, et al., Shear-thinning nanocomposite hydrogels for the treatment of hemorrhage, ACS Nano 8 (2014) 9833–9842, http://dx.doi.org/10.1021/nn503719n.
[9] N.Q. Tran, Y.K. Joung, E. Lih, K.D. Park, In situ forming and rutin-releasing chitosan hydrogels as injectable dressings for dermal wound healing, Biomacromolecules 12 (2011) 2872–2880, http://dx.doi.org/10.1021/bm200326g.
[10] A. Sannino, C. Demitri, M. Madaghiele, Biodegradable cellulose-based hydrogels: design and applications, Materials 2 (2009) 353–373, http://dx.doi.org/10.3390/ma2020353.
[11] E. Joussein, S. Petit, J. Churchman, B. Theng, D. Righi, B. Delvaux, Halloysite clay minerals—a review, Clay Miner. 40 (2005) 383–426, http://dx.doi.org/10.1180/0009855054040180.
[12] V. Vergaro, E. Abdullayev, Y.M. Lvov, A. Zeitoun, R. Cingolani, R. Rinaldi, et al., Cytocompatibility and uptake of halloysite clay nanotubes, Biomacromolecules 11 (2010) 820–826, http://dx.doi.org/10.1021/bm9014446.
[13] M. Liu, Y. Zhang, C. Wu, S. Xiong, C. Zhou, Chitosan/halloysite nanotubes bionanocomposites: structure, mechanical properties and biocompatibility, Int. J. Biol. Macromol. 51 (2012) 566–575, http://dx.doi.org/10.1016/j.ijbiomac.2012.06.022.
[14] U.A. Handge, K. Hedicke-Höchstötter, V. Altstädt, Composites of polyamide 6 and silicate nanotubes of the mineral halloysite: influence of molecular weight on thermal, mechanical and rheological properties, Polymer 51 (2010) 2690–2699, http://dx.doi.org/10.1016/j.polymer.2010.04.041.
[15] J. Yuan, H.H. Murray, The importance of crystal morphology on the viscosity of concentrated suspensions of kaolins, Appl. Clay Sci. 12 (1997) 209–219, http://dx.doi.org/10.1016/S0169-1317(97)00006-9.
[16] S. Del Buffa, M. Bonini, F. Ridi, M. Severi, P. Losi, S. Volpi, et al., Design and characterization of a composite material based on Sr(II)-loaded clay nanotubes included within a biopolymer matrix, J. Colloid Interface Sci. 448 (2015) 501–507, http://dx.doi.org/10.1016/j.jcis.2015.02.043.
[17] S. Del Buffa, E. Grifoni, F. Ridi, P. Baglioni, The effect of charge on the release kinetics from polysaccharide–nanoclay composites, J. Nanoparticle Res. 17 (2015) 1–12, http://dx.doi.org/10.1007/s11051-015-2947-z.
[18] S.B. Campbell, M. Patenaude, T. Hoare, Injectable superparamagnets: highly elastic and degradable poly(*N*-isopropylacrylamide)–superparamagnetic iron oxide nanoparticle (SPION) composite hydrogels, Biomacromolecules 14 (2013) 644–653, http://dx.doi.org/10.1021/bm301703x.
[19] M. Patenaude, T. Hoare, Injectable, mixed natural-synthetic polymer hydrogels with modular properties, Biomacromolecules 13 (2012) 369–378, http://dx.doi.org/10.1021/bm2013982.
[20] D.G. Shchukin, G.B. Sukhorukov, R.R. Price, Y.M. Lvov, Halloysite nanotubes as biomimetic nanoreactors, Small 1 (2005) 510–513, http://dx.doi.org/10.1002/smll.200400120.
[21] V. Burckbuchler, G. Mekhloufi, A.P. Giteau, J.L. Grossiord, S. Huille, F. Agnely, Rheological and syringeability properties of highly concentrated human polyclonal immunoglobulin solutions, Eur. J. Pharm. Biopharm. 76 (2010) 351–356, http://dx.doi.org/10.1016/j.ejpb.2010.08.002.
[22] H. Li, B. Wu, C. Mu, W. Lin, Concomitant degradation in periodate oxidation of carboxymethyl cellulose, Carbohydr. Polym. 84 (2011) 881–886, http://dx.doi.org/10.1016/j.carbpol.2010.12.026.
[23] M. Bonini, S. Lenz, E. Falletta, F. Ridi, E. Carretti, E. Fratini, et al., Acrylamide-Based magnetic nanosponges: a new smart nanocomposite material, Langmuir 24 (2008) 12644–12650, http://dx.doi.org/10.1021/la802425k.
[24] R.A. Sperling, W.J. Parak, Surface modification, functionalization and bioconjugation of colloidal inorganic nanoparticles, Philos. Trans. R. Soc. Lond. Math. Phys. Eng. Sci. 368 (2010) 1333–1383, http://dx.doi.org/10.1098/rsta.2009.0273.
[25] E.M.J. Johansson, S. Plogmaker, L.E. Walle, R. Schölin, A. Borg, A. Sandell, et al., Comparing surface binding of the maleic anhydride anchor group on single crystalline anatase TiO_2 (101), (100), and (001) Surfaces, J. Phys. Chem. C 114 (2010) 15015–15020, http://dx.doi.org/10.1021/jp104897k.
[26] M. Edali, M.N. Esmail, G.H. Vatistas, Rheological properties of high concentrations of carboxymethyl cellulose solutions, J. Appl. Polym. Sci. 79 (2001) 1787–1801, http://dx.doi.org/10.1002/1097-4628(20010307)79:10<1787:AID-APP70>3.0.CO;2-2.
[27] J. Ding, T. Tian, Q. Meng, Z. Guo, W. Li, P. Zhang, et al., Smart multifunctional fluids for lithium ion batteries: enhanced rate performance and intrinsic mechanical protection, Sci. Rep. 3 (2013), http://dx.doi.org/10.1038/srep02485.

SUPPLEMENTARY MATERIAL

Injectable composites *via* functionalization of 1D nanoclays and biodegradable coupling with a polysaccharide hydrogel

Stefano Del Buffa, Elia Rinaldi, Emiliano Carretti, Francesca Ridi, Massimo Bonini, Piero Baglioni*

Department of Chemistry "Ugo Schiff" and CSGI, University of Florence,
via della Lastruccia 3, Sesto Fiorentino, 50019 Florence, Italy.

Table of Contents

1. Surface Area and Pore Volume Analysis of HNT

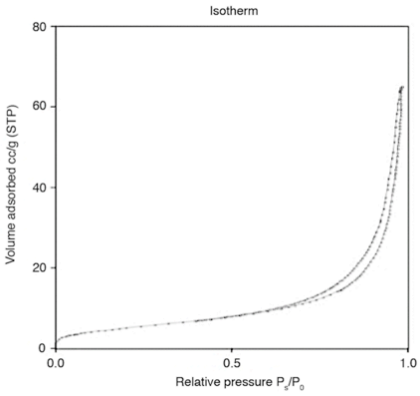

Pore Dia. Range(nm)	Pore Volume (ml/g)	%
Under 6	0.00630	3.45
6 - 8	0.00326	1.78
8 - 10	0.00326	1.79
10 - 12	0.00401	2.19
12 - 16	0.00671	3.67
16 - 20	0.00844	4.62
20 - 80	0.07260	39.72
Over 80	0.07821	42.79
BJH Total	0.18279	100.00

Figure S1. N_2 adsorption isotherm and pore size distribution, as obtained with BJH calculation, of a HNT sample. BET surface area was found to be 25 ± 3 m^2/g.

2. Preparation of NC-MA Composite Hydrogel

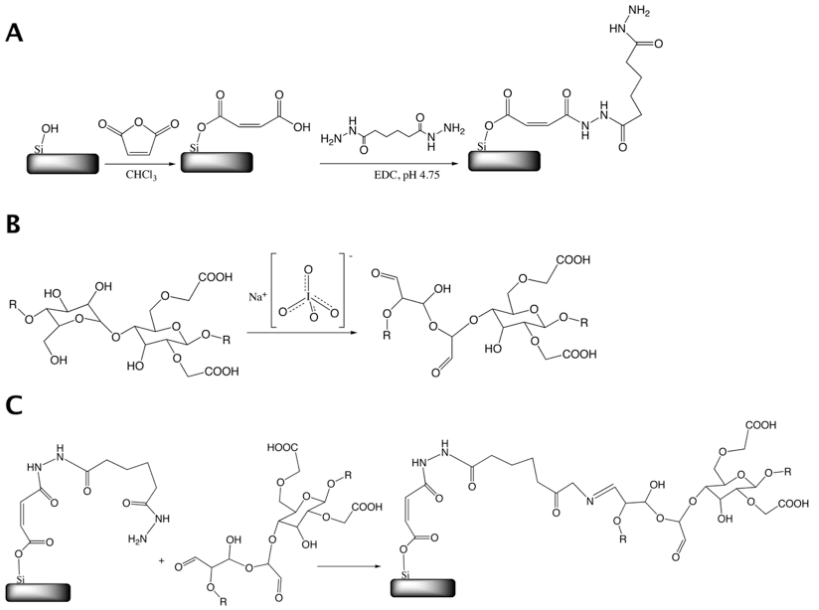

Figure S2. Synthetic route for the fabrication of NC-MA composite hydrogel.

(A) HNT surface was firstly modified by the reaction of the external silanol groups with maleic anhydride (MA). 10 g of clay and 10 g of anhydride were added to 100 ml of chloroform, previously bubbled with N_2, and kept at 37 °C under stirring overnight. The solid product was recovered by centrifugation, washed with chloroform and dried. HNT-MA was further reacted with adipic acid dihydrazide (AAD) to introduce a hydrazine moiety on the clay surface. 1.5 g of AAD was added to a 0.5 %w/v water dispersion of HNT-MA, at room temperature. Then, 780 µl of EDC were added (pH of the dispersion is about 4) and the reaction was allowed to run during 5 hours, checking and eventually adjusting the pH with HCl 0.1 M to remain constant. After 5 hours the pH was adjusted to pH = 7 with NaOH and the dispersion was dialyzed (membrane cut-off = 12.4 kDa) against milliQ water. The solid product was then recovered by centrifugation.
(B) To partially oxidize carboxymethyl cellulose (CMC), 10 g of solid was dissolved in water (at a concentration of 1% w/v), then 5.3 g of sodium periodate were added and the solution was kept under agitation for two hours, at room temperature. Ethylene glycol (2.7 ml) was then added to quench the oxidation reaction. The polymer solution was dialyzed (membrane cut-off = 12.4 kDa) and the solvent was partially removed by rotavapor. The obtained oxidized CMC (oxCMC) was finally freeze-dried. The short reaction time and the low concentration of oxidizing agent prevent a marked degradation of the polymer [Li, H.; Wu, B.; Mu, C.; Lin, W. Concomitant Degradation in Periodate Oxidation of Carboxymethyl Cellulose. *Carbohydr. Polym.* **2011**, *84* (3), 881–886.].
(C) In the last step, oxCMC was mixed with modified HNT in milliQ water under mechanical stirring. The final concentration of both oxCMC and HNT-MA was 10 %wt. The NC-MA nanocomposite hydrogel was finally obtained by adding pristine CMC to a final concentration of 2 %wt.

3. IR Characterization of HNT-MA

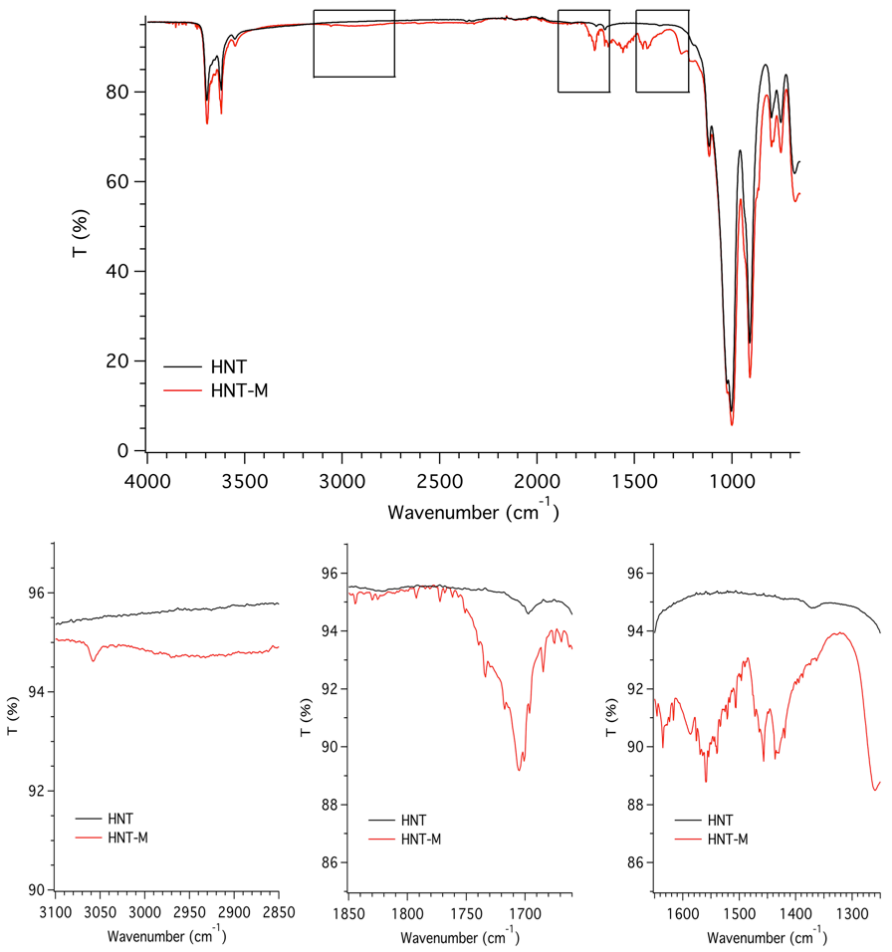

Figure S3. ATR FT-IR spectra of HNT-MA in the 650 - 4000 cm^{-1} range (the spectrum of pure HNT is also shown for comparison). In the HNT-MA spectrum signals attributable to saturated and unsaturated C-H stretching are detected at 2931 cm^{-1}, corresponding to maleic residues. Carbonyl C=O stretching is observed around 1700 cm^{-1} and the signal corresponding to C=C stretching at ~1600 cm^{-1} is clearly observed.

4. Zeta potential values of the products obtained from the functionalization of Halloysite nanotubes surface

Sample	**Zeta Potential**
HNT	- 42.9 ± 1.1 mV
HNT-MA	- 27.6 ± 0.6 mV
HNT-MA-AAD	- 12.2 ± 0.3 mV

5. Characterization of Oxidized CMC (oxCMC)

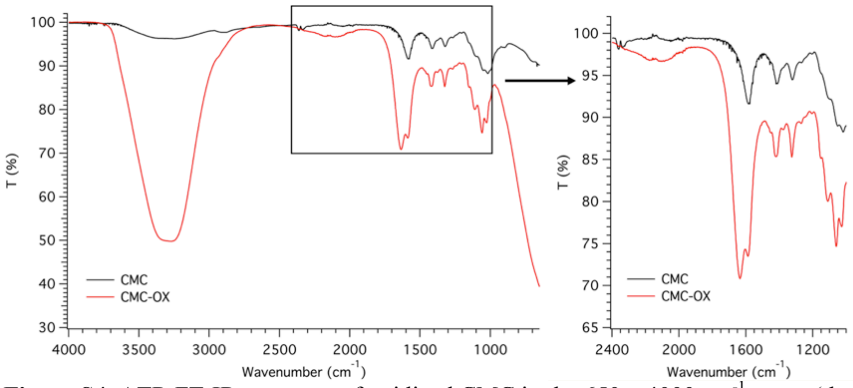

Figure S4. ATR FT-IR spectrum of oxidized CMC in the 650 – 4000 cm^{-1} range (the spectrum of pristine CMC is also shown for comparison). The appearance of a peak at ~1630 cm^{-1}, in addition to the carboxylate peak at ~1590 cm^{-1} is the evidence that oxidation of CMC actually took place [Biswas, A.; Kim, S.; Selling, G. W.; Cheng, H. N. Conversion of Agricultural Residues to Carboxymethylcellulose and Carboxymethylcellulose Acetate. *Ind. Crops Prod.* **2014**, *60*, 259–265.].

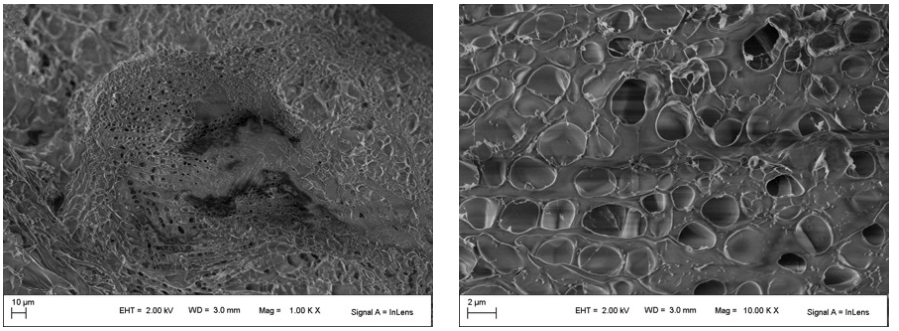

Figure S5. SEM images of freeze-dried samples of oxidized CMC in water. As can be deduced from the SEM image, oxCMC maintains the ability to form the typical porous structure of pristine cellulose hydrogels. The result is consistent with a modest level of degradation of the polymer [Li, H.; Wu, B.; Mu, C.; Lin, W. Concomitant Degradation in Periodate Oxidation of Carboxymethyl Cellulose. *Carbohydr. Polym.* **2011**, *84* (3), 881–886].

6. Thermogravimetry of NC-MA composite

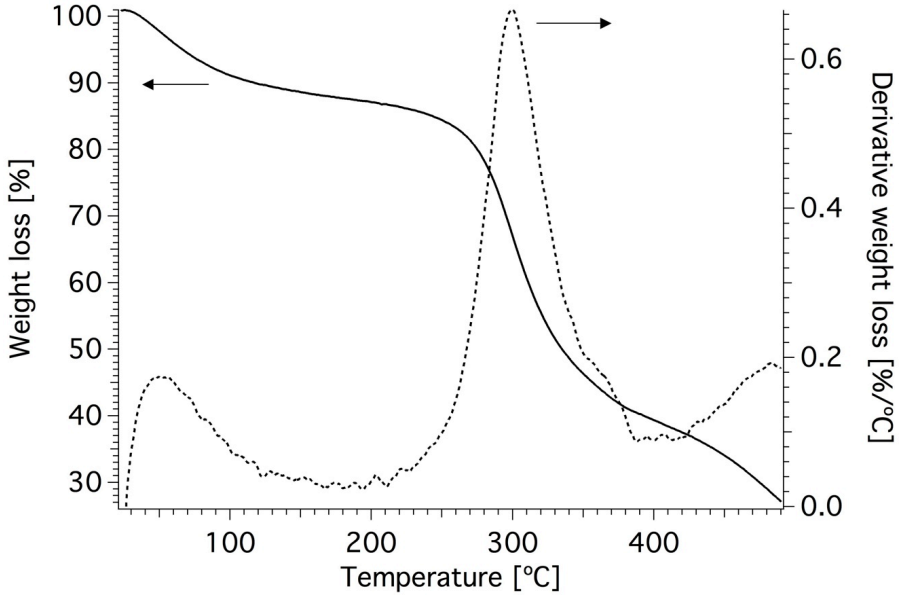

Figure S6. TGA and DTG thermograms of the NC-MA composite showing that, once water is removed from the material, the organic and inorganic contents are about 50% w/w.

7. Dynamic rheology of CMC/oxCMC and NC-MA aqueous systems

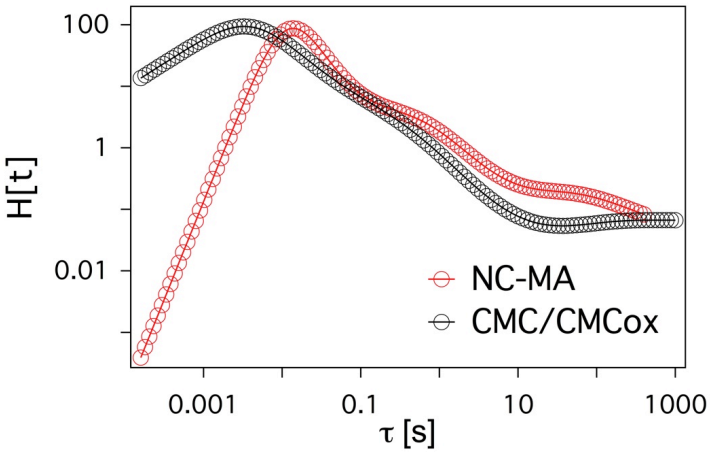

Figure S7. Continuous relaxation spectra *H[τ]* of the CMC/oxCMC water based system before (black) and after (red) the loading of NC-MA composite. The spectra *H[t]* have been obtained from the frequency sweep curves of the two systems collected in the linear viscoelastic regime [Honerkamp, J., Weese, J. A nonlinear regularization method for the calculation of relaxation spectra. *Rheol. Acta.* **1993,** *32*, 65-73], since the dynamic of the two systems cannot be described by a single-element Maxwell model.

8. Injectability tests: wall shear rates *vs* applied load curves

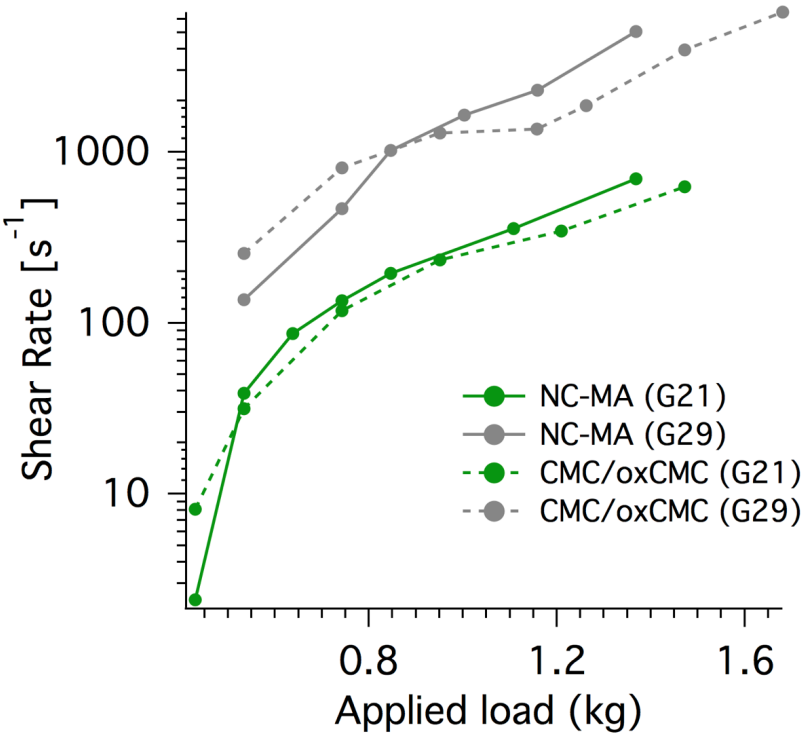

Figure S8. Apparent wall shear rate as a function of the applied load during injectability tests. The shear rate is calculated by considering a Newtonian fluid flowing within a pipe of radius *r*, and it is approximately given by $4Q/\pi r^3$ (Q=measured flow of the material exiting the syringe needle).

9. Injectability tests: apparent viscosity *vs* wall shear rates

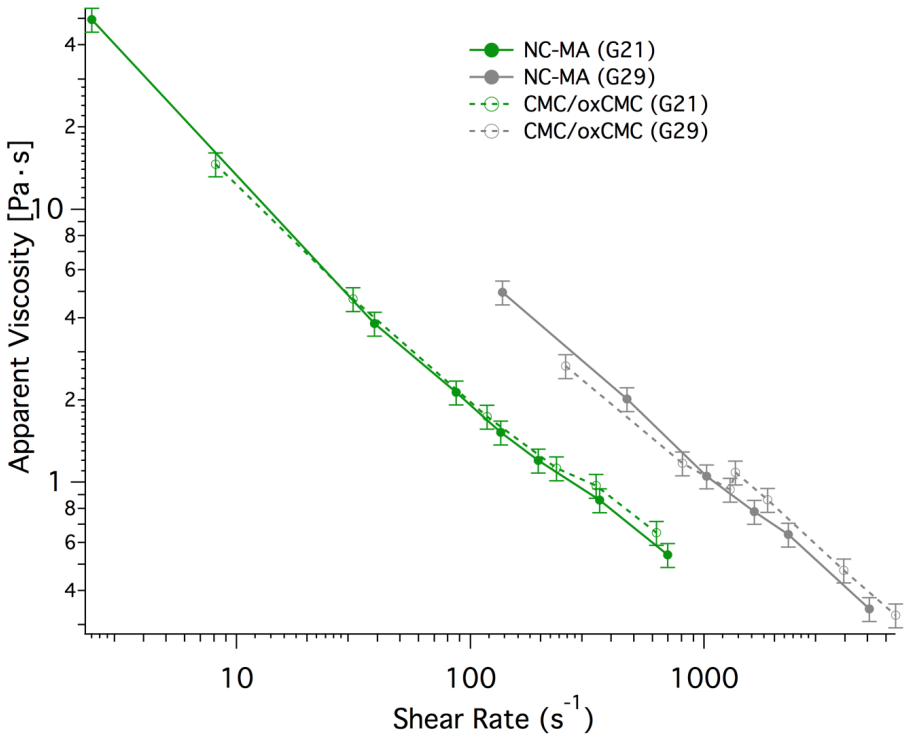

Figure S9. Flow curves of NC-MA composite and CMC/oxCMC derived from the results of injectability tests. The apparent viscosity is estimated from the Poiseuille law by knowing the load applied to the syringe, the geometrical parameters of the syringe and the needle and by measuring the corresponding flow, while the wall shear rate is approximately given by $4Q/\pi r^3$ (Q= measured flow, r= inner radius of the needle).

Enhanced formation of hydroxyapatite in imogolite-reinforced macroporous hydrogels

Rita Gelli, Stefano Del Buffa, Paolo Tempesti, Massimo Bonini, Francesca Ridi, Piero Baglioni*

Department of Chemistry "Ugo Schiff" and CSGI, University of Florence, via della Lastruccia 3, Sesto Fiorentino, 50019 Florence, Italy

piero.baglioni@unifi.it

Abstract

This paper reports on the inclusion of imogolite nanotubes in biocompatible hydrogels and on the use of such hybrid materials as a scaffold for the formation of hydroxyapatite. The results demonstrate that imogolite nanotubes can be successfully included within a gelatin-based macroporous hydrogel, whose dissolution is slowed down by the addition of a non-toxic chemical cross-linker. Imogolite nanotubes synergistically contribute with the cross-linker to the stabilization against dissolution of the hydrogel. Noteworthy, they are able to support and promote the formation in the hydrogel matrix of hydroxyapatite enriched in carbonate ions, mimicking the composition of bone mineral phase. This suggests the use of imogolite nanotubes as fillers in mineralizable hydrogel scaffolds in the field of bone tissue engineering.

Keywords: clay materials, hydrogels, gelatin, nanotubes, tissue engineering

1. Introduction

Hydroxyapatite, $Ca_{10}(PO_4)_6(OH)_2$ (HA), composes the main mineral fraction of human bones and teeth. In bones, it is found as non-stoichiometric, calcium-deficient apatite, containing carbonate and impurities such as sodium and magnesium ions.[1,2] The presence of these inclusions, especially carbonate, contributes to the unique features of bone in terms of mechanical and biological properties.[3] The growth of HA nanocrystals takes place through the alignment of their *c*-axes to the self-assembled collagen fibrils, finally displaying a platelet shape with average lengths and widths of 50 x 25 nm, and thickness of 2-3 nm.[4]

Great efforts have been recently devoted to rationalize HA formation and crystallization in organic matrices,[5] in the attempt to unravel the process of bone tissue formation and remodelling. This is of particular interest in the fields of bone and dental tissue engineering, where synthetic scaffolds are designed to support and promote the growth of new tissue, including HA crystals with tuneable composition and structural properties.[6,7] One of the most investigated class of matrices suitable to this purpose are hydrogels because of the high amount of water they can upload, and because of the variety of biocompatible polymers able to form a 3-dimensional network in water.[8] Hydrogels are often endowed with the right features required in the design of a scaffold for bone tissue engineering. Biocompatibility is the most important prerequisite.[9] Furthermore, the scaffold should also be osteoconductive, osteoinductive,[10] and display an interconnected and macroporous structure, with pore diameter of at least 100 μm to allow penetration by cells and adequate diffusion of nutrients into the material.[11] Cryogenic formation is typically used to generate pores in hydrogels.[12] The polymeric material is frozen and the water inside the matrix crystallizes producing porosities whose dimension depends on cooling rate and polymer concentration. After sublimation of ice, a scaffold with pores that can reach the size of tenths of millimetres could be typically obtained.

Gelatin (Gel) is one of the hydrogel-forming materials mostly investigated in bone tissue engineering applications,[8] having the same chemical composition of bone organic matrix: in fact, it is produced by partial hydrolysis of collagen, which undergoes a strong alkali or acid treatment which denatures the protein and breaks down the characteristic triple-helix structure. Unfortunately, its application in this field is limited because of its fast dissolution rates at physiological conditions, making necessary the increase of the stability of gelatin-based material.[13,14]

The most frequent methods to increase the stability of gelatin scaffolds are the introduction of covalent cross-linking sites that can be obtained by using ionizing radiation, such as electrons or gamma rays,[15] by fabricating composite materials,[16] or by employing chemical cross-linking agents that react with the functional groups of gelatin; glutaraldehyde,[17] 1-Ethyl-3-(3-dimethylaminopropyl)carbodiimide (EDC) [18] and genipin [19] are among the most frequently used. Bis-epoxy molecules, such as glycerol diglycidyl ether (GDE) and ethylene glycol diglycidyl ether (EGDE), have also been reported to enhance the stability of gelatin hydrogels,[20] as the epoxide ring could be opened by the gelatin nucleophilic functional groups, namely amine, hydroxyl and carboxyl groups. In the perspective of a biomedical application, the cross-linker toxicity is a parameter that should be considered, since unreacted molecules can affect the final biocompatibility. Bis-epoxy cross-linking agents display a lower toxicity compared to glutaraldehyde and EDC, representing a better alternative to typical gelatin cross-linkers.[21]

Another strategy that has been employed to enhance the mechanical properties and the stability of a polymeric hydrogel is its integration with inorganic fillers (fibres and nanotubes are the most used) to obtain a composite material.[22] Carbon nanotubes (CNTs) have been extensively studied for the fabrication of polymer composites with superior mechanical properties, but there are still concerns about their toxicity.[23]

Imogolite (Imo) is a naturally occurring hydrous aluminosilicate with empirical formula $(OH)_3Al_2O_3SiOH$, displaying a single wall nanotube structure. It was first discovered in volcanic soils deposits (Kyushu Island, Japan) by Yoshinaga and Aomine in 1962,[24] and it was first synthetized by Farmer *et al.* in 1977.[25] The structure proposed by Cradwick *et al.*[26] is shown in Figure 1a and it consists of single-walled nanotube made of gibbsite ($Al(OH)_3$), where the inner hydroxyl groups are replaced by O_3SiOH groups. Typical external and internal diameters are ~2.5 nm and 1 nm, respectively,[27] with lengths up to few microns.[22] Given their very high aspect ratio, Imo application as inorganic filler for the reinforcement of polymeric matrices is well reported in literature,[28–30] in addition to its use in gas storage,[31–33] and in the realization of hybrid hydrogels with DNA [34] or enzymes.[35] Furthermore, Imo nanotubes display a reduced cyto- and geno-toxicity with respect to CNTs.[36] In the field of bone tissue engineering, the presence of Imo has been demonstrated to enhance osteoblastic proliferation and differentiation.[37]

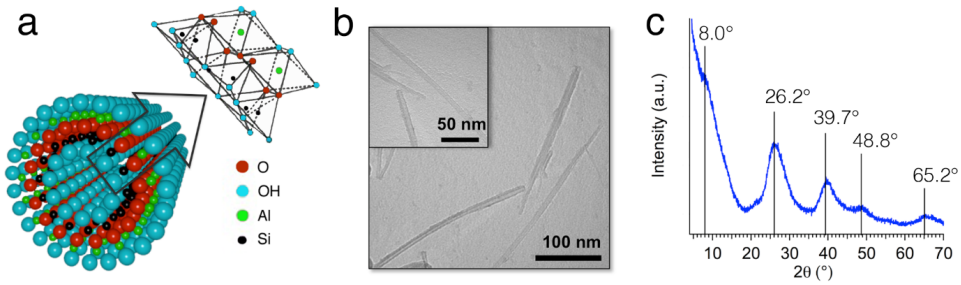

Figure 1. (a) Schematic structure of imogolite nanotubes showing octahedral AlOH and tetrahedral SiO sheets forming the outer and inner surface of the tube, respectively; (b) TEM images of synthesized imogolite nanotubes taken at two different magnifications; (c) XRD spectrum of synthesized imogolite nanotubes.

An imogolite reinforced gelatin composite was recently studied and the reported results show that these clay nanotubes increase the mechanical strength and the storage modulus of the hydrogel.[28] In order to fully exploit the characteristics of Gel/Imo system in the field of bone tissue engineering, in this paper we describe the preparation of a gelatin scaffold whose dissolution rate at physiological temperature is slowed down due to the synergistic effect of an organic cross-linker (GDE) and Imo nanotubes. Using the cryogenic method, we were able to generate macropores in the hydrogel network, matching the proper dimensions for the permeation of cells. We performed mineralization experiments and the results, obtained by means of X-ray crystallography, electron and optical microscopy, thermogravimetry and dissolution tests demonstrated that the hydrogel was able to support the formation of apatites. Moreover, for the first time, we showed that Imo acts as nucleation site for the calcium phosphate and for this reason enhances the formation of both HA and carbonated HA (CHA), thus producing a material with suitable properties for applications in bone tissue engineering.

2. Experimental

2.1 Materials

Tetraethyl orthosilicate (TEOS) was obtained from Fluka (Milan, Italy) and Aluminium-tri-sec-butoxide (ASB, 97 %) was purchased from Sigma Aldrich (Milan, Italy). Perchloric acid (70 %) was obtained from Merck (Milan, Italy). Calcium hydroxide was purchased from Acros (Belgium) and Phosphoric acid (85 %) from Carlo Erba (Milan, Italy). Gelatin from porcine skin, 250 Bloom, was obtained from Fluka and Glycerol diglycidyl ether (GDE) was purchased from Sigma Aldrich.

2.2 Imogolite synthesis

Imo nanotubes were synthesized following a procedure reported in the literature.[38] Tetraethyl orthosilicate (TEOS, 840 μL) and aluminium-tri-sec-butoxide (ASB, 1.90 g) were added to a $HClO_4$ solution (150 mL, 0.025 M) pre-heated at 70 °C so to reach a Si:Al:$HClO_4$ molar ratio of 1:2:1. The dispersion was kept at 70 °C during 5 hours under continuous stirring, and then refluxed at 100 °C during 3 days. The reaction mixture was then cooled down, dialyzed with cellulose membranes (cut-off=14.4 kDa) against MilliQ water to remove unreacted reagents, and freeze-dried (-50 °C, $3 \cdot 10^{-2}$ mmHg). The obtained fluffy powder displays a specific surface of 340 m^2/g, as determined by N_2 porosimetry.

2.3 Hydroxyapatite synthesis

HA has been synthetized according to a method reported in the literature [39] and schematized in Figure 2a. The reaction was performed at 37 ºC to simulate the physiological temperature. Imogolites were added to calcium hydroxide suspension (5 mL, 0.5 M) before adding H_3PO_4. The concentration of Imo was chosen so to be 5 %wt and 10 %wt of the calculated weight of precipitated HA. The slow addition of H_3PO_4 enables obtaining crystalline HA with nanometric size (~ 50 nm), according to the literature:[39] for this reason, H_3PO_4 solution (5 mL, 0.3 M) was added in aliquots of 200 μl every 5 minutes, during 2 hours. The suspensions ware maintained under stirring at 37 °C for 15 hours, and then at room temperature for three days. During this time a gelatinous product gradually precipitated from initially white suspensions. The obtained products were collected by centrifugation and dried in oven at 120 °C during three days.

2.4 Hydrogels preparation

Gelatin hydrogels were prepared using the following procedure, schematized in Figure 3a: the amount of gelatin necessary to reach the concentration of 5 %wt was dissolved in MilliQ water (0.5 g of gelatin in 9.5 g of water) and heated at 50 °C under magnetic stirring. After complete dissolution, the appropriate amount of imogolite and/or GDE was added to gelatin solution, which was stirred for about 10 minutes. The amounts of reactant used and the respective %wt are summarized in Table 1. After homogenization, the hot dispersions were poured in polyethylene cylindrical moulds (diameter 1 cm, height 1 cm) and were allowed to gel at room temperature. The formation of macropores was obtained by means of a cryogenic formation procedure:

the hydrogels were cooled overnight in a freezer to -18 °C (cooling rate 1 °C/min) and then freeze-dried at -50 °C and 30 mTorr for two days.

Table 1. Composition and dissolution behaviour of hydrogels.

Sample	Gelatin [g]	Water [g]	GDE [g]	Imo [g]	GDE %wt [a)]	Imo %wt[b)]	Dissolution time[c)]
Gel	0.5	9.5	/	/	/	/	~ 2 hours
Gel_{GDE}	0.5	9.5	0.025	/	5	/	~ 2 days
Gel_{GDE}-Imo	0.5	9.5	0.025	0.0525	5	10	~ 3 days
Gel-Imo5	0.5	9.5	/	0.0250	/	5	~ 6 hours
Gel-Imo10	0.5	9.5	/	0.0500	/	10	~ 6 hours
Gel_{GDE5}-Imo5	0.5	9.5	0.025	0.0262	5	5	~ 3 days
Gel_{GDE10}-Imo5	0.5	9.5	0.050	0.0275	10	5	> 5 days
Gel_{GDE10}-Imo10	0.5	9.5	0.050	0.0550	10	10	> 5 days

[a)] %wt with respect to gelatin; [b)] %wt with respect to organic content (gelatin+GDE); [c)] time required to observe full dissolution in water at 37 ºC.

2.5 Mineralization experiment

The synthesis of CaP inside the gels was performed using the synthetic conditions previously described for hydroxyapatite synthesis. A portion of the freeze-dried Gel_{GDE} and Gel_{GDE}-Imo was cut and each portion was soaked in $Ca(OH)_2$ suspension (2.5 mL, 0.5 M at 37 °C. H_3PO_4 solution (2.5 mL 0.3 M) was added in aliquots of 105 µl every 5 minutes. At the end of the experiment, gels were recovered and dried in air.

2.6 Transmission electron microscopy

TEM analysis of imogolite nanotubes and HA was performed with a TEM Philips CM12 (Eindhoven, The Netherlands), working with an electron gun operating at 80 kV. Samples were prepared by depositing a droplet of Imo/HA dispersion onto a carbon coated copper grid.

2.7 Scanning Electron Microscopy

SEM was performed on non-metallized samples using a ∑IGMA Field Emission SEM (Carl Zeiss Microscopy GmbH, Germany). A cross section of the xerogel was cut and mounted on aluminium stub. Energy dispersive X-ray spectroscopy (EDX) was carried out using X-act Silicon Drift Detector (Oxford Instruments, England).

2.8 Optical Microscopy

OM images were obtained using Nikon Diaphot 300 and images were collected by means of a Nikon DS5M CCD camera directly connected to a PC. A thin slice of the freeze-dried hydrogels was cut using a razor blade, put on a microscope slide and observed in transmission.

2.9 X-ray Diffraction

XRD spectra were collected with a D8 Advance with DAVINCI design (Bruker, Milan, Italy), using Cu K_α radiation (λ=1.54Å), a range of 2θ of 5°-70° with a step size of 0.03°, and a time/step of 0.5 s. Characteristic dimensions were extrapolated from the position of the reflection peaks by applying Bragg's law. Quantitative phase analysis was conducted by means of Rietveld method, using the software Topas (Bruker). The % error associated to the obtained value is ±5 %.

2.10 Small Angle X-Ray Scattering

SAXS experiments were carried out with a S3-MICRO instrument (HECUS GmbH, Graz, Austria) equipped with a position-sensitive detector (OED 50M) containing 1024 channels of width 54 μm. Cu Kα radiation (λ=1.542 Å) was provided by a GeniX X-ray source (Xenocs, Grenoble, France), operating at a maximum power of 50 W (50 kV and 1 mA). Gel samples were placed into 1 mm demountable cells having Kapton films as windows. The temperature was maintained at 25 °C by means of a Peltier TCCS-3 Hecus. All scattering curves were corrected for the empty cell contribution considering the relative transmission factor. SAXS curves were fitted using the Ornstein-Zernike function describing polymers in a semi-dilute regime:

$$I(q) = \frac{I_0}{1 + \xi^2 q^2} \quad (1)$$

where I_0 is the scattered intensity at q=0, and ξ is the correlation length of the polymer.

Additional fittings were performed with power law functions to obtain information about the fractal nature of the scattering objects:

$$I(q) \propto q^{-p} \quad (2)$$

where p is the fractal dimension. When $1 \leq p \leq 3$, p is the mass fractal dimension (D_m) that is 1 for 1D objects and 3 for full solid materials. [40]

2.11 Thermogravimetric analysis

TGA was performed with a SDT Q600 from TA Instruments (Philadelphia, USA). Measurements were conducted in N_2 atmosphere (flow rate 100 mL/min) from RT to 1000 °C at 10 °C/min.

3. Results and discussion

3.1 Imogolite characterization

A representative Transmission Electron Microscopy (TEM) micrograph of the synthesized imogolite nanotubes (see Experimental Section) is reported in Figure 1b. In agreement with the literature,[27,38,41,42] Imo shows a strong tendency to form bundles. The observed bundles of nanotubes have external diameters ranging from 5 to 15 nm, internal diameters ranging from 1 to 3 nm, and lengths of about 250-300 nm. The X-ray Diffraction (XRD) pattern (Figure 1c) confirms the successful preparation, showing a very good agreement with previous results [38,43] and with the pattern reported in the International Centre for Diffraction Data database, ICDD, [PDF 38-0447].

3.2 Characterization of HA prepared in the presence of Imo

The characterization of the products of the precipitation reactions highlights that the presence of Imo does not inhibit the formation of HA: Figure 2b and Figure 2c show that the morphology of the HA obtained in water without and in the presence of 10 %wt of Imo does not significantly change. It is worth noting that TEM images of HA-Imo sample do not reveal the characteristic nanotubular morphology of Imo, suggesting that HA nucleates on the surface of these structures, and that the nanotubes are included in the final HA crystals. Their XRD patterns (Figure 2d) are nearly unaffected by the presence of Imo, apart from a hump at low angles in the diffractogram of HA-Imo sample, due to the presence of Imo. The XRD

peaks were compared to the patterns in the ICDD database and clearly indicate the formation of hydroxyapatite [PDF 03-0747]. The Field Emission Scanning Electron Microscopy (FE-SEM) investigation of HA and HA-Imo samples shows the same homogeneous morphology (see Supplementary material). The homogeneous distribution of aluminium and silicon obtained from Energy Dispersive X-ray (EDX) analysis of HA-Imo (see Figure 2e and Figure 2f) further confirms that Imo is well distributed all over the sample.

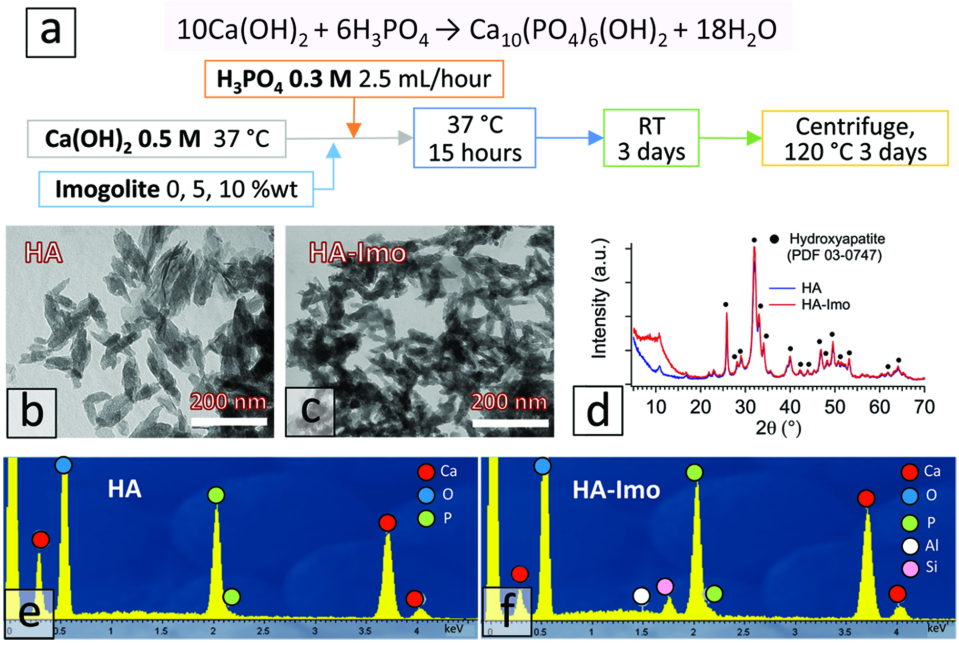

Figure 2. (a) Precipitation reaction of HA and scheme of the experimental conditions; (b) TEM image of HA obtained without Imo; (c) TEM image of HA obtained in the presence of Imo; (d) XRD patterns of HA and HA-Imo samples; (e) EDX spectrum of HA sample; (f) EDX spectrum of HA-Imo sample.

3.3 Hydrogels characterization

The effects of GDE and Imo on the stability toward dissolution of the scaffolds (obtained by freeze-drying the hydrogels) was evaluated by preparing samples at different combinations containing GDE and Imo, both at 5 and 10 %wt (see composition and nomenclature in Table 1), placing them in an excess of water and checking the time needed before their full dissolution at 37 °C. The results are summarized in Table 1 (last column), showing that the concentration of GDE strongly affects the behaviour of the hydrogel. Imo

nanotubes are also effective, at smaller extent, in enhancing the stability against dissolution. These results highlight the possibility to control the dissolution rate by introducing different amounts of GDE and Imo, and to tune it according to the tissue regeneration process of interest. Notably, the mineralization process will occur before the dissolution of the scaffold.

Based on their intermediate dissolution behaviour, we selected as case of study the samples identified as Gel_{GDE}, and Gel_{GDE}-Imo (see Table 1). The morphology of the xerogels, prepared as it is summarized in Figure 3a, was investigated by optical and scanning electron microscopy. Figure 3b, 3c and 3d report FE-SEM micrographs, together with the optical microscopy images, of Gel, Gel_{GDE} and Gel_{GDE}-Imo, respectively. All the samples display a macroporous structure, with interconnected pores whose dimensions range from tens to hundreds of microns. The cryo-formation procedure adopted in the preparation of porous hydrogels leads to a macroscopic deformation of the gel structure, clearly visible in the photos. Nevertheless, the formation of macropores, which is one of the key parameters to take into account in the design of a scaffold for tissue engineering,[11] is successfully obtained. The presence of the cross-linker, as well as imogolite integration in the polymeric matrix, does not significantly alter the gelatin microstructure. The inorganic fillers appear homogeneously dispersed in gelatin matrix, since no imogolite bundle can be observed in Gel_{GDE}-Imo FE-SEM micrograph (Figure 3d).

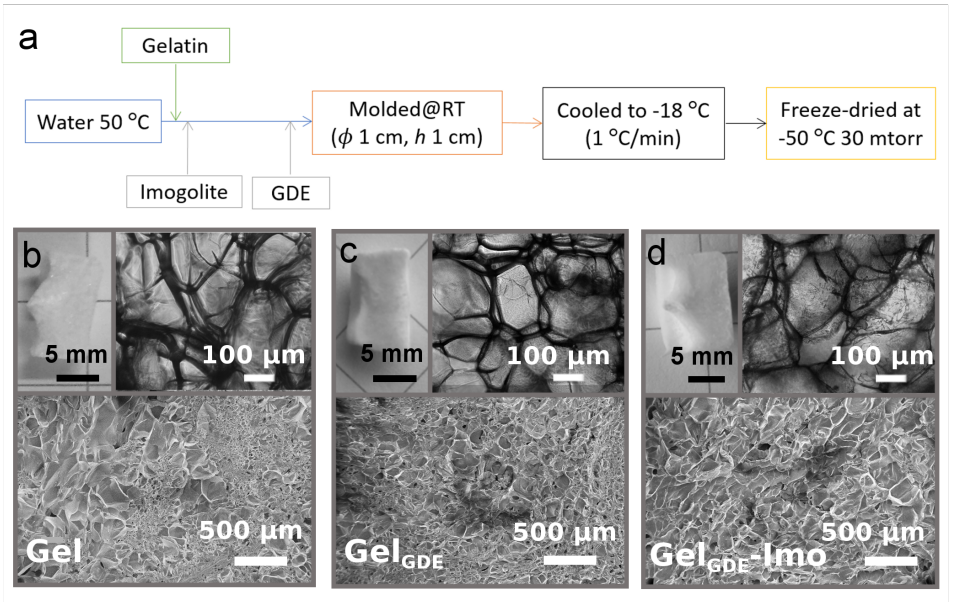

Figure 3. (a) Block diagram summarizing hydrogels preparation; (b), (c), (d) Photo (top left), OM image (top right) and SEM micrograph (bottom) of (from the left) Gel, Gel_{GDE} and Gel_{GDE}-Imo.

The nanostructure of the hydrogels was investigated by means of small angle X-rays scattering (SAXS). SAXS curves for Gel, Gel_{GDE}, and Gel_{GDE}-Imo (Figure 4) have been collected in order to evaluate the influence of both cross-linker and imogolites to the nanostructure of the gels. The SAXS curves are almost superimposable in the mid-to-high q range ($0.03 \leq q \leq 0.5$ Å^{-1}) and the correlation lengths obtained from the fittings of the curves according to Eq. 1 are 27 ± 1 Å, 28 ±1 Å, and 32 ± 2 Å for Gel, Gel_{GDE}, and Gel_{GDE}-Imo, respectively. This is a strong indication that the main contribution to the scattering profiles in this region is due to the polymer matrix and that the modifications of GDE and/or Imo to the gel network are negligible. The increase in the scattered intensity in the low q region ($0.009 \leq q < 0.3$ Å^{-1}) in Gel_{GDE}-Imo SAXS curve is a consequence of the presence of Imo in the gel, as it is not present in the other two profiles. Fitting according to Eq. 2 results in a mass fractal dimension of 1.7 that is typical of aggregated rod-like structures.[44]

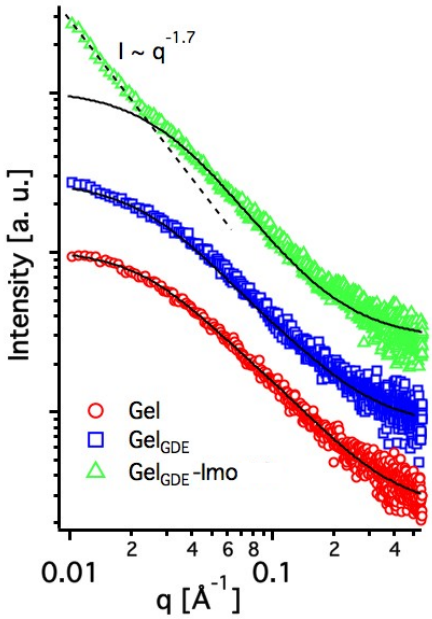

Figure 4. SAXS curves of Gel (circles), Gel_{GDE} (squares), and Gel_{GDE}-Imo (triangles). The curves are offset for display purposes. Full solid lined represent the curve fittings according to the Ornstein-Zernike function, while the dotted line is the power law fitting.

To evaluate the ability of our samples to induce the formation of HA, we adopted the same procedure used to prepare HA, but in the presence of the xerogel. Figure 5a reports a FE-SEM image of the xerogel obtained after the HA synthesis (Gel_{GDE}-CaP), clearly showing that the gel phase is homogeneously filled with sub-micrometric particles with the typical platelet shape (lateral size in the order of 100-200 nm, thickness of few tens of nm) displayed by HA in bones. The EDX spectrum (Figure 5c) confirms the presence of Ca and P, together with the signals corresponding to the elements present in gelatin. XRD analysis (Figure 5e) demonstrates that the mineral phase effectively consists of HA. We can therefore conclude that the hydrogel scaffold does not hinder the formation of hydroxyapatite, as the crystal size, shape composition and phase obtained in the hydrogel are nearly identical to that obtained in the HA reference synthesis (see Supplementary material).

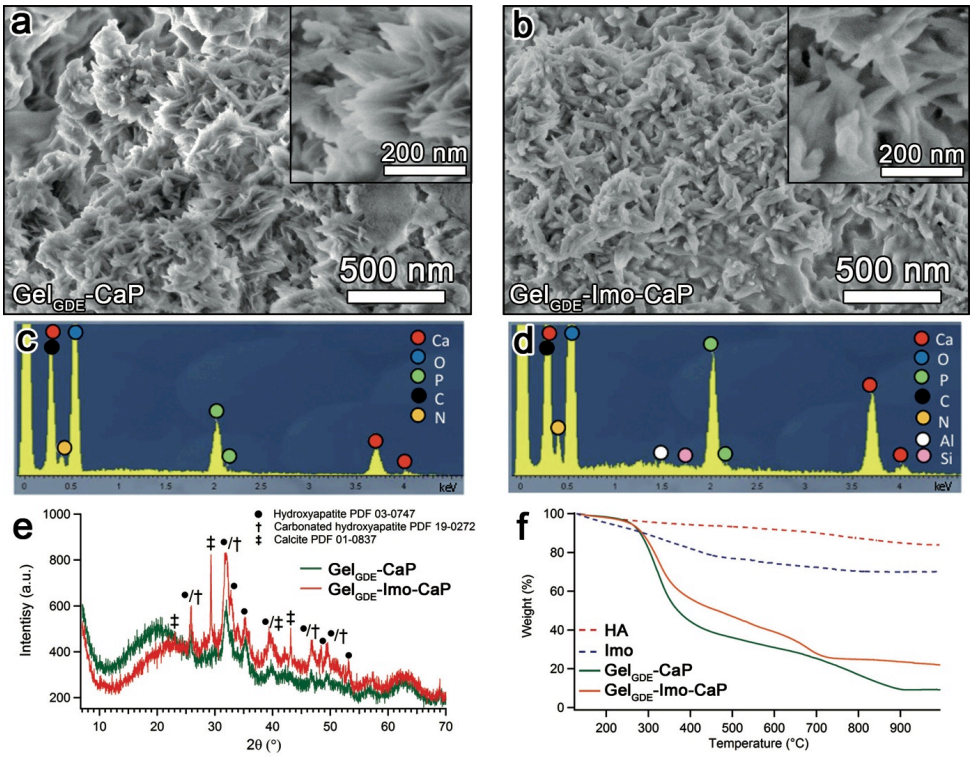

Figure 5. a,b) SEM images of Gel_{GDE}-CaP and Gel_{GDE}-Imo-CaP, respectively; c,d) EDX spectra of Gel_{GDE}-CaP and Gel_{GDE}-Imo-CaP, respectively; e) XRD patterns of Gel_{GDE}-CaP and Gel_{GDE}-Imo-CaP, together with the peak assignments according to HA, carbonated HA and calcite data; f) TGA profiles of Gel_{GDE}-CaP and Gel_{GDE}-Imo-CaP, together with pure HA and Imo.

The effect of Imo on the HA formation, when already embedded in the hydrogel (sample Gel_{GDE}-Imo-CaP), have been also evaluated. The FE-SEM micrographs evidence that the morphology of the Imo-containing mineralized sample (see Figure 5b) does not show the well-defined platelets typical of HA that are instead visible in Gel_{GDE}-CaP (Figure 5a). This suggests that Imo is able to template the growth of HA particles also in the hydrogel system. The EDX spectrum (reported in Figure 5d) confirms the presence of all the expected elements, while the XRD pattern (Figure 5e) demonstrate the formation of HA.

To understand if the presence of Imo is not only able to support the nucleation of HA, but also enhances its formation, we evaluated by means of Thermogravimetric Analysis (TGA) the amount of mineral phase formed (Figure 5f). The results are normalized by equilibrating the samples at 130 °C (*i.e.*, to remove water) and then corrected to take into account the loss of weight in the investigated range of temperature associated to pure HA and Imo. Very interestingly, we found that the inorganic fraction (after mineralization) is 10.4 %wt in the Gel_{GDE} sample, while it increases up to 21.3 %wt in Gel_{GDE}-Imo. This result is of outmost importance, as it shows that Imo is able to significantly promote the mineralization of the scaffold.

The presence of Imo not only affects the amount of mineral, but also which crystal phase is formed. The XRD spectra were analysed according to the Rietveld method and we compared the results obtained both as a function of the presence of Imo and of the hydrogel scaffold. We found that the presence of Imo promotes the carbonation of hydroxyapatite both in solution and in the scaffold: in HA and HA-Imo samples, CHA is present in the amounts of 18 % and 39 %, respectively (see Figure S4 and Figure S5 in the Supplementary material), together with HA. On the other hand, in the hydrogel matrix the percentage of carbonation is even higher (CHA 34 % in Gel_{GDE}-CaP vs 65 % in Gel_{GDE}-Imo-CaP, see Figure S6 and Figure S7), and a small amount of calcite (4 %) is also observed. These results are especially important considering the beneficial effect of carbonate on both the mechanical and osteoconductive/osteoinductive properties in bones. The superior characteristics of CHA with respect to HA are indeed well reported in literature.[45] Being our material very effective in promoting the formation of CHA, we believe that this contribution represents a significant step forward in the field of bone tissue engineering.

4. Conclusions

The results reported in this paper demonstrate that imogolite nanotubes could be effectively employed as fillers in macroporous gelatin-based hydrogels of interest in the field of bone tissue engineering. In

particular, the presence of Imo produced two beneficial effects: i) the inclusion of nanotubes synergistically enhances the effect of a chemical cross-linker (namely, GDE) in improving the hydrogel stabilization against dissolution and ii) most importantly, imogolites are shown to promote the formation of hydroxyapatite and carbonated hydroxyapatite, both when dispersed in water and when included in the macroporous scaffold. We believe that these results clearly highlight the potentials of Imo when introduced in the design of hydrogel-based scaffolds, especially thanks to the combination of their nanotubular shape and their affinity towards HA.

Acknowledgements

CSGI is acknowledged for financially supporting this work.

References

[1] M.J. Olszta, X. Cheng, S.S. Jee, R. Kumar, Y.-Y. Kim, M.J. Kaufman, E.P. Douglas, L.B. Gower, Bone structure and formation: A new perspective, Mater. Sci. Eng. R Rep. 58 (2007) 77–116. doi:10.1016/j.mser.2007.05.001.

[2] S.V. Dorozhkin, Calcium orthophosphates (CaPO4): occurrence and properties, Prog. Biomater. 5 (2016) 9–70. doi:10.1007/s40204-015-0045-z.

[3] J.-Y. Rho, L. Kuhn-Spearing, P. Zioupos, Mechanical properties and the hierarchical structure of bone, Med. Eng. Phys. 20 (1998) 92–102. doi:10.1016/S1350-4533(98)00007-1.

[4] S. Weiner, H.D. Wagner, THE MATERIAL BONE: Structure-Mechanical Function Relations, Annu. Rev. Mater. Sci. 28 (1998) 271–298. doi:10.1146/annurev.matsci.28.1.271.

[5] F. Ridi, I. Meazzini, B. Castroflorio, M. Bonini, D. Berti, P. Baglioni, Functional calcium phosphate composites in nanomedicine, Adv. Colloid Interface Sci. (2016). doi:10.1016/j.cis.2016.03.006.

[6] T.G. Kim, H. Shin, D.W. Lim, Biomimetic Scaffolds for Tissue Engineering, Adv. Funct. Mater. 22 (2012) 2446–2468. doi:10.1002/adfm.201103083.

[7] E.K. Moioli, P.A. Clark, X. Xin, S. Lal, J.J. Mao, Matrices and scaffolds for drug delivery in dental, oral and craniofacial tissue engineering, Adv. Drug Deliv. Rev. 59 (2007) 308–324. doi:10.1016/j.addr.2007.03.019.

[8] S. Van Vlierberghe, P. Dubruel, E. Schacht, Biopolymer-Based Hydrogels As Scaffolds for Tissue Engineering Applications: A Review, Biomacromolecules. 12 (2011) 1387–1408. doi:10.1021/bm200083n.

[9] F.J. O'Brien, Biomaterials & scaffolds for tissue engineering, Mater. Today. 14 (2011) 88–95. doi:10.1016/S1369-7021(11)70058-X.

[10] T. Albrektsson, C. Johansson, Osteoinduction, osteoconduction and osseointegration, Eur. Spine J. 10 (2001) S96–S101. doi:10.1007/s005860100282.

[11] V. Karageorgiou, D. Kaplan, Porosity of 3D biomaterial scaffolds and osteogenesis, Biomaterials. 26 (2005) 5474–5491. doi:10.1016/j.biomaterials.2005.02.002.

[12] S. Van Vlierberghe, V. Cnudde, P. Dubruel, B. Masschaele, A. Cosijns, I. De Paepe, P.J.S. Jacobs, L. Van Hoorebeke, J.P. Remon, E. Schacht, Porous Gelatin Hydrogels: 1. Cryogenic Formation and Structure Analysis, Biomacromolecules. 8 (2007) 331–337. doi:10.1021/bm060684o.

[13] S.J. Buwalda, K.W.M. Boere, P.J. Dijkstra, J. Feijen, T. Vermonden, W.E. Hennink, Hydrogels in a historical perspective: From simple networks to smart materials, J. Controlled Release. 190 (2014) 254–273. doi:10.1016/j.jconrel.2014.03.052.

[14] M. Santoro, A.M. Tatara, A.G. Mikos, Gelatin carriers for drug and cell delivery in tissue engineering, J. Controlled Release. 190 (2014) 210–218. doi:10.1016/j.jconrel.2014.04.014.

[15] E.I. Wisotzki, M. Hennes, C. Schuldt, F. Engert, W. Knolle, U. Decker, J.A. Käs, M. Zink, S.G. Mayr, Tailoring the material properties of gelatin hydrogels by high energy electron irradiation, J. Mater. Chem. B. 2 (2014) 4297–4309. doi:10.1039/C4TB00429A.

[16] D. Tatini, P. Tempesti, F. Ridi, E. Fratini, M. Bonini, P. Baglioni, Pluronic/gelatin composites for controlled release of actives, Colloids Surf. B Biointerfaces. 135 (2015) 400–407. doi:10.1016/j.colsurfb.2015.08.002.

[17] A. Bigi, G. Cojazzi, S. Panzavolta, K. Rubini, N. Roveri, Mechanical and thermal properties of gelatin films at different degrees of glutaraldehyde crosslinking, Biomaterials. 22 (2001) 763–768. doi:10.1016/S0142-9612(00)00236-2.

[18] K. Ulubayram, E. Aksu, S.I.D. Gurhan, K. Serbetci, N. Hasirci, Cytotoxicity evaluation of gelatin sponges prepared with different cross-linking agents, J. Biomater. Sci. Polym. Ed. 13 (2002) 1203–1219. doi:10.1163/156856202320892966.

[19] A. Bigi, G. Cojazzi, S. Panzavolta, N. Roveri, K. Rubini, Stabilization of gelatin films by crosslinking with genipin, Biomaterials. 23 (2002) 4827–4832. doi:10.1016/S0142-9612(02)00235-1.

[20] G. Vargas, J.L. Acevedo, J. López, J. Romero, Study of cross-linking of gelatin by ethylene glycol diglycidyl ether, Mater. Lett. 62 (2008) 3656–3658. doi:10.1016/j.matlet.2008.04.020.

[21] C. Nishi, N. Nakajima, Y. Ikada, In vitro evaluation of cytotoxicity of diepoxy compounds used for biomaterial modification, J. Biomed. Mater. Res. 29 (1995) 829–834. doi:10.1002/jbm.820290707.

[22] Y. Lvov, E. Abdullayev, Functional polymer–clay nanotube composites with sustained release of chemical agents, Prog. Polym. Sci. 38 (2013) 1690–1719. doi:10.1016/j.progpolymsci.2013.05.009.

[23] Y. Liu, Y. Zhao, B. Sun, C. Chen, Understanding the Toxicity of Carbon Nanotubes, Acc. Chem. Res. 46 (2013) 702–713. doi:10.1021/ar300028m.

[24] N. Yoshinaga, S. Aomine, Imogolite in some ando soils, Soil Sci. Plant Nutr. 8 (1962) 22–29. doi:10.1080/00380768.1962.10430993.

[25] V.C. Farmer, A.R. Fraser, J.M. Tait, Synthesis of imogolite: a tubular aluminium silicate polymer, J. Chem. Soc. Chem. Commun. (1977) 462–463. doi:10.1039/C39770000462.

[26] P.D.G. Cradwick, V.C. Farmer, J.D. Russell, C.R. Masson, K. Wada, N. Yoshinaga, Imogolite, a Hydrated Aluminium Silicate of Tubular Structure, Nature. 240 (1972) 187–189. doi:10.1038/10.1038/physci240187a0.

[27] V.C. Farmer, M.J. Adams, A.R. Fraser, F. Palmieri, Synthetic imogolite: properties, synthesis, and possible applications, Clay Min. 18 (1983) 459–472. doi:10.1180/claymin.1983.018.4.11.

[28] N. Teramoto, A. Hayashi, K. Yamanaka, A. Sakiyama, A. Nakano, M. Shibata, Preparation and Mechanical Properties of Photo-Crosslinked Fish Gelatin/Imogolite Nanofiber Composite Hydrogel, Materials. 5 (2012) 2573–2585. doi:10.3390/ma5122573.

[29] K. Yamamoto, H. Otsuka, S.-I. Wada, D. Sohn, A. Takahara, Preparation and properties of [poly(methyl methacrylate)/imogolite] hybrid via surface modification using phosphoric acid ester, Polymer. 46 (2005) 12386–12392. doi:10.1016/j.polymer.2005.10.108.

[30] K. Yamamoto, H. Otsuka, S.-I. Wada, D. Sohn, A. Takahara, Transparent polymer nanohybrid prepared by in situ synthesis of aluminosilicate nanofibers in poly(vinyl alcohol) solution, Soft Matter. 1 (2005) 372–377. doi:10.1039/B508669H.

[31] I. Bottero, B. Bonelli, S.E. Ashbrook, P.A. Wright, W. Zhou, M. Tagliabue, M. Armandi, E. Garrone, Synthesis and characterization of hybrid organic/inorganic nanotubes of the imogolite type and their behaviour towards methane adsorption, Phys. Chem. Chem. Phys. 13 (2011) 744. doi:10.1039/c0cp00438c.

[32] F. Ohashi, S. Tomura, K. Akaku, S. Hayashi, S.-I. Wada, Characterization of synthetic imogolite nanotubes as gas storage, J. Mater. Sci. 39 (2004) 1799–1801. doi: 10.1023/B:JMSC.0000016188.04444.36

[33] W.C. Ackerman, D.M. Smith, J.C. Huling, Y.W. Kim, J.K. Bailey, C.J. Brinker, Gas/vapor adsorption in imogolite: a microporous tubular aluminosilicate, Langmuir. 9 (1993) 1051–1057. doi:10.1021/la00028a029.

[34] N. Jiravanichanun, K. Yamamoto, K. Kato, J. Kim, S. Horiuchi, W.-O. Yah, H. Otsuka, A. Takahara, Preparation and Characterization of Imogolite/DNA Hybrid Hydrogels, Biomacromolecules. 13 (2012) 276–281. doi:10.1021/bm201616m.

[35] N. Inoue, H. Otsuka, S.-I. Wada, A. Takahara, (Inorganic Nanofiber/Enzyme) Hybrid Hydrogel: Preparation, Characterization, and Enzymatic Activity of Imogolite/Pepsin Conjugate, Chem. Lett. 35 (2006) 194–195. doi:10.1246/cl.2006.194.

[36] B.M. Rotoli, P. Guidi, B. Bonelli, M. Bernardeschi, M.G. Bianchi, S. Esposito, G. Frenzilli, P. Lucchesi, M. Nigro, V. Scarcelli, M. Tomatis, P.P. Zanello, B. Fubini, O. Bussolati, E. Bergamaschi, Imogolite: An Aluminosilicate Nanotube Endowed with Low Cytotoxicity and Genotoxicity, Chem. Res. Toxicol. 27 (2014) 1142–1154. doi:10.1021/tx500002d.

[37] K. Ishikawa, T. Akasaka, S. Abe, Y. Yawaka, M. Suzuki, F. Watari, Application of Imogolite, Almino-Silicate Nanotube, as Scaffold for the Mineralization of Osteoblasts, Bioceram. Dev. Appl. 1 (2010) 1–3. doi:10.4303/bda/D110133.

[38] G.H. Koenderink, S.G.J.M. Kluijtmans, A.P. Philipse, On the Synthesis of Colloidal Imogolite Fibers, J. Colloid Interface Sci. 216 (1999) 429–431. doi:10.1006/jcis.1999.6323.

[39] E. Bouyer, F. Gitzhofer, M.I. Boulos, Morphological study of hydroxyapatite nanocrystal suspension, J. Mater. Sci. Mater. Med. 11 (2000) 523–531. doi:10.1023/A:1008918110156.

[40] D.W. Schaefer, Fractal Models and the Structure of Materials, MRS Bull. 13 (1988) 22–27. doi:10.1557/S088376940006632X.

[41] W.O. Yah, K. Yamamoto, N. Jiravanichanun, H. Otsuka, A. Takahara, Imogolite Reinforced Nanocomposites: Multifaceted Green Materials, Materials. 3 (2010) 1709–1745. doi:10.3390/ma3031709.

[42] B. Bonelli, I. Bottero, N. Ballarini, S. Passeri, F. Cavani, E. Garrone, IR spectroscopic and catalytic characterization of the acidity of imogolite-based systems, J. Catal. 264 (2009) 15–30. doi:10.1016/j.jcat.2009.03.003.

[43] N. Arancibia-Miranda, M. Escudey, M. Molina, M.T. García-González, Use of isoelectric point and pH to evaluate the synthesis of a nanotubular aluminosilicate, J. Non-Cryst. Solids. 357 (2011) 1750–1756. doi:10.1016/j.jnoncrysol.2011.01.012.

[44] H. Wang, W. Zhou, D.L. Ho, K.I. Winey, J.E. Fischer, C.J. Glinka, E.K. Hobbie, Dispersing Single-Walled Carbon Nanotubes with Surfactants: A Small Angle Neutron Scattering Study, Nano Lett. 4 (2004) 1789–1793. doi:10.1021/nl048969z.

[45] E.F. Morgan, D.N. Yetkinler, B.R. Constantz, R.H. Dauskardt, Mechanical properties of carbonated apatite bone mineral substitute: strength, fracture and fatigue behaviour, J. Mater. Sci. Mater. Med. 8 (n.d.) 559–570. doi:10.1023/A:1018550831834.

Supplementary material

Enhanced formation of hydroxyapatite in imogolite-reinforced macroporous hydrogels

Rita Gelli, Stefano Del Buffa, Paolo Tempesti, Massimo Bonini, Francesca Ridi and Piero Baglioni

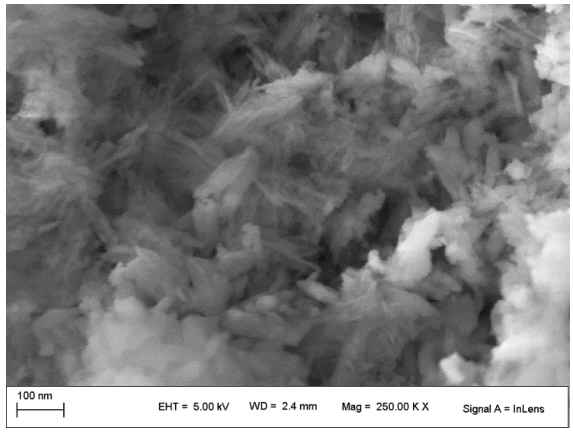

Figure S1: SEM micrograph of HA.

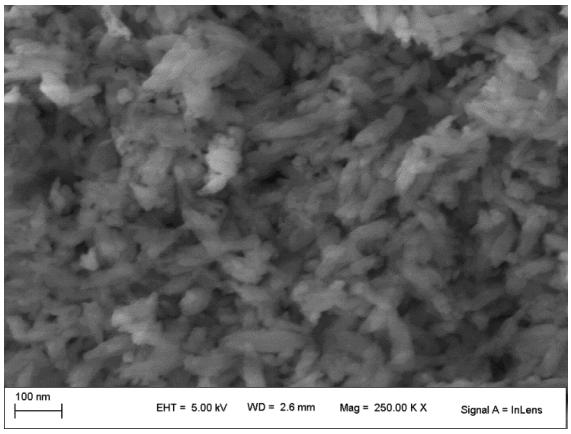

Figure S2: SEM micrograph of HA-Imo.

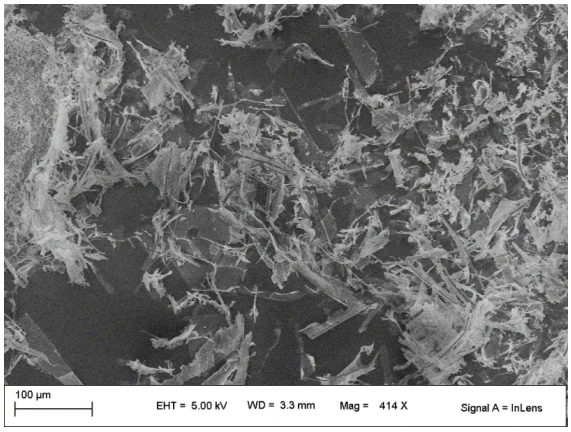

Figure S3: SEM micrograph of Imo bundles.

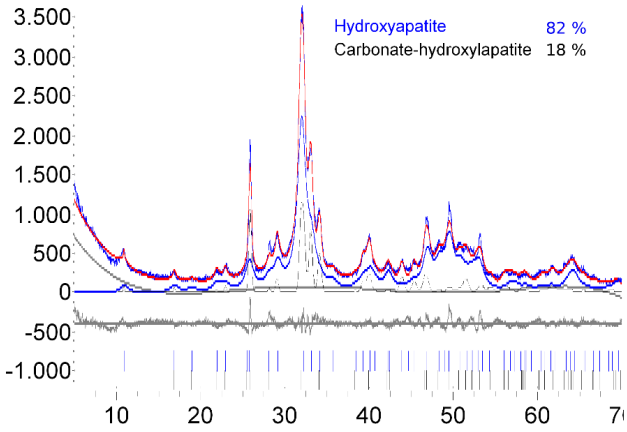

Figure S4: Rietveld fitting of HA.

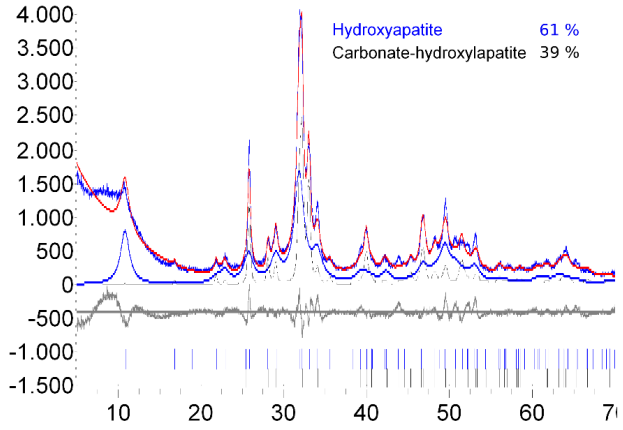

Figure S5: Rietveld fitting of HA-Imo.

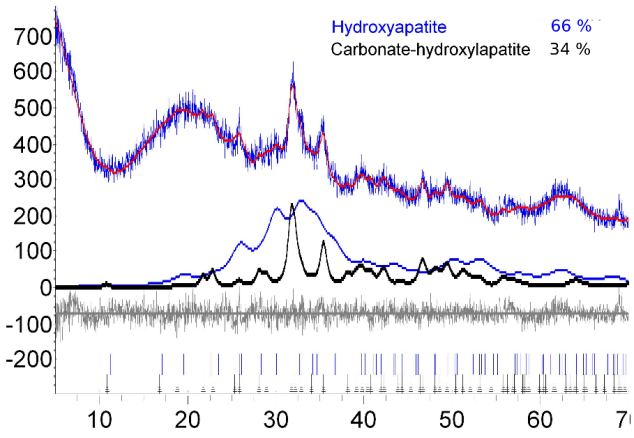

Figure S6: Rietveld fitting of Gel_{GDE}-CaP.

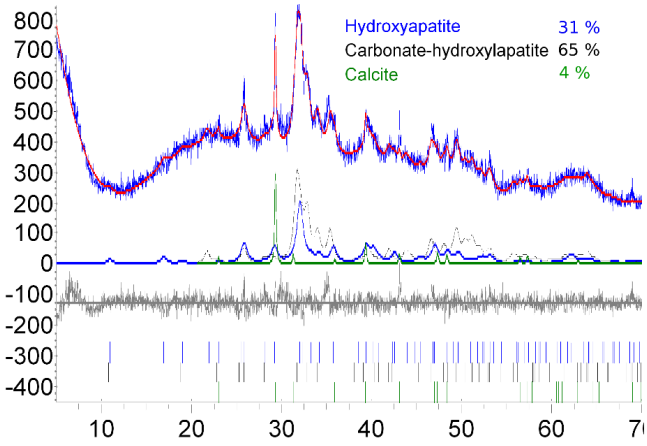

Figure S7: Rietveld fitting of Gel_{GDE}-Imo

Adsorption of amino acids and glutamic acid-based surfactants on imogolite nanotubes

Alessio Gabbani[a], *Stefano Del Buffa*[a], *Francesca Ridi*[a], *Massimo Bonini*[a], *and Piero Baglioni*[a]*

Romain Bordes[b,c], *Krister Holmberg*[b]

[a] Department of Chemistry "Ugo Schiff" and CSGI, University of Florence, via della Lastruccia 3, 50019 Sesto Fiorentino, Florence, Italy; [b] Department of Chemistry and Chemical Engineering, Chalmers University of Technology, 41296 Göteborg, Sweden; [c] Vinn Excellence Center SuMo Biomaterials, Chalmers University of Technology, 41296 Göteborg, Sweden

KEYWORDS

Imogolite, nanocomposites, glutamic acid, sodium lauroyl glutamate, amino acids, turbidimetry

ABSTRACT

Aluminum oxide surfaces are of outmost interest in different biotech applications, in particular for their use as adjuvants (*i.e.*, booster of the immune response against infectious agents in vaccines production). In this framework, imogolite nanotubes combine the chemical flexibility of the exposed alumina surface with the 1D nanostructure. This work reports on the interaction between amino acids and imogolite, using turbidimetry, ζ-potential measurements, and FT-IR spectroscopy as main characterization tools. Amino acids with different side chain functional groups were investigated, showing that glutamic acid (Glu) has the strongest affinity for imogolite surface. This was exploited to prepare a composite material made of a synthetic surfactant bearing a Glu polar head and a hydrophobic C_{12} alkyl tail, adsorbed onto the surface of imogolite. The adsorption of a model drug (rhodamine B isothiocyanate) by the hybrid was evaluated both in water and in physiological saline conditions. The findings of this paper suggest that the combination between the glutamate head-group and imogolite represents a promising platform for the fabrication of hybrid nanostructures with tailored functionalities.

INTRODUCTION

Aluminum oxide/hydroxide surfaces find use in a wide range of biotechnological applications. Porous aluminum oxide and alumina membranes are currently used for size selective cell separation, micro colony growth and imaging, in the fabrication of scaffolds for tissue engineering, and as templates for the fabrication of precisely sized nanostructures (nanowires, nanotubes, nanoparticles).[1] Porous anodic alumina membranes and patterned aluminum foils with hierarchical structures were shown to be suitable as non-lithographic replication masters for the preparation of 2D or 3D arrays of periodic nanostructures of biotechnological interest.[2] Alumina particles have also found use as carriers for enzyme immobilization,[3] while adjuvants based on aluminum compounds are commonly used in vaccines to boost the immune response against infectious agents.[4,5] As an example, α-Al_2O_3 nanoparticles have been recently proposed as efficient carriers for the delivery of antigens to the autophagosome-related cross-presentation pathway in antigen-presenting cells.[6] The adjuvant effects of aluminum-based materials is known to depend upon several properties such as shape, specific surface area, crystallinity, and density of surface hydroxyl groups. Therefore, tuning the aspect ratio of aluminum-based structures could be effectively used to increase inflammasome activation in dendritic cells *in vitro* and *in vivo*.[7]

In the last decade 1D-nanostructures, especially carbon nanotubes, have progressively assumed an increasing importance for the design of novel devices for biosensing applications,[8] catalysis,[9] photoelectrochemistry,[10] and tissue engineering.[11] Recently, tubular clay minerals have emerged as promising alternatives to artificial fibers in mechanically reinforced composites[12] and bionanocomposites.[13] In this framework, imogolite (IMO) is a natural material with very intriguing properties. Its structure closely resembles that of single walled carbon nanotubes[14–16],

displaying a hollow tubular structure with diameter typically ranging from 1 to 3 nm, and length ranging from ~ 60 nm to ~ 2 μm (Figure 1A). In terms of composition, IMO is a hydrous aluminosilicate, exposing aluminum oxide/hydroxide surface. The presence of two accessible surfaces (the outer aluminum oxide/hydroxide layer and the inner silicon oxide sheet) with different reactivity and surface charge,[17] and a lumen with nanometric size that can be exploited for the adsorption and release of actives and drugs,[18] open a wide range of applications in material science.[19–22] The low toxicity of IMOs is important for applications in the field of biomaterials, and some works have already been reported in the literature.[23-26] Thanks to its structural and mechanical properties, IMO is expected to be particularly useful as a reinforcing material in scaffolds for bone tissue engineering: in fact, good biocompatibility between osteoblast-like cells and an imogolite scaffold has already been demonstrated, together with an enhancement in the proliferation and osteoblastic differentiation.[27]

In the framework of bone tissue engineering, amino acids are of particular interest as they possess a broad spectrum of chemical reactivity and they are involved in many biochemical processes. For instance, negatively charged amino acids (e.g., glutamic acid and phosphoserine) are highly expressed in non-collagenous proteins involved in the mineralization of bones[28] and they can either promote[29] or inhibit[30] hydroxyapatite formation, as well as alter its morphology and crystalline structure[31]. Thanks to their chemical versatility and to the possibility of modulating their interactions with solid surfaces (e.g., by varying pH, ionic strength, etc.) amino acids could likely be used as biocompatible building blocks in the fabrication of hybrid nanostructures with tailored functionalities. Amino acids have also been employed as the polar head-group in the synthesis of amphiphilic compounds.[32] One of the most important properties of these surfactants is their easy biodegradability, which is a general prerequisite for most consumer

and biomedical products in order to reduce the impact on the environment and the residence time in living organisms. All α-amino acids have a carboxyl group and a primary amino group, and a surfactant can be obtained by attaching a hydrophobic moiety (*i.e.*, an alkyl chain) at either of these sites, resulting in the formation of cationic, anionic or zwitterionic surfactants, depending on the synthetic procedure. If the starting amino acid contains an extra carboxyl group, as in the case of aspartic acid and glutamic acid, attaching a hydrophobic residue via the α-amino group results in the formation of dicarboxylic amino acid-based surfactants with chelating properties.[33] Besides their use as "green" solubilization or emulsification agents, the presence of a bioactive polar head-group allows for selective targeting of biological surfaces, and for the use of these biomimetic surfactants as carriers for actives and drugs.

In this work we report on the adsorption of amino acids onto IMO nanotubes, investigated by means of turbidimetry, ζ-potential measurements, and FT-IR spectroscopy. Amino acids with different side chain functional groups were investigated: Arg and Lys, Glu, Gly, Ser were chosen as representative examples for basic, acidic, non-polar and polar amino acids, respectively. The high affinity of glutamic acid for alumina-based surfaces triggered an experiment to adsorb a synthetic surfactant, bearing a Glu polar head and a hydrophobic C_{12} alkyl tail, onto the outer surface of IMOs. This hybrid organic-inorganic material was characterized in term of its ability to upload a model drug both in water and in physiological saline conditions.

EXPERIMENTAL SECTION

Materials. Sodium hydroxide (NaOH), hydrochloric acid (HCl, 37%), tetraethyl orthosilicate (TEOS, 97%), aluminum sec-butoxide (ASB), glutamic acid (Glu), serine (Ser), lysine (Lys), glycine (Gly) and rhodamine B isothiocyanate (RHO) were all purchased from Sigma-Aldrich. Arginine (Arg) was purchased from Fluka. Perchloric acid ($HClO_4$, 70%) was purchased from Merck. Milli-Q water (resistivity of about 18.2 MΩ·cm) was used for the preparation of all aqueous solutions and dispersions.

Synthesis of imogolite nanotubes. IMO nanotubes were synthesized following the procedure reported by Koenderink *et al*.[34] TEOS (840 μL) and ASB (1.90 g) were added to a 150 ml $HClO_4$ solution (0.025 M), pre-heated at 70 °C. The final Si:Al:$HClO_4$ molar ratios were 1:2:1. The dispersion was kept at 70 °C during 5 hours under continuous stirring, and then refluxed at 100 °C during 10 days. The reaction mixture was then cooled down, dialyzed against deionized water to remove unreacted reagents, and freeze-dried (-50 °C, $3 \cdot 10^{-2}$ mmHg). The obtained fluffy material was thoroughly characterized by means of TEM, XRD, TGA, FTIR, DLS and porosimetry.

Amino acid adsorption onto imogolite nanotubes. 1 ml of an aqueous IMO dispersion (4 g/L) was sonicated with a Labsonic LBS2-4 (Falc Instruments, Italy) operating at 60 kHz during 2 hours, and the selected amino acid was then added. The amount was chosen to theoretically cover twice the surface area of the IMO in the sample. This value was calculated by taking into account the specific surface area of IMO resulting from porosimetry (317 ± 7 m^2/g) and considering a value of 0.2 nm^2 for the area occupied by the polar head of the amino acid.[35] Water was then added to reach a total volume of 5 mL; the final concentration of amino acid was 4 mM, while the final concentration of IMO was 0.8 g/L. A 0.8 g/L dispersion of IMO without

amino acid was prepared and then used as a reference for the adsorption experiments. Experiments at different pHs were carried out by adding HCl 1M and NaOH 1M dropwise, and checking the final pH with a pH-meter (HI9025c, Hanna Instruments, Italy). The adsorption experiments in saline physiological conditions were performed by making up the samples to the final volume with NaCl 0.9 %w/v. At the end of the adsorption experiments, the precipitate was separated from the supernatant by centrifugation at 19500 g for 40 minutes, and freeze-dried (-50 °C, $3 \cdot 10^{-2}$ mmHg).

Synthesis of disodium lauroyl glutamate (C_{12}Glu). Disodium lauroyl glutamate was prepared as previously described in the literature.[36]

C_{12}Glu adsorption onto imogolite nanotubes and RHO uploading experiments. The adsorption of lauroyl glutamate onto IMO nanotubes was achieved by adding 3.7 mg of disodium lauroyl glutamate to 5 mL of a 0.8 g/L IMO dispersion, and allowing the system to equilibrate under constant stirring at room temperature. An aqueous solution of rhodamine B isothiocyanate (RHO, 1 mL, 8 mg/L) was added to the dispersion (IMO-C_{12}Glu-RHO), left to equilibrate under constant stirring for 3 hours at room temperature, and then centrifuged for 40 min at 12500 g. To evaluate the effect of physiological saline conditions on the uploading of RHO, IMO was dispersed in a 0.9 %w/v NaCl solution and then the same procedure was followed. The supernatant solutions were collected, and UV-Vis spectra were acquired in order to quantify the residual amount of dye in solution. As a reference, a sample containing RHO and IMO (but without disodium lauroyl glutamate) was used.

Characterization techniques.

Transmission electron microscopy. Transmission electron microscopy (TEM) analysis of imogolite nanotubes was performed with a TEM Philips CM12 (Eindhoven, The Netherlands),

working with an electron gun operating at 80 kV. Samples were prepared by depositing a droplet of IMO dispersion onto a carbon coated copper grid.

X-ray diffraction. X-ray diffractograms of imogolite nanotubes were collected with a D8 Advance with DAVINCI design (Bruker, Milano, Italy), using Cu K_α radiation (λ=1.54Å), a range of 2θ of 5°-70° with a step size of 0.03°, and a time/step of 0.5 s.

Thermogravimetry. Thermogravimetric analysis (TGA) was carried out on a SDT Q600 (TA Instruments, Philadelphia, PA, USA) from 25 °C to 1000 °C at 10 °C/min, under N_2 atmosphere with a flow rate of 50 ml/min.

Infrared Spectroscopy. Fourier transform infrared spectroscopy (FTIR) experiments were performed in attenuated total reflectance mode (ATR-FTIR) with a Nexus Thermo-Nicolet 870 FTIR spectrometer (Madison, WI, USA) equipped with a MCT detector and a Golden Gate diamond cell. The spectra were acquired in the 500-4000 cm^{-1} range with a nominal resolution of 2 cm^{-1}.

Dynamic light scattering. Dynamic light scattering (DLS) and ζ-potential measurements were carried out by means of a 90Plus/BI-MAS system by Brookhaven Instruments (New York, NY, USA) working with a 15 mW solid state laser (λ = 635 nm) as the light source. The time autocorrelation functions of the scattered light were analyzed through a Laplace Inversion by CONTIN algorithm. ζ-potential was determined from the electrophoretic mobility using the Helmholtz-Smoluchowski approximation. All measurements were performed at 25 °C.

Specific surface area. Specific surface area (SSA) of imogolite nanotubes was determined from N_2 adsorption isotherms with a Beckman-Coulter SA 3100 (Milano, Italy), using the multiple-point Brunauer-Emmet-Teller (BET) method. The solid samples were outgassed for 30 minutes at 120 °C before each measurement.

Turbidimetry. Turbidimetry curves were collected at 25 °C using a Cary Bio 100 UV-vis spectrophotometer by Varian (Milano, Italy). The samples were sonicated for 15 minutes before each measurement. The transmittance at λ=650 nm was recorded as a function of time. For the fittings, the curves were corrected for the optical path, converted into relative turbidity (τ/τ_0, where τ_0 is the initial turbidity) and simulated according to a model commonly employed in the study of the early stages of aggregation of colloidal particles:[37]

$$k_{11} = \frac{[d(\tau/\tau_0)/dt]_0}{\left[\left(\frac{C_2}{2C_1}\right)-1\right]N_1} = \frac{R}{\left[\left(\frac{C_2}{2C_1}\right)-1\right]N_1} \quad (1)$$

Eq.1 connects the coagulation rate constant k_{11} (*i.e.*, the rate of formation of clusters made by two single particles) to the rate of turbidity change. Assuming the denominator in Eq. 1 to be constant, the coagulation rate is proportional to the quantity $R = [d(\tau/\tau_0)/dt]_0$, usually defined as the relative coagulation rate. In the early stages of the process, the coagulation takes place through the collision of single particles to form dimers, and the coagulation rate can be determined from the slope of the initial part of the relative turbidity curve.[38] Details of the fitting procedure are given in the Supporting Information.

Elemental analysis. Elemental analysis was performed with a CHN-S Flash E1112 Thermofinnigan (Rodano, Italy) analyser.

UV-Visible spectroscopy. UV-Visible spectroscopy experiments to evaluate the amount of uploaded Rhodamine B isothiocyanate were performed with a LAMBDA900 (Perkin Elmer, Milano, Italy) in the 400 – 700 nm range, at room temperature. The amount of uploaded dye was calculated from Equation 2:

$$\%\, Ads = \frac{A_{RHO} - A_{Sample}}{A_{RHO}} x100 \quad (2)$$

where A_{RHO} and A_{Sample} are the absorbance at 552 nm of the starting RHO solution and of the supernatant solution obtained after centrifugation of the IMO-RHO and the IMO-C_{12}Glu-RHO dispersions, respectively.

Quartz Crystal Microbalance with monitoring of the dissipation (QCM-D). A QCM-D instrument (model D300) from Q-sense AB (Göteborg, Sweden) was used and the measurements were carried out under non-flowing conditions. The AT-cut crystals coated with Al_2O_3 (QSX309) were also from Q-sense AB (Göteborg, Sweden). The cleaning procedure, prior to use, was done as follows: sonication in ethanol for 10 minutes, rinsing with Milli-Q water, drying with N_2, and finally 10 minutes of UV-ozone treatment.

CMC determination of C_{12}Glu in NaCl 0.9 %w/v by tensiometry. Surface tension measurements were carried out on an Attension Theta goniometer (Biolin Scientific Oy, Espoo, Finland) using the pendant drop method. CMC was taken at the concentration the surface tension remained constant.

RESULTS AND DISCUSSION

Characterization of Imogolite nanotubes. A representative TEM micrograph of the obtained imogolite nanotubes is reported in Figure 1B (and Figure S1), showing the presence of tubular structures with external diameters ranging from 5 to 15 nm, internal diameters from 1 to 3 nm, and lengths of about 250-300 nm. Consistent with results in the literature, IMO shows a strong tendency to form bundles:[14,34,39,40] in fact, TEM results suggest that most of the imogolite nanotubes are packed to form tubular clusters. Figure 1C displays the XRD spectrum of the synthesized imogolite nanotubes, showing very good agreement with the data reported in literature.[34,41] The first two peaks at $2\theta = 5.8°$ and $2\theta = 8.1°$ correspond to characteristic

dimensions of ~15 Å and ~11 Å, respectively, which can be assigned to the regular distances resulting from hexagonal packing of nanotubes. The peaks at higher angles can be assigned to bond distances between atoms composing the sample. For instance, the diagnostic peak at 2θ = 26.3° corresponds to 3.4 Å and can be attributed to the Al-O-Si bond distance, *i.e.* the thickness of a tube wall (the sum of Al-O and Si-O bond distances gives 3.5 Å).

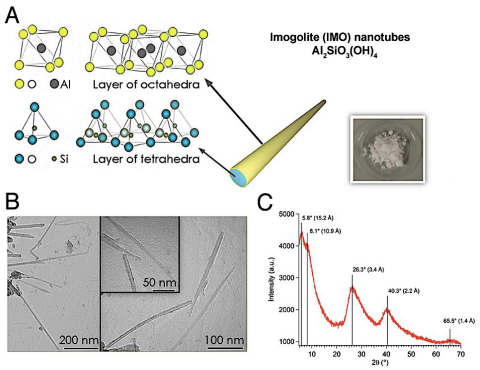

Figure 1. Schematic representation of an imogolite nanotube showing octahedral AlOH and tetrahedral SiO sheets forming the outer and inner surface of the tube, respectively (A). TEM images (B) and XRD pattern (C) of synthesized imogolite nanotubes are also shown in the figure.

Thermogravimetric analysis (Figure S2) shows that IMO has a moisture content of ~ 23 %wt (calculated from the weight loss in the 25-150 °C range). The structural dehydroxylation, *i.e.* loss of chemisorbed water, takes place in the 150-800 °C range producing a weight loss of ~20 %wt, consistent with the theoretical values obtained from the molecular formula $Al_2SiO_3(OH)_4$.

Imogolites were also characterized by ATR-FTIR. The spectrum (Figure 2) shows the characteristic peaks of aluminosilicate materials. The signals at 930 and 590 cm^{-1} are assigned to

Si-O-Si stretching and O-Si-O bending, respectively.[34] The shoulder at 685 cm^{-1} corresponds to Al-O-Si stretching. The peak at ~1640 cm^{-1} is assigned to OH bending of physisorbed water,[42] while the broad band around 3350 cm^{-1} is assigned to OH stretching of surface hydroxyl groups and physisorbed water.

DLS analysis was performed on imogolite aqueous dispersions, revealing the presence of two populations of scatterers. The most abundant population consists of objects with hydrodynamic diameter of ~ 750 nm, while the second consists of large agglomerates. DLS results confirmed TEM observations, in which bundles of IMO nanotubes are always detected.

Specific surface area (SSA) of imogolite was determined from nitrogen adsorption isotherms. Type I isotherm was observed, typical of mesoporous solids, with a small hysteresis loop that is associated to particle aggregates giving rise to slit-shaped pores, most likely deriving from mesopores among imogolite bundles (Figure S3). The specific surface area of the synthesized imogolite sample is 317 ± 7 m^2/g, in good agreement with the typical values reported in the literature,[18,40,43] ranging from 300 to 400 m^2/g.

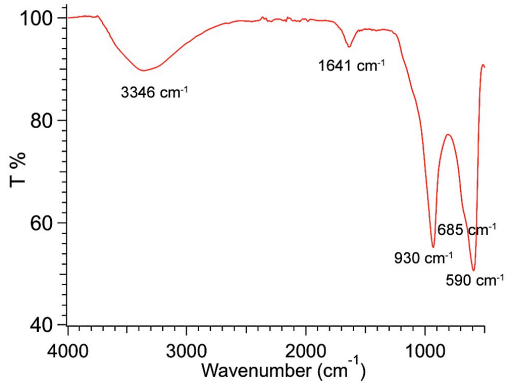

Figure 2. ATR FT-IR spectrum of synthesized imogolite in the 500-4000 cm^{-1} range.

Adsorption of amino acids on imogolite. To evaluate the adsorption of the amino acids onto IMO surface and to elucidate their effect on the colloidal stability of IMO dispersions in water, we extracted the coagulation rate from a linear regression of the turbidity curve in the early stage of the aggregation process (see Experimental section). The results are summarized in Figure 3A. The kinetics of aggregation is differently affected by the presence of amino acids: basic amino acids, such as Arg and Lys, display a destabilizing effect on the IMO dispersions, while Glu, Ser and Gly slightly increase the stability (Figure 3B).

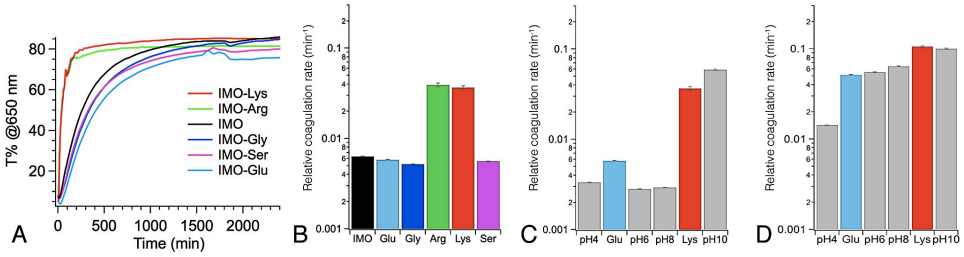

Figure 3. A) Transmittance @650 nm of the various IMO-amino acid dispersions as a function of time (an amino acid-free IMO dispersion is also shown for comparison); B) coagulation rate of IMO-amino acid dispersions; C) coagulation rate of IMO dispersions as a function of pH, together with the coagulation rates of IMO-Glu (spontaneous pH = 4.2) and IMO-Lys (spontaneous pH = 9.0); D) coagulation rate of the same IMO dispersions as in C) but under physiological saline conditions (NaCl 0.9 %w/v).

The destabilizing effect of Lys and Arg corresponds to a decrease of the particle surface charge, as evidenced by the drop in the ζ-potential of IMO-Lys and IMO-Arg (see Table 1). This suggests that the colloidal stability of the dispersions is primarily due to electrostatic forces. Two

hypotheses can be drawn about the effect of amino acids on the surface charge of IMOs. In the first, the physisorption of amino acids on the external surface of IMO takes place thanks to the affinity of the α-amino acid for the alumina surface. This will normally lead to a decrease of the IMO net charge, but if the amino acid contains an extra carboxyl group or an extra amino group, this functional group will be oriented towards water, which may lead to an increase in the net charge. In the second hypothesis, amino acids with a pronounced acidic or basic character are able to change the pH of the system, thereby inducing changes in the surface charge of IMO by protonating or deprotonating aluminol and silanol groups, according to the following equilibria:

$$\text{Al-(OH)-Al} + \text{H}^+ \rightleftharpoons \text{Al-(OH}_2)^+\text{-Al} \qquad \text{(i)}$$

$$\text{SiO-H} \rightleftharpoons \text{Si-O}^- + \text{H}^+ \qquad \text{(ii)}$$

At pH values lower than the point of zero charge (PZC) of IMO (pH 10÷11)[41,44] equilibrium (i) is shifted to the right, leading to an increased positive charge of the outer surface, thus enhancing the colloidal stability. On the other hand, at pH values higher than the PZC, the equilibrium (i) is shifted to the left and the external surface of IMO progressively becomes neutral. Equilibrium (ii) accounts for the internal charge of IMO, having therefore a much smaller influence on the surface charge and consequently on the dispersion stability.[17,45]

Table 1. ζ-potential, pH values, and relative coagulation rate of IMO dispersions with and without addition of the amino acid (pH values of pure amino acid solutions are given within parentheses).

Sample	ζ-potential [mV]	pH	Rel. coagulation rate [1/min]
IMO pH 4.2	+46.7 ± 0.8	4.2	$3.33 \cdot 10^{-3}$
IMO	+34.1 ± 1.7	6.0	$6.35 \cdot 10^{-3}$
IMO-Glu	+48.5 ± 2.3	4.2 (3.5)	$5.80 \cdot 10^{-3}$
IMO-Gly	+32.8 ± 1.9	7.0 (6.3)	$5.20 \cdot 10^{-3}$
IMO-Ser	+33.7 ± 1.7	6.5 (6.2)	$5.60 \cdot 10^{-3}$
IMO-Arg	+11.7 ± 1.0	9.3 (10.1)	$3.92 \cdot 10^{-2}$
IMO-Lys	+12.1 ± 0.3	9.0 (9.8)	$3.67 \cdot 10^{-2}$
IMO pH 10	n.a.*	10.0	$5.91 \cdot 10^{-2}$

* Results not reliable, the error being larger than the experimental value.

Table 1 reports the pH of the IMO dispersions in the presence of amino acids (the pH of the corresponding amino acid solutions are given in parenthesis), as well as the ζ-potential values and the relative coagulation rates. Results show that the pH of the IMO dispersions differs from that of the corresponding amino acid solution. Furthermore, the presence of amino acids causes a significant change in the pH of the IMO dispersions with respect to the pristine sample. The trend in the ζ-potential correlates well with the pH induced by the presence of the amino acid, highlighting the progressive decrease in the surface charge as the pH is increased towards the point of zero charge of the aluminol groups. Looking at the relative coagulation rates, two general behaviors could be identified: (i) Arg and Lys produces pH values approaching the PZC of IMO, resulting in relative coagulation rates of the same order of magnitude as for IMO at pH = 10, (ii) the relative coagulation rates obtained with all the other tested amino acids are generally one order of magnitude smaller.

To further investigate the effect of pH and amino acids, we selected Glu and Lys as examples of the two general behaviors and we first evaluated the coagulation rates at different pH values, but in absence of amino acid (Figure 3C). The same experiments were also conducted under physiological saline conditions (Figure 3D). Addition of Lys brings the pH to 9, which is one unit lower than the PZC of IMO, and results in a high coagulation rate, just below the one observed at pH = 10. On the other hand, the effect of Glu cannot be simply justified by the pH: in fact, the surface charge of IMO in the presence of Glu is very similar to that of IMO at the corresponding pH, but the coagulation rate in the presence of Glu is almost doubled. We explain this peculiar behavior of Glu by taking into account its molecular structure, especially focusing on the presence of the two carboxyl groups. The interaction between Glu and the surface of γ-Al_2O_3 has been shown to be strong and pH dependent, decreasing with increasing pH.[46] Two modes of chelation are suggested in the literature based on FT-IR data. Either both the carboxylate groups of Glu are involved in bonding to surface Al atoms through covalent bonds or via hydrogen bonds, or only one of the two carboxylates(*i.e.*, the side chain COOH group) is bound to surface Al atoms.[46]

Since the external surface of IMO consists of alumina, it is reasonable to assume that glutamate physisorbs onto IMO similar to what happens in γ-Al_2O_3 crystals. As a result, the surface of the IMO particles will then expose the Glu amino group (which is protonated at pH = 4) and also one of the carboxylate groups in the case of a bidentate binuclear complex being formed. The increased aggregation rate of IMO-Glu compared to IMO without Glu at the same pH could thus be explained by invoking electrostatic attraction between protonated amino groups and carboxylate groups belonging to different particles.

As discussed before, the kinetics of aggregation of IMO dispersions was also evaluated under physiological conditions (see Figure 3D). The results show that the increased ionic strength destabilizes all the samples with a leveling in the coagulation rates, as it is expected in dispersions where electrostatic stabilization plays a major role.[47] In the specific case of IMO-Glu, a ten-fold increase is observed.

To verify and quantify the adsorption of the amino acids on IMO nanotubes, IMO-amino acid dispersions were centrifuged, the resulting solid was collected and investigated by FT-IR and elemental analysis. The ATR-FTIR results (Figure 4) provide evidence that amino acids are adsorbed onto imogolite nanotubes, and that Glu is adsorbed in higher amount. The symmetric and asymmetric stretching of deprotonated carboxyl groups is observed at 1405 cm^{-1} and 1590 cm^{-1}, respectively. The absence of a peak above 1700 cm^{-1} supports the lack of protonated carboxyl groups and it is consistent with previous studies on the adsorption of amino acids on TiO_2 and γ-Al_2O_3 surfaces.[46,48,49] The signals at ~1460 and ~1350 cm^{-1} are attributed to CH_2 bending. The intense band centered at 1635 cm^{-1} (also present in the spectrum of pure imogolite, see Figure 2) is attributed to OH bending of physisorbed water.

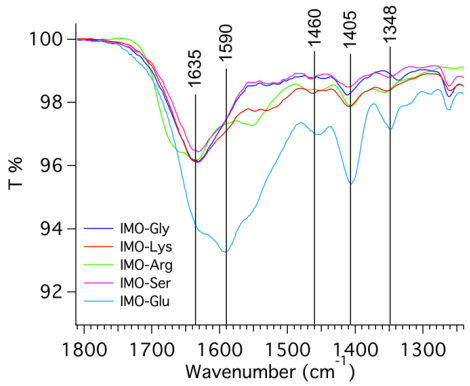

Figure 4. ATR FT-IR spectra of IMO-amino acid samples in the 1250-1800 cm^{-1} range.

Elemental analysis results indicate that a significant amount of carbon is detected in the case of IMO-Glu, corresponding to 11.6 %wt of Glu adsorbed onto IMO (Supporting Information). Taking into account the specific surface area of the nanotubular clays and by assuming that the entire surface is available for the physisorption, we could then estimate an effective head group area of 0.33 nm^2 (details of the calculation are reported in the Supporting Information), a value which is ~1.5 times larger to what is found in tightly packed self-assembled monolayers formed by surfactants based on a carboxyl head group.[35] Even more interesting is the comparison with the head group area at the air-water interface found in Glu-derived surfactants (0.88 nm^2).[50] These findings suggest a quite dense packing of Glu molecules onto the IMO surface, paving the way towards the use of glutamic acid as a building block in the design and fabrication of hybrid materials based on imogolites.

C_{12}Glu adsorption onto imogolite nanotubes and RHO uploading experiments. The marked affinity of glutamic acid for the IMO surface was exploited to prepare a composite material consisting of imogolite nanotubes coated with a Glu-based surfactant able to upload a drug model. The surfactant chosen for this experiment was lauroyl glutamate (C_{12}Glu) in the disodium form, which in water displays a CMC of 50 mM.[51] This surfactant has already been shown to favorably adsorb on the surface of Al_2O_3, while no adsorption was detected on SiO_2.[36] A value of about 285 ng/cm^2 was determined by QCM-D at the CMC, in salt-free conditions.

The mechanism of formation of the hybrid is sketched in Figure 5A. IMO nanotubes and C_{12}Glu are first equilibrated together in water. The concentration of C_{12}Glu in the experiment was 2 mM; *i.e.*, well below the CMC (50 mM in salt-free conditions and 22 mM, determined by

tensiometry, in NaCl 0.9 %w/v) and also below the Critical Surface Association Concentration (CSAC), which is typically around 1/10 of the CMC.[52] At this level of concentration, one would expect that the adsorption of C_{12}Glu on IMO results in patches of micelle-covered surface separated by areas of naked surface. The micelle-covered surface would be strongly anionic and the naked surface in-between would be cationic. Thus, with such an incomplete adsorption one would expect to have attraction between the particles, *i.e.*, fast aggregation (sometimes referred to as patchwise flocculation). This is actually the case in our experiment, where a precipitate is formed after just a few minutes (Figure 5A). Taking into account the good biocompatibility of imogolite,[27,53] this very simple strategy could be exploited for the design of hybrid carriers exposing a bioactive surface. As an example, we tested the uploading properties of the composite towards a model drug (RHO). First, an aliquot of the dye solution was added to the IMO-C_{12}Glu dispersion (see Experimental section). Then, the system was left to equilibrate under agitation during a few hours, the precipitate was discarded by centrifugation and the absorbance of the supernatant was measured to quantify the amount of dye still present in solution.

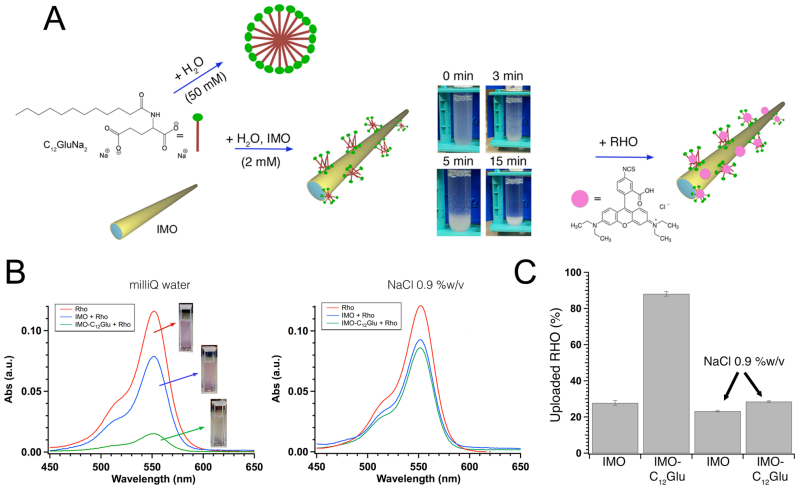

Figure 5. A) Schematic representation of the adsorption-uploading experiment performed with IMO-C_{12}Glu; B) adsorption spectra of Rhodamine B-ITC (RHO) and of IMO+RHO and IMO-C_{12}Glu+Rho supernatant solutions in Milli-Q water (left) and in physiological saline solution (right); C) amount of uploaded dye calculated from the adsorption spectra.

As shown in Figure 5B, pristine IMO is able to adsorb a certain amount of dye, most reasonably through electrostatic and van der Waals interactions with its external surface: in fact, due to its molecular size[54], the access of the dye inside the lumen of IMO is limited by geometrical constraints. When the same experiment is performed in physiological saline solution (NaCl 0.9 %w/v), the uploaded amount is nearly unchanged. On the other hand, the amount of adsorbed dye (Figure 5C) drastically increases (nearly threefold) when C_{12}Glu is present, suggesting the direct role of the surfactant on the uploading process. When the adsorption of C_{12}Glu and RHO is carried out in physiological saline conditions, the amount of uploaded RHO is nearly the same as for pristine IMOs. We explain this finding by taking into account the shielding effect of sodium chloride on the IMO surface charges, resulting in a decreased interaction between the C_{12}Glu polar headgroups and the surface. This is also consistent with the relative coagulation rates in table 1 showing that IMO nanotubes undergo a fast aggregation in the presence of NaCl, also in the presence of Glu.

CONCLUSIONS

In this work we report on the adsorption of amino acids onto imogolite nanotubes, exploring their potentials as building blocks in the preparation of functional hybrid materials. Our results highlight that imogolite nanotubes represent a flexible multifunctional platform, thanks both to

the nanotubular structure and to the exposed alumina surface, which dictates the interaction with amino acids bearing different side chain functional groups. We investigated representative cases for basic, acidic, non-polar and polar amino acids, finding that Glu displays the strongest affinity for the IMO surface. We exploited this finding to prepare a hybrid organic-inorganic material through the adsorption onto the outer surface of IMO of a synthetic surfactant bearing a Glu polar head and a hydrophobic C_{12} alkyl tail. The obtained composite was used in a proof of concept experiment for the upload of a model drug (rhodamine B isothiocyanate), showing that an increased amount of dye is adsorbed when C_{12}Glu is present. We believe that the results reported in this paper could foster the use of imogolite clays in biotechnological applications. Furthermore, our findings could be generalized toward the adsorption of any Glu-containing surfactant on any aluminum oxide surface.

ASSOCIATED CONTENT

The following files are available free of charge.

Supporting Information: Characterization of imogolite sample (TEM, TGA, ATR-FTIR, DLS, N_2 adsorption iosotherm); Turbidimetry of imogolite dispersions; Amino acid adsorption onto imogolite nanotubes; Calculation of the effective amino acid head surface area in the IMO-Glu and IMO-Lys samples (file type, PDF).

AUTHOR INFORMATION

Corresponding Author

* Piero Baglioni

phone: +39 055 457 3033

fax: +39 055 457 3032

e-mail: piero.baglioni@unifi.it

www.csgi.unifi.it

Author Contributions

The manuscript was written through contributions of all authors. All authors have given approval to the final version of the manuscript.

ACKNOWLEDGMENT

CSGI is acknowledged for financial support.

ABBREVIATIONS

IMO, imogolite; TEOS, tetraethyl orthosilicate; ASB, aluminum sec-butoxide; RHO, rhodamine B isothiocyanate; C_{12}Glu, lauroyl glutamate (disodium salt); Arg, arginine; Gly, glycine; Glu, glutamic acid; Lys, lysine; Ser, serine; TEM, transmission electron microscopy; XRD, X-ray diffraction; TGA, thermogravimetric analysis; ATR-FTIR, attenuated total reflectance-Fourier transformed infrared; MCT, mercury cadmium telluride; DLS, dynamic light scattering; SSA, specific surface area; QCM-D, quartz crystal microbalance with monitoring of the dissipation; CMC, critical micelle concentration; PZC, point of zero charge; CSAC, critical surface association concentration.

REFERENCES

(1) Ingham, C. J.; ter Maat, J.; de Vos, W. M. Where Bio Meets Nano: The Many Uses for Nanoporous Aluminum Oxide in Biotechnology. *Biotechnol. Adv.* **2012**, *30* (5), 1089–1099.

(2) Sousa, C. T.; Leitao, D. C.; Proenca, M. P.; Ventura, J.; Pereira, A. M.; Araujo, J. P. Nanoporous Alumina as Templates for Multifunctional Applications. *Appl. Phys. Rev.* **2014**, *1* (3), 031102.

(3) Vinogradov, V. V.; Avnir, D. Exceptional Thermal Stability of Industrially-Important Enzymes by Entrapment within Nano-Boehmite Derived Alumina. *RSC Adv.* **2015**, *5* (15), 10862–10868.

(4) Gupta, R. K. Aluminum Compounds as Vaccine Adjuvants. *Adv. Drug Deliv. Rev.* **1998**, *32* (3), 155–172.

(5) He, P.; Zou, Y.; Hu, Z. Advances in Aluminum Hydroxide-Based Adjuvant Research and Its Mechanism. *Hum. Vaccines Immunother.* **2015**, *11* (2), 477–488.

(6) Li, H.; Li, Y.; Jiao, J.; Hu, H.-M. Alpha-Alumina Nanoparticles Induce Efficient Autophagy-Dependent Cross-Presentation and Potent Antitumour Response. *Nat. Nanotechnol.* **2011**, *6* (10), 645–650.

(7) Sun, B.; Ji, Z.; Liao, Y.-P.; Wang, M.; Wang, X.; Dong, J.; Chang, C. H.; Li, R.; Zhang, H.; Nel, A. E.; Xia, T. Engineering an Effective Immune Adjuvant by Designed Control of Shape and Crystallinity of Aluminum Oxyhydroxide Nanoparticles. *ACS Nano* **2013**, *7* (12), 10834–10849.

(8) Gruner, G. Carbon Nanotube Transistors for Biosensing Applications. *Anal. Bioanal. Chem.* **2005**, *384* (2), 322–335.

(9) Serp, P.; Corrias, M.; Kalck, P. Carbon Nanotubes and Nanofibers in Catalysis. *Appl. Catal. Gen.* **2003**, *253* (2), 337–358.

(10) Shankar, K.; Basham, J. I.; Allam, N. K.; Varghese, O. K.; Mor, G. K.; Feng, X.; Paulose, M.; Seabold, J. A.; Choi, K.-S.; Grimes, C. A. Recent Advances in the Use of TiO2 Nanotube and Nanowire Arrays for Oxidative Photoelectrochemistry. *J. Phys. Chem. C* **2009**, *113* (16), 6327–6359.
(11) Fabbro, A.; Bosi, S.; Ballerini, L.; Prato, M. Carbon Nanotubes: Artificial Nanomaterials to Engineer Single Neurons and Neuronal Networks. *ACS Chem. Neurosci.* **2012**, *3* (8), 611–618.
(12) Du, M.; Guo, B.; Jia, D. Newly Emerging Applications of Halloysite Nanotubes: A Review. *Polym. Int.* **2010**, *59* (5), 574–582.
(13) Ruiz-Hitzky, E.; Darder, M.; Fernandes, F. M.; Wicklein, B.; Alcântara, A. C. S.; Aranda, P. Fibrous Clays Based Bionanocomposites. *Prog. Polym. Sci.* **2013**, *38* (10–11), 1392–1414.
(14) Farmer, V. C.; Adams, M. J.; Fraser, A. R.; Palmieri, F. Synthetic Imogolite: Properties, Synthesis, and Possible Applications. *Clay Min.* **1983**, *18*, 459–472.
(15) Yah, W. O.; Yamamoto, K.; Jiravanichanun, N.; Otsuka, H.; Takahara, A. Imogolite Reinforced Nanocomposites: Multifaceted Green Materials. *Materials* **2010**, *3* (3), 1709–1745.
(16) Lee, S. U.; Choi, Y. C.; Youm, S. G.; Sohn, D. Origin of the Strain Energy Minimum in Imogolite Nanotubes. *J. Phys. Chem. C* **2011**, *115* (13), 5226–5231.
(17) Gustafsson, J. P. The Surface Chemistry of Imogolite. *Clays Clay Miner.* **2001**, *49* (1), 73–80.
(18) Lvov, Y.; Abdullayev, E. Functional Polymer–clay Nanotube Composites with Sustained Release of Chemical Agents. *Prog. Polym. Sci.* **2013**, *38* (10-11), 1690–1719.
(19) Yamamoto, K.; Otsuka, H.; Wada, S.-I.; Sohn, D.; Takahara, A. Transparent Polymer Nanohybrid Prepared by in Situ Synthesis of Aluminosilicate Nanofibers in Poly(vinyl Alcohol) Solution. *Soft Matter* **2005**, *1* (5), 372–377.
(20) Yang, H.; Chen, Y.; Su, Z. Microtubes via Assembly of Imogolite with Polyelectrolyte. *Chem. Mater.* **2007**, *19* (13), 3087–3089.
(21) Kang, D.-Y.; Tong, H. M.; Zang, J.; Choudhury, R. P.; Sholl, D. S.; Beckham, H. W.; Jones, C. W.; Nair, S. Single-Walled Aluminosilicate Nanotube/Poly(vinyl Alcohol) Nanocomposite Membranes. *ACS Appl. Mater. Interfaces* **2012**, *4* (2), 965–976.
(22) Ohashi, F.; Tomura, S.; Akaku, K.; Hayashi, S.; Wada, S.-I. Characterization of Synthetic Imogolite Nanotubes as Gas Storage. *J. Mater. Sci.* **2004**, *39* (5), 1799–1801.
(23) Nakano, A.; Teramoto, N.; Chen, G.; Miura, Y.; Shibata, M. Preparation and Characterization of Complex Gel of Type I Collagen and Aluminosilicate Containing Imogolite Nanofibers. *J. Appl. Polym. Sci.* **2010**, *118* (4), 2284–2290.
(24) Teramoto, N.; Hayashi, A.; Yamanaka, K.; Sakiyama, A.; Nakano, A.; Shibata, M. Preparation and Mechanical Properties of Photo-Crosslinked Fish Gelatin/Imogolite Nanofiber Composite Hydrogel. *Materials* **2012**, *5* (12), 2573–2585.
(25) Jiravanichanun, N.; Yamamoto, K.; Kato, K.; Kim, J.; Horiuchi, S.; Yah, W.-O.; Otsuka, H.; Takahara, A. Preparation and Characterization of Imogolite/DNA Hybrid Hydrogels. *Biomacromolecules* **2012**, *13* (1), 276–281.
(26) Inoue, N.; Otsuka, H.; Wada, S.-I.; Takahara, A. (Inorganic Nanofiber/enzyme) Hybrid Hydrogel: Preparation, Characterization, and Enzymatic Activity of Imogolite/pepsin Conjugate. *Chem. Lett.* **2006**, *35* (2), 194–195.

(27) Ishikawa, K.; Akasaka, T.; Yawaka, Y.; Watari, F. High Functional Expression of Osteoblasts on Imogolite, Aluminosilicate Nanotubes. *J. Biomed. Nanotechnol.* **2010**, *6* (1), 59–65.
(28) Jahromi, M. T.; Yao, G.; Cerruti, M. The Importance of Amino Acid Interactions in the Crystallization of Hydroxyapatite. *J. R. Soc. Interface* **2013**, *10* (80), 20120906.
(29) Sugino, A.; Miyazaki, T.; Ohtsuki, C. Apatite-Forming Ability of Polyglutamic Acid Hydrogels in a Body-Simulating Environment. *J. Mater. Sci. Mater. Med.* **2008**, *19* (6), 2269–2274.
(30) Koutsopoulos, S.; Kontogeorgou, A.; Dalas, E.; Petroheilos, J. Calcification of Porcine and Human Cardiac Valves: Testing of Various Inhibitors for Antimineralization. *J. Mater. Sci. Mater. Med.* **1998**, *9* (7), 421–424.
(31) Eiden-Aßmann, S.; Viertelhaus, M.; Heiß, A.; Hoetzer, K. A.; Felsche, J. The Influence of Amino Acids on the Biomineralization of Hydroxyapatite in Gelatin. *J. Inorg. Biochem.* **2002**, *91* (3), 481–486.
(32) Lu, J. R.; Zhao, X. B.; Yaseen, M. Biomimetic Amphiphiles: Biosurfactants. *Curr. Opin. Colloid Interface Sci.* **2007**, *12* (2), 60–67.
(33) Bordes, R.; Holmberg, K. Amino Acid-Based Surfactants – Do They Deserve More Attention? *Adv. Colloid Interface Sci.* **2015**, *222*, 79–91.
(34) Koenderink, G. H.; Kluijtmans, S. G. J. M.; Philipse, A. P. On the Synthesis of Colloidal Imogolite Fibers. *J. Colloid Interface Sci.* **1999**, *216* (2), 429–431.
(35) Kim, K. S.; Moller, M. A.; Tildesley, D. J.; Quirke, N. Molecular Dynamics Simulations of Langmuir-Blodgett Monolayers with Explicit Head-Group Interactions. *Mol. Simul.* **1994**, *13* (2), 77–99.
(36) Bordes, R.; Tropsch, J.; Holmberg, K. Adsorption of Dianionic Surfactants Based on Amino Acids at Different Surfaces Studied by QCM-D and SPR. *Langmuir* **2010**, 26 (13), 10935-10942
(37) Xu, S.; Sun, Z. Progress in Coagulation Rate Measurements of Colloidal Dispersions. *Soft Matter* **2011**, *7* (24), 11298.
(38) Sun, Z.; Liu, J.; Xu, S. Study on Improving the Turbidity Measurement of the Absolute Coagulation Rate Constant. *Langmuir* **2006**, *22* (11), 4946–4951.
(39) Yah, W. O.; Yamamoto, K.; Jiravanichanun, N.; Otsuka, H.; Takahara, A. Imogolite Reinforced Nanocomposites: Multifaceted Green. *Materials* **2010**, *3* (3), 1709–1745.
(40) Bonelli, B.; Bottero, I.; Ballarini, N.; Passeri, S.; Cavani, F.; Garrone, E. IR Spectroscopic and Catalytic Characterization of the Acidity of Imogolite-Based Systems. *J. Catal.* **2009**, *264* (1), 15–30.
(41) Arancibia-Miranda, N.; Escudey, M.; Molina, M.; García-González, M. T. Use of Isoelectric Point and pH to Evaluate the Synthesis of a Nanotubular Aluminosilicate. *J. Non-Cryst. Solids* **2011**, *357* (7), 1750–1756.
(42) Johnston, C. T.; Sposito, G.; Erickson, C. Vibrational Probe Studies of Water Interactions with Montmorillonite. *Clays Clay Miner.* **1992**, *40* (6), 722–730.
(43) Bonelli, B.; Zanzottera, C.; Armandi, M.; Esposito, S.; Garrone, E. IR Spectroscopic Study of the Acidic Properties of Alumino-Silicate Single-Walled Nanotubes of the Imogolite Type. *Catal. Today* **2013**, *218–219*, 3–9.
(44) Chunming, S.; Harsh, J. B. The Electrophoretic Mobility of Imogolite and Allophane in the Presence of Inorganic Anions and Citrate. *Clays Clay Miner.* **1993**, *41* (4), 461–471.

(45) Harsh, J. B.; Traina, S. J.; Boyle, J.; Yang, Y. Adsorption of Cations on Imogolite and Their Effect on Surface Charge Characteristics. *Clays Clay Miner.* **1992**, *40* (6), 700–706.
(46) Greiner, E.; Kumar, K.; Sumit, M.; Giuffre, A.; Zhao, W.; Pedersen, J.; Sahai, N. Adsorption of L-Glutamic Acid and L-Aspartic Acid to γ-Al2O3. *Geochim. Cosmochim. Acta* **2014**, *133*, 142–155.
(47) Israelachvili, J. N. *Intermolecular and Surface Forces*, 3. ed.; Elsevier, Acad. Press: Amsterdam, 2011.
(48) Roddick-Lanzilotta, A. D.; Connor, P. A.; McQuillan, A. J. An In Situ Infrared Spectroscopic Study of the Adsorption of Lysine to TiO_2 from an Aqueous Solution. *Langmuir* **1998**, *14* (22), 6479–6484.
(49) Roddick-Lanzilotta, A. D.; McQuillan, A. J. An in Situ Infrared Spectroscopic Study of Glutamic Acid and of Aspartic Acid Adsorbed on TiO2: Implications for the Biocompatibility of Titanium. *J. Colloid Interface Sci.* **2000**, *227* (1), 48–54.
(50) Bordes, R.; Holmberg, K. Physical Chemical Characteristics of Dicarboxylic Amino Acid-Based Surfactants. *Colloids Surf. Physicochem. Eng. Asp.* **2011**, *391* (1–3), 32–41.
(51) Bordes, R.; Tropsch, J.; Holmberg, K. Counterion Specificity of Surfactants Based on Dicarboxylic Amino Acids. *J. Colloid Interface Sci.* **2009**, *338* (2), 529–536.
(52) Kronberg, Bengt K, Holmberg K, Lindman B. *Surface Chemistry of Surfactants and Polymer*. Wiley; **2004**.
(53) Rotoli, B. M.; Guidi, P.; Bonelli, B.; Bernardeschi, M.; Bianchi, M. G.; Esposito, S.; Frenzilli, G.; Lucchesi, P.; Nigro, M.; Scarcelli, V.; Tomatis, M.; Zanello, P. P.; Fubini, B.; Bussolati, O.; Bergamaschi, E. Imogolite: An Aluminosilicate Nanotube Endowed with Low Cytotoxicity and Genotoxicity. *Chem. Res. Toxicol.* **2014**, *27* (7), 1142–1154.
(54) Guo, Y.; Zhao, J.; Zhang, H.; Yang, S.; Qi, J.; Wang, Z.; Xu, H. Use of Rice Husk-Based Porous Carbon for Adsorption of Rhodamine B from Aqueous Solutions. *Dyes Pigments* **2005**, *66* (2), 123–128.

Adsorption of amino acids and glutamic acid-based surfactants on imogolite nanotubes

Alessio Gabbani, Stefano Del Buffa, Francesca Ridi, Romain Bordes, Massimo Bonini, Krister Holmberg, Piero Baglioni

Characterization of imogolite nanotubes

TEM

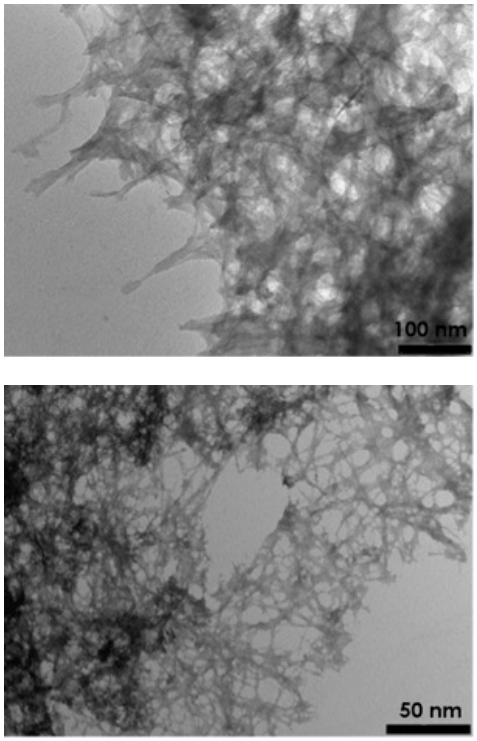

Figure S1. TEM images of synthesized imogolite nanotubes.

Thermogravimetry (TGA)

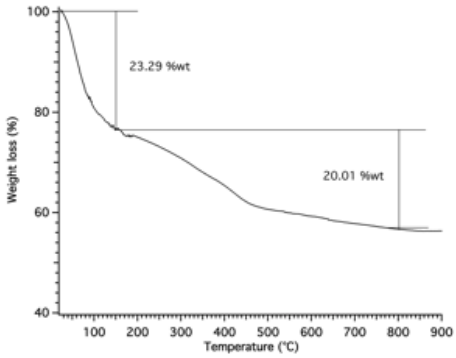

Figure S2. Thermogravimetry curve of imogolite sample in the 25-900 °C temperature range. Indicated weight losses correspond to the loss of physisorbed water (25-150 °C) and to structural dehydroxylation (150-800 °C)[1,2].

Dynamic light scattering (DLS)

Dynamic light scattering measurements were carried out by means of a 90Plus/BI-MAS system by Brookhaven Instrument (New York, USA), working with a 15 mW solid state laser (λ = 635 nm) as the light source. The time autocorrelation functions of the scattered field were analyzed through a Laplace Inversion by CONTIN algorithm. The imogolite sample is constituted by two populations of objects: the most abundant corresponds to dimensions of ~750 nm (with a polydispersity of ~50%), while the second population is given by large aggregates with dimensions in the 30-50 μm range.

N_2 adsorption isotherm

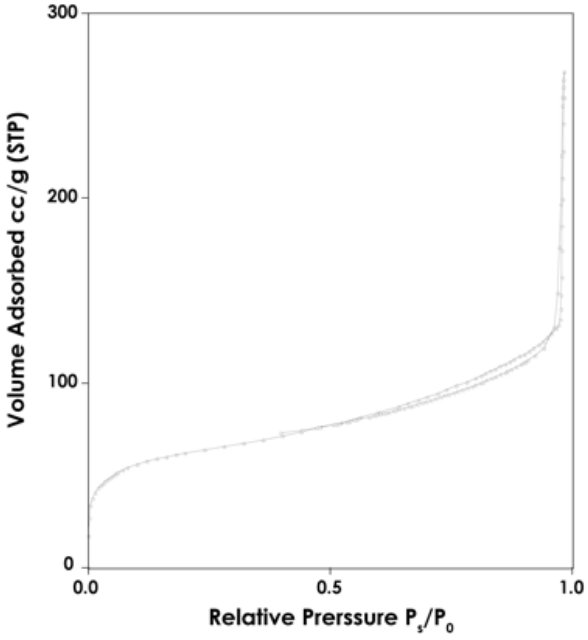

Figure S3. Nitrogen adsorption isotherm of imogolite sample, showing Type I isotherm with a small hysteresis loops that is associated to slit-shaped mesopores, most likely deriving from aggregation of nanotubes into bundles[5,6].

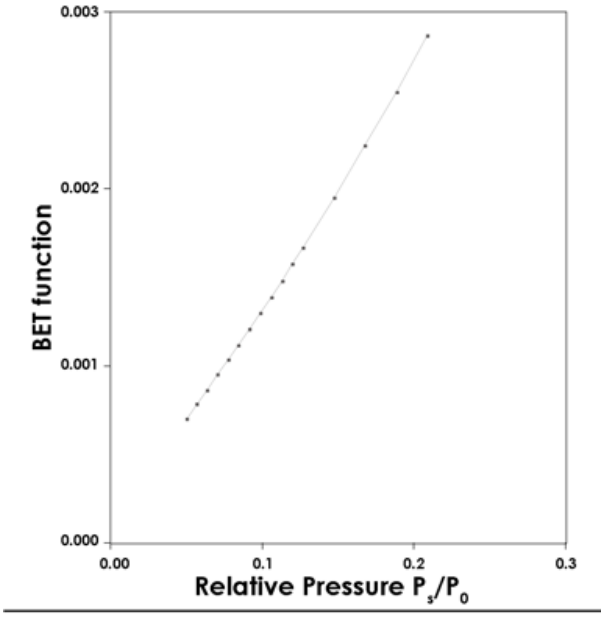

Surface Area Report

BET Surface area	321.50	sq.m/g
Slope	0.013560	
Intercept	-0.000022	
C_value	0.000	
Monolayer Volume	73.8680	cc/g (STP)
Correlation Coefficient	0.99911	

Figure S4. Example of BET surface area calculation on imogolite sample.

Turbidimetry of imogolite dispersions

The absolute coagulation rate constant is an important parameter used to characterize the coagulation kinetics of colloidal systems, and accurate experimental data are particularly important for the development of relevant theories or for deriving information about colloidal interactions. To determine the absolute coagulation rate constant of suspensions, the turbidity measurement has been extensively adopted[7] because of its simplicity and easy implementation. However, to determine the absolute coagulation rate by turbidity measurements, the difference between extinction (or attenuation) cross sections of one doublet or dimer (two adhered particles) and of two single particles has to be evaluated from theory. For spheres, the extinction cross section can be calculated exactly from Mie theory. However, the doublets are not spherical, so it cannot be calculated exactly. The same applies to non-spherical particles, already as singlets.

To improve the applicability of the turbidity measurement, the T-matrix method[8,9] has been proposed to accurately calculate extinction cross sections of non-spherical particles, as well as real doublets in the turbidity measurement. In particular, Mie and Rayleigh-Gans-Debye (RGD) theories are severely inadequate when the parameter ($\alpha=2\pi a/\lambda$ where a represents the radius of the particle) increases.

In the earliest stage of the coagulation process for a monodisperse colloidal system, only collisions of single particles to form doubles need to be considered. Therefore, the change in particle number concentration can be approximately expressed as:

$$\left(\frac{dN_1}{dt}\right)_{t=0} = -k_{11}N_1^2 \tag{1}$$

$$\left(\frac{dN_2}{dt}\right)_{t=0} = \frac{k_{11}N_1^2}{2} \tag{2}$$

where N_1 and N_2 are the number concentrations of single particles and doublets, respectively, t is time, and k_{11} is the coagulation rate constant. Because the turbidity is expressed as $\tau = N_1C_1 + N_2C_2$, where C_1 and C_2 are the extinction cross sections for the single particle and doublet, respectively, and τ is the turbidity, the change rate in turbidity due to the aggregation of single particles can be written as:

$$\frac{d\tau}{dt} = C_1\frac{dN_1}{dt} + C_2\frac{dN_2}{dt} \tag{3}$$

Combining eqs 1, 2, and 3, the coagulation rate constant can be connected to the rate of turbidity change in the turbidity measurement by the following equation[10]:

$$k_{11} = \frac{[d(\tau/\tau_0)/dt]_0}{[(C_2/2C_1) - 1]N_1} \tag{4}$$

where τ_0 is the turbidity at the coagulation starting time $t = 0$. Assuming the denominator in eq. 4 can be taken to be a constant, the coagulation rate will be proportional to the quantity $R = [d(\tau/\tau_0)/dt]_0$, the relative rate of turbidity change. Thus, $|R|$ is usually used to represent the relative coagulation rate. The dimensionless parameter $F = [(C_2/2C_1) - 1]$ is referred to the optical factor. R can be obtained from the turbidity measurement, but the optical factor has to be calculated by means of light scattering theory[8,11–15]. In this study, the data of transmission percentage (T%) versus time were recorded during the coagulation and sedimentation process. The wavelength was 650 nm, while temperature was set to RT (=25 °C). The transmission percentages were transformed into turbidity by the equation:

$$\tau = \frac{1}{l} \ln \frac{I_0}{I} \tag{5}$$

where l is the path length through the dispersion. The slope of the τ/τ_0 versus time plot (the relative coagulation rate) was calculated by the procedure of linear regression in the early stages of coagulation, and was used to compare the colloidal stability of the various IMO dispersions. To ensure that the experiments were really done in the early stages, the experimental window should be much smaller than the coagulation time or half-life $t_{1/2}$, which is the time required for the reduction of the number of particles by one-half. The theoretical coagulation time is given by the Smoluchowski coagulation equation[16]:

$$t_{1/2} = \frac{3\eta}{4kTN_1} \tag{6}$$

where η and k are the viscosity and Boltzmann constant, respectively. More specifically, for the case of water as the medium at $T = 25$°C, we simply have[17]:

$$t_{1/2} \approx \frac{2 \times 10^{17}}{N_1} (\text{seconds}) \tag{7}$$

For imogolite nanotubes, due to their small dimensions, the number of particles in the investigated sample is quite large (around $1 \cdot 10^{15}$), and it corresponds to a $t_{1/2}$ in the order of few minutes. It is not therefore safe to assume that the experiments were done in the early stages of coagulation, except for the very beginning (t<10min).

Amino acid adsorption onto imogolite nanotubes

1 ml of an aqueous IMO dispersion (4 g/L) was sonicated during 2 hours and then added to a test tube. The selected amino acid was then added to each test tube. The amount was chosen so to theoretically cover twice the surface area of the IMO in the sample. This value was calculated by taking into account the specific surface area of IMO resulting from porosimetry (317 ± 7 m^2/g) and adopting a value of 0.2 nm^2 for the cross-section ($S_{a.a.}$) of all the tested amino acids[18]. The mass of amino acid ($m_{a.a.}$) was calculated from:

$$m_{a.a.} = \left(\frac{SSA_{IMO}\ m_{IMO}\ \%_{coverage}\ Mw_{a.a.}}{S_{a.a.}\ N_A}\right)$$

where m_{IMO} and SSA_{IMO} are the mass and the specific surface area of imogolite, respectively, $Mw_{a.a.}$ is the molecular weight of the amino acid, and N_A is the Avogadro number.

Calculation of the effective amino acid head surface area in the IMO-Glu and IMO-Lys samples

From elemental analysis, the amount of total carbon in the IMO-Glu sample is 4.75 %wt that corresponds to 11.64 %wt of glutamic acid (considering that all the detected carbon derives from the amino acid).

%wt Glu= (%wt C/M_C *5)*M_{Glu} = (4.75/12*5)*147.13 = 11.64 %wt

The moles of glutamic acid result to be $7.91x10^{-4}$ per gram of sample that correspond to $4.76x10^{20}$ adsorbed molecules per gram of sample (mol_{Glu}*N_A). Assuming that i) the imogolite external surface is approximately half of the total surface, ii) the external surface is completely available for the interaction with Glu and iii) no multiple layers are formed, the effective surface area of Glu, is calculated from:

S_{Glu} = S_{IMO} [m^2/g] / adsorbed molecules per gram * 10^{18} = (317/2) / $4.76x10^{20}$ * 10^{18} = 0.33 nm^2

The amount of carbon detected in the IMO-Lys sample is 2.11 %wt that corresponds to 4.28 %wt of lysine.

%wt Lys= (%wt C/M_C *6)*M_{Lys} = (2.11/12*6)*146.19 = 4.28 %wt

The moles of lysine result to be $2.93x10^{-4}$ per gram of sample that correspond to $1.76x10^{20}$ adsorbed molecule per gram of sample. The effective surface area of Lys resulted to be 0.90 nm^2.

References

(1) Farmer, V. C.; Adams, M. J.; Fraser, A. R.; Palmieri, F. Synthetic Imogolite: Properties, Synthesis, and Possible Applications. *Clay Min.* **1983**, *18*, 459–472.

(2) Ookawa, M. Synthesis and Characterization of Fe-Imogolite as an Oxidation Catalyst. In *Clay Minerals in Nature - Their Characterization, Modification and Application*; Valaskova, M., Ed.; InTech, 2012.

(3) Koenderink, G. H.; Kluijtmans, S. G. J. M.; Philipse, A. P. On the Synthesis of Colloidal Imogolite Fibers. *J. Colloid Interface Sci.* **1999**, *216* (2), 429–431.

(4) Johnston, C. T.; Sposito, G.; Erickson, C. Vibrational Probe Studies of Water Interactions with Montmorillonite. *Clays Clay Miner.* **1992**, *40* (6), 722–730.

(5) Pierotti, R. A.; Rouquerol, J. Reporting Physisorption Data for Gas/solid Systems with Special Reference to the Determination of Surface Area and Porosity. *Pure Appl Chem* **1985**, *57* (4), 603–619.

(6) Bonelli, B.; Bottero, I.; Ballarini, N.; Passeri, S.; Cavani, F.; Garrone, E. IR Spectroscopic and Catalytic Characterization of the Acidity of Imogolite-Based Systems. *J. Catal.* **2009**, *264* (1), 15–30.

(7) Elimelech, M. *Particle Deposition and Aggregation Measurement, Modelling, and Simulation*; Butterworth-Heinemann: [Oxford [England]; Boston, 1998.

(8) Mishchenko, M. I. Light Scattering by Randomly Oriented Axially Symmetric Particles. *J. Opt. Soc. Am. A* **1991**, *8* (6), 871–882.

(9) Mishchenko, M. I.; Travis, L. D.; Lacis, A. A. *Scattering, Absorption, and Emission of Light by Small Particles*; Cambridge University Press, 2002.

(10) Lichtenbelt, J. W. T.; Ras, H. J. M. C.; Wiersema, P. H. Turbidity of Coagulating Lyophobic Sols. *J. Colloid Interface Sci.* **1974**, *46* (3), 522–527.

(11) Waterman, P. C. New Formulation of Acoustic Scattering. *J. Acoust. Soc. Am.* **1969**, *45* (6), 1417–1429.

(12) Waterman, P. C. Symmetry, Unitarity, and Geometry in Electromagnetic Scattering. *Phys. Rev. D* **1971**, *3* (4), 825–839.

(13) Waterman, P. C. Matrix Formulation of Electromagnetic Scattering. *Proc. IEEE* **1965**, *53* (8), 805–812.

(14) Wriedt, T. Using the T-Matrix Method for Light Scattering Computations by Non-Axisymmetric Particles: Superellipsoids and Realistically Shaped Particles. *Part. Part. Syst. Charact.* **2002**, *19* (4), 256–268.

(15) Doicu, A.; Wriedt, T. Extended Boundary Condition Method with Multipole Sources Located in the Complex Plane. *Opt. Commun.* **1997**, *139* (1–3), 85–91.

(16) Smoluchowski, M. Drei Vorträge Über Diffusion, Brownsche Molekularbewegung Und Koagulation von Kolloidteilchen. *Phys. Zeit* **1916**, *17*, 557–585.

(17) Myers, D. *Surfaces, Interfaces, and Colloids: Principles and Applications, 2nd Ed.*; John Wiley & Sons, New York, 1999.

(18) Kim, K. S.; Moller, M. A.; Tildesley, D. J.; Quirke, N. Molecular Dynamics Simulations of Langmuir-Blodgett Monolayers with Explicit Head-Group Interactions. *Mol. Simul.* **1994**, *13* (2), 77–99.

THE JOURNAL OF PHYSICAL CHEMISTRY C

Article

pubs.acs.org/JPCC

State of Water in Hydrating Tricalcium Silicate Pastes: The Effect of a Cellulose Ether

Stefano Del Buffa,[†] Emiliano Fratini,[†] Francesca Ridi,[†] Antonio Faraone,[‡,§] and Piero Baglioni*[,†]

[†]Department of Chemistry "Ugo Schiff" and CSGI, University of Florence, via della Lastruccia 3, 50019 Sesto Fiorentino, Florence, Italy

[‡]NIST Center for Neutron Research, 100 Bureau Drive, Gaithersburg, Maryland 20899-6102, United States

[§]Department of Materials Science and Engineering, University of Maryland, College Park, Maryland 20742, United States

Supporting Information

ABSTRACT: Time-dependent quasi-elastic neutron scattering (QENS) and differential scanning calorimetry (DSC) were applied to study water dynamics and hydration kinetic of the hydration reaction of tricalcium silicate in the presence of a methyl hydroxyethyl cellulose (MHEC) additive. The translational dynamics of the water confined in the developing hydrated calcium silicate matrix was probed at the molecular scale by QENS during the first 4 days, while the evolution of the matrix porosity and the hydration kinetics were determined up to 28 days of hydration by differential scanning calorimetry. The application of the boundary nucleation and growth model consistently improved the hydration kinetics picture, usually obtained from the application of the classical Avrami-Erove'ev model, allowing the evaluation of the individual contributions of nucleation and growth over the entire hydration process. In the presence of the cellulose ether the nature of the nucleation process is strongly modified, approaching a "spatially random" hydration mechanism. The water contained in the nanometric porosity of the hydrated calcium silicate matrix, which is fundamental for the efficiency of the hydration process, results increased when MHEC is added, leading to a delay of the onset of the hydration process and the enhancement of the efficiency of the reaction.

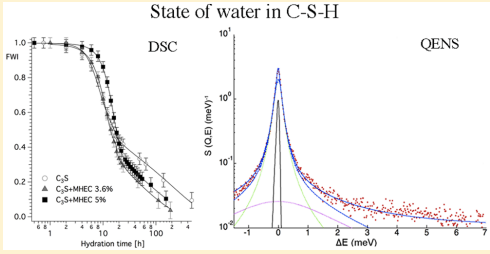

INTRODUCTION

Ordinary Portland Cement (OPC) is the most used binder for construction purposes. Tricalcium silicate (shortened to C_3S in the cement chemistry notation) generally contributes up to 70% of the total weight of OPC and is the main ingredient responsible for the mechanical properties of a cured paste.[1] For these reasons, C_3S can be considered as a model for the study of the setting and hardening processes of cement pastes. During cement hydration, C_3S is progressively converted to amorphous calcium silicate hydrate (C−S−H) and crystalline calcium hydroxide.[1] From a mechanical point of view, the dry powder mixed with water forms a paste that develops rigidity and steadily increases in compressive strength as a consequence of the hydration reaction. In the first stages of this complex process, a thin layer of C−S−H covers the silicate anhydrous grain's surface then C−S−H globules start to flocculate producing a tridimensional fractal network held together by hydrogen bonds and weak intermolecular forces. As the hydration proceeds, water is consumed and the gel phase progressively forms a solid network with a compact yet porous structure.[2,3] The water molecules that have not reacted with C_3S are confined in micro- and nanosized porosities formed as a consequence of the packing of hydrated globules. Depending on the confining degree, these molecules can have different physical and chemical properties compared to bulk water at the same temperature.[3−5] For instance, recent theoretical works have rationalized the slow dynamics of the water confined in the interlayer of the silicatic chains in terms of the local chemical environment provided by the C−S−H gel phase, attributing a crucial role to H-bond connections between water molecules and C−S−H interfacial hydroxyl groups.[6,7]

Among the various organic compounds often used in the industry to modulate water retention and rheology of the mortar, cellulose ethers (CEs) are very popular. Several works[8−12] have been devoted to the characterization of cement hydration in the presence of cellulose ethers, showing that CEs play a key role in affecting the hydration kinetics, the porosity, and the microstructure of fresh and hardened cement materials. Despite the broad use of CEs in the cement industry, the effect of their water retaining properties on the hydration of cement pastes is still not understood. This paper is aimed at shedding light on the effect of a water retainer additive, namely methyl hydroxyethyl cellulose (MHEC), on the hydration kinetics of a C_3S paste, from the nanoscale (translational water dynamics)

Received: January 21, 2016
Revised: March 23, 2016
Published: March 23, 2016

DOI: 10.1021/acs.jpcc.6b00691
J. Phys. Chem. C 2016, 120, 7612−7620

up to the macroscale (bulk hydration kinetics). The concentration of MHEC in the investigated samples was chosen in the range commonly used for extrusion processing of cementitious materials.[8] In particular, time-dependent quasi-elastic neutron scattering (QENS) and differential scanning calorimetry (DSC) techniques were applied to study the hydration reaction of C_3S in real time from both a dynamic and a kinetic point of view. The translational dynamics of the water confined in the developing C−S−H matrix was probed at the molecular scale by QENS during the first 4 days, while the evolution of the matrix porosity and the hydration kinetics were determined during 28 days of hydration by DSC. The description of the hydration kinetics according to the boundary nucleation and growth model (BNGM)[13] allowed for the evaluation of the individual contributions of nucleation and of growth to the entire hydration process thus improving the picture previously obtained with the Avrami-Erove'ev model.[8,14] All the results taken together highlight the role of the MHEC additive on the water dynamics and hydration kinetics, as well as on the developing C−S−H microstructure.

MATERIALS AND METHODS

Materials. Tricalcium silicate was provided by CTG Italcementi (Italy). The specimen has a specific surface area of 0.65 m^2/g and a CaO content of 71.7%. The MHEC is Walocel MKX 40000 (Dow Chemical Company, U.S.A.) and was used as received. To prepare the samples, a certain amount of the C_3S powder was mixed with water to reach a water to cement ratio (w/c) of 0.4. MHEC was dissolved in water at a concentration of 3.6 and 5% wt and then added to C_3S so that the final amount of MHEC was 0.27% (M_low) and 0.54% (M_high) with respect to the C_3S weight, respectively. The three samples (pure C_3S, C_3S + M_low, and C_3S + M_high) were hydrated at a constant temperature of 30 °C. The water was Milli-Q grade (resistivity >18 MΩcm).

Methods. Incoherent quasi-elastic neutron scattering (QENS) experiment was performed at the intense pulsed neutron source (IPNS) of the Argonne National Laboratory (Argonne, IL, U.S.A.) on the inverse geometry spectrometer QENS.[15] In this spectrometer, the white pulsed neutron beam from the solid methane moderator of the spallation source, scattered by the sample, is deflected by 22 graphite analyzer arms onto the corresponding detector banks. The final energy of the detected neutrons is fixed by the analyzer to be around 3.3 meV. From the measured time-of-flight of the detected neutrons the energy exchanged by the neutrons with the sample can be calculated. The obtained energy transfer ranges from −2.5 to 200 meV, and the accessible scattering vector, **Q**, at the elastic channel ranges from 0.3 to 2.6 $Å^{-1}$. The energy resolution at the elastic peak was determined using a thin V foil and resulted to be about 90 μeV (full width at half-maximum) corresponding to an accessible time window of about 50 ps. The samples were spread evenly into a rectangular aluminum cell making a layer of 0.5 mm thickness. The volume fraction of water in the sample was 0.40, making a film of H_2O of an effective thickness of 0.20 mm. The cell was reassembled and sealed by means of an indium gasket. This ensures a negligible loss of water as well as no contamination of the paste by carbon dioxide during the experiment. The interior of the cell was Teflon-coated to avoid any interaction between the cement paste and the Al cell, which was proven to change the hydration kinetic.[16] The rectangular sample cell was placed at 45° to the direction of the incident neutron beam. The frame of the cell was masked using a Cd foil to avoid parasitic scattering. Some of the detector banks were shadowed by the edge of the cell and the corresponding data have been discarded. The data from the six highest angle detectors have been grouped two by two in three sets of data. The error in **Q** involved with this procedure is about 3%. We obtained two sets of eight and three spectra in transmission geometry at low scattering angles and in reflection geometry at high scattering angles, respectively. Data were corrected for scattering from the Al sample holder containing dry tricalcium silicate powder, standardized dividing by the scattering intensity from a thin vanadium plate, and finally converted in double differential scattering cross sections using standard routines available at IPNS. The vanadium signal has been used both as a standard for the calibration of detectors and for the calibration of the elastic response of the instrument.

Differential scanning calorimetry (DSC) was performed by means of a DSC-Q2000 (TA Instruments, Philadelphia, U.S.A.). For the determination of kinetic parameters, samples were frozen at −60 °C and then heated to 30 °C at 5 °C/min. Melting enthalpy of water was obtained from the integration of the endothermic peak between −40 and 23 °C. The area of the melting peak of ice is directly proportional to the amount of water able to freeze inside the sample and for this reason it decreases as the hydration goes on, because water is consumed to form C−S−H and $Ca(OH)_2$. By knowing the total amount of water present in the sample, it is possible to convert the melting enthalpy in the free water index (FWI) according to eq 1[17,18]

$$\mathrm{FWI} = \frac{\Delta H_{\mathrm{exp}}}{\Phi_{\mathrm{W}} \Delta H_0} \tag{1}$$

where ΔH_{exp} is the experimental melting enthalpy, ΔH_0 is the standard melting enthalpy of water (333.4 J/g) and Φ_{W} is the weight fraction of water in the sample.

To get insights into morphology and structure, low temperature DSC measurements were performed by cooling the samples to −80 °C at a very slow rate (0.5 °C/min).

QENS Data Analysis. QENS is a state-of-art technique especially suited for the in situ investigation of individual relaxation dynamics of hydrogenated species from the pico-second to nanosecond time-scale. A considerable amount of literature is devoted, for instance, to the study of water-based systems, supercooled water,[19,20] water confined in Vycor glass,[21] hydration water of complex systems like proteins[22,23] or nucleic acids,[24] and cementitious pastes of various composition,[4,25,26] just to cite some.

Because the incoherent scattering cross section of hydrogen, σ_{H}, is much larger than its coherent counterpart and also than that of oxygen, calcium, and silicon, the double differential scattering cross section in a QENS experiment on a cementitious paste is dominated by the hydrogen self-dynamics term, $S_s(\vec{Q},E)$:

$$\frac{\partial^2 \sigma}{\partial E \partial \sigma} = N \frac{\sigma_{\mathrm{H}}}{4\pi} \frac{k}{k_0} S_s(\vec{Q}, E) \tag{2}$$

where $\hbar\omega = E_0 - E$ is the energy transfer, k_0 and E_0 are the wave vector and energy of the incident neutrons, respectively, and k and E are those of the scattered neutrons. It is important to remember that if motions are too slow for the spectrometer resolution they will contribute to the elastic line; on the other hand, if motions are too fast they will appear as a flat background. The information contained in the $S_s(\vec{Q},E)$

DOI: 10.1021/acs.jpcc.6b00691
J. Phys. Chem. C 2016, 120, 7612−7620

connected to a cement paste accounts for the individual motions of all the hydrogenated species present in the scattering volume (i.e., H_2O, C−S−H, and CH) referring to their characteristic mobility. For this reason, signals of immobile species, like water or OH chemically bound to C−S−H and CH will generate an elastic contribution to the QENS spectrum (see for example Figure S1 in the Supporting Information), while the mobile water molecules will produce the quasi-elastic broadening.

Considering the literature, QENS data obtained from cement pastes have been interpreted using two distinct approaches in the description of $S_s(Q,E)$. In the first one,[27,28] a delta function takes into account the immobile water fraction coming from C−S−H and CH and the dependence of the quasi-elastic broadening as a function of $\mathbf{Q}$ is explicitly considered, either using the relaxing cage model for translation alone (i.e., valid for $\mathbf{Q}$ below 1 $Å^{-1}$)[27] or a combination of translational and rotational motions in the case of a wider interval of momentum transfer.[28,29] In the second approach[30] only the average QENS spectrum at $\mathbf{Q}$ values around 2 $Å^{-1}$ is considered, implying that the motion in the scattering volume of about $(\pi/2)^3$ $Å^3$ (i.e. ∼3 $Å^3$) is localized (mainly due to rotations). In this case the spectrum is modeled as a sum of a delta function (for the immobile fraction corresponding to C−S−H and CH), two Lorentzian functions used to fit the freely diffusing water, and one Lorentzian to specifically consider the existence of pseudobound or constrained water. Shortly, the two approaches differ in the number of functions adopted to describe the scattering of mobile hydrogenated species, that is, those with a relaxation time larger than the experimental time resolution. In both cases, the elastic contribution of all QENS spectra was described by a delta function centered at $\Delta E = 0$ meV.

In this work, we simultaneously considered both approaches in order to have a unified picture of the dynamics of water confined in a cement paste. In the first model, the quasi-elastic contribution was represented by two Lorentzian functions (1, 2 in eq 3) associated with translational and rotational motion of hydrogen atoms. In the second model, the quasi-elastic contribution was represented by one Lorentzian function describing the confined water (C in eq 4) and two Lorentzian functions accounting for bulk water (F_1 and F_2 in eq 4).

$$S(\mathbf{Q},E) = p\delta(E-E_1) \otimes R(\mathbf{Q},E) + (1-p)\left\{\frac{B_1}{\pi}\frac{\Gamma_1}{\Gamma_1^2(E-E_1)} + \frac{B_2}{\pi}\frac{\Gamma_2}{\Gamma_1^2(E-E_1)}\right\} \otimes R(Q,E) + \mathrm{bkg} \quad (3)$$

$$S(\mathbf{Q},E) = P\delta(E-E_1) \otimes R(\mathbf{Q},E) + \left\{\frac{C}{\pi}\frac{\Gamma_C^2}{\Gamma_C^2+(E-E_1)} + \frac{F_1}{\pi}\frac{\Gamma_{F_1}^2}{\Gamma_{F_1}^2+(E-E_1)} + \frac{F_2}{\pi}\frac{\Gamma_{F_2}^2}{\Gamma_{F_2}^2+(E-E_1)}\right\} \otimes R(Q,E) \quad (4)$$

Both expressions must be convoluted with the experimental resolution, $R(Q,E)$, to take into account the finite resolution of the QENS spectrometer. In the above equations, p or P are the elastic fraction of the total QENS signal, directly proportional to the amount of $Ca(OH)_2$ and C−S−H formed; Γ_1 and Γ_2 are the half width at half-maximum (HWHM) of the two Lorentzian functions with amplitude B_1 and B_2, respectively; E_1 is the energy shift of the elastic peak with respect to $E = 0$; bkg is a term of linear background; P represents the fraction of immobile water and OH species bound into solids ($Ca(OH)_2$ and C−S−H); C represents the confined water fraction; F_1 and F_2 represent the free water fraction.

In this particular case, the Lorentzian functions have been adopted instead of the stretched exponential function because the resolution of the spectrometer was not optimal to distinguish between the two functional forms.[31]

A particular case of the QENS technique is the measurement of the elastic intensity as a function of temperature, usually referred as the elastic scan mode. Considering a system where the only dynamics is a harmonic vibration, $S(\mathbf{Q},E)$ reduces to a delta function with amplitude $\mathrm{DW}(\mathbf{Q}) = \exp[-\langle u^2\rangle \mathbf{Q}^2/3]$, where $\mathrm{DW}(\mathbf{Q})$ is referred to as the Debye−Waller factor and $\langle u^2\rangle$ is the mean square displacement of the hydrogen atoms around the equilibrium position. Elastic scan technique is a simple way to quantify the dynamics entering the time window of the neutron spectrometer. In the case of cement pastes we can extract the mean square displacement as a function of time by plotting $-3\ln[S(\mathbf{Q},E \approx 0,t)]$ as a function of $\mathbf{Q}^2$, where $S(\mathbf{Q},E \approx 0,t)$ is the integral of $S(\mathbf{Q},E)$ at a given time t done using ± the instrumental resolution as integration limits.

DSC Data Analysis. The FWI versus hydration time curves were fitted adopting the BNGM.[13] According to this model, hydration products nucleate at random locations on the surface of the C_3S particles and then grow to cover the particle surfaces and fill the pores between the particles leading to coalescence between adjacent hydrated regions and, finally, to the hardening of the paste. The equation used to fit the experimental data is the following

$$X = (1 - \mathrm{FWI_d}) + \mathrm{FWI_d}\exp[-2k_G\int_t^0 (1-\exp(-Y^e))dz] \quad (5)$$

where X is the fraction of transformed volume, $\mathrm{FWI_d}$ is the free water index at time t_d, and Y^e is the extended area fraction of the intersection between a reference plane and all regions nucleated on the grain boundary. With the assumption that the nucleation rate per unit area of untransformed boundary I_B is constant, Y^e can be integrated directly to give

$$Y^e = \frac{\pi I_B}{3}G^2t^3\left[1 - \frac{3y^2}{G^2t^2} + \frac{2y^3}{G^3t^3}\right] \quad \text{if } t > \frac{y}{G} \quad (6)$$

$$Y^e = 0 \quad \text{if } t < \frac{y}{G} \quad (7)$$

The transformed volume fraction depends on three covariant parameters, the linear growth rate G, the nucleation rate I_B, and the boundary area per unit volume O_v^B. However, only two degrees of freedom exist, and in the original model developed by Thomas[13] these were identified as two independent rate constants: k_B that describes the rate at which the nucleated boundary area transforms in hydration products, and k_G that describes the rate at which the porosity are filled with hydration products. The k_B/k_G ratio determines which of the two effects is predominant.

These rate constants are connected to G and I_B by the following relationships

$$k_B = (I_B O_v^B)^{1/4} G^{3/4} \quad (8)$$

DOI: 10.1021/acs.jpcc.6b00691
J. Phys. Chem. C 2016, 120, 7612−7620

$$k_G = O_v^B G \quad (9)$$

If O_v^B can be determined independently, G and I_B can be calculated. In the case of the C_3S powder used in this study, O_v^B is 0.98 μm^{-1}, as calculated from the value of the surface area of the dry powder (0.65 m^2/g), scaled by the volume occupied by the hydration products after complete hydration (0.662 cm^3/g). More details are provided in the Supporting Information.

The rate-limiting process determining the hydration reaction in the final part of the kinetics is the diffusion of the water through the layer of C−S−H surrounding the unreacted grains. For this reason, the last part of the hydration was described by means of the diffusional model

$$\mathrm{FWI}(t > t_d) = \left\{ \mathrm{FWI}_d^{1/3} - \frac{(2D)^2}{\langle R \rangle}(t - t_d)^{1/2} \right\}^3 \quad (10)$$

where D is the diffusional constant, and $\langle R \rangle$ is the average radius of the anhydrous C_3S grains (4.66 μm). The BNGM equations have been combined with the diffusion-limited model and numerically solved in Igor Pro, version 6.36.

RESULTS AND DISCUSSION

The combination of DSC and QENS allows acquiring a complete picture of C_3S hydration process in the presence of MHEC. While DSC provides information on the bulk matrix developing during the hydration process, QENS gives information on the water dynamics whose motion is restricted by the growing C−S−H phase. The main results obtained from these techniques will be discussed separately in the following.

Differential Scanning Calorimetry. Figure 1 shows the trend of the free water index versus time for C_3S, C_3S + M_low, and C_3S + M_high samples. FWI has a similar trend to the p parameter extracted from the fitting of QENS data and reported in Figure 7. The already mentioned kinetic stages can be unambiguously identified. The effect of the cellulosic additive is dual: on one hand, it delays the setting process while on the other hand it increases the efficiency of the hydration process, as evidenced by the lower value of FWI reached at the end of the acceleration period in the samples containing MHEC.

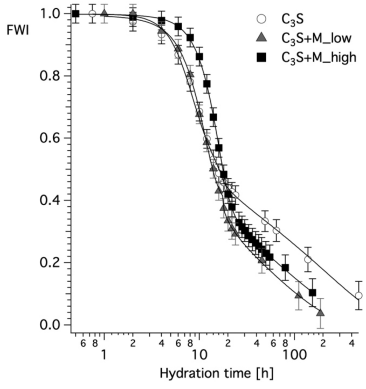

Figure 1. Time evolution of FWI (markers) and best fitting obtained by the combination of BNG and diffusional models (solid lines).

This feature can be ascribed to the hydrophilic character of MHEC that strongly binds water and, upon adsorption onto the silicate grains surface, makes it homogeneously distributed over the solid phase. Water is thus more prone to react and hydration results more efficient, as also shown by QENS. Induction time t_i (obtained as the junction point of the lines describing the induction and the acceleration points) increases from 6 ± 1 h (C_3S) to 9 ± 1 h (C_3S + M_low), while the FWI at the end of nucleation and growth period (FWI_d) for C_3S + M_low sample is more than 15% less than that of C_3S. This is in agreement with data reported previously on a similar sample.[14] When the amount of MHEC inside the paste is doubled (C_3S + M_high), t_i further increases to 12 ± 1 h but the efficiency of hydration is not significantly improved (FWI_d remains almost unchanged). Table 1 summarizes the parameters extracted from the BNGM + diffusional fitting of the FWI versus time curves.

The k_B and k_G values obtained for the C_3S sample are in very good accordance with those reported in previous investigations.[11] When the cellulose ether is added in the formulation, the k_B rate decreases proportionally with the increasing of MHEC amount. On the other hand, the presence of the polymer causes an increase in k_G of 1 order of magnitude with respect to the pure C_3S sample. These findings are in full accordance with those reported in a previous paper, where the effect of a very high amount of MHEC was investigated.[11]

These changes in k_B and k_G values are reflected in significant differences in k_B/k_G ratios of the samples containing MHEC with respect to the k_B/k_G ratio of the C_3S sample. In the original formulation of BNG model,[13] Thomas described this ratio as indicative of the kinetic behavior of the pastes. In particular, the following two limiting conditions have been identified: (a) $k_B/k_G \gg 1$ when the boundary area per unit volume O_v^B is small and I_B/G (nucleation rate/linear growth rate ratio) is large; and (b) $k_B/k_G \ll 1$ when O_v^B is large and I_B/G is small, corresponding to nuclei sparsely distributed on the internal boundaries. In the first case, the boundary area is densely populated with nuclei, and the whole transformation occurs in the very early stages of the process, while in the second case the conditions approach to a spatially random nucleation. The C_3S sample does not perfectly fit none of these two states[11,13,32,33] while both the samples containing MHEC show a decrease of 1 order of magnitude with k_B/k_G values around 0.1. This indicates the approaching to a "spatially random nucleation" condition. A value of k_B/k_G = 0.1 has been

Table 1. Kinetic Parameters Extracted from the Combination of BNG and Diffusion Limited Model

	t_i[a] (h)	k_B (h^{-1})	k_G (h^{-1})	k_B/k_G	t_D (h)	FWI_d	G ($\mu m\ h^{-1}$)	I_B ($\mu m^{-2}\ h^{-1}$)	$D \times 10^{-15}$ ($m^2\ h^{-1}$)
C_3S	6(1)	0.098(8)	0.049(2)	2.00	17(2)	0.49	0.050(2)	0.75(5)	3.1(9)
C_3S+M_low	9(1)	0.068(2)	0.46(6)	0.15	17(2)	0.39	0.47(6)	0.00021(2)	9(3)
C_3S+M_high	12(1)	0.053(1)	0.39(2)	0.14	21(2)	0.40	0.40(2)	0.00012(3)	5(2)

[a]The induction time t_i was evaluated by graphical method, as described in the text.

DOI: 10.1021/acs.jpcc.6b00691
J. Phys. Chem. C 2016, 120, 7612−7620

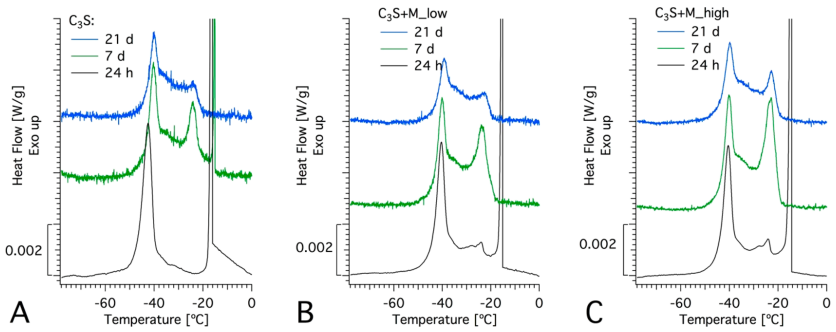

Figure 2. LT-DSC thermograms of hydrated C_3S (A), C_3S + M_low (B), and C_3S + M_high (C) samples.

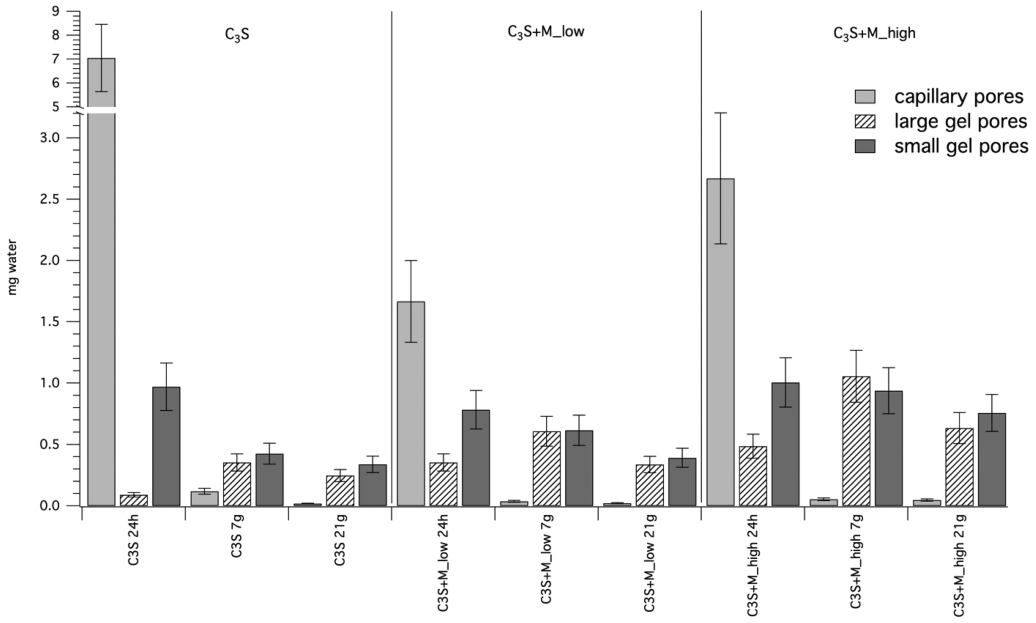

Figure 3. Histograms showing the amount of water contained in the porosity of the three samples during the hydration process.

reported in a previous paper, where even higher MHEC concentrations were used.[11] This indicates that the nature of the nucleation process does not depend on the concentration but only on the chemistry of the organic additive.

The linear growth rate G and the nucleation rate I_B have been calculated according to the eqs 10 and 11 and the obtained values are reported in Table 1. The cellulose−ether does not modify significantly the growth rate, but it is very effective in reducing the nucleation rate whose value decreases of 3 orders of magnitude with respect to the C_3S/water sample.

The samples have been analyzed by means of low-temperature differential scanning calorimetry (LT-DSC) in order to monitor the state of the water confined inside the hydrating matrix during a time range spanning from 24 h to 21 days. By slowly cooling down the samples[34] (the cooling rate must be slow enough to maintain the equilibrium conditions), the freezing of the water confined inside the matrix produces some exothermic features at temperatures well below 0 °C, whose position are strongly dependent on the C−S−H microstructure characteristics. In particular, the thermograms shown in Figure 2A−C evidence that in the three samples cured for 24 h, a sharp peak is present around −15 °C and this is ascribable to the freezing of bulk water still present in the largest cavities (capillary pores). The freezing of the water entrapped in nanometric pores causes the peaks to shift at lower temperature. The literature reports that the thermal feature in the range −20/−35 °C are due to water in cavities ranging between 4 and 12 nm (large gel pores, LGP) while the peak at −40 °C stems from the freezing of the water in the small gel pores, SGP, with size 1−3 nm.[3] It is worth reminding

DOI: 10.1021/acs.jpcc.6b00691
J. Phys. Chem. C 2016, 120, 7612−7620

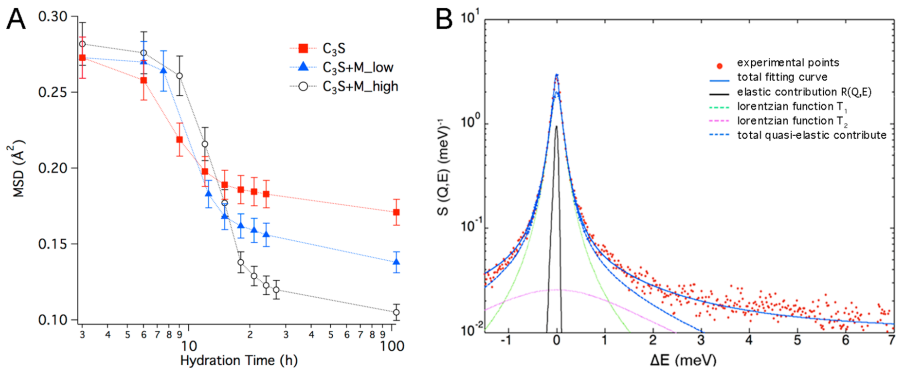

Figure 4. (A) MSD obtained by the elastic component of the QENS spectra during the first 4 days of hydration for pure C_3S and in the presence of different concentrations of MHEC. An example of the calculation of MSD in the case of the C_3S sample at different times can be found in Figure S2 (see Supporting Information). (B) QENS spectrum of C_3S sample after 2.5 h of hydration, registered at $\mathbf{Q} = 0.67$ Å^{-1}, fitted with eq 3.

here that, according to the Jennings' Colloidal Model II, another class of pores exists in C−S−H, named interlayer gel pores (IGP), whose size is <1 nm, due to the quasi-two-dimensional spaces[7] between the silicate chains in the basic globules of C−S−H. The water in the IGP does not show signals in DSC, because the extreme confinement prevents these molecules from freezing.[5]

After 24 h of curing (black line), the C_3S/water sample (Figure 2A) contains water in capillary pores and in SGP, as evidenced by the presence of the peaks centered respectively at −15 and −40 °C. The samples containing MHEC (Figure 2A,B) also show the typical feature of LGP, indicating that the cellulose ether affects the formation of the microstructure. After 7 days (green lines), the C_3S sample still contains water in capillary pores, while in the two other samples all the remaining water is confined in the nanometric porosity (both SGP and LGP). As time increases, the intensity of the peaks decreases due to the consumption of the water in the reaction of formation of the hydrated phases.

The area of the peaks was measured, and the amount of water confined in the three types of pores was estimated according to a procedure described elsewhere.[5] The histograms in Figure 3 show how the water still present in the samples is distributed in the three classes of pores during the hydration process. The MHEC has the effect of reducing the amount of capillary water due to a more efficient hydration reaction. At the same time, the water contained in the nanometric porosity (both SGP and LGP) at later stages is increased in the presence of the cellulose ether with respect to the plain sample. The presence of these "nanoreservoirs" with size ranging approximately from 1 to 12 nm is very important because they entrap the water in the matrix and allow for its diffusion toward the anhydrous phases ensuring the continuation of the hydration reaction in a very efficient way.

QENS Analysis. As shown in Figure 4A, the mean square displacement extracted by the elastic part of QENS as a function of $\mathbf{Q}^2$ decreases as time passes, its evolution mirroring the three stages of the hydration kinetics (see, for example, Figures 1 or 3). While the initial $\langle u^2 \rangle$ value is about 0.28 Å^2 for all the stages of the hydration kinetics the addition of MHEC leads to a reduction in the plateau value from 0.17 Å^2 for C_3S in pure water to 0.1 Å^2 in the presence of 0.54% MHEC as a clear result of the increase in the confinement imposed by the presence of the additive. The extracted mean-square displacement (MSD) values are in good agreement with recent MD simulations[35] run on water and −OH groups confined in the C−S−H model systems while at the same time scale probed by our neutron scattering experiment.

Figure 4B shows, as an example, the semilogarithmic representation of a QENS spectrum in the case of a 2.5 h hydrated C_3S paste at $\mathbf{Q} = 0.67$ Å^{-1}. The width of the quasi-elastic components is usually inversely proportional to the relaxation time of the considered dissipative phenomenon, according to $\tau = h/2\pi\Gamma$.

The analysis of Γ_1 with respect to the scattering vector $\mathbf{Q}$ allows for the characterization of the dynamic response of the system due to the external perturbation. In the case of a Brownian liquid, the broadening of the scattering curve grows linearly with $\mathbf{Q}^2$ and the diffusion coefficient can be simply extracted by the slope of the curve.[36] When the system is confined, the translational symmetry vanishes and an elastic peak appears in the spectrum. The broadening of such an elastic contribute is overestimated by the simplistic Brownian model, and a more detailed representation of the system is needed. Water has many features that make it different from other liquid systems. However, in an attempt to rationalize its peculiar chemical and physical properties it could be pictured as a tetrahedral network of molecules held together by intermolecular hydrogen bonds.[37] A drop in temperature determines a slowing down of the individual dynamics of water molecules caused by the increasing extension of the hydrogen bond framework. Free diffusion turns out to be hindered, and translations of a single water molecule can take place only after the rearrangement of a great number of molecules and the collapse of the aqueous network.[28] Similarly, the dynamics of water entrapped in a solid matrix of calcium silicate hydrate is affected by the spatial confinement imposed by the C−S−H developing architecture, which changes the hydrogen bonds connectivity (i.e., both OH and water dynamics). The molecular mechanism behind H-bonds effect in water confined in a C−S−H model system has been clearly discussed in a recent paper.[35] In the present case, due to the resolution of the QENS experiment, to interpret the broadening of the scattering curve of C_3S and C_3S + MHEC samples

DOI: 10.1021/acs.jpcc.6b00691
J. Phys. Chem. C 2016, 120, 7612−7620

the random jump diffusion model[38,39] was adopted. This model considers the motion of a particle (in our case the H atom) as composed by the continuous repetition of a vibration around a certain equilibrium position and by a diffusional translation characterized by a diffusion time τ_0.

The trend of Γ_1 (relative to the translational component) versus $\mathbf{Q}^2$ for the three investigated samples shows a good agreement with the random jump diffusion model in the low $\mathbf{Q}^2$ range. As an example, the fitting obtained for the C_3S sample is shown in the Supporting Information in Figure S2.

The width Γ_2 of the Lorentzian function, associated with rotational motions of water molecules, is much broader but clearly recognizable. The width of this function is constant over the whole $\mathbf{Q}$ range investigated, confirming that the confinement effect of the matrix exerts an influence only on water translational dynamics.

The fitting function derived from the jump diffusion model is

$$\Gamma_1(\mathbf{Q}) = \frac{D\mathbf{Q}^2}{1 + D\mathbf{Q}^2\tau_0} \quad (11)$$

where D is the translational diffusion coefficient and τ_0 is the time between the breaking and the restoring of the hydrogen-bonded network. The relaxation time τ_0 is related to the local environment experienced by the water molecules. The increasing hydration degree of the calcium silicate paste and the development of the C−S−H matrix progressively confine water molecules in the nano- and microsized pores of the gel leading to a pronounced slowing down of H dynamics. This trend is shown in Figure 5, which shows τ_0 as a function of

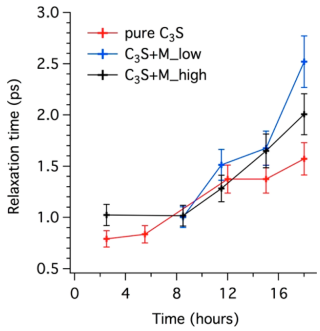

Figure 5. Translational relaxation times τ_0 derived from the fitting of Γ_1 for the first 18 h of hydration.

hydration time. In the case of the C_3S paste, τ_0 increases with time as a result of the confinement imposed by the C−S−H matrix, passing from 0.8 ps to about 1.4 ps after 18 h of hydration. For hydration times longer than 12 h the presence of MHEC causes the increase of τ_0 with respect to the C_3S sample. After 18 h, τ_0 increases from 1.6 ps to more than 2.0 ps. Such a trend could be explained assuming that MHEC induces a faster development of the C−S−H structure. In particular, this effect is more prominent for C_3S + M_low than C_3S + M_high due to the longer delay (see Figure 1) imposed at the early stage of the hydration reaction by the presence of a higher MHEC concentration.

Figure 6 shows the semilogarithmic representation of the QENS spectrum from the C_3S paste at $\mathbf{Q} = 0.67$ Å^{-1} fitted with

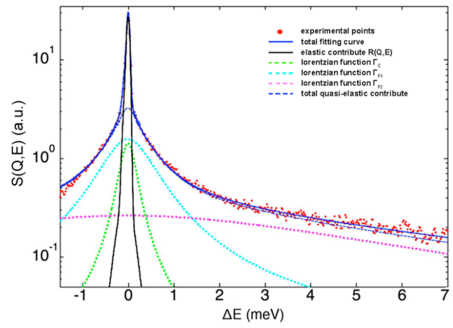

Figure 6. QENS spectrum averaged at high $\mathbf{Q}$ (1.9−2.5 Å^{-1}) for C_3S sample after 2.5 h of hydration. Continuous and dashed lines represent the total intensity obtained with eq 4 and all the different contributions present in the model.

eq 4. Considering the scattering law expressed by this model, the amplitudes P, C, F_1, and F_2 represent the absolute abundance of immobile water ($Ca(OH)_2$ and C−S−H), chemically bound water, and free water, respectively. The main difference from the previous model is that each species contributing to scattering is explicitly taken into account by a single function, instead of considering only an average contribute. The limit of this approach is that the molecular information connected to the type of dynamics is lost. On the other hand, quantitative information on the different fraction of hydrogen populations classified according to their mobility can be extracted.

The values of Γ_{F1} and Γ_{F2} associated with free water have been extracted from the fitting of the QENS spectrum relative to freshly hydrated samples (i.e., 2.5 h), assuming that the hydration was negligible at this time. Γ_{F1} and Γ_{F2} have been constrained to these values for all spectra with $t > 2.5$ h.

By plotting the immobile water fraction against the hydration time it is possible to gain insights on the reaction kinetics. Three distinct kinetic stages (as in the DSC analysis of the hydration process were the FWI is followed) can be recognized from Figure 7. In the first 5 h during the induction period, the hydration reaction occurs very slowly. After 5 h, the hydration reaction goes faster (acceleration stage) and the new hydrated

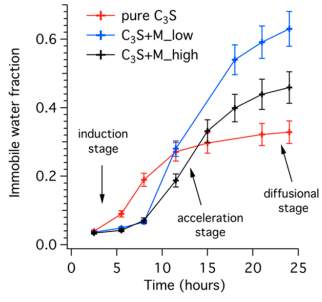

Figure 7. Immobile water fraction of the three samples as a function of hydration time. The immobile water fraction has been obtained by dividing the parameter P of the four-components model for the total area of the spectrum.

DOI: 10.1021/acs.jpcc.6b00691
J. Phys. Chem. C 2016, 120, 7612−7620

phases nucleate and grow. Finally, in the later stages (>15 h) the hydration rate is controlled by the diffusion of the reactants through the C−S−H gel phase covering the anhydrous silicate grains, and the immobile water fraction reaches a plateau (diffusional stage). All these results provide information at molecular level and confirm the DSC findings at the macroscale.

CONCLUSIONS

The hydration kinetics of C_3S obtained in the presence of two different concentrations of MHEC show that this cellulose ether retards the beginning of the hydration process while enhancing the efficiency of the reaction. In terms of water used during the acceleration stage, the enhancement does not depend on the concentration. The analysis of the hydration kinetics by means of the boundary nucleation and growth model allows recognizing that the presence of MHEC modifies the nucleation process with respect to the plain C_3S sample; in particular, the presence of the cellulose−ether dramatically reduces the overall I_B nucleation rate (while the linear growth rate G is almost unaffected) and modifies the nature of the nucleation process approaching a "spatially random" mechanism. The low-temperature DSC measurements indicated that the sample prepared with MHEC has a lower amount of capillary water than the sample without additive, tested at the same time after the mixing. Moreover, the water contained in the nanometric porosity at later stages increases in the presence of the cellulose−ether with respect to the plain sample. The presence of these "nanoreservoirs" is very important because they entrap the water in the matrix and the progress of the hydration reaction occurs in a very efficient way. Similarly QENS shows that the dynamics of water is affected by the spatial confinement imposed by the C−S−H developing architecture. The C−S−H matrix progressively confines water molecules in the nano- and microsized pores of the gel leading to a pronounced slowing down of the translational dynamics of water. Moreover, the translational relaxation times τ_0 increases with time as a result of the confinement imposed by the C−S−H matrix, passing from 0.8 to about 1.4 ps after 18 h of hydration, and the presence of MHEC further increases the water translational relaxation time, suggesting that MHEC induces a faster development of the C−S−H structure. The data taken together provide a complete picture of the C_3S hydration process providing valuable information at nano and meso-microscale.

ASSOCIATED CONTENT

Supporting Information

The Supporting Information is available free of charge on the ACS Publications website at DOI: 10.1021/acs.jpcc.6b00691.

Kinetic models, Avrami and boundary nucleation and growth; example of the calculation of the MSD from the elastic fraction of the QENS spectra; fitting of Γ_1 (HWHM of the Lorentzian function associated with translations of H atoms) versus Q^2 with the jump diffusion model at various hydration times for C_3S sample; QENS spectra of C_3S sample at various hydration times (Q = 1.11 Å^{-1}). (PDF)

AUTHOR INFORMATION

Corresponding Author

*E-mail: piero.baglioni@unifi.it. Internet: http://www.csgi.unifi.it/.

Author Contributions

The manuscript was written through contributions of all authors. All authors have given approval to the final version of the manuscript.

Notes

The authors declare no competing financial interest.

ACKNOWLEDGMENTS

S.D.B., E.F., F.R., and P.B. acknowledge financial support from Ministero dell'Istruzione, dell'Università e della Ricerca Scientifica (MiUR), and Consorzio Interuniversitario per lo Sviluppo dei Sistemi a Grande Interfase (CSGI). Authors kindly acknowledge Dr. J. M. Zanotti and R. Connatser for the help with the setup of the QENS spectrometer. Dr. J. M. Zanotti is also acknowledged for providing the data reduction routines. E.F. acknowledges Dr. I. Ciullini for the practical help during the QENS experiment.

ABBREVIATIONS

C_3S, tricalcium silicate; C−S−H, calcium silicate hydrate; MHEC, methyl hydroxyethyl cellulose; QENS, quasi elastic neutron scattering; fwhm, full width at half-maximum; HWHM, half width at half-maximum; DSC, differential scanning calorimetry; LT-DSC, low-temperature differential scanning calorimetry; BNG, boundary nucleation and growth; FWI, free water index; LGP, large gel pores; SGP, small gel pores

REFERENCES

(1) Taylor, H. *Cement Chemistry*; Thomas Telford Publishing: London, 1997.

(2) Thomas, J. J.; Jennings, H. M. A Colloidal Interpretation of Chemical Aging of the C-S-H Gel and Its Effects on the Properties of Cement Paste. *Cem. Concr. Res.* **2006**, *36*, 30−38.

(3) Jennings, H. M. Refinements to Colloid Model of C-S-H in Cement: CM-II. *Cem. Concr. Res.* **2008**, *38*, 275−289.

(4) Fratini, E.; Ridi, F.; Chen, S.-H.; Baglioni, P. Hydration Water and Microstructure in Calcium Silicate and Aluminate Hydrates. *J. Phys.: Condens. Matter* **2006**, *18*, S2467.

(5) Ridi, F.; Luciani, P.; Fratini, E.; Baglioni, P. Water Confined in Cement Pastes as a Probe of Cement Microstructure Evolution. *J. Phys. Chem. B* **2009**, *113*, 3080−3087.

(6) Hou, D.; Li, Z.; Zhao, T.; Zhang, P. Water Transport in the Nano-Pore of the Calcium Silicate Phase: Reactivity, Structure and Dynamics. *Phys. Chem. Chem. Phys.* **2015**, *17*, 1411−1423.

(7) Youssef, M.; Pellenq, R. J.-M.; Yildiz, B. Glassy Nature of Water in an Ultraconfining Disordered Material: The Case of Calcium−Silicate−Hydrate. *J. Am. Chem. Soc.* **2011**, *133*, 2499−2510.

(8) Ridi, F.; Fratini, E.; Mannelli, F.; Baglioni, P. Hydration Process of Cement in the Presence of a Cellulosic Additive. A Calorimetric Investigation. *J. Phys. Chem. B* **2005**, *109*, 14727−14734.

(9) Pourchez, J.; Grosseau, P.; Rouèche-Pourchez, E.; Debayle, J.; Pinoli, J.-C.; Maire, E.; Boller, E.; Parra-Denis, E. Impact of Cellulose Ethers on the Cement Paste Microstructure. *Proceedings of the 10th International Conference and Exhibition of the European Ceramic Society* **2007**, 2045−2050.

(10) Marliere, C.; Mabrouk, E.; Lamblet, M.; Coussot, P. How Water Retention in Porous Media with Cellulose Ethers Works. *Cem. Concr. Res.* **2012**, *42*, 1501−1512.

(11) Ridi, F.; Fratini, E.; Alfani, R.; Baglioni, P. Influence of Acrylic Superplasticizer and Cellulose-Ether on the Kinetics of Tricalcium Silicate Hydration Reaction. *J. Colloid Interface Sci.* **2013**, *395*, 68−74.

DOI: 10.1021/acs.jpcc.6b00691
J. Phys. Chem. C 2016, 120, 7612−7620

(12) Pierre, A.; Perrot, A.; Picandet, V.; Guevel, Y. Cellulose Ethers and Cement Paste Permeability. *Cem. Concr. Res.* **2015**, *72*, 117−127.
(13) Thomas, J. J. A New Approach to Modeling the Nucleation and Growth Kinetics of Tricalcium Silicate Hydration. *J. Am. Ceram. Soc.* **2007**, *90*, 3282−3288.
(14) Alesiani, M.; Capuani, S.; Giorgi, R.; Maraviglia, B.; Pirazzoli, I.; Ridi, F.; Baglioni, P. Influence of Cellulosic Additives on Tricalcium Silicate Hydration: Nuclear Magnetic Resonance Relaxation Time Analysis. *J. Phys. Chem. B* **2004**, *108*, 4869−4874.
(15) Bradley, K. F.; Chen, S.-H.; Brun, T. O.; Kleb, R.; Loomis, W. A.; Newsam, J. M. The Design and Performance of QENS, a Medium Resolution, Inverted Geometry, Tof Quasielastic and Inelastic Spectrometer at IPNS. *Nucl. Instrum. Methods Phys. Res., Sect. A* **1988**, *270*, 78−89.
(16) FitzGerald, S. A.; Neumann, D. A.; Rush, J. J.; Bentz, D. P.; Livingston, R. A. In Situ Quasi-Elastic Neutron Scattering Study of the Hydration of Tricalcium Silicate. *Chem. Mater.* **1998**, *10*, 397−402.
(17) Damasceni, A.; Dei, L.; Fratini, E.; Ridi, F.; Chen, S.-H.; Baglioni, P. A Novel Approach Based on Differential Scanning Calorimetry Applied to the Study of Tricalcium Silicate Hydration Kinetics. *J. Phys. Chem. B* **2002**, *106*, 11572−11578.
(18) Ridi, F.; Dei, L.; Fratini, E.; Chen, S.-H.; Baglioni, P. Hydration Kinetics of Tri-Calcium Silicate in the Presence of Superplasticizers. *J. Phys. Chem. B* **2003**, *107*, 1056−1061.
(19) Chen, S.-H.; Teixeira, J.; Nicklow, R. Incoherent Quasielastic Neutron Scattering from Water in Supercooled Regime. *Phys. Rev. A: At., Mol., Opt. Phys.* **1982**, *26*, 3477−3482.
(20) Gotze, W.; Sjogren, L. Relaxation Processes in Supercooled Liquids. *Rep. Prog. Phys.* **1992**, *55*, 241.
(21) Zanotti, J.-M.; Bellissent-Funel, M.-C.; Chen, S.-H. Relaxational Dynamics of Supercooled Water in Porous Glass. *Phys. Rev. E: Stat. Phys., Plasmas, Fluids, Relat. Interdiscip. Top.* **1999**, *59*, 3084−3093.
(22) Zhang, Y.; Lagi, M.; Liu, D.; Mallamace, F.; Fratini, E.; Baglioni, P.; Mamontov, E.; Hagen, M.; Chen, S.-H. Observation of High-Temperature Dynamic Crossover in Protein Hydration Water and Its Relation to Reversible Denaturation of Lysozyme. *J. Chem. Phys.* **2009**, *130*, 135101.
(23) Chen, S.-H.; Liu, L.; Fratini, E.; Baglioni, P.; Faraone, A.; Mamontov, E. Observation of Fragile-to-Strong Dynamic Crossover in Protein Hydration Water. *Proc. Natl. Acad. Sci. U. S. A.* **2006**, *103*, 9012−9016.
(24) Chu, X.; Fratini, E.; Baglioni, P.; Faraone, A.; Chen, S.-H. Observation of a Dynamic Crossover in RNA Hydration Water Which Triggers a Dynamic Transition in the Biopolymer. *Phys. Rev. E* **2008**, *77*, 011908.
(25) Zhang, Y.; Lagi, M.; Ridi, F.; Fratini, E.; Baglioni, P.; Mamontov, E.; Chen, S. H. Observation of Dynamic Crossover and Dynamic Heterogeneity in Hydration Water Confined in Aged Cement Paste. *J. Phys.: Condens. Matter* **2008**, *20*, 502101.
(26) Ridi, F.; Fratini, E.; Baglioni, P. Cement: A Two Thousand Year Old Nano-Colloid. *J. Colloid Interface Sci.* **2011**, *357*, 255−264.
(27) Fratini, E.; Chen, S. H.; Baglioni, P.; Bellissent-Funel, M. C. Quasi-Elastic Neutron Scattering Study of Translational Dynamics of Hydration Water in Tricalcium Silicate. *J. Phys. Chem. B* **2002**, *106*, 158−166.
(28) Bordallo, H. N.; Aldridge, L. P.; Desmedt, A. Water Dynamics in Hardened Ordinary Portland Cement Paste or Concrete: From Quasielastic Neutron Scattering. *J. Phys. Chem. B* **2006**, *110*, 17966−17976.
(29) Faraone, A.; Chen, S. H.; Fratini, E.; Baglioni, P.; Liu, L.; Brown, C. Rotational Dynamics of Hydration Water in Dicalcium Silicate by Quasielastic Neutron Scattering. *Phys. Rev. E: Stat. Phys., Plasmas, Fluids, Relat. Interdiscip. Top.* **2002**, *65*, 040501.
(30) Peterson, V. K.; Neumann, D. A.; Livingston, R. A. Hydration of Tricalcium and Dicalcium Silicate Mixtures Studied Using Quasielastic Neutron Scattering. *J. Phys. Chem. B* **2005**, *109*, 14449−14453.
(31) Fratini, E.; Faraone, A.; Ridi, F.; Chen, S.-H.; Baglioni, P. Hydration Water Dynamics in Tricalcium Silicate Pastes by Time-Resolved Incoherent Elastic Neutron Scattering. *J. Phys. Chem. C* **2013**, *117*, 7358−7364.
(32) Thomas, J. J.; Allen, A. J.; Jennings, H. M. Hydration Kinetics and Microstructure Development of Normal and CaCl2-Accelerated Tricalcium Silicate Pastes. *J. Phys. Chem. C* **2009**, *113*, 19836−19844.
(33) Ridi, F.; Fratini, E.; Luciani, P.; Winnefeld, F.; Baglioni, P. Hydration Kinetics of Tricalcium Silicate by Calorimetric Methods. *J. Colloid Interface Sci.* **2011**, *364*, 118−124.
(34) Neffati, R.; Rault, J. Pore Size Distribution in Porous Glass: Fractal Dimension Obtained by Calorimetry. *Eur. Phys. J. B* **2001**, *21*, 205−210.
(35) Hou, D.; Li, Z.; Zhao, T.; Zhang, P. Water Transport in the Nano-Pore of the Calcium Silicate Phase: Reactivity, Structure and Dynamics. *Phys. Chem. Chem. Phys.* **2015**, *17*, 1411−1423.
(36) Teixeira, J.; Bellissent-Funel, M.-C.; Chen, S. H.; Dianoux, A. J. Experimental Determination of the Nature of Diffusive Motions of Water Molecules at Low Temperatures. *Phys. Rev. A: At., Mol., Opt. Phys.* **1985**, *31*, 1913−1917.
(37) Dore, J. C.; Teixeira, J. Hydrogen-Bonded Liquids: Proceedings of the NATO Advanced Study Institute on Hydrogen-Bonded Liquids; Cargèse, Corsica, France, April 3−15, 1989; Kluwer: Norwell, MA, 1991.
(38) Singwi, K. S.; Sjölander, A. Resonance Absorption of Nuclear Gamma Rays and the Dynamics of Atomic Motions. *Phys. Rev.* **1960**, *120*, 1093−1102.
(39) Chudley, C. T.; Elliott, R. J. Neutron Scattering from a Liquid on a Jump Diffusion Model. *Proc. Phys. Soc., London* **1961**, *77*, 353.

DOI: 10.1021/acs.jpcc.6b00691
J. Phys. Chem. C 2016, 120, 7612−7620

SUPPORTING INFORMATION

State Of Water In Hydrating Tricalcium Silicate Pastes: The Effect Of A Cellulose Ether

Stefano Del Buffa[†], *Emiliano Fratini*[†], *Francesca Ridi*[†], *Antonio Faraone*[‡], *Piero Baglioni*[†*]

[†]Department of Chemistry "Ugo Schiff" and CSGI, University of Florence, via della Lastruccia 3, 50019 -Sesto Fiorentino, I-50019, Florence, Italy.

[‡]NIST Center for Neutron Research, 100 Bureau Drive, Gaithersburg, MD, 20899-6102, USA. [¶]Department of Materials Science and Engineering, University of Maryland, College Park, MD, 20742, USA

Kinetic models: Avrami and Boundary Nucleation and Growth

The tricalcium silicate hydration process has been frequently fitted in literature [1–5] to a standard Avrami-Erove'ev (A-E) equation, in order to rationalize the nucleation-and-growth process and to extract the parameters controlling it. The A-E equation is reported as:

$$X = 1 - \exp\left[-\left(k_{avr} t\right)^{n}\right] \quad (1)$$

where X is the volume fraction of transformed phase, k_{avr} is an effective rate constant and n is a parameter depending on the morphology of the growing phases, the type of nucleation and growth. This equation provides satisfactory results, allowing the evaluation of the rate constants of the nucleation-and-growth process for the hydration kinetic. However it has been pointed out that the characteristics of the cement pastes hydration kinetics do not completely satisfy the conditions under which the A-E model was derived. [6,7] In particular, the most critical point is that one of the assumptions in the A-E derivation is that the probability of nucleation is the same everywhere in the untransformed volume, while the nucleation process in the hydration reaction of tricalcium silicate (and of cement, in general) occurs at the grain boundaries. This incongruity has been recently overcome with the "*Boundary Nucleation and Growth Model*" (BNGM) [J.J. Thomas, J. Am. Ceram. Soc. 90 (2007) 3282–3288.] that satisfies the requirement of the initial products formation on the surface of the particles. This model, firstly developed for solid phases transformations [J. Cahn, Acta Metall. 4 (1956) 449–459.], is demonstrated to describe very well the C_3S hydration, using a minor number of parameters than A-E model.

According to the BNGM, the volume fraction of transformed phase originating from nuclei on the same grain boundary, X, can be expressed by

$$\mathrm{X} = 1 - \exp\left[-2\mathrm{O}_{\mathrm{V}}^{\mathrm{B}} \int_{0}^{\mathrm{Gt}} \left(1 - \exp\left(-\mathrm{Y}^{\mathrm{e}}\right)\right) \mathrm{dy}\right] \quad (2)$$

where $\mathrm{O}_{\mathrm{V}}^{\mathrm{B}}$ is the total area of the grain boundaries (randomly distributed in the original untransformed volume) per unit volume; G is the linear growth rate; t is the time; y is the distance from the transforming boundary; Y^e is the extended area fraction of the

intersection between a plane at distance y from the boundary and all regions nucleated on the grain boundary. Y^e results in:

$$Y^e = \frac{\pi I_B}{3} G^2 t^3 \left[1 - \frac{3y^2}{G^2 t^2} + \frac{2y^3}{G^3 t^3}\right] \qquad (\text{if } t>y/G) \qquad (3)$$

$$Y^e = 0 \qquad (\text{if } t<y/G)$$

where I_B is the nucleation rate per unit area of untransformed boundary.

The volume of the transformed phase depends on three covariant parameters, G, I_B and O_V^B, while only two degrees of freedom exist. For this reason, the hydration kinetics is described in the model in terms of two independent rates constants, k_B and k_G, k_B being the rate at which the C_3S particles are covered by the hydration products, and k_G the rate at which the hydration products fill the porosity inside the paste. Mathematically:

$$\begin{aligned} k_B &= \left(I_B O_V^B\right)^{1/4} G^{3/4} \\ k_G &= O_V^B G \end{aligned} \qquad (4)$$

To achieve a numerically solvable equation a change of variable from y=Gt to z=y/G is mandatory, so to obtain:

$$Y^e = \frac{\pi}{3} \frac{k_B^4}{k_G} t^3 \left[1 - \frac{3z^2}{t^2} + \frac{2z^3}{t^3}\right] \qquad (\text{if } t>z) \qquad (5)$$

and

$$X = 1 - \exp\left[-2k_G \int_0^t \left(1 - \exp\left(-Y^e\right)\right) dz\right] \qquad (6)$$

Equations 5 and 6 can now be computed numerically and the parameters k_B and k_G can be directly accessed by the fitting procedure implemented in the analysis software. The only independent variables are k_B and k_G while G, I_B can be univocally determined by equations 4, once O_V^B is measured by sorption isotherms or Small Angle Neutron Scattering and the rate constants (k_B and k_G) have been extracted by the fitting procedure.

Calculation of MSD

Figure S1 shows the graphical calculation of the MSD, $\langle u^2 \rangle$ from the elastic contribution of the dynamic structure factor, $S_s(\vec{Q}, E)$. In particular, at each hydration time, *t*, the mean square displacement of the hydrogen atoms in the sample can be easily calculated for the slope of straight-line obtained from the plot[M. Bée, Quasielastic neutron scattering: principles and applications in solid state chemistry, biology and materials science, Adam Hilger, Bristol and Philadelphia (1988).] $ln\{S_s(\vec{Q}, E \approx 0, t)\}$ *vs* Q^2:

$$ln\{S_s(\vec{Q}, E \approx 0, t)\} = -\frac{\langle u^2 \rangle}{3} Q^2 + \text{const}$$

where $S_s(\vec{Q}, E \approx 0, t)$ is the elastic contribution of the QENS spectrum at time *t* and scattering vector *Q*.

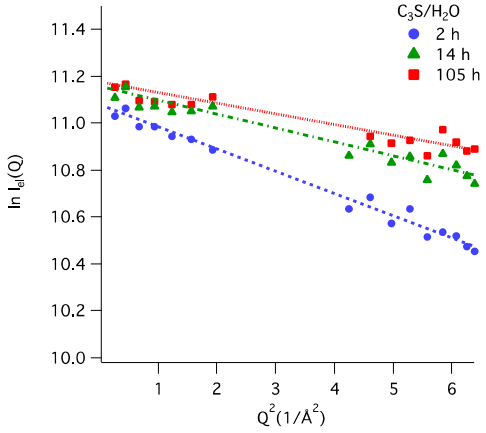

Figure S1. Example of the calculation of MSD in the case of the C_3S sample at three different times (2 h, 14h and 105h). All time steps are not shown for the sake of clarity.

Fitting of Γ_1 vs Q^2 with the Jump Diffusion Model

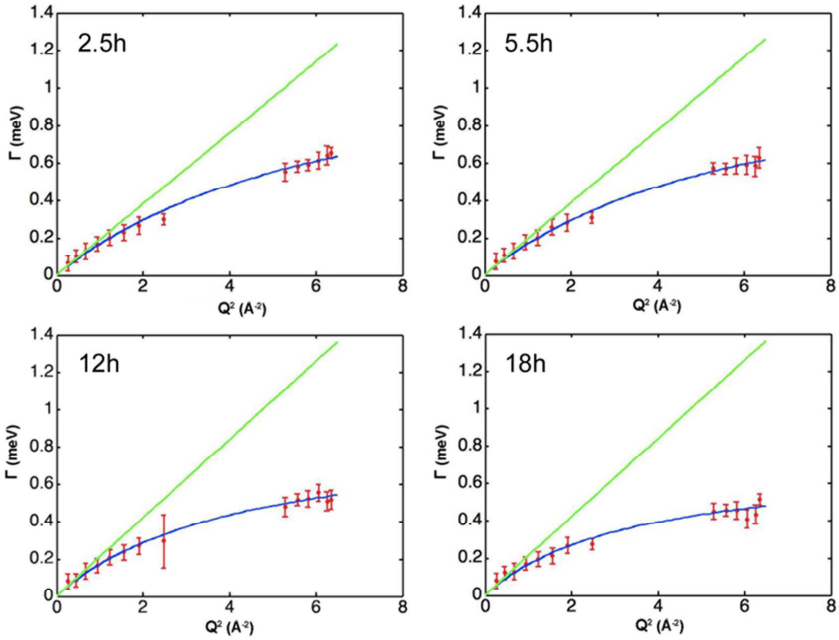

Figure S2. Fitting of Γ_1 (HWHM of the lorentzian function associated to translations of H atoms) vs Q^2 with the Jump Diffusion Model, at various hydration times for C_3S. The green line represents the trend for a brownian liquid.

QENS spectra of hydrated C_3S sample

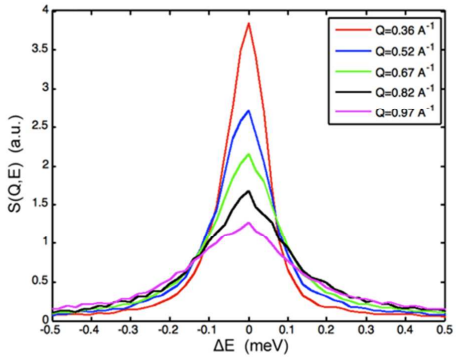

Figure S3. QENS spectra of hydrated C_3S sample (2.5 hours f hydration) obtained at Q values ranging from 0.36^{-1} to 0.97 $Å^{-1}$.

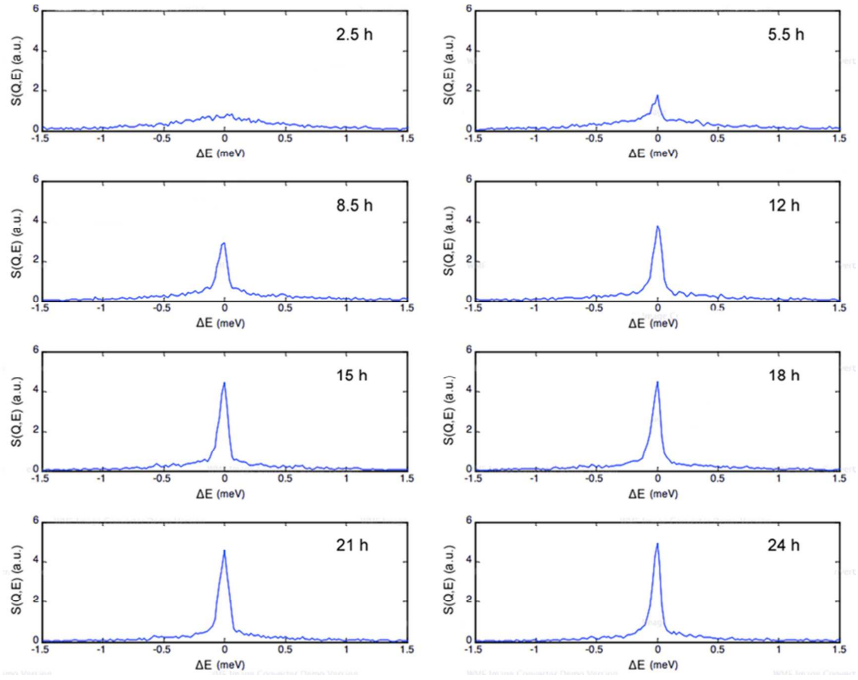

Figure S4. QENS spectra of C_3S sample at various hydration times (Q=1.11 $Å^{-1}$).

Ringraziamenti

Il ringraziamento più sentito va al mio tutore Prof. Massimo Bonini che ha rappresentato in questi tre anni di lavoro una figura di riferimento sia dal punto di vista scientifico che personale. La sua passione per la scienza, l'estrema competenza e la sua professionalità sono stati di esempio per me, spingendomi a dare sempre il massimo e ad affrontare anche i momenti più critici con entusiasmo e tenacia. Ho apprezzato tantissimo il suo fondamentale contributo in termini di idee e disponibilità, oltre alla sua fiducia nei miei confronti, e per questo lo ringrazio profondamente. L'esperienza positiva del mio dottorato, sia in termini di risultati accademici che di realizzazione personale, è in gran parte dovuta a lui.

Il lavoro di questi tre anni rappresenta il frutto di una proficua collaborazione tra diverse persone, senza le quali la realizzazione di questa tesi non sarebbe stata possibile. Un ringraziamento speciale va alla Dr. Francesca Ridi, che pur non essendo supervisore del progetto di dottorato è come se lo fosse stata, grazie alla sua continua disponibilità e al suo importante contributo durante tutto lo svolgimento del mio lavoro.
Un sentito ringraziamento va anche a tutti gli studenti e colleghi del gruppo di ricerca CSGI di Firenze, in particolare a Paolo, Rita, Claudio e Monica, che hanno contribuito a vario titolo alla realizzazione di questo lavoro e, soprattutto, a rendere estremamente piacevole e stimolante il tempo passato dentro e fuori dal laboratorio.
Un ringraziamento particolare va poi al Prof. Piero Baglioni e a tutte le persone con le quali ho lavorato nel corso di questi tre anni, in particolare Giulia Bianchetti, Micheal Remus, Emily Boswell e il gruppo del Dr. Giorgio Soldani presso l'istituto di fisiologia clinica del CNR.

Infine, un ringraziamento speciale va ai miei genitori, a tutta la mia famiglia e alle persone che mi sono state vicine, per il loro affetto e per il continuo sostegno durante questi anni.